INRS - Centre Énergie Matériaux Télécommunications

Développement d'électrocatalyseurs à base de niobium et de tantale pour la réaction d'évolution de l'oxygène

Developing Nb- and Ta-based Electrocatalysts for Oxygen Evolution Reaction

Par

Ebrahim Ghasemy

Thèse présentée pour l'obtention du grade de Philosophiae Doctor (Ph.D.)
en sciences de Énergie et Matériaux

Jury d'évaluation

Président du jury et examinateur interne	Prof. Francois Vidal
Examinateur externe	Prof. Ali Seifitokaldani
Examinateur externe	Prof. Gabriel Antonius
Directrice de recherche	Prof. Kulbir K. Ghuman
Co-directrice de recherche	Prof. Ana C. Tavares

Dedicated to

my Father, Mother, Brother,

and Grandfather

ACKNOWLEDGEMENTS

I would like to express my deepest gratitude to everyone who helped me complete this thesis. First and foremost, I am truly grateful to my supervisors, Prof. Kulbir Kaur Ghuman and Prof. Ana C. Tavares. I have learned so much from them, and their insightful guidance was invaluable at every stage of this research. It is difficult to fully express my appreciation in just a few words, but I hope they know how much their efforts, patience, and guidance have meant to me.

I would also like to thank the staff at INRS for their helpful assistance with all inquiries. A special thanks to Christophe Chabanier for his kind help in conducting XRD analyses.

Undoubtedly, conducting research for more than four consecutive years is challenging. However, the presence of friends can make this journey much easier. I was fortunate to have friends who were indeed more than just companions. So, here, I would like to express my deepest gratitude to my dearest friends whose presence continuously fueled my motivation (Parastoo, Navid, Mahmoud, and many more).

I would also like to extend my gratitude to my groupmates. In particular, I am grateful to Parastoo, Jose, Tanay, Yasser, Lakshmi, Aldo, Youssef, and Megha in Prof. Ghuman's group. Likewise, I deeply appreciate the support of Uriel, Ludmila, Hela, Benjamin, Joseph, Peyman, Shahab, Safa, and Parul in Prof. Tavares' group. Additionally, I am especially thankful to two incredible interns, Pauline and Noah, whose assistance was truly invaluable.

Finally, the most important part: nothing would have been possible without the unwavering support of my parents. Although they never had the opportunity to attend university, they wholeheartedly and unconditionally supported me in every aspect of my journey—from the first grade of elementary school to the final moments of my PhD. They mean the world to me and are my greatest pillars of strength, to whom I would like to dedicate this thesis (hoping it contributes to a more sustainable future). I am also deeply grateful to my younger brother, who has always been my best friend and a constant source of support. His encouragement has meant so much to me, and I truly appreciate all he has done. I officially began my PhD just 20 days after my grandfather passed away—a man who was, and always will be, my role model. Though he will never read this, I want to express my deepest gratitude to him for instilling in me a mindset of resilience and perseverance. His wisdom and values continue to guide me, and I carry his lessons in my heart. Lastly, I would like to conclude this acknowledgment by

expressing my heartfelt thanks to my uncles, who were the first friends in my life and have always been there to support me.

Ebrahim

ABSTRACT

Global warming and climate change are significant threats to the health of humans and the environment. One of the strategies to tackle this issue is to decarbonize industries using green hydrogen. Water electrolysis is the most sustainable method of producing green hydrogen, which comprises oxygen evolution reaction (OER) on the anode and hydrogen evolution reaction (HER) on the cathode. The superiority of proton exchange membrane (PEM) electrolyzers over other electrolysis technologies has attracted attention to this technology, which works in acidic media. However, the acidic environment imposes challenges for the anode materials due to the corrosive conditions and sluggish kinetics of the OER. In addition, OER is thermodynamically more challenging than HER, and its high energy input limits the overall efficiency of electrolyzers. The OER consists of four proton-coupled electron transfer steps, which involve adsorbed intermediates OH*, O*, and OOH* on the catalyst surface. Therefore, both the adsorption energies and stability of the electrocatalyst affect its activity and durability.

The most active and stable OER electrocatalysts under the acidic medium are Ir- and Ru-based, which are expensive and rare. Thus, this thesis aimed to propose cost-effective OER electrocatalysts using non-precious Nb- and Ta-based materials due to their abundance in Canada and their high degree of freedom, which indicates that their electronic properties can be modified by doping, creating defects via heat treatment, etc. To this end, we employed density functional theory (DFT) calculations, a powerful tool to predict the electrocatalytic performance of materials prior to experimental tests. The computational hydrogen electrode (CHE) model was applied to evaluate the OER overpotential and free energy diagram on various sites of these materials. In this model, the adsorption free energies of OER intermediates are used to determine the Gibbs free energy change (ΔG) of each step, from which the theoretical overpotential can be calculated.

Starting with Nb-based materials, Nb-based two-dimensional (2D) transition metal carbide (MXene) was first studied. The methods to modulate the electronic and catalytic properties of Nb_2C using terminating groups and surface defects were investigated. The terminations, including S, F, Cl, and their combinations, were chosen to functionalize the Nb_2C surface. The results showed that terminating the Nb_2C surface leads to a work function range of 3.79 to 5.07 eV, where S- and Cl-terminated surfaces exhibited the highest and lowest work functions, respectively. Moreover, in terms of the reactivity of MXene, the *d*-band center relative to the

Fermi level was in the range of -2.53 to -1.53 eV, where all terminating groups shifted it far from the Fermi level. According to d-band theory, the position of the d-band center with respect to the Fermi level shows the adsorption strength of reaction intermediates. This is crucial because too strong adsorption can prevent the desorption of intermediates, while too weak adsorption can limit the activation. Therefore, optimal catalytic activity is associated with a moderate d-band position. Based on this theory, the closer the *d*-band center to the Fermi level, the stronger the affinity of the surface toward the adsorption of reaction intermediates, which is the major problem of bare Nb_2C in OER electrocatalysis.

Then, on Nb_2C-S and Nb_2C-Cl, a surface defect was created by removing a terminating atom. The dissociation of H_2O, O_2, N_2, and CO_2 on Nb_2C-S_{x-1} and Nb_2C-Cl_{x-1} with a defect was analyzed using Climbing Image Nudge Elastic Band (CI-NEB) calculations. These molecules were chosen since they are relevant to the OER environment and gas-phase processes: water dissociation is the initial step of OER, and oxygen, nitrogen, and CO_2 are relevant for other electrocatalytic applications. The Nb_2C-S surface with a defect had the lowest dissociation barrier compared to Nb_2C-Cl, as low as 0 eV for O_2 and CO_2, and 0.16 and 0.17 eV for H_2O and N_2, respectively. This showed that terminating Nb_2C with sulfur can improve its catalytic activity, making it a potential candidate for reactions involving the dissociation of the investigated molecules.

Given the significance of catalyst durability in acidic and oxidative conditions, the stability of terminated Nb_2C MXenes was also investigated. MXenes are vulnerable to degradation under oxidative and aqueous environments. The stability of Nb_2C MXene with S, F, or Cl terminations was studied using DFT calculations. In addition, Nb_2C-X (X=S, F, or Cl)/graphene heterostructures were also studied. The results showed that the heterostructures are less prone to oxidation; in particular, Nb_2C-F/graphene had higher stability compared to other terminations. Then, NEB calculations were carried out to analyze the resistance of Nb_2C-S and Nb_2C-S/graphene to hydrolysis, which is the first decomposition step of MXenes in aqueous media. We found that the adsorption and dissociation of water were harder on Nb_2C-S/graphene, showing its better stability toward hydrolysis. Furthermore, the OER performance of Nb_2C-S/graphene (0.93 V) was better than Nb_2C-S (2.15 V). These results proved that terminating Nb_2C with S and making a heterostructure with graphene can improve the OER performance and stability of Nb_2C.

For Ta-based materials, we started with Ta_2O_5, which is the most common Ta-based material in electrocatalysis. Three different Ta_2O_5 facets, (200), (120), and (001), were studied for OER.

We found that the electronic properties and OER performance of Ta_2O_5 are strongly facet-dependent. The OER performance of facets followed the trend of Ta density on the topmost layer, where (200) with the lowest had the best OER performance and (001) with the highest had the worst performance. Moreover, we studied the correlations between OER performance metrics (including adsorption Free energy of OH*, O*, and OOH* intermediates, and Gibbs Free energy of each four steps) and electronic properties of Ta_2O_5. These correlations were explored to identify computational descriptors that could predict OER activity and guide future material design without full OER calculations. We found that the adsorption Free energy of OOH* and OH*, and $\Delta G_{Step1-4}$ on the (200) facet shows moderate correlations with the sum of valence electrons in radii of 3 Å of the studied Ta site. Moreover, on the (120) facet, the Bader charge of the active site and information derived from PDOS of *d* orbitals of Ta atoms could modulate the OER performance metrics. Finally, the (200) Ta_2O_5/graphene heterostructure was also analyzed, which showed a low overpotential of 0.39 V. This project revealed that synthesizing Ta_2O_5/graphene heterostructure, while preventing the formation (001) facet, could provide an active electrocatalyst for OER under acidic media.

In addition to Ta_2O_5, sodium tantalates, including $NaTaO_3$ and $NaTa_3O_8$, were investigated for OER. The DFT calculations showed that (020) $NaTaO_3$, as well as (220) and (022) $NaTa_3O_8$ facets had metallic behavior, while (202) $NaTa_3O_8$ and (101) $NaTaO_3$ were insulating with bandgaps of 1.72 and 1.03 eV, respectively. However, both NaTaO3 facets showed large OER overpotentials (> 4.8 V). Among $NaTa_3O_8$ facets, only the (202) facet had a comparatively low overpotential of 1.13 V on Ta sites. The lower overpotential of Ta sites on the (202) $NaTa_3O_8$ can be attributed to the lower contribution of Ta d orbitals at the Fermi level compared to (220) and (022) facets. In addition, Na sites on (202) $NaTa_3O_8$ had the lowest overpotential of 0.59 V. In this study, only the pristine form of $NaTa_3O_8$ was investigated. Also, since it showed a comparatively low overpotential, we believe that $NaTa_3O_8$ has the potential to show better OER activity after doping or creating defects.

Keywords: Oxygen evolution reaction (OER), Water electrolysis, Electrocatalysis, Density functional theory (DFT), Two-dimensional transition metal carbide (MXene), Nb_2C, Graphene, Terminating groups, Defects, Ta_2O_5, $NaTaO_3$, $NaTa_3O_8$.

RÉSUMÉ

Le réchauffement climatique et les changements climatiques représentent des menaces majeures pour la santé humaine et l'environnement. L'une des stratégies pour faire face à ce problème consiste à décarboner les industries à l'aide de l'hydrogène vert. L'électrolyse de l'eau est la méthode la plus durable pour produire de l'hydrogène vert, reposant sur la réaction d'évolution de l'oxygène (OER) à l'anode et la réaction d'évolution de l'hydrogène (HER) à la cathode. La supériorité des électrolyseurs à membrane échangeuse de protons (PEM) par rapport aux autres technologies d'électrolyse a suscité un vif intérêt, notamment parce qu'ils fonctionnent en milieu acide. Toutefois, cet environnement acide pose des défis importants pour les matériaux d'anode, en raison de conditions corrosives et de la cinétique lente de l'OER. En outre, l'OER est thermodynamiquement plus contraignante que la HER, et son exigence énergétique élevée limite l'efficacité globale des électrolyseurs. L'OER se compose de quatre étapes de transfert d'électrons couplées à des transferts de protons, impliquant des intermédiaires adsorbés de type OH*, O* et OOH* à la surface du catalyseur. Ainsi, les énergies d'adsorption et la stabilité du catalyseur électrochimique influencent directement son activité et sa durabilité.

Les catalyseurs électrochimiques les plus actifs et stables pour l'OER en milieu acide sont à base d'iridium ou de ruthénium, des métaux rares et coûteux. Cette thèse vise donc à proposer des catalyseurs alternatifs et économiques à base de niobium (Nb) et de tantale (Ta), qui sont abondants au Canada et dont les propriétés électroniques peuvent être modulées (dopage, création de défauts par traitement thermique, etc.). Pour cela, nous avons utilisé la théorie de la fonctionnelle de la densité (DFT), un outil puissant permettant de prédire la performance électrocatalytique des matériaux avant les essais expérimentaux. Le modèle de l'électrode hydrogène computationnelle (CHE) a été utilisé pour évaluer la surtension d'OER et le diagramme d'énergie libre sur différentes surfaces. Dans ce modèle, les énergies libres d'adsorption des intermédiaires sont utilisées pour calculer les variations d'énergie libre de Gibbs (ΔG) de chaque étape, ce qui permet d'estimer la surtension théorique.

Nous avons d'abord étudié les matériaux à base de Nb, en commençant par un carbure métallique bidimensionnel de type MXène (Nb_2C). Des méthodes de modification des propriétés électroniques et catalytiques de Nb_2C ont été explorées via l'ajout de groupes terminaux et la création de défauts de surface. Les terminaisons choisies (S, F, Cl et leurs combinaisons) permettent de fonctionnaliser la surface de Nb_2C. Les résultats ont montré que la terminaison

de la surface modifie la fonction de travail dans la plage de 3,79 à 5,07 eV, les surfaces S-terminées et Cl-terminées présentant respectivement les valeurs les plus élevées et les plus faibles. En ce qui concerne la réactivité, la position du centre de bande d par rapport au niveau de Fermi varie entre -2,53 et -1,53 eV, indiquant un éloignement induit par les groupes terminaux. Selon la théorie de la bande d, cette position reflète la force d'adsorption des intermédiaires réactionnels : trop proche du niveau de Fermi, l'adsorption est trop forte et entrave la désorption ; trop éloignée, elle limite l'activation. Une position modérée du centre de bande d est donc optimale. Dans le cas de Nb_2C nu, une affinité trop élevée des intermédiaires constitue un inconvénient majeur pour l'OER.

Ensuite, des défauts de surface ont été introduits sur Nb_2C-S et Nb_2C-Cl en retirant un atome de terminaison. La dissociation de H_2O, O_2, N_2 et CO_2 sur les surfaces défectueuses Nb_2C-Sx-1 et Nb_2C-Clx-1 a été analysée à l'aide de la méthode CI-NEB (Climbing Image Nudged Elastic Band). Ces molécules ont été choisies pour leur pertinence dans l'environnement de l'OER et dans d'autres processus électrocatalytiques : la dissociation de l'eau est l'étape initiale de l'OER, tandis que l'interaction avec l'oxygène, l'azote et le CO_2 est également critique. La surface Nb_2C-S avec défaut a présenté les barrières de dissociation les plus faibles, atteignant 0 eV pour O_2 et CO_2, et respectivement 0,16 et 0,17 eV pour H_2O et N_2. Cela montre que la terminaison soufrée de Nb_2C améliore son activité catalytique et en fait un candidat prometteur pour des réactions de dissociation.

Compte tenu de l'importance de la durabilité en milieu acide et oxydant, la stabilité des MXènes Nb_2C terminés a été évaluée. Les MXènes sont vulnérables à la dégradation en environnement aqueux oxydant. Nous avons étudié par DFT la stabilité de Nb_2C avec des terminaisons S, F ou Cl. De plus, des hétérostructures Nb_2C-X (X=S, F ou Cl)/graphène ont été analysées. Les résultats indiquent que les hétérostructures sont moins sensibles à l'oxydation ; en particulier, Nb_2C-F/graphène s'est révélée plus stable. Des calculs NEB ont ensuite été effectués pour étudier la résistance à l'hydrolyse (première étape de décomposition en solution aqueuse) des surfaces Nb_2C-S et Nb_2C-S/graphène. L'adsorption et la dissociation de l'eau y sont plus difficiles, ce qui indique une meilleure stabilité. Par ailleurs, la performance OER de Nb_2C-S/graphène (0,93 V) dépasse celle de Nb_2C-S (2,15 V). Ces résultats confirment que la terminaison soufrée et la structuration en hétérostructure avec le graphène améliorent la stabilité et l'activité électrocatalytique de Nb_2C.

Pour les matériaux à base de Ta, nous avons d'abord étudié Ta_2O_5, le composé le plus couramment utilisé en électrocatalyse. Trois facettes cristallines de Ta_2O_5, à savoir (200), (120) et (001), ont été examinées pour l'OER. Les propriétés électroniques et la performance OER de Ta_2O_5 se sont révélées fortement dépendantes de la facette. La performance suivait la densité de Ta en surface : la facette (200), avec la densité la plus faible, offrait la meilleure activité, tandis que (001), avec la plus élevée, présentait les performances les plus faibles. Des corrélations entre les métriques de performance OER (énergies libres d'adsorption de OH*, O*, OOH* et ΔG des quatre étapes) et les propriétés électroniques de Ta_2O_5 ont été explorées afin d'identifier des descripteurs prédictifs utiles à la conception rationnelle de catalyseurs. Sur la facette (200), des corrélations modérées ont été observées avec la somme des électrons de valence dans un rayon de 3 Å autour du site Ta. Sur (120), la charge de Bader du site actif et la densité d'états projetée (PDOS) des orbitales d des atomes de Ta ont montré un impact notable sur la performance. Enfin, une hétérostructure Ta_2O_5(200)/graphène a été modélisée et a présenté une faible surtension de 0,39 V. Ce projet a révélé que la synthèse d'hétérostructures Ta_2O_5/graphène tout en évitant la formation de la facette (001) pourrait conduire à des catalyseurs actifs pour l'OER en milieu acide.

En plus de Ta_2O_5, des tantalates de sodium, notamment $NaTaO_3$ et $NaTa_3O_8$, ont été étudiés. Les calculs DFT ont montré que les facettes (020) de $NaTaO_3$ ainsi que (220) et (022) de $NaTa_3O_8$ présentent un comportement métallique, tandis que (202) de $NaTa_3O_8$ et (101) de $NaTaO_3$ sont isolantes, avec des bandes interdites de 1,72 et 1,03 eV, respectivement. Toutefois, les deux facettes de $NaTaO_3$ ont montré de fortes surtensions OER (> 4,8 V). Parmi les facettes de $NaTa_3O_8$, seule la facette (202) présentait une surtension modérée de 1,13 V sur les sites Ta. Cette meilleure performance est attribuée à une plus faible contribution des orbitales d de Ta au niveau de Fermi par rapport aux autres facettes. Par ailleurs, les sites Na sur (202) ont montré la plus faible surtension, avec 0,59 V. Dans cette étude, seule la forme parfaite (pristine) de $NaTa_3O_8$ a été explorée. Étant donné ses performances prometteuses, $NaTa_3O_8$ pourrait offrir une meilleure activité OER après dopage ou introduction de défauts.

Mots-clés: Réaction d'évolution de l'oxygène (OER), Électrolyse de l'eau, Électrocatalyse, Théorie de la fonctionnelle de la densité (DFT), Carbure de métal de transition bidimensionnel (MXène), Nb_2C, Graphène, Groupes terminaux, Défauts, Ta_2O_5, $NaTaO_3$, $NaTa_3O_8$.

SOMMAIRE RÉCAPITULATIF

Introduction

Le réchauffement climatique et le changement climatique posent des risques significatifs et menacent la santé et le bien-être des humains et des animaux. Selon l'Accord de Paris [1], le réchauffement climatique doit être maintenu en dessous de 2 °C par rapport aux niveaux préindustriels, avec pour objectif de le limiter à 1,5 °C. La décarbonisation des industries, par le biais de solutions telles que l'utilisation de l'hydrogène vert, est cruciale pour atteindre ces objectifs. En effet, l'hydrogène constitue une voie durable pour réduire les émissions, en tant que vecteur énergétique à faible teneur en carbone et matière première pour divers processus industriels**[2, 3].** Conformément aux efforts mondiaux, le gouvernement du Canada s'est engagé à réduire les émissions de gaz à effet de serre (GES) de 40 à 45 % par rapport aux niveaux de 2005 d'ici 2030, et à atteindre la carboneutralité des émissions de GES d'ici 2050 [4]. La Stratégie canadienne sur l'hydrogène met en avant le potentiel de l'hydrogène propre pour couvrir jusqu'à 30 % de la demande énergétique du Canada d'ici 2050, réduisant potentiellement les émissions de CO_2 équivalent jusqu'à 190 millions de tonnes grâce à son utilisation dans le transport, le chauffage et l'industrie [5].

Malgré le grand potentiel de l'hydrogène vert, avec des émissions minimales de CO_2 (alimenté par des sources d'énergie renouvelables telles que l'éolien, le solaire, l'hydroélectricité, etc.), son coût de production (variant de 4,15 à 10,4 USD/kg [6]) est plus élevé que celui des technologies à base de combustibles fossiles, en raison du coût élevé des électrolyseurs (y compris le prix de l'électricité d'entrée et les composants de l'empilement, tels que les électrocatalyseurs à base d'iridium) [7], ce qui limite sa viabilité économique et son utilisation à grande échelle dans les applications industrielles et énergétiques. À un coût de production de 2,50 USD/kg, l'hydrogène vert peut répondre à 8 % de la demande énergétique mondiale, et la réduction de son coût à 1,80 USD/kg d'ici 2030 devrait augmenter sa part à 15–18 % de la demande énergétique mondiale [8]. Les sections suivantes examinent les méthodes de production d'hydrogène, en mettant l'accent sur les technologies de production d'hydrogène vert. De plus, des stratégies pour développer des électrocatalyseurs à faible coût sont explorées, afin de réduire le coût de l'hydrogène vert produit par électrolyse.

Méthodes de production d'hydrogène

Plus de 100 technologies ont été mises au point pour la production d'hydrogène, tandis que plus de 80 % d'entre elles se concentrent sur la conversion à la vapeur des combustibles fossiles, et environ 70 % sur le vaporeformage du gaz naturel [9]. Les méthodes de production d'hydrogène sont catégorisées par des « couleurs » en fonction de leurs sources d'énergie et de leurs émissions de GES, afin de mieux comprendre leurs impacts environnementaux, comme résumé dans la Figure 1 [10]. Les méthodes de production d'hydrogène telles que le brun, le gris et le noir émettent des quantités importantes de GES, ce qui les rend particulièrement nuisibles pour l'environnement [10]. Les méthodes de production d'hydrogène les plus dominantes à base de combustibles fossiles sont étudiées dans les sous-sections suivantes.

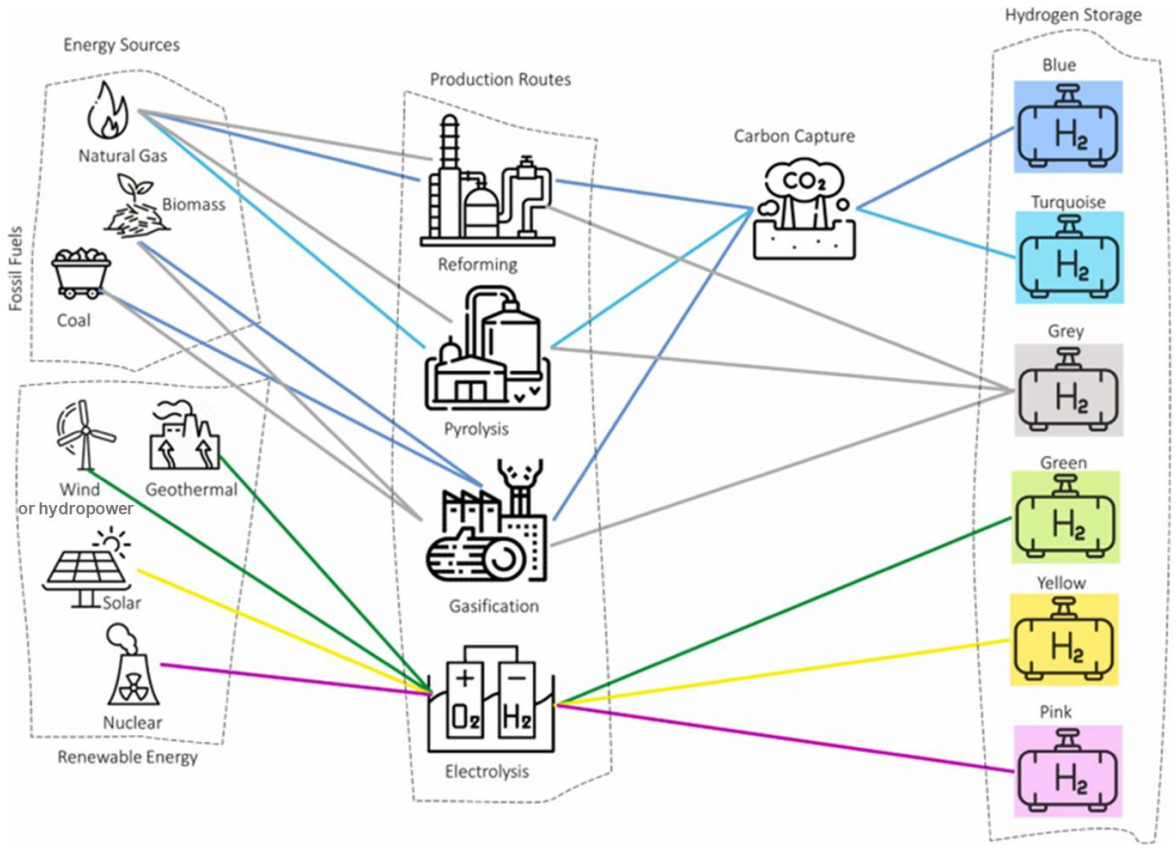

Figure 1. Classification des méthodes de production d'hydrogène en fonction de la source, de la méthode et de la couleur attribuée (Réutilisé avec l'autorisation de [11]).

Les méthodes de production d'hydrogène utilisant des ressources renouvelables incluent l'électrolyse de l'eau, la photocatalyse, le cycle thermochimique solaire de dissociation de l'eau, l'électrolyse photovoltaïque, la gazéification de la biomasse en eau supercritique, ainsi que la fermentation sombre combinée à la digestion anaérobie [12]. Parmi elles, la dissociation

électrochimique de l'eau se distingue, car elle est plus mature et envisagée pour une production d'hydrogène à grande échelle [12]. De plus, l'électrolyse de l'eau est considérée comme la technologie la plus durable pour la production d'hydrogène [13]. Différentes technologies basées sur l'électrolyse de l'eau ont été développées pour produire de l'hydrogène, notamment les électrolyseurs alcalins, les électrolyseurs à oxyde solide, les électrolyseurs à membrane échangeuse de protons (PEM), entre autres.

Électrolyseur à membrane échangeuse de protons (PEM)

L'électrolyse de l'eau à membrane échangeuse de protons (PEM) est l'une des technologies les plus prometteuses et durables pour la production d'hydrogène. Dans les électrolyseurs PEM, les réactions d'oxydation de l'eau (OER) et de réduction de l'hydrogène (HER) se produisent en milieu acide selon les équations suivantes:

Anode reaction $2H_2O \rightarrow O_2 + 4H^+ + 4e^-$

Cathode reaction $4H^+ + 4e^- \rightarrow 2H_2$

La Figure 2(a) montre l'installation d'électrolyse PEM, la Figure 2(b) représente le système d'électrolyseur PEM, et les principaux composants de la cellule sont illustrés dans la Figure 2(c). De plus, la répartition des coûts d'un électrolyseur PEM est présentée dans la Figure 2(d), mettant en évidence la part attribuée aux matériaux d'électrocatalyseurs. Dans ce système, l'eau est introduite du côté de l'anode, où elle est dissociée en oxygène, protons et électrons. Les protons traversent la membrane conductrice de protons jusqu'à la cathode. En parallèle, les électrons circulent à travers le circuit électrique externe et se recombinent avec les protons à la cathode pour former du gaz hydrogène.

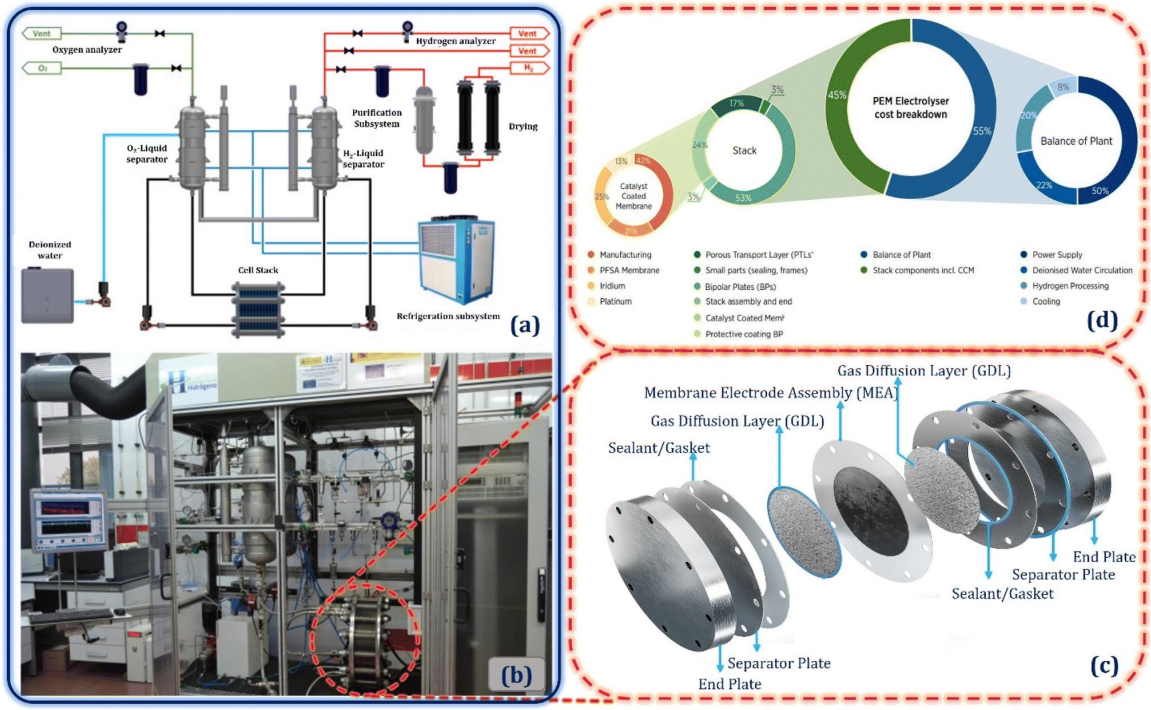

Figure 2. (a) Représentation schématique d'une installation d'électrolyse PEM. (b) Photo d'un système d'électrolyseur PEM avec (c) les principaux composants d'une cellule. (d) Répartition des coûts d'un électrolyseur PEM (Réutilisé avec l'autorisation de [14]).

Les principaux composants des électrolyseurs PEM sont la membrane, les électrodes, les couches de diffusion des gaz, les plaques bipolaires et l'équilibre de l'installation (BoP, Balance of Plant). Les avantages des électrolyseurs PEM incluent une densité de courant de fonctionnement plus élevée, une meilleure efficacité énergétique, un design compact, une réponse rapide et dynamique en combinaison avec des sources d'énergie renouvelables, ainsi qu'une grande pureté de l'hydrogène produit. Ces atouts les rendent préférables aux autres types d'électrolyseurs. L'inconvénient principal des électrolyseurs PEM réside dans la complexité du développement d'électrocatalyseurs sans métaux précieux. Actuellement, des électrocatalyseurs à base d'iridium ou de ruthénium sont utilisés pour l'OER, tandis que ceux à base de platine sont employés pour l'HER [14].

Électrocatalyse de l'OER

L'OER est l'un des processus clés dans les technologies de dissociation de l'eau pour la production d'hydrogène vert. Cette section examine les mécanismes et les critères d'évaluation

des performances des électrocatalyseurs pour l'OER, ainsi que les défis liés au développement de ces électrocatalyseurs en milieu acide.

Pour réduire les risques économiques associés à l'utilisation des électrolyseurs pour la production d'hydrogène à l'avenir, il est essentiel de développer des catalyseurs sans métaux précieux et de diversifier l'approvisionnement en matériaux catalytiques. Même la diversification des catalyseurs à base de métaux précieux peut être bénéfique [15].

Afin d'identifier des électrocatalyseurs rentables, hautement stables et efficaces pour l'OER, cette thèse s'est concentrée sur les matériaux à base de Nb et de Ta, reconnus pour leur grande stabilité [16]. Le niobium [17, 18] et le tantale [18] sont considérés comme critiques au Canada, et 8,6 % du niobium mondial y est produit. La Figure 3(a) illustre la tendance croissante des publications utilisant le niobium ou le tantale en catalyse, électrocatalyse ou photocatalyse, tandis que la Figure 3(b) montre les pays contribuant le plus à ces publications.

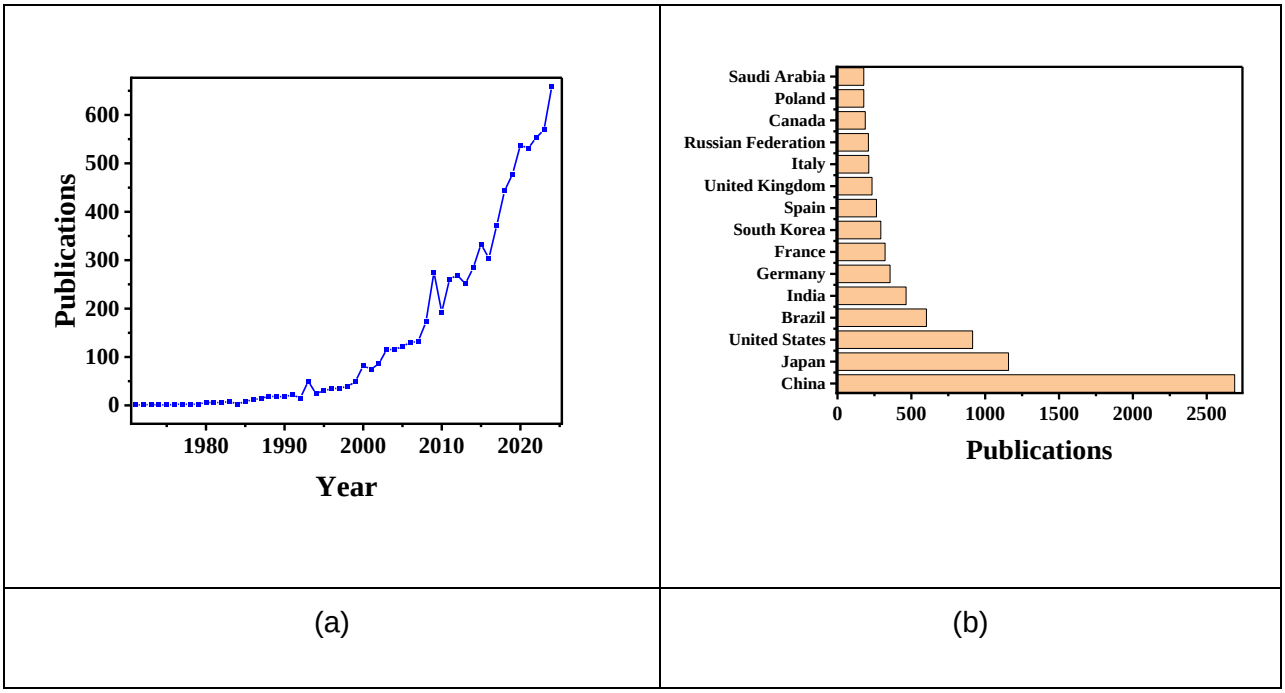

Figure 3. (a) Tendances des publications pour les mots-clés incluant catalyseur, électrocatalyseur ou photocatalyseur en combinaison avec tantale ou niobium, et (b) principaux pays contributeurs aux publications.

L'un des principaux avantages des métaux tels que le Nb et le Ta est leur grand degré de liberté [19]. Dans ce contexte, cela signifie qu'après divers traitements, tels que le dopage et le traitement thermique, ces matériaux peuvent présenter différentes propriétés électroniques et

états cristallins [19]. Cela permet de moduler les propriétés des matériaux à base de Nb et de Ta. Cependant, le principal défi de l'utilisation de ces matériaux réside dans leur faible activité pour l'OER.

Concernant l'utilisation du Nb dans l'OER, les publications de pointe se sont concentrées sur son utilisation comme dopant [20], ou sur la conception d'oxydes mixtes avec IrO_2 [21]. Par exemple, Ke et al. ont dopé le Nb dans une phase 1T d'IrO_2 (1T-IrO_2) en structure Van der Waals à arêtes partagées. Ils ont montré qu'un dopage de 5 % en Nb dans le 1T-IrO_2 pouvait réduire la surtension à 0,191 V à 10 mA/cm², avec une stabilité de plus de 50 jours à une densité de courant élevée de 1,2 A/cm² [20]. De plus, Wu et al. ont créé des lacunes en oxygène dans des oxydes métalliques tels que Nb_2O_5, puis ont immobilisé IrO_2 sur ces structures. Le matériau IrO_2/Nb_2O_{5-x} ainsi préparé a présenté une surtension de 0,225 V à 10 mA/cm² et une durabilité de plus de 200 heures [21].

Dans cette thèse, des matériaux de type carbure de métal de transition bidimensionnel (MXène), une nouvelle classe de matériaux 2D, ont été étudiés en raison de leur grande conductivité et de la possibilité de moduler leurs propriétés électroniques. Jusqu'à présent, les MXènes à base de Ti ont été les plus étudiés, tandis que ceux à base de Nb ont reçu moins d'attention [22]. Les MXènes à base de Nb ont été examinés pour l'OER, où leur forte affinité d'adsorption avec les terminaisons F, O ou OH a entraîné de faibles performances [23]. Kan et al. [23] ont montré que le dopage du Pt dans le MXène Nb_2C pouvait réduire la surtension de l'OER. Toutefois, avant le début de ce projet, aucune étude n'avait exploré l'optimisation des propriétés catalytiques des MXènes à base de Nb à l'aide de terminaisons telles que S, Cl et F, ni leurs combinaisons. En outre, un autre défi des MXènes est leur faible stabilité face à l'oxydation et à l'hydrolyse, qui détruisent leur structure lors des réactions catalytiques en solution aqueuse [24]. Il est donc essentiel de trouver des méthodes permettant d'améliorer les propriétés catalytiques des MXènes à base de Nb sans utiliser de métaux précieux, et d'augmenter leur stabilité pour leur application dans l'électrocatalyse de l'OER.

Par ailleurs, les matériaux à base de Ta, en particulier Ta_2O_5, ont été largement utilisés dans l'OER en milieu acide pour améliorer la stabilité de l'oxyde d'iridium et réduire la charge en Ir [25, 26], avec un rapport Ir/Ta de 70:30 [27]. Liu et al. ont ancré $IrRuO_x$ sur Ta_2O_5, qui contenait de nombreuses lacunes en oxygène et une grande surface spécifique. Grâce au rôle synergique d'$IrRuO_x$ et de Ta_2O_5, ils ont rapporté une faible surtension de 0,235 V à 10 mA/cm², avec une charge en Ir de 0,3 mgIr/cm² et une tension de cellule de 1,91 V pour atteindre 2 A/cm²

[28]. Huang et al. ont incorporé du bore dans un revêtement d'IrO_2-Ta_2O_5 sur une plaque de Ti via une méthode de décomposition thermique. L'échantillon préparé avec une concentration de H_3BO_3 de 0,6 M a montré une surtension de 0,210 V à 10 mA/cm², attribuée au rôle du bore dans l'ajustement de l'énergie des intermédiaires [26].

Une autre stratégie pour l'utilisation du Ta dans l'électrocatalyse de l'OER est son dopage dans d'autres oxydes, tels que le RuO_2 [29, 30]. Par exemple, Wang et al. ont dopé des atomes uniques de Ta dans le RuO_2, ce qui a déformé le réseau cristallin de RuO_2 et modifié son centre de bande d. Cela a conduit à une surtension de 0,201 V à 10 mA/cm² et une stabilité à long terme de 280 h [30]. Zhang et al. ont également stabilisé le RuO_2 en le dopant avec du Ta, obtenant un taux de dégradation de seulement 14 µV/h sur 2800 h de test. L'oxyde $Ta_{0.1}Ru_{0.9}O_{2-x}$ a affiché une surtension de 0,226 V à 10 mA/cm², démontrant son potentiel pour des applications industrielles. Ils ont aussi utilisé des calculs DFT pour expliquer comment le dopage au Ta augmentait la stabilité du RuO_2 en renforçant la liaison des intermédiaires de dissolution du RuO_4 aux sites de Ta [29].

Dans les applications industrielles, le Ta est également utilisé dans les anodes dimensionnellement stables (DSA) pour l'OER. Les DSA sont constituées d'un support métallique, tel que le Ti ou le Ta, recouvert d'une fine couche d'oxydes métalliques, comme l'IrO_2. La société De Nora a commercialisé des DSA à base de RuO_2-TiO_2 et Ti/IrO_2-Ta_2O_5 (45:55 en pourcentage atomique) [31]. Les avantages des DSA incluent leur stabilité chimique élevée, leur résistance à la corrosion et leur longue durée de vie, qui est estimée entre 8 et 9 ans [31]. Dans ce contexte, Amano et al. ont utilisé un feutre de Ti poreux composé de nanofibres comme substrat pour l'IrO_2-Ta_2O_5. Ils ont étudié l'effet du substrat en Ti et de la température de calcination sur la performance de l'électrocatalyseur. Les meilleures performances ont été obtenues à une température de calcination de 350 °C, où une fine couche amorphe d'IrO_2-Ta_2O_5 s'est formée sur le feutre de Ti. Cet électrocatalyseur a montré une surtension de 0,27 V à 10 mA/cm², avec une grande surface électrochimiquement active (ECSA [32]).

Cependant, peu de recherches ont été menées sur l'utilisation des matériaux à base de Ta comme phase active pour l'OER en milieu acide. Aucune étude n'a exploré le rôle des propriétés électroniques et des orbitales d du Ta_2O_5 dans l'amélioration des performances de l'OER. De plus, les tantalates de sodium tels que $NaTaO_3$ et $NaTa_3O_8$, qui sont stables en milieu acide, n'ont pas encore été étudiés pour l'électrocatalyse de l'OER.

Objectifs de la thèse

L'objectif principal de cette thèse est de proposer des stratégies pour moduler la performance de l'OER des MXènes à base de Nb et de développer des matériaux à base de Ta présentant une bonne activité pour l'OER. Les objectifs spécifiques incluent:

- Étudier l'effet des groupes terminaux et des défauts sur les propriétés catalytiques et électroniques des MXènes Nb_2C;
- Explorer la possibilité d'améliorer la stabilité des MXènes en modélisant une hétérostructure MXène/graphène;
- Développer des électrocatalyseurs à base d'oxydes de Ta pour l'OER, en créant des défauts, en modélisant une hétérostructure avec du graphène, et en établissant une corrélation entre les propriétés des sites de Ta et la performance de l'OER;
- Étudier les électrocatalyseurs à base de tantalates de sodium, tels que $NaTaO_3$ et $NaTa_3O_8$, pour l'OER en milieu acide.

Structure de la thèse

Le Chapitre 2 examine l'effet des groupes terminaux sur les propriétés catalytiques et électroniques des MXènes Nb_2C. Le Chapitre 3 présente les résultats des calculs DFT sur la stabilité aqueuse et oxydative de l'hétérostructure Nb_2C/graphène, ainsi que ses performances en OER. Le Chapitre 4 analyse l'activité OER de trois facettes du Ta_2O_5 et l'effet du graphène sur son amélioration. Le Chapitre 5 présente les résultats des calculs DFT sur la performance OER de $NaTaO_3$ et $NaTa_3O_8$. Enfin, le chapitre 6 conclut les résultats de la thèse et propose des perspectives futures. L'annexe A discute de la méthode DFT.

Chapitre 2: Optimisation de l'activité catalytique des MXènes Nb_2C par fonctionnalisation de surface et défauts

Les MXènes à base de Nb ont été rapportés pour diverses applications, notamment la biosurveillance électrochimique [33], les supercondensateurs [34], les batteries lithium-oxygène [35], les cellules solaires à pérovskite [36], et la réaction de dégagement d'hydrogène (HER) [37]. Les calculs DFT ont porté sur l'amélioration des performances des MXènes à base de Nb pour la HER, la OER et la réaction de réduction de l'oxygène (ORR) par l'ajout de Pd [38] et de

Pt/Pd [23]. Dans une étude DFT, Kan et al. [23] ont démontré que, en raison des états d intenses du Nb autour du niveau de Fermi, de fortes interactions se produisent entre les MXènes Nb_2C et leurs versions terminées par O et F, ainsi qu'avec les intermédiaires d'électrocatalyse de l'oxygène, ce qui entrave l'ORR et l'OER. Chu et al. [39] ont décoré des points quantiques de nitrure de bore sur le MXène Nb_2CT_x afin d'améliorer les performances de la NRR. Jusqu'à présent, seuls les MXènes Nb_2C terminés par OH, O et F ont été étudiés pour des applications catalytiques [22].

Il a été rapporté que la terminaison S améliore la stabilité et les performances électrocatalytiques des MXènes à base de Hf [40], tandis que la terminaison Cl est presque inévitable dans la synthèse des MXènes par gravure électrochimique utilisant HCl [41]. Malgré l'abondance de recherches sur les MXènes, aucune étude systématique n'a été réalisée sur les MXènes à base de Nb avec différentes terminaisons, visant à analyser leurs propriétés électroniques et catalytiques pour la dissociation de O_2, H_2O, N_2 et CO_2, ce qui pourrait s'avérer essentiel pour les recherches en cours sur la conception de catalyseurs à base de Nb_2C. De plus, l'effet des défauts dans les groupes terminaux des MXènes sur leurs propriétés catalytiques — qui apparaissent spontanément en raison des conditions de réaction ou de synthèse [42] — n'a pas été étudié.

Ce travail présente une analyse ab initio approfondie de l'effet des groupes terminaux sur les propriétés électroniques des MXènes Nb_2C pour l'adsorption et la dissociation de H_2O, O_2, N_2 et CO_2. En prenant en compte des propriétés essentielles telles que la fonction de travail, le centre de bande d, les sites actifs et les barrières de réaction, nous avons démontré le rôle des groupes terminaux S, Cl, F, ClS, FS et FCl dans l'ajustement des propriétés électroniques et de la réactivité des MXènes à base de Nb. De plus, des MXènes Nb_2C–T présentant des défauts (notés $Nb_2C–T_{x-1}$) ont également été étudiés, exposant les métaux de transition aux adsorbats. Les résultats obtenus dans cette étude mettent en évidence le rôle de la fonctionnalisation de surface et des défauts dans l'amélioration de l'activité catalytique des MXènes Nb_2C, ouvrant ainsi la voie à leur utilisation pour des réactions impliquant l'adsorption et la dissociation de O_2, H_2O, N_2 et CO_2. Les vues latérales et supérieures du Nb_2C non modifié et du Nb_2C fonctionnalisé sont illustrées à la Figure 4.

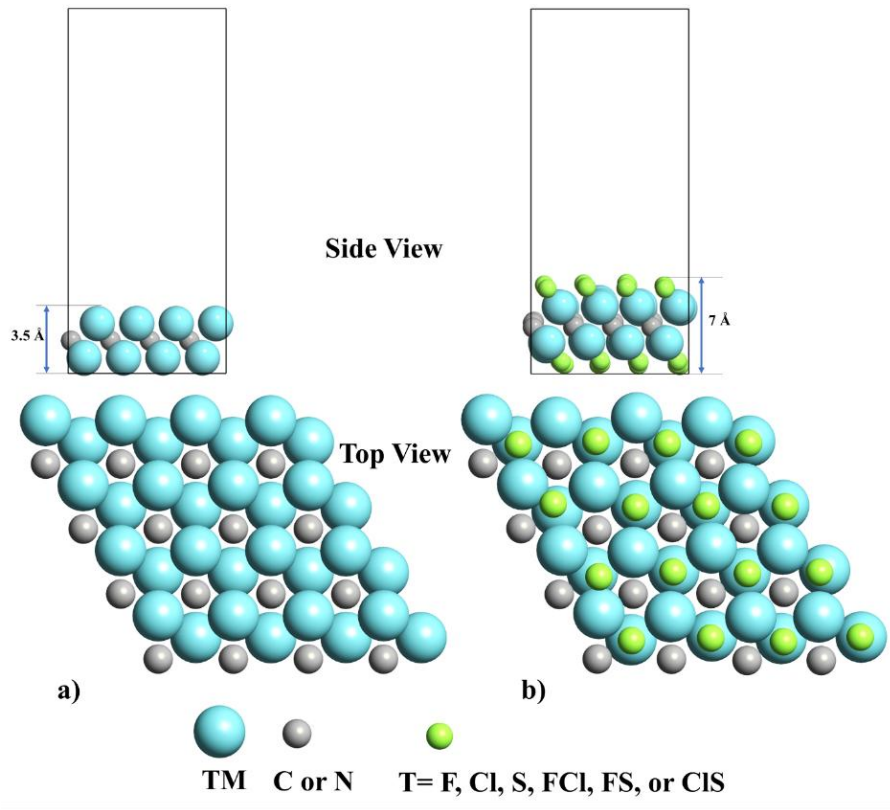

Figure 4. Vues latérale et supérieure de (a) Nb_2C pristine et (b) MXènes Nb_2C fonctionnalisés (Nb_2C-T), où T = F, Cl, S, FCl, FS ou ClS. Les atomes de Nb, C et T sont représentés respectivement par des sphères bleues, grises et vertes.

Ce travail a mis en évidence le rôle crucial des groupes terminaux S, Cl, F, ainsi que de leurs combinaisons, dans l'ajustement de la réactivité et des propriétés électroniques des MXènes Nb_2C. Nous avons constaté qu'en variant les groupes terminaux, des valeurs de fonction de travail comprises entre 3,79 et 5,07 eV peuvent être obtenues, les valeurs les plus basses et les plus élevées correspondant respectivement aux MXènes Nb_2C terminés par Cl et S.

De plus, le centre de bande d, qui détermine l'affinité d'adsorption des métaux de transition envers les intermédiaires électrocatalytiques, peut être modifié de –1,53 eV (pour le Nb_2C sans terminaison) à –2,53 eV (pour le Nb_2C avec une terminaison en S). À cet égard, les terminaisons S et Cl permettent de surmonter l'inconvénient majeur des MXènes à base de Nb, à savoir leur forte affinité d'adsorption, en décalant le centre de bande d du Nb loin de l'énergie de Fermi.

Par ailleurs, le chemin énergétique minimum associé à la dissociation de O_2, N_2, H_2O et CO_2 a confirmé que la barrière de dissociation est fortement influencée par les groupes terminaux. En particulier, la surface Nb_2C terminée par S (avec ou sans défauts) a montré la meilleure activité catalytique pour l'activation de O_2, CO_2, N_2 et H_2O parmi toutes les surfaces étudiées. Les résultats des calculs NEB sur le Nb_2C–S pristine ont révélé des énergies d'activation totales de 1,04 et 2,19 eV pour la dissociation de O_2 et H_2O, respectivement. En introduisant une lacune dans les groupes terminaux, les énergies d'activation pour la dissociation de ces molécules ont encore diminué. Des énergies d'activation totales de 0,46, 1,2, 3,2 et 3,18 eV ont été obtenues pour la dissociation de O_2, H_2O, N_2 et CO_2 sur Nb_2C–S_{x-1}, respectivement.

Ce travail ouvre de nouvelles perspectives pour améliorer l'activité catalytique des MXènes Nb_2C. Il démontre qu'en ajustant les conditions de synthèse des MXènes Nb_2C lors des expériences, il est possible d'obtenir des surfaces fonctionnalisées possédant les propriétés requises pour catalyser des réactions chimiques spécifiques.

Chapitre 3: Étude par premiers principes des hétérostructures Nb_2C-X (X = S, Cl, F)/graphène: Évaluation de la stabilité en milieu aqueux et implications pour l'électrocatalyse

Une stratégie alternative pour stabiliser les MXènes consiste à concevoir des structures hybrides. Jusqu'à présent, des recherches ont été menées sur diverses hétérostructures de MXènes, y compris des matériaux 0D/2D, 1D/2D et 2D/2D [43–47]. De manière générale, l'activité catalytique était préservée, voire améliorée, après l'hybridation [47]. Récemment, des hétérostructures MXène/graphène à base de Sc, V et Ti ont été étudiées pour des applications dans les batteries à ions métalliques [48, 49]. Les calculs ab initio ont prédit que l'intégration de couches de graphène dans la structure des MXènes empêcherait les effets de réempilement et améliorerait la conductivité électrique [49]. Il est donc largement reconnu que les hétérostructures de van der Waals MXène/graphène sont des candidates prometteuses pour stabiliser les MXènes sans dégrader leur activité catalytique. Cependant, aucune étude n'a encore examiné la stabilité et la résistance à l'oxydation des hétérostructures fonctionnalisées Nb_2C MXène/graphène.

Dans ce travail, nous cherchons à déterminer si la formation d'une hétérostructure entre les MXènes Nb_2C et le graphène permettrait d'améliorer la résistance à l'oxydation et à l'hydrolyse des Nb_2C–X. Comme les stratégies de calcul permettant d'explorer la stabilité à l'oxydation sont

limitées, nous avons comparé les énergies de formation thermodynamique de MXènes uniformément terminés avec celles des MXènes où un atome d'oxygène remplace l'un des groupes terminaux. De plus, nous avons réalisé des calculs de la théorie de la fonctionnelle de la densité (DFT) pour les hétérostructures Nb_2C/graphène et Nb_2C–X/graphène, avec une fonctionnalisation de surface par F, S et Cl, afin d'explorer la stabilité à l'oxydation des hétérostructures Nb_2C–X/graphène par rapport aux matériaux Nb_2C–X non modifiés.

Le fluor et le chlore sont des terminaisons couramment formées lors de l'exfoliation conventionnelle par HF et de l'exfoliation électrochimique par HCl, respectivement. De plus, nos travaux précédents ont montré la grande activité catalytique du Nb_2C terminé par S [50]. Des calculs de la bande élastique nudgée (NEB) ont été réalisés afin d'analyser la résistance à l'hydrolyse des MXènes et des hétérostructures, car la décomposition des MXènes en présence d'eau commence par l'adsorption et la dissociation de l'eau [24].

Enfin, nous avons exploré l'activité électrocatalytique du Nb_2C–S et du Nb_2C–S/graphène en analysant les diagrammes d'énergie libre pour l'OER. Cette étude apporte un éclairage sur les mécanismes potentiels d'oxydation des MXènes Nb_2C, permettant ainsi de formuler des stratégies pour améliorer leur résistance à l'oxydation et à l'hydrolyse, comme discuté dans la conclusion. Les structures optimisées des hétérostructures Nb_2C–S/graphène, Nb_2C–Cl/graphène et Nb_2C–F/graphène sont présentées dans la Figure 5.

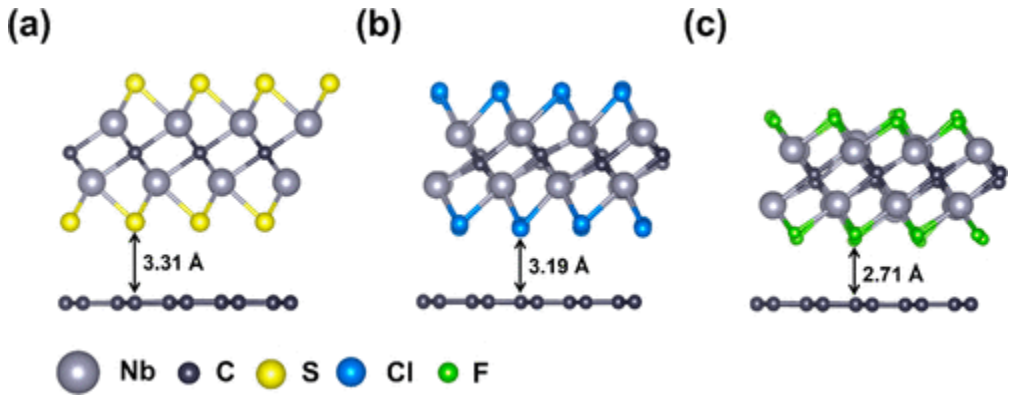

Figure 5. Structures optimisées de Nb_2C-S/graphène (a), Nb_2C-Cl/graphène (b) et Nb_2C-F/graphène (c).

En résumé, notre étude a révélé plusieurs résultats clés. Les hétérostructures MXène/graphène Nb_2C–X, avec des groupes terminaux S, Cl et F, possèdent des énergies de liaison interfaciale et de formation négatives, suggérant leur stabilité structurelle. L'analyse des propriétés

électroniques a montré que la densité d'états électroniques (DOS) augmentait à des niveaux d'énergie intermédiaires, indiquant une amélioration de la conductivité après la formation des hétérostructures MXène/graphène. Notamment, l'introduction du graphène a modifié la densité d'états projetée (PDOS) des orbitales d du Nb, déplaçant le centre de bande d vers l'énergie de Fermi, ce qui pourrait influencer la performance catalytique de l'hétérostructure Nb_2C–X/graphène. Cet effet était particulièrement prononcé pour l'hétérostructure Nb_2C–S/graphène.

Nous avons effectué une analyse thermodynamique afin d'évaluer la probabilité de remplacement des groupes fonctionnels S, Cl et F par de l'oxygène, explorant ainsi la stabilité à l'oxydation des hétérostructures. Comparées aux MXènes Nb_2C–X non modifiés, la stabilité à l'oxydation serait améliorée d'un facteur deux pour Nb_2C–S/graphène et Nb_2C–Cl/graphène. De plus, Nb_2C–F/graphène n'est plus sujet à l'oxydation, affichant une stabilité nettement supérieure à celle de Nb_2C–S/graphène, Nb_2C–Cl/graphène et du Nb_2C–F pristine.

Par ailleurs, les calculs NEB ont montré que l'énergie d'activation pour l'adsorption et la dissociation de l'eau sur Nb_2C–S/graphène est d'environ 1,55 eV plus élevée que sur Nb_2C–S pristine, démontrant ainsi une meilleure stabilité en milieu aqueux de l'hétérostructure. Nos résultats apportent des preuves solides que le graphène peut améliorer la résistance à l'oxydation et à l'hydrolyse des MXènes Nb_2C, ce qui est pertinent pour des applications électrochimiques et biomédicales, et suggère qu'ils pourraient être utilisés comme (électro)catalyseurs stables.

De plus, nous avons comparé la performance OER de Nb_2C–S et Nb_2C–S/graphène, et avons constaté que la surtension était significativement plus faible sur la surface de l'hétérostructure, indiquant une amélioration de l'activité électrocatalytique pour l'OER. Par conséquent, notre étude théorique encourage des investigations expérimentales supplémentaires sur les propriétés et la stabilité des hétérostructures MXène/graphène Nb_2C.

Chapitre 4: Activité d'évolution de l'oxygène dépendant du support graphène et des facettes de Ta_2O_5

Pour développer des électrocatalyseurs à base de Ta_2O_5 stables et actifs pour l'OER en milieu acide, il est essentiel d'identifier des stratégies permettant d'améliorer leurs performances et d'établir des relations claires entre structure et propriétés. Par exemple, il existe des rapports contradictoires dans la littérature concernant le rôle du rapport O/Ta en milieu alcalin. Xiao et al.

[51] ont rapporté de meilleures performances OER avec du Ta_2O_5 riche en oxygène, tandis que Ruiz-Cornejo et al. [52] ont constaté qu'un rapport O/Ta plus faible entraînait de meilleures performances. De plus, bien que l'utilisation de matériaux à base de carbone pour améliorer le transfert de charge dans les électrocatalyseurs à base de Ta_2O_5 ait été explorée, leur rôle dans la modification des propriétés électroniques et électrocatalytiques du Ta_2O_5 reste inexploré.

Dans cette étude, nous avons effectué des calculs de théorie de la fonctionnelle de la densité (DFT) sur les facettes (200), (120) et (100) du Ta_2O_5 afin d'identifier des stratégies permettant de débloquer les performances OER du Ta_2O_5 en milieu acide. L'effet d'un défaut de Ta ou d'O sur les propriétés électroniques des facettes (200) et (120) a été étudié, et trente-cinq sites différents, sur des facettes avec ou sans défaut, ont été considérés pour l'évaluation de l'activité OER. Ensuite, des corrélations ont été établies entre les performances OER et les propriétés structurelles et électroniques, telles que la charge de Bader (BC), les électrons de valence et la densité d'états (DOS) des surfaces de Ta_2O_5. Enfin, l'effet du graphène sur les propriétés électroniques et les performances OER de la surface Ta_2O_5 la plus active a été étudié. Les vues de dessus et de côté des surfaces Ta_2O_5 (200), (120), (001), ainsi que de l'hétérostructure Ta_2O_5/graphène (200), sont présentées dans la Figure 6.

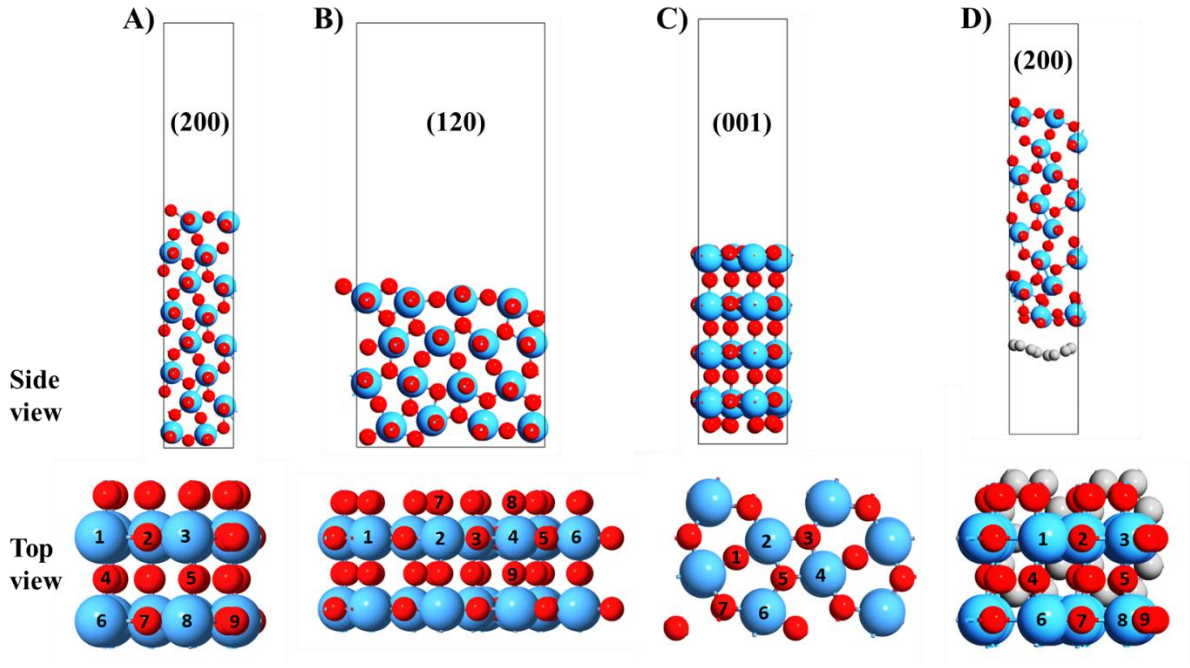

Figure 6. Vues latérale et supérieure des facettes Ta_2O_5 (A) (200), (B) (120) et (C) (001), respectivement. (D) Vues latérale et supérieure du modèle 200-Ta_2O_5/graphène. Les atomes avec des nombres dans le panneau inférieur représentent les sites Ta et O uniques sur la

surface. Les atomes O, Ta et C sont représentés par des sphères rouges, bleues et grises, respectivement.

Dans ce travail, des calculs DFT ont été effectués sur les surfaces (200), (120) et (001) de Ta_2O_5, ainsi que sur l'hétérostructure Ta_2O_5(200)/graphène, afin d'identifier des stratégies visant à améliorer les performances OER du Ta_2O_5. De nouvelles connaissances sur l'activité OER des sites Ta sur des facettes vierges ont été établies. La facette (200), avec la densité de sites Ta la plus faible et une DOS modérée au niveau de Fermi, a montré la surtension la plus faible par rapport aux facettes (120) et (001). La création de défauts de Ta pourrait diminuer la surtension sur les facettes (200) et (120). Cependant, l'introduction de défauts d'O a induit une bande interdite dans la facette (200) et a augmenté la surtension sur les facettes (200) et (120). Des cartes thermiques de corrélation ont été établies entre les propriétés de chaque site Ta sur les facettes (200) et (120) et les mesures de performance OER. Sur la deuxième facette la plus performante, la (120), la charge de Bader et les orbitales d des sites Ta dans la bande de valence ont modulé de manière significative les performances, en forte corrélation avec l'énergie libre de Gibbs (ΔG) des étapes 1, 2 et 4. Cependant, sur la facette (200), seule la somme des électrons de valence dans un rayon de 3 Å et la largeur du PDOS au niveau de Fermi ont montré des corrélations modérées. L'hétérostructure Ta_2O_5(200)/graphène a montré une surtension substantiellement faible de 0,39 V sur un site Ta–O. L'analyse PDOS a montré que l'amélioration des performances OER de l'hétérostructure était due au déplacement des orbitales d des sites Ta vers des énergies plus faibles, ainsi qu'à l'augmentation de l'intensité de la DOS après l'ajout de graphène. Dans l'ensemble, les meilleures stratégies pour exploiter le potentiel de l'oxyde de Ta dans les REL consistent à synthétiser une hétérostructure formée de Ta_2O_5(200)/graphène, à empêcher la formation de la facette (001), et/ou à introduire des défauts de Ta dans des nanoparticules ou films minces de Ta_2O_5. Si ces résultats sont validés expérimentalement, ils feraient des matériaux à base de Ta_2O_5 des électrocatalyseurs OER non précieux prometteurs pour des applications en milieu acide.

Chapitre 5: Aperçu de la DFT sur l'activité de la OER du tantalate de sodium

Dans ce chapitre, les tantalates de sodium ont été étudiés pour la réaction d'évolution de l'oxygène (OER), en tant que matériaux à base de Ta, en raison de leur application réussie dans les électrocatalyseurs de la réaction de réduction de l'oxygène (ORR) [53, 54]. Par exemple, Sebastián et al. ont préparé du graphène supporté par $Na_2Ta_8O_{x-21}$ par précipitation d'oxyde de tantale sur le graphène, suivie d'un traitement thermique. Cet électrocatalyseur

contenant du tantalate de sodium avec des lacunes en oxygène a montré une activité prometteuse pour l'ORR en milieu acide, ainsi qu'une bonne stabilité face à l'empoisonnement au méthanol [53]. Selon la littérature, les principales structures de tantalates de sodium comprennent $NaTaO_3$ [55], $Na_2Ta_4O_{11}$ [55], $Na_2Ta_8O_{21}$ [54] et $NaTa_3O_8$ [56]. Parmi elles, les cellules unitaires de $Na_2Ta_4O_{11}$ (102 atomes) et $NaTa_7O_{19}$ (108 atomes) sont relativement grandes, ce qui rend les calculs de théorie de la fonctionnelle de la densité (DFT) sur ces systèmes particulièrement coûteux en ressources de calcul.

$NaTaO_3$ possède une large bande interdite d'environ 4 eV [51] et a été largement étudié pour la photocatalyse. La recherche sur $NaTaO_3$ s'est principalement concentrée sur l'ingénierie de sa bande interdite et l'amélioration de ses propriétés catalytiques via des dopants tels que Bi [57], N [58], S, C, P [59], etc. Par exemple, en utilisant des calculs DFT, Tang et al. ont montré que le dopage de $NaTaO_3$ avec du Sr améliore ses performances OER. Lorsqu'une concentration élevée de Sr a été introduite, une surtension de 0,55 V a été observée [60]. Cai et al. ont étudié l'effet de l'adsorption d'atomes métalliques simples (M = Fe, Co, Ni, Cu, Ru, Rh, Pd, Ag, Ir, Pt, Au) sur les propriétés électroniques et les performances catalytiques de $NaTaO_3$ [61]. Ils ont montré que l'adsorption de Co pouvait diminuer la surtension OER à 0,68 V [61]. Contrairement à $NaTaO_3$, la structure de $NaTa_3O_8$ a été rarement étudiée, notamment en raison de la difficulté associée à sa synthèse [56]. Ainsi, notre étude s'est principalement concentrée sur $NaTa_3O_8$ en tant que nouveau matériau prometteur pour des applications en chimie de surface. Les vues de dessus et de côté des différentes facettes des surfaces de $NaTaO_3$ et $NaTa_3O_8$ sont présentées dans les Figures 7 et 8, respectivement.

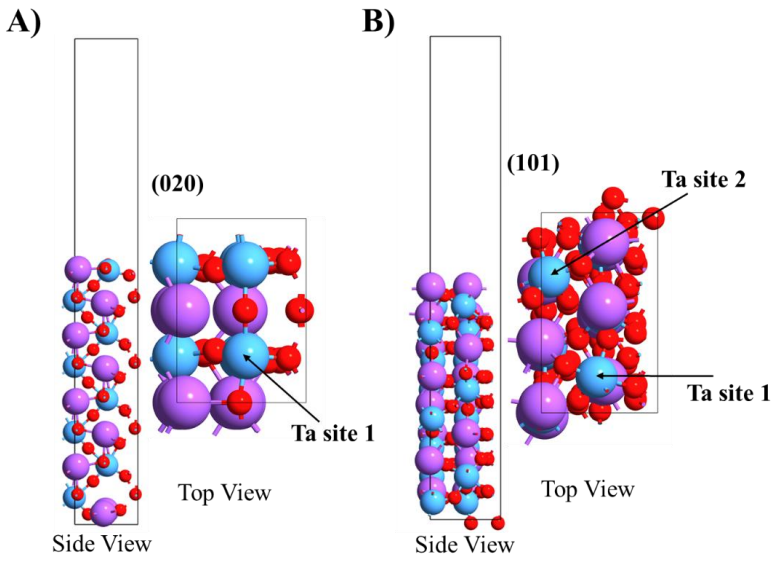

Figure 7. Les modèles de A) (020) et B) (101) $NaTaO_3$ avec des sites Ta étudiés pour l'évaluation de l'activité OER.

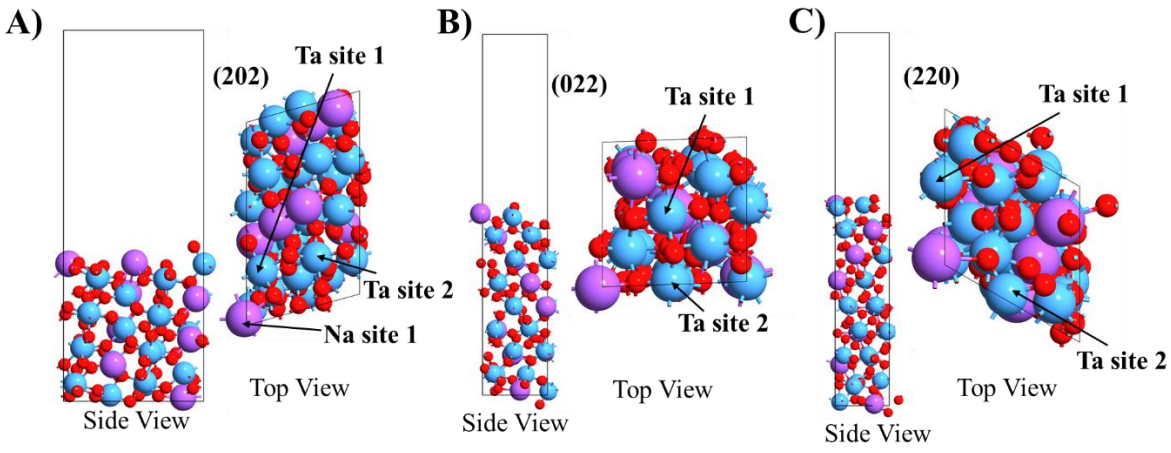

Figure 8. Les modèles de A) (022), B) (202) et C) (220) $NaTa_3O_8$ avec des sites Ta et un site Na étudiés pour l'évaluation de l'activité OER.

Ce chapitre examine les propriétés électroniques ainsi que les performances en réaction d'évolution de l'oxygène (OER) de $NaTaO_3$ et $NaTa_3O_8$. Les analyses de la densité d'états totale (DOS) et projetée (PDOS) révèlent une forte dépendance des propriétés électroniques et des orbitales d du tantale à la nature des facettes cristallographiques. Les facettes (220) et (022) de $NaTa_3O_8$, ainsi que la facette (020) de $NaTaO_3$, ont montré un comportement métallique. Cependant, les facettes (202) de $NaTa_3O_8$ et (101) de $NaTaO_3$ ont présenté un comportement semi-conducteur, avec des bandes interdites de 1,72 et 1,03 eV, respectivement. Les performances OER des facettes de $NaTa_3O_8$ (dans l'intervalle de 1,13 à 3,21 V) étaient meilleures que celles de $NaTaO_3$ (dans l'intervalle de 4,85 à 6,08 V). Dans la structure $NaTa_3O_8$, la facette (202) a montré la surtension la plus faible, de 1,13 V pour les sites Ta, ce qui est significativement inférieur à celle des facettes (220) et (022). La surtension sur les facettes de $NaTa_3O_8$ a suivi la tendance de la densité de Ta sur la couche supérieure, où la facette (202), avec la densité Ta la plus élevée (0,0565 atomes Ta/Å²), a montré la meilleure performance. Par ailleurs, la faible surtension observée pour la facette (202) de $NaTa_3O_8$ pourrait s'expliquer par l'absence de contribution des orbitales d du tantale au niveau de Fermi, ce qui pourrait favoriser une forte adsorption des intermédiaires de l'OER et, par conséquent, limiter les performances catalytiques. En outre, le site Na présent sur la facette (202) de $NaTa_3O_8$ a affiché la surtension la plus faible, avec une valeur de 0,59 V. Dans les études

futures, des stratégies telles que le dopage et la création de défauts pourront être envisagées pour améliorer davantage l'activité OER de $NaTa_3O_8$.

Chapitre 6: Conclusion

Cette thèse met en évidence le potentiel des matériaux à base de niobium (Nb) et de tantale (Ta) en tant qu'alternatives non précieuses prometteuses pour la réaction d'évolution de l'oxygène (OER) en milieu acide. L'évaluation de leurs performances catalytiques a été réalisée à l'aide de calculs de théorie de la fonctionnelle de la densité (DFT). Les principaux résultats de chaque étude sont synthétisés ci-dessous.

La première étude sur les MXènes Nb_2C a montré que les groupes terminaux pouvaient moduler efficacement les propriétés électroniques et catalytiques du Nb_2C. Parmi les terminaisons étudiées, le Nb_2C à terminaison S présentait la fonction de travail la plus élevée (5,07 eV) avec un centre de bande d positionné à –2,53 eV. En particulier, ce centre de bande d s'est éloigné du niveau de Fermi par rapport au Nb_2C vierge (–1,53 eV), indiquant que le défaut du Nb_2C vierge — une forte adsorption des intermédiaires de réaction — pouvait être atténué grâce à la terminaison S. De plus, le Nb_2C–S avec un défaut a montré une activité significative dans la dissociation de H_2O, O_2, N_2 et CO_2. La barrière de dissociation du Nb_2C–S_{x-1} était d'environ 0 eV pour O_2 et CO_2, et de 0,16 et 0,17 eV pour H_2O et N_2, respectivement. Ces résultats ont démontré qu'en modifiant simplement les groupes terminaux du Nb_2C, une large gamme de propriétés électroniques (telles que la fonction de travail) et catalytiques peut être obtenue.

Sur cette base, la deuxième étude s'est concentrée sur la stabilité du Nb_2C–X (X = S, F ou Cl) et de l'hétérostructure Nb_2C–X/graphène vis-à-vis de l'oxydation et de l'hydrolyse, qui sont des facteurs essentiels pour les applications pratiques. Les résultats ont révélé que, dans l'hétérostructure Nb_2C–X/graphène, la stabilité à l'oxydation partielle était améliorée par rapport au Nb_2C–X vierge. En particulier, Nb_2C–S/graphène et Nb_2C–Cl/graphène ont montré une meilleure stabilité contre l'oxydation partielle que Nb_2C–S et Nb_2C–Cl, respectivement, tandis que Nb_2C–F/graphène n'était pas davantage sujet à l'oxydation. De plus, la stabilité aqueuse de Nb_2C–S/graphène et Nb_2C–S a été évaluée en analysant la barrière de dissociation de l'eau — l'hydrolyse étant la première étape de décomposition des MXènes en solution aqueuse. Les résultats ont montré une barrière énergétique plus élevée pour l'adsorption et la dissociation de l'eau sur Nb_2C–S/graphène que sur Nb_2C–S, indiquant une meilleure stabilité face à

l'hydrolyse. Enfin, Nb_2C–S/graphène a montré une surtension OER plus faible (0,93 V) par rapport à Nb_2C–S (2,15 V), soulignant le double avantage d'une stabilité accrue et de performances catalytiques améliorées.

Les résultats obtenus sur les MXènes Nb_2C–X ont ainsi montré qu'un électrocatalyseur OER potentiel peut être préparé en combinant la création de défauts, la terminaison au soufre et la formation d'une hétérostructure avec du graphène.

En complément des matériaux à base de niobium, cette thèse a également investigué les performances en réaction d'évolution de l'oxygène (OER) des matériaux à base de tantale. Bien que le Ta_2O_5 figure parmi les rares oxydes présentant une stabilité en milieu acide sous conditions OER, son potentiel demeure largement inexploité. Ainsi, une étude approfondie de ce matériau a été menée, mettant en évidence l'influence des facettes cristallographiques (200), (120) et (001) sur ses performances électrocatalytiques. Les résultats obtenus offrent de nouvelles perspectives sur la forte dépendance de l'activité OER aux propriétés structurales du Ta_2O_5. Notre étude a montré que l'hétérostructure Ta_2O_5(200)/graphène pouvait atteindre une surtension aussi faible que 0,39 V, ce qui en fait un candidat prometteur pour l'OER acide. De plus, des corrélations ont été établies entre les propriétés électroniques des sites Ta (orbitales d, charge de Bader, somme des électrons de valence) et les mesures de performance OER. La somme des électrons de valence et la largeur du PDOS au niveau de Fermi ont montré des corrélations modérées avec l'activité OER des surfaces (200). Par ailleurs, les variations de charge de Bader et les orbitales d des sites Ta ont affecté de manière significative l'activité OER de la facette (120), fournissant des informations précieuses pour l'optimisation des catalyseurs à base de Ta_2O_5.

Enfin, les tantalates de sodium, notamment $NaTaO_3$ et $NaTa_3O_8$, ont été étudiés comme matériaux alternatifs à base de Ta pour l'électrocatalyse OER. Les calculs DFT ont indiqué que la facette (202) de $NaTa_3O_8$ présentait une surtension comparativement plus faible (1,13 V) sur les sites Ta. De plus, les sites Na sur le même système ont affiché une surtension encore plus basse, de 0,59 V. L'analyse du PDOS a révélé que la présence d'orbitales d du tantale au niveau de Fermi pourrait jouer un rôle clé dans la détermination de l'activité OER.

En conclusion, cette thèse a démontré que les matériaux à base de niobium (Nb) et de tantale (Ta) constituent des candidats prometteurs pour le développement d'électrocatalyseurs OER efficaces et économiquement viables en milieu acide. Ces résultats apportent des informations

précieuses sur les stratégies de conception de ces matériaux, bien que leur validation expérimentale reste nécessaire pour évaluer leur potentiel en conditions réelles d'application.

Références

1. Horowitz, C.A., Paris agreement. International Legal Materials, 2016. 55(4): p. 740-755.

2. Cho, H.H., V. Strezov, and T.J. Evans, A review on global warming potential, challenges and opportunities of renewable hydrogen production technologies. Sustainable Materials and Technologies, 2023. 35: p. e00567.

3. Hren, R., et al., Hydrogen production, storage and transport for renewable energy and chemicals: An environmental footprint assessment. Renewable and Sustainable Energy Reviews, 2023. 173: p. 113113.

4. Environment and C.C. Canada, Canadian Environmental Sustainability Indicators: Greenhouse Gas Emissions. Consulted on April, 2022, 2022.

5. HYDROGEN STRATEGY FOR CANADA: Seizing the Opportunities for Hydrogen. 2020; Available from: https://publications.gc.ca/site/eng/9.894114/publication.html.

6. Sun, B., et al., Review on natural hydrogen wells safety. Nature Communications, 2025. 16(1): p. 369.

7. Mayyas, A.T., et al., Manufacturing cost analysis for proton exchange membrane water electrolyzers. 2019, National Renewable Energy Laboratory (NREL), Golden, CO (United States).

8. Ahmed, S.F., et al., Sustainable hydrogen production: technological advancements and economic analysis. International Journal of Hydrogen Energy, 2021.

9. Osman, A.I., et al., Hydrogen production, storage, utilisation and environmental impacts: a review. Environmental Chemistry Letters, 2021. 20(1): p. 153-188.

10. Zainal, B.S., et al., Recent advancement and assessment of green hydrogen production technologies. Renewable and Sustainable Energy Reviews, 2024. 189: p. 113941.

11. Ayub, H.M.U., et al., A cost comparison study for hydrogen production between conventional and renewable methods. Process Safety and Environmental Protection, 2024. 186: p. 921-932.

12. Guan, D., et al., Hydrogen society: from present to future. Energy & Environmental Science, 2023. 16(11): p. 4926-4943.

13. Muhammed, N.S., et al., Hydrogen production, transportation, utilization, and storage: Recent advances towards sustainable energy. Journal of Energy Storage, 2023. 73.

14. Kumar, S.S. and H. Lim, Recent advances in hydrogen production through proton exchange membrane water electrolysis–a review. Sustainable Energy & Fuels, 2023. 7(15): p. 3560-3583.

15. Hubert, M.A., L.A. King, and T.F. Jaramillo, Evaluating the case for reduced precious metal catalysts in proton exchange membrane electrolyzers. ACS Energy Letters, 2021. 7(1): p. 17-23.

16. Ma, J., et al., Niobium/tantalum-based materials: Synthesis and applications in electrochemical energy storage. Chemical Engineering Journal, 2020. 380: p. 122428.

17. Gómez, M., J. Li, and X. Zeng, Niobium: The unseen element-A comprehensive examination of its evolution, global dynamics, and outlook. Resources, Conservation and Recycling, 2024. 209: p. 107744.

18. 16/12/2024]; Available from: https://www.canada.ca/en/campaign/critical-minerals-in-canada/canadian-critical-minerals-strategy.html.

19. Ishihara, A., et al., Challenge of advanced low temperature fuel cells based on high degree of freedom of group 4 and 5 metal oxides. Current Opinion in Electrochemistry, 2020. 21: p. 234-241.

20. Ke, J., et al., Optimizing Acidic Oxygen Evolution Reaction via Modulation Doping in Van der Waals Layered Iridium Oxide. Angewandte Chemie, 2025: p. e202422740.

21. Wu, Y., et al., Modulating Carrier Oxygen Vacancies to Enhance Strong Oxide-Support Interaction in IrO2/Nb2O5-x Catalysts for Promoting Acidic Oxygen Evolution Reaction. Advanced Functional Materials, 2024. 34(51): p. 2410193.

22. VahidMohammadi, A., J. Rosen, and Y. Gogotsi, The world of two-dimensional carbides and nitrides (MXenes). Science, 2021. 372(6547): p. eabf1581.

23. Kan, D., et al., Rational design of bifunctional ORR/OER catalysts based on Pt/Pd-doped Nb 2 CT 2 MXene by first-principles calculations. Journal of Materials Chemistry A, 2020. 8(6): p. 3097-3108.

24. Wu, T., et al., How water attacks MXene. Chemistry of Materials, 2022. 34(11): p. 4975-4982.

25. Li, H., et al., Highly active and stable IrO2 and IrO2–Ta2O5 catalysts for oxygen evolution reaction. International Journal of Hydrogen Energy, 2023. 48(67): p. 26021-26031.

26. Huang, Q., et al., Boron-incorporated IrO2-Ta2O5 coating as an efficient electrocatalyst for acidic oxygen evolution reaction. Chemical Engineering Journal, 2024. 491: p. 152040.

27. Amano, F., et al., Structure–stability relationship of amorphous IrO2–Ta2O5 electrocatalysts on Ti felt for oxygen evolution in sulfuric acid. The Journal of Physical Chemistry C, 2022. 126(4): p. 1817-1827.

28. Liu, Y., et al., An IrRuO x catalyst supported by oxygen-vacant Ta oxide for the oxygen evolution reaction and proton exchange membrane water electrolysis. Nanoscale, 2024. 16(19): p. 9382-9391.

29. Zhang, J., et al., Tantalum-stabilized ruthenium oxide electrocatalysts for industrial water electrolysis. Science, 2025. 387(6729): p. 48-55.

30. Wang, X., et al., RuO2 with Short-Range Ordered Tantalum Single Atoms for Enhanced Acidic Oxygen Evolution Reaction. Advanced Energy Materials, 2024: p. 2403388.

31. Maria de Lourdes, S.V., et al., Electrocatalytic properties of Ti/RuO2-TiO2 dimensionally stable anode type electrodes modified with SnO2 and Ta2O5 for the oxygen evolution reaction. Applied Catalysis O: Open, 2025. 198: p. 207025.

32. Amano, F., Y. Furusho, and Y.-M. Hwang, Amorphous iridium and tantalum oxide layers coated on titanium felt for electrocatalytic oxygen evolution reaction. ACS Applied Energy Materials, 2020. 3(5): p. 4531-4538.

33. Song, M., et al., Fluoride-Free 2D Niobium Carbide MXenes as Stable and Biocompatible Nanoplatforms for Electrochemical Biosensors with Ultrahigh Sensitivity. Advanced Science, 2020. 7(24): p. 2001546.

34. Xiao, J., et al., A safe etching route to synthesize highly crystalline Nb2CTx MXene for high performance asymmetric supercapacitor applications. Electrochimica Acta, 2020. 337: p. 135803.

35. Li, G., et al., Highly Efficient Nb2C MXene Cathode Catalyst with Uniform O-Terminated Surface for Lithium–Oxygen Batteries. Advanced Energy Materials, 2021. 11(1): p. 2002721.

36. Zhang, J., C. Huang, and H. Yu, Modulate the work function of Nb2CTx MXene as the hole transport layer for perovskite solar cells. Applied Physics Letters, 2021. 119(3): p. 033506.

37. Tan, Y., et al., Nb4C3Tx (MXene) as a new stable catalyst for the hydrogen evolution reaction. International Journal of Hydrogen Energy, 2021. 46(2): p. 1955-1966.

38. Zhang, X., et al., Regulation of CO oxidation with Pd additives on Nb2CO2 MXene. International Journal of Hydrogen Energy, 2021. 46(12): p. 8477-8485.

39. Chu, K., et al., Synergistic Enhancement of Electrocatalytic Nitrogen Reduction Over Boron Nitride Quantum Dots Decorated Nb2CTx-MXene. Small, 2021. 17(40): p. 2102363.

40. Ougherb, C., et al., Effect of the sulfur termination on the properties of Hf 2 CO 2 MXene. Physical Chemistry Chemical Physics, 2022. 24(12): p. 7243-7252.

41. Sun, W., et al., Electrochemical etching of Ti 2 AlC to Ti 2 CT x (MXene) in low-concentration hydrochloric acid solution. Journal of Materials Chemistry A, 2017. 5(41): p. 21663-21668.

42. Bjork, J. and J. Rosen, Functionalizing MXenes by tailoring surface terminations in different chemical environments. Chemistry of Materials, 2021. 33(23): p. 9108-9118.

43. Pang, J., et al., Potential of MXene-based heterostructures for energy conversion and storage. ACS Energy Letters, 2021. 7(1): p. 78-96.

44. Gao, L., et al., Hetero-MXenes: theory, synthesis, and emerging applications. Advanced Materials, 2021. 33(10): p. 2004129.

45. Abbasi, N.M., et al., Heterostructures of titanium-based MXenes in energy conversion and storage devices. Journal of Materials Chemistry C, 2021. 9(27): p. 8395-8465.

46. Lim, K.R.G., et al., 2h-Mos2 on Mo2ct X Mxene nanohybrid for efficient and durable electrocatalytic hydrogen evolution. ACS nano, 2020. 14(11): p. 16140-16155.

47. Jiang, L., et al., Iron-cluster-directed synthesis of 2D/2D Fe–N–C/MXene superlattice-like heterostructure with enhanced oxygen reduction electrocatalysis. ACS nano, 2020. 14(2): p. 2436-2444.

48. Aierken, Y., et al., MXenes/graphene heterostructures for Li battery applications: a first principles study. Journal of Materials Chemistry A, 2018. 6(5): p. 2337-2345.

49. Du, Y.-T., et al., MXene/graphene heterostructures as high-performance electrodes for Li-ion batteries. ACS applied materials & interfaces, 2018. 10(38): p. 32867-32873.

50. Ghasemy, E., A.C. Tavares, and K.K. Ghuman, Tuning the catalytic activity of Nb2C MXenes via surface functionalization and defects. Applied Materials Today, 2023. 32: p. 101858.

51. Xiao, W., et al., High catalytic activity of oxygen-induced (200) surface of Ta2O5 nanolayer towards durable oxygen evolution reaction. Nano Energy, 2016. 25: p. 60-67.

52. Ruiz-Cornejo, J.C., et al., Carbon nanofiber-supported tantalum oxides as durable catalyst for the oxygen evolution reaction in alkaline media. Renewable Energy, 2021. 178: p. 307-317.

53. Sebastián, D., et al., Graphene-Supported Substoichiometric Sodium Tantalate as a Methanol-Tolerant, Non-Noble-Metal Catalyst for the Electroreduction of Oxygen. ChemCatChem, 2015. 7(6): p. 911-915.

54. Zhang, G., et al., Engineering of a Low-Cost, Highly Active, and Durable Tantalate–Graphene Hybrid Electrocatalyst for Oxygen Reduction. Advanced Energy Materials, 2020. 10(24): p. 2000075.

55. Şahin, E.O., et al., Sodium tantalates: monitoring crystallization via in situ total X-ray scattering. CrystEngComm, 2023. 25(15): p. 2256-2263.

56. Heyns, A., K.-J. Range, and M. Wildenauer, The vibrational spectra of NbBO4, TaBO4, NaNb3O8 and NaTa3O8. Spectrochimica Acta Part A: Molecular Spectroscopy, 1990. 46(11): p. 1621-1628.

57. Alves, G.A., et al., Band gap narrowing of Bi-doped NaTaO3 for photocatalytic hydrogen evolution under simulated sunlight: a pseudocubic phase induced by doping. ACS Applied Energy Materials, 2020. 4(1): p. 671-679.

58. Modak, B., K. Srinivasu, and S.K. Ghosh, Band gap engineering of natao 3 using density functional theory: a charge compensated codoping strategy. Physical Chemistry Chemical Physics, 2014. 16(32): p. 17116-17124.

59. Wang, B., et al., Anion-doped NaTaO3 for visible light photocatalysis. The Journal of Physical Chemistry C, 2013. 117(44): p. 22518-22524.

60. Tang, Z.-K., et al., Understanding the influence of cation doping on the surface chemistry of NaTaO3 from first principles. ACS Catalysis, 2019. 9(11): p. 10528-10535.

61. Cai, J., et al., First-Principles Investigation on Electronic Properties and Surface Reactions of NaTaO3 Adsorbed with Single-Metal Atoms. The Journal of Physical Chemistry C, 2023. 127(14): p. 6702-6713.

Table of Contents

List of Tables

List of Figures

LIST OF ABBREVIATIONS

2D	Two-dimensional
AEM	Adsorbate evolution mechanism
ATR	Authothermal reforming
BC	Bader charge
BFGS	Broyden–Fetcher–Goldfarb–Shannon
BoP	Balance of plant
CB	Conduction band
CBM	Conduction band minima
CA	Chronoamperometry
CCS	Capture and storage
CHE	Computational hydrogen electrode
CI-NEB	Climbing Image Nudge Elastic Band
CIF	Crystallographic information file
CL	Catalyst layer
CNF	Carbon nanofiber
CO_2RR	Carbon dioxide reduction
CP	Chronopotentiometry
CV	Cyclic voltammetry
DFT	Density functional theory
DSA	Dimensionally stable anode
DOS	Density of states
ECSA	Electrochemically active surface area
FTO	Fluorine-doped tin oxide
GHG	Greenhouse gas
GGA	Generalized gradient approximation
HER	Hydrogen evolution reaction
HSE	Heyd-Scuseria-Ernzerhof
HUPD	Hydrogen underpotential deposition
LDA	Local-density approximation
LOM	Lattice oxygen mediated
LSV	Linear sweep voltammetry
MEP	Minimum energy path
MPWC	Maximum PDOS width in the conduction band
MPWV	Maximum PDOS width in the valence band
MXene	Two-dimensional (2D) transition metal carbide/nitride
nSCF	Non-self-consistent field
NRR	N_2 electroreduction
OER	Oxygen evolution reaction
ORR	Oxygen reduction reaction

PBE	Perdew–Burke–Ernzerhof
PDOS	Partial density of states
PEM	Proton exchange membrane
PFSA	Perfluoro sulfonic acid
POX	Partial oxidation
PTLs	Porous transport layers
RDS	Rate-determining step
RHE	Reversible hydrogen electrode
S-number	Stability number
SCF	Self-consistent field
SMR	Steam methane reforming
STD	Sintered titanium disk
SVE	Sum of valence electrons
TOF	Turnover frequency
TS	Transition states
UPD	Underpotential deposition
VB	Valence band
VBM	Valence band maxima
vdW	Van der Waals
WF	Work function
XRD	X-ray diffraction
YSZ	Yttria-stabilized zirconia

1 Introduction

1.1. Overview

Global warming and climate change pose significant risks and threaten the health and well-being of humans and animals. According to the Paris Agreement [1], global warming must be kept below 2°C above pre-industrial levels, with a goal of limiting it to 1.5°C. Decarbonization of industries through solutions such as the use of green hydrogen is critical for meeting these targets, since hydrogen offers a sustainable pathway for reducing emissions by serving as both a low-carbon energy carrier and a feedstock for industrial processes [2, 3]. In line with global efforts, Canada's government has committed to reduce greenhouse gas (GHG) emissions by 40 to 45% from 2005 levels by 2030, and reach net-zero GHG emissions by 2050 [4]. Canada's Hydrogen Strategy highlights that clean hydrogen can deliver up to 30% of Canada's end-use energy by 2050, potentially reducing CO_2-equivalent emissions by up to 190 million tons through its use in transportation, heating, and industrial [5]. With a high calorific value (~282 kJ/mol), hydrogen is the ideal energy carrier to achieve a carbon-neutral society [6] and generate clean electricity [7]. Clean hydrogen can decarbonize various industries [8], including iron and steel, chemicals, cement and lime, food and drink, pulp and paper, glass, aluminum, etc. For instance, the carbon-intensive steel production industry accounts for 8% of global energy used [9] and emits around 1.9 tons of CO_2 per ton of crude steel produced [10]. The emissions of this industry should be decreased by 24% by 2030 and 90% by 2050 [11]. Using hydrogen as a reducing agent in the steel production processes can decrease emissions by more than 80% [8].

Despite the great potential of green hydrogen with minimal CO_2 emission (powered by renewable energy sources such as wind, solar, hydropower, etc.), its production cost (ranging from 4.15 to 10.4 USD/kg [12]) is higher than that of fossil-fuel-based technologies due to high cost of electrolyzers (including input electricity price and stack components such Ir-based electrocatalysts) [13], which limits its economic viability and extensive use in industrial and energy applications. At a production cost of 2.50 USD/kg, green hydrogen can meet 8% of the global energy demand, and decreasing the cost to 1.80 USD/kg by 2030 is projected to increase its share to 15-18% of the global energy demand [14]. The following sections discuss the hydrogen production methods, with a focus on green hydrogen production technologies. In addition, strategies for developing cost-effective electrocatalysts are explored to reduce the cost of green hydrogen produced through electrolysis.

1.2. Fossil fuel-based hydrogen production methods

Over 100 technologies have been developed for hydrogen production, while more than 80% of them focus on the steam conversion of fossil fuels, and 70% rely on the steam reforming of natural gas [15]. Hydrogen production methods are categorized by "colors" based on their energy sources and GHG emissions to better understand their environmental impacts, as summarized in Table 1-1 and Figure 1-1 [16]. Hydrogen production methods such as brown, grey, and black significantly emit GHGs, which are most detrimental to the environment [16]. The most dominant fossil fuel-based hydrogen production methods are investigated in the following subsections.

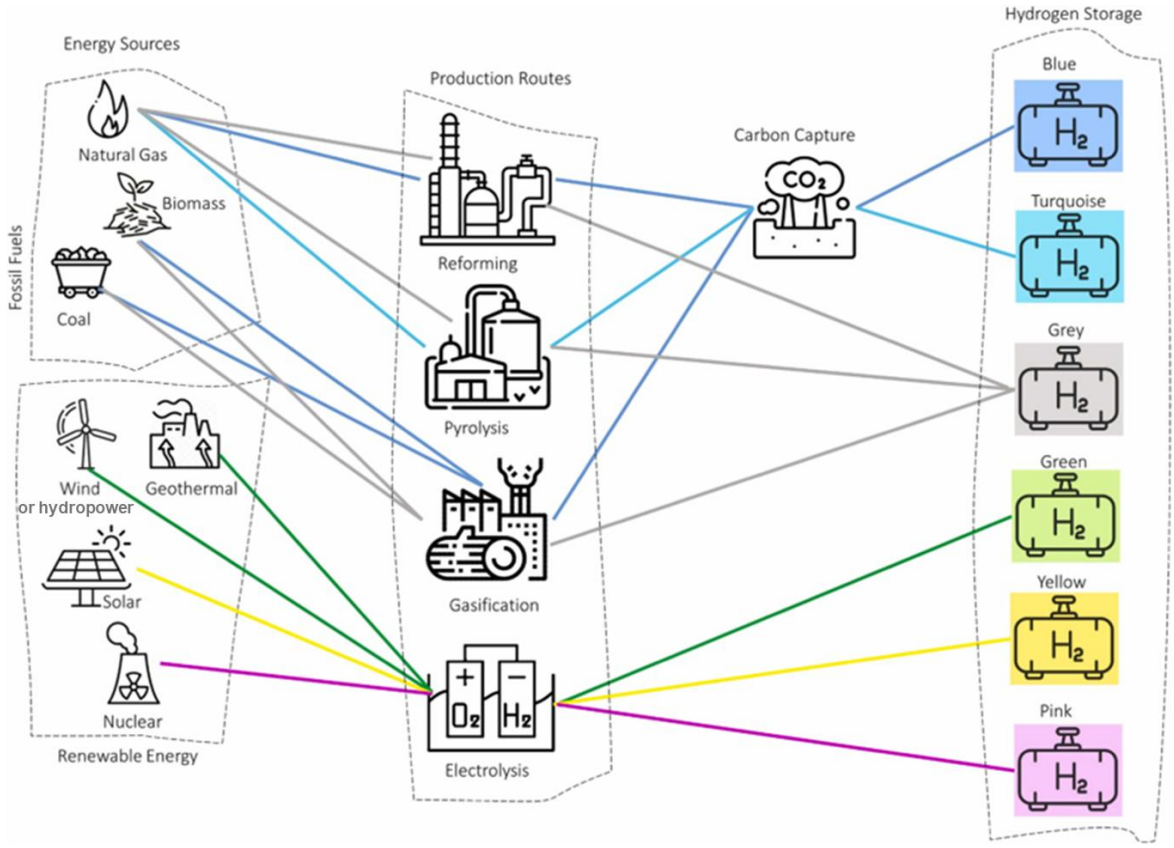

Figure 1-1. Classification of hydrogen production methods based on the source, method, and assigned color (Reused with permission from [17]).

Table 1-1. Comparing the advantages and drawbacks of hydrogen with different colors (Reproduced with permission from [16]).

Types of hydrogen colors	Definition by technologies used	Advantages	Drawbacks
Green	Hydrogen is produced by water electrolysis using renewable energy sources such as solar, wind, and hydro.	1. Promote bioenergy 2. Does not emit GHGs 3. Produce from clean electricity	1. High production costs 2. Energy losses 3. Lack of dedicated infrastructure 4. Lack of value recognition
Grey	Hydrogen is produced by steam methane reforming (SMR) from fossil fuels (other than coal).	Produces low-cost hydrogen.	1. Emits carbon dioxide 2. Emits other GHG 3. Continued use of some fossil fuels.
Blue	Hydrogen from natural gas is produced through the SMR process to capture and bury GHGs.	Could capture and remove GHGs using carbon capture and storage (CCS) technology.	Produce carbon dioxide as a byproduct
Cyan	Steam methanation of renewable natural gas with CCS.	Could be combined with capture and store carbon.	The process emits a large amount of carbon dioxide.
Turquoise	Hydrogen is derived from the pyrolysis of methane (thermal splitting).	1. Produce hydrogen and solid carbon. 2. In the future, it may be valued as low-emission hydrogen, depending on several factors.	Tar formation, fluctuating H_2 amount, and seasonal availability [18]
Black/ Brown	Hydrogen is produced by coal gasification.	Produce liquefied hydrogen for low-emission usage.	This process emits large amounts of carbon dioxide, carbon monoxide, and other GHGs. (Opposite of green hydrogen)
Purple	Hydrogen is produced using nuclear power plants. This chemo-thermal electrolysis process uses nuclear power and heat to split water.	Low carbon emissions	More technological improvement is needed [19].
Pink	Hydrogen is produced using nuclear energy to power water electrolysis.	1. The steam generated from the nuclear reactors could be used for other hydrogen productions for more efficient electrolysis	1. Use very high temperatures from nuclear reactors. 2. Generate a small amount of GHGs.
Yellow	Hydrogen is produced from the energy grid via water electrolysis.	Minimum direct CO_2 emission.	1. Carbon emissions vary greatly depending on the sources used to power the grid.

1.2.1. Steam methane reforming (SMR)

SMR is the leading hydrogen production technology, which includes the reaction between methane and steam at high temperatures (above 800°C) while using a catalyst. As shown in Equation 1-1, this reaction forms hydrogen and carbon monoxide:

$$CH_4 + H_2O \rightarrow CO + 3H_2 \qquad \text{Equation 1-1}$$

Then, the produced carbon monoxide reacts with additional steam to produce more hydrogen and carbon dioxide through the water-gas shift reaction:

$$CO + H_2O \rightarrow CO_2 + H_2 \qquad \text{Equation 1-2}$$

Around 48% of hydrogen is produced through SMR globally [20], making it the dominant method for hydrogen production. However, this process emits around 9.35 kg CO_2 per kg of hydrogen [21]. Although using techniques such as carbon capture and storage (CCS) can reduce CO_2 emissions by 90%, it increases the production cost by about 13% [22]. The cost of hydrogen produced through SMR varies between 1.22 to 2.55 USD/kg, which is dependent on the plant size and CCS integration [20]. The disadvantages of SMR include the emission of CO_2, dependence on fossil fuels, demand for high energy, water usage, etc., which highlight the drawbacks of this method. These challenges underscore the need for the development and utilization of techniques that are both efficient and sustainable.

1.2.2. Partial oxidation (POX)

In the POX method, hydrocarbon feedstock, such as natural gas, reacts with a limited amount of oxygen. The oxygen amount is typically insufficient for complete combustion, which results in the production of hydrogen and carbon dioxide.

$$CH_4 + 1/2\ O_2 \rightarrow CO + 2H_2 \qquad \text{Equation 1-3}$$

In contrast to SMR, the POX method is exothermic, which means that it generates its own heat through partial combustion. This reduces the need for external energy inputs. This process occurs at 800-900°C in the presence of a catalyst and at 1200-1500°C without a catalyst [23]. The hydrogen production price through thermal POX (without using a catalyst) is estimated to be 1.34-1.63 USD/kg [24]. The advantages of POX over SMR include good response time, compactness, and less sensitivity for fuel variation [25]. The disadvantages of the POX method

include the formation of carbon, the need for catalyst management, and the high operating temperatures [26].

1.2.3. Authothermal reforming (ATR)

The ATR process combines SMR and POX, which is attractive for reforming complex hydrocarbon feedstock like kerosene and diesel to produce hydrogen for fuel cells. In this process, steam is added to the POX production method, as shown in the following:

$$C_nH_mO_p + x(O_2 + 3.76N_2) + (2n - 2x - p)H_2O \leftrightarrow nCO_2 + (2n - 2x - p + m2)H_2 + 3.76xN_2 \quad \text{Equation 1-4}$$

The ATR process is beneficial since it does not need an additional heat source and is more cost-effective than the SMR method in producing hydrogen [16]. The hydrogen production cost through the ATR method is 1.48 $/kg [27]. Despite the widespread use and cost-effectiveness of fossil fuel-based hydrogen production methods, they pose significant environmental challenges, highlighting the need for cleaner alternatives.

1.3. Renewable resource-based hydrogen production methods

Hydrogen production methods using renewable resources include water electrolysis, photocatalysis, solar thermochemical water-splitting cycle, photovoltaic electrolysis, supercritical water gasification of biomass, and combined dark fermentation and anaerobic digestion [6]. Among them, electrochemical water splitting stands out since it is more mature and is considered for large-scale production of hydrogen [6]. In addition, water electrolysis is the most sustainable technology for hydrogen production [28]. Various technologies based on water electrolysis have been developed for producing hydrogen, including alkaline water electrolyzers, solid oxide electrolyzers, proton exchange membrane (PEM) electrolyzers, etc. The advantages and disadvantages of different electrolyzers are compared in Table 1-2, and their technical characteristics are presented in Table 1-3, which will be discussed in the following subsections.

1.3.1. Water electrolyzers

According to Trasatti, water splitting to produce H_2 and O_2 in the gas phase occurs using input electricity according to the following equation:

$$H_2O + 2F \rightarrow H_2 + ½\ O_2 \quad \text{Equation 1-5}$$

in this equation, F shows the Faraday constant of 1 mol of electricity (96,485 C) [29]. Water electrolyzers comprise two electrodes for oxygen evolution reaction (OER) and hydrogen evolution reaction (HER) on the anode and cathode, respectively.

The equilibrium condition for electrochemical systems is presented using the following equation:

$$\Delta G = -n\mathrm{F}\Delta E \qquad \text{Equation 1-6}$$

In this equation, n shows the number of moles of electricity used for the production of 1 mol of product, and ΔE denotes the potential difference between the two electrodes. Assuming the following reaction:

$$H_2O \rightarrow H_2 + ½\ O_2 \qquad \text{Equation 1-7}$$

we can find the minimum potential difference required in a water electrolyzer without producing electrolysis:

$$\Delta E = \frac{-\Delta G}{n\mathrm{F}}\ (n{=}2) \qquad \text{Equation 1-8}$$

Under standard conditions at 25°C and considering ΔG = 237.178 kJ/mol, we will have:

$$\Delta E^0 = 1.229\ \mathrm{V} \qquad \text{Equation 1-9}$$

This is the theoretical minimum voltage needed for water splitting under equilibrium conditions [29].

Table 1-2. Comparing the most common water electrolysis techniques (Reused from [30]).

Electrolysis technology	Advantages	Disadvantages
Alkaline water electrolysis	• Well-established Technology • Commercialized for industrial applications • Noble metal-free electrocatalysts • Relatively low cost • Long-term stability	• Limited current densities • Crossover of the gasses • High-concentrated (5M KOH) liquid electrolyte
Anion exchange membrane water electrolysis	• Noble metal-free electrocatalysts • Low-concentrated (1M KOH) liquid electrolyte.	• Limited stability of membrane electrode assembly • Under development
Solid oxide water electrolysis	• High working temperature • High efficiency	• Limited stability of electrode materials • Under development
PEM water electrolysis	• Commercialized technology	• Cost of the cell components

	• Operates higher current densities • High purity of the gases • Compact system design • Quick response	• Noble metal electrocatalysts • Acidic electrolyte (such as Nafion, which requires the use of noble metal catalysts with a high cost)

Table 1-3. A comparison of the technical characteristics of typical water electrolysis technologies (Reproduced with permission from [31]).

Specifications	Alkaline	Anion exchange membrane	PEM	Solid Oxide
Working temperature (°C)	30-90	30-60	30-80	500-850
Cell efficiency (%)	50-78	57-60	50-83	80-89
Cell voltages (V)	1.4-2.5	1.4-2	1.4-2.5	1-2
Nominal current density (A cm^{-2})	0.2-0.8	0.2-2	1-3	0.3-1
Hydrogen purity (%)	99.5–99.9998	99.9–99.999	99.9–99.9999	99.9
Durability (hours)	100,000	30,000	50,000–100,000	20,000
Electrode active area (cm^2)	> 10,000	≤ 300	1500	200
Electrolyte	Alkaline solution (20–30% KOH)	Solid polymer membrane with low concentrated alkaline solution (0–2% KOH)	Solid polymer membrane with deionized water	Solid ceramic separator with steam water
State-of-the-art separator	Asbestos/Zirfon	Aemion, Fumasep	Perfluoro sulfonic acid (PFSA)	Yttria-stabilized zirconium
Anode gas diffusion layer	Porous nickel/nickel mesh	Nickel foam	Sintered titanium disk (STD)	Nickel foam/mesh
Cathode porous transport layer	Porous nickel/nickel mesh	Nickel foam/carbon cloth	Carbon cloth/paper/STD	Nickel foam/mesh
Separator plate	Nickel-coated stainless steel	Nickel-coated stainless steel	Gold/platinum-coated titanium	Cobalt-coated stainless steel
Development status	Mature	R&D	Commercialized	R&D

Alkaline water electrolyzers

Alkaline water electrolysis has been employed since the beginning of the 20th century and can operate for up to 15 years. In the cell shown in Figure 1-2, two half-reactions of OER and hydrogen evolution reaction (HER) occur on the anode and cathode, respectively, as shown in the following:

$2H_2O + 2e^- \rightarrow H_2 + 2OH^-$ (Cathode) Equation 1-10

$4OH^- \rightarrow O_2 + 2H_2O + 4e^-$ (Anode) Equation 1-11

The hydroxide ions formed at the cathode diffuse through the electrolyte to the anode, where the OER occurs. The flow of hydroxide ions in alkaline electrolyzers is governed by the ionic conductivity of the electrolyte [32]. An external DC power supply is used to begin the water-splitting process. Since water has poor conductivity, acidic or basic compounds are added to water to improve its conductivity. In the case of alkaline water electrolyzers, KOH or NaOH are commonly utilized [32]. Various cell arrangements and stack designs have been developed for alkaline water electrolyzers. Table 1-4 compares the monopolar, bipolar, filter-press, and zero-gap configurations [33]. The main advantage of alkaline water electrolysis is the possibility of using inexpensive and non-precious metals as catalysts [34]. However, disadvantages, such as a limited current density (below 0.45 A/cm^2), lower efficiency (60-70%) compared to other technologies, and the corrosive nature of alkaline media, have limited its application [35].

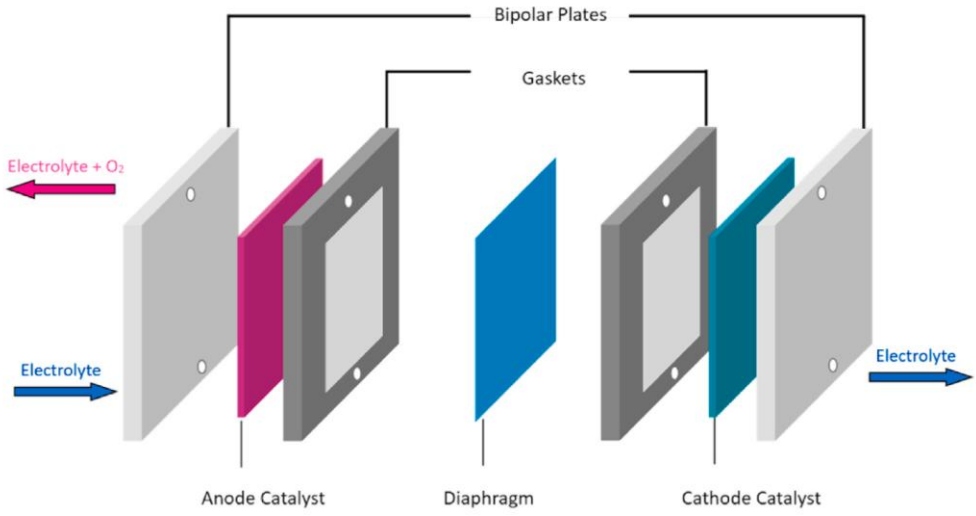

Figure 1-2. The schematic of a cell of an alkaline water electrolyzer (Reused with permission from [35]).

Table 1-4. Highlights of different designs of alkaline water electrolyzers (Reused with permission from [33]).

Electrolyser Design	Design Features	Advantages	Disadvantages	Typical Cell Arrangement	System Components
Monopolar/ Unipolar	Single electrode per cell, parallel electrical connections, external electrical insulation	Simple construction, easy maintenance, modular design	High electrical resistance, limited current density, lower energy efficiency	Cells connected in parallel	Electrodes, separators, end plates, electrical connections, sealing gaskets
Bipolar	Single electrode per cell, series electrical connections, bipolar plates for separation	High current density, high energy efficiency, compact design	Complex construction, difficult maintenance, potential shunt currents	Cells connected in series	Electrodes, bipolar plates, end plates, electrical connections, sealing gaskets
Filter-press	Multiple electrodes per cell, parallel electrical connections, external compression	High active area, modular design, easy maintenance	High electrical resistance, limited current density, larger footprint	Cells connected in parallel or series parallel	Electrodes, separators, end plates, compression system, electrical connections, sealing gaskets
Zero-gap	Electrolyte flow between electrodes, high compression	High current density, high energy efficiency, compact design	Complex construction, challenging electrolyte management, potential electrode shorting	Electrodes arranged in a zero-gap configuration	Electrodes, electrolyte circulation system, compression system, electrical connections

Anion exchange membrane water electrolysis

The structure of the anion exchange membrane electrolyzer is shown in Figure 1-3, in which an anion exchange membrane is between the catalyst layers (CLs) [36]. The anion exchange membrane acts as a gas-impermeable separator through which hydroxide ions can diffuse from the cathode to the anode. Similar to alkaline water electrolyzers, an anion exchange membrane electrolyzer contains HER and OER electrocatalysts. In addition, these devices use surface-treated metal foams or felt, which act as porous transport layers (PTLs). The PTLs can promote the transport of gases and liquids and also provide mechanical support [36]. The advantages of anion exchange membrane water electrolyzers are the use of precious metal-free electrocatalysts and low-concentrated liquid electrolytes [30]. However, they suffer from limited stability of membrane electrode assembly [37] and are still under development.

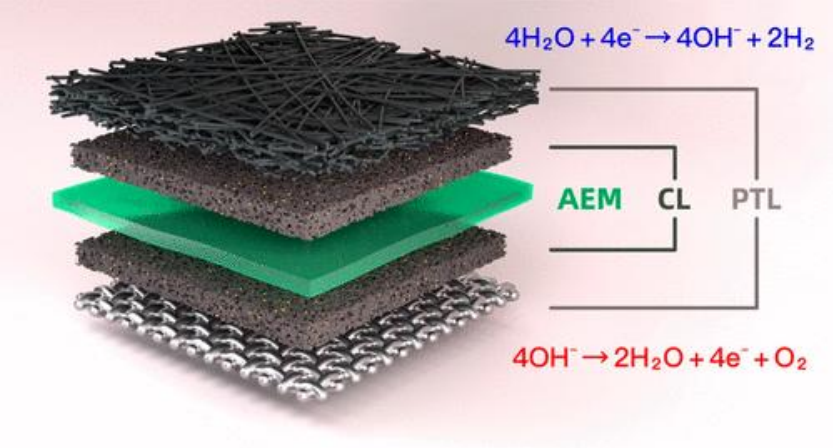

Figure 1-3. The schematic diagram showing the main components of the anion exchange membrane water electrolyzer: CL, catalysts layers, and PTL, porous transport layers (Reused with permission from [36]).

Solid oxide water electrolyzer

In solid oxide water electrolyzers (shown in Figure 1-4), steam is used at high temperatures (500-850°C), which can significantly decrease the power consumption for water splitting. This has the potential to decrease the production cost of hydrogen. In these devices, two porous electrodes (anode and cathode) are used along with the dense ceramic electrolyte to transport oxide ions (O^{2-}). Yttria-stabilized zirconia (YSZ) is mostly used as a ceramic electrolyte. The advantage of this device is that it does not need a noble metal electrocatalyst and has a high conversion efficiency. However, the inappropriate long-term stability of electrode materials has hindered their commercialization, and they are still under development [30].

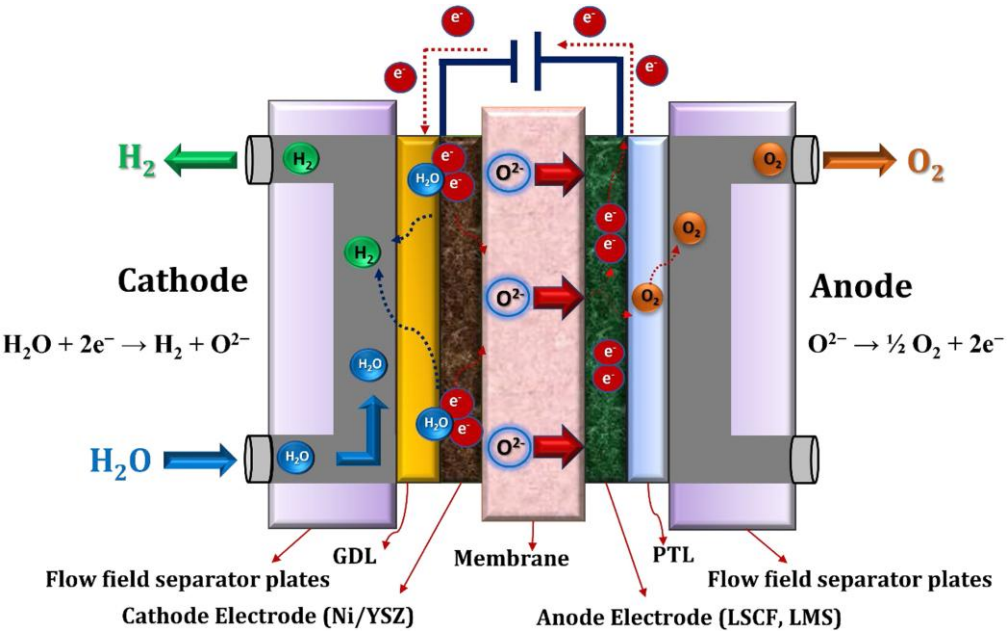

Figure 1-4. Schematic representation of solid oxide water electrolysis system (Reused with permission from [30]).

PEM water electrolyzer

PEM water electrolysis is one of the promising and sustainable technologies for hydrogen production. In PEM electrolyzers, OER and HER occur according to the following equations under acidic media:

Anode reaction $2H_2O \rightarrow O_2 + 4H^+ + 4e^-$ Equation 1-12

Cathode reaction $4H^+ + 4e^- \rightarrow 2H_2$ Equation 1-13

Figure 1-5 (a) shows the schematic of the PEM electrolysis setup, Figure 1-5 (b) represents the photo of a PEM electrolyzer system, and the major components of the cell are shown in Figure 1-5 (c). Moreover, the cost breakdown of a PEM electrolyzer is illustrated in Figure 1-5 (d), showing the share of electrocatalyst materials. In this setup, water is fed into the anode site and is split into oxygen, protons, and electrons. The protons cross the proton-conducting membrane to the cathode. At the same time, electrons move through the external electrical circuit and recombine with protons at the cathode to form hydrogen gas.

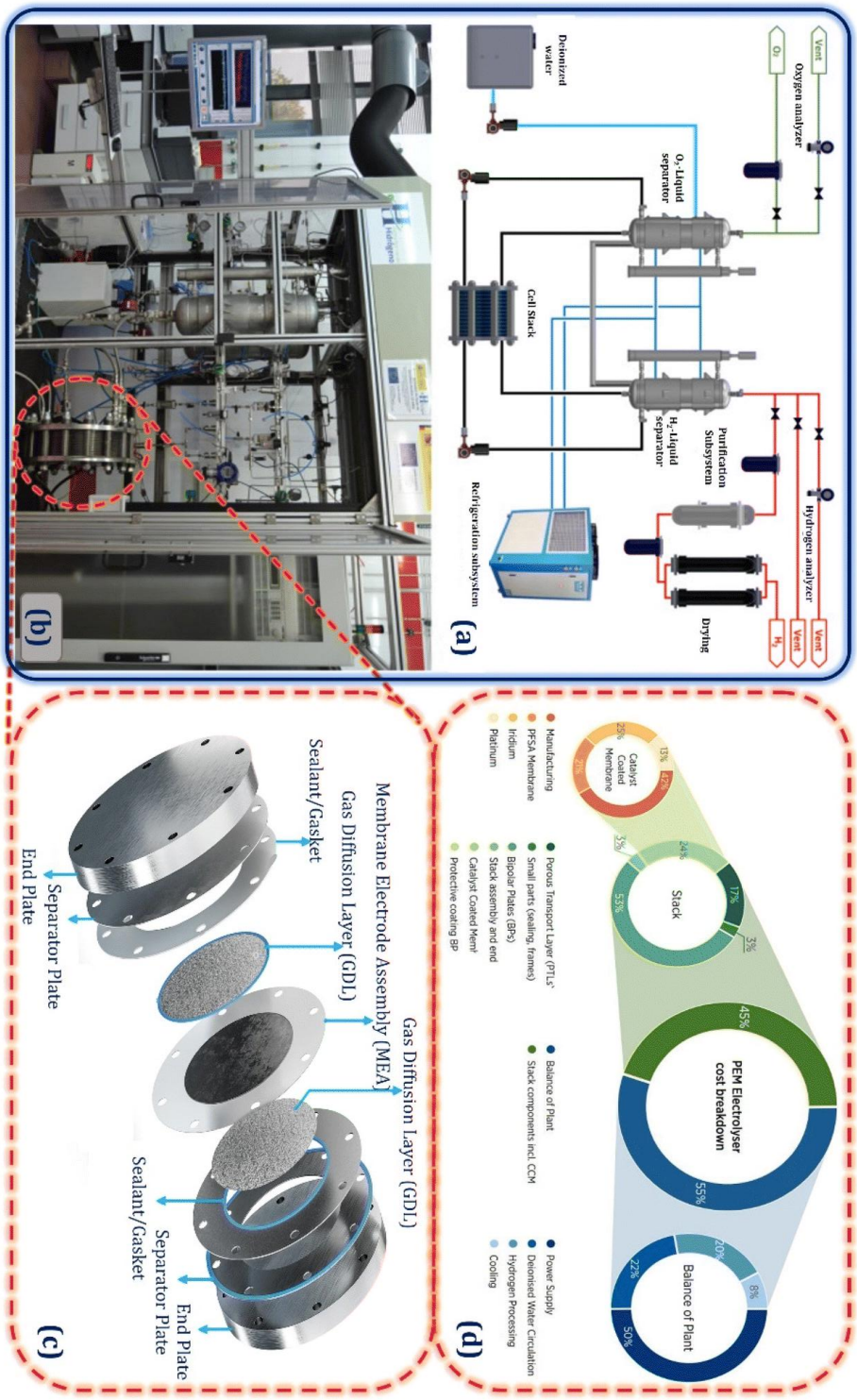

Figure 1-5. (a) The schematic representation of a PEM electrolysis setup. (b) The photo of a PEM electrolyzer system with (c) major components of a cell. (d) Cost breakdown of a PEM electrolyzer (Reused with permission from [31]).

The main components of the PEM electrolyzers are the membrane, electrodes, gas diffusion layers, bipolar plates, and balance of plant (BoP). The advantages of PEM electrolyzers are higher operating current density, higher energy efficiency, compact system design, rapid and dynamic response in combination with renewable energy sources, and high purity of produced hydrogen. These advantages have made them superior to other electrolyzers. The disadvantage of PEM electrolyzers is the complexity of developing precious metal-free electrocatalysts. Currently, Ir- or Ru-based and Pt-based electrocatalysts are being used for OER and HER, respectively [31].

The theoretical minimum energy for water splitting in water electrolysis systems is 1.23 V, but due to the kinetic and ohmic losses, the actual operative voltage is more than 1.4 V. The cell voltage (U_{cell}) in PEM electrolyzers includes reversible cell voltage (U_{rev}) and voltage losses, as shown in Figure 1-6. The voltage loss in PEM electrolyzers is due to kinetic, ohmic, and mass transfer losses:

$$U_{cell} = U_{rev} + i\left(R^{mem} + R_{el} + R_{H^+}^{a,eff} + R_{H^+}^{c,eff}\right) + \left(\eta_{act}^{a} + |\eta_{act}^{c}|\right) + \eta_{mt} \qquad \text{Equation 1-14}$$

In this equation, $i\left(R^{mem} + R_{el} + R_{H^+}^{a,eff} + R_{H^+}^{c,eff}\right)$, $+\left(\eta_{act}^{a} + |\eta_{act}^{c}|\right)$, and η_{mt} correspond to ohmic loss, kinetic loss, and mass transport loss, respectively. R^{mem}, R_{el}, $R_{H^+}^{a,eff}$, and $R_{H^+}^{c,eff}$ denote membrane resistance of the proton transport, the cell's electrical resistance, and effective proton resistance of the anode and cathode layers of the cell, respectively. η_{act}^{a} and η_{act}^{c} show the activation overpotential of anodic and cathodic reactions, respectively, which lead to mass transport loss (η_{mt}) [38].

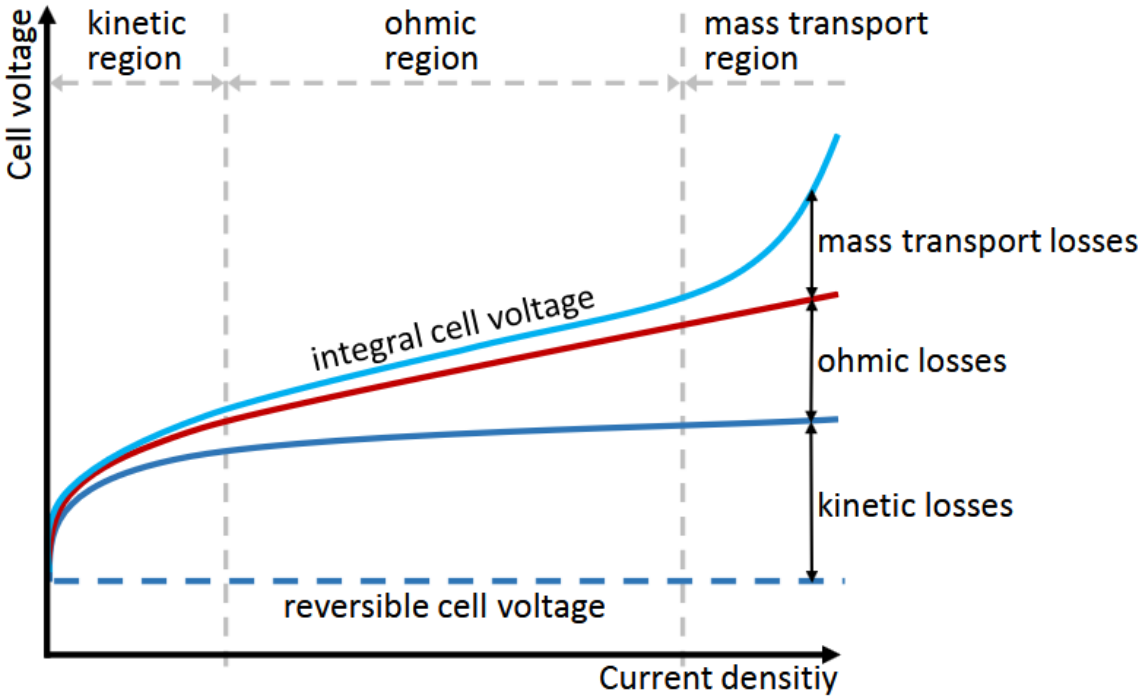

Figure 1-6. The schematic representation of the polarization behavior of a PEM electrolyzer with cell voltage breakdown (showing voltage loss due to kinetic, ohmic, and mass transfer losses, reused from [38]).

1.4. OER electrocatalysis

OER is one of the critical processes in water splitting technologies for the production of green hydrogen. This section discusses the mechanisms and performance evaluation metrics of OER electrocatalysts, as well as the challenges of developing OER electrocatalysts for acidic media. OER occurs on the anode of electrolyzers for hydrogen production, which depends on the electrolyte pH:

$$4OH^- \rightarrow O_2 + 2H_2O + 4e^- \quad (pH = 14)$$ Equation 1-15

$$2H_2O \rightarrow O_2 + 4H^+ + 4e^- \quad (pH = 7)$$ Equation 1-16

$$2H_2O \rightarrow O_2 + 4H^+ + 4e^- \quad (pH = 0)$$ Equation 1-17

In addition, PEM electrolyzers, working under acidic media, are superior to other water electrolyzers, as explained in the previous section. This motivates the extensive research on developing OER electrocatalysts under acidic media. Ru- and Ir-based materials are the best acidic OER electrocatalysts, which are expensive [39]. The research on developing OER

electrocatalysts for acidic media focuses on proposing precious metal-free electrocatalysts or decreasing the loading of Ir or Ru. In the next section, mechanisms and performance evaluation metrics of OER electrocatalysts are discussed.

1.4.1. OER mechanisms

Mechanisms Based on Kinetic Studies

Many different mechanisms have been proposed for OER based on kinetic studies or density functional theory (DFT) calculations. In mechanisms based on kinetic studies, it is assumed that the Tafel slope, which is determined through electrochemical tests and means how fast the current is increased with the applied overpotential [40], is associated with the rate-determining step (RDS) of the reaction mechanism [41]. To show how the Tafel slope can be obtained, we need to refer to the well-known Butler–Volmer equation, which describes the relationship between current density (*i*) and the applied overpotential when there is no mass transfer effect [40, 42]:

$$i = i_0[\exp\left(\frac{\alpha_a nF}{RT}\eta\right) - \exp\left(-\frac{\alpha_c nF}{RT}\eta\right)] \quad \text{Equation 1-18}$$

In the above equation, i_0 refers to the exchange current density, α_a is anodic charge transfer coefficient, α_c is cathodic charge transfer coefficient, n is the number of electrons in the reaction, F is the Faraday constant, η is the overpotential, R is the universal gas constant, and T is the temperature. At high anodic overpotentials, the anodic end of the equation dominates, and the contribution of the cathodic end is considered negligible. So, the Butler–Volmer equation can be simplified to this form, also known as the Tafel equation:

$$i \approx i_0 \exp\left(\frac{\alpha_a nF\eta}{RT}\right) \quad \text{Equation 1-19}$$

By translating the Tafel equation to the logarithm function, we will have the following equation:

$$\log(i) = \log(i_0) + \frac{\eta}{b} \quad \text{Equation 1-20}$$

Tafel slope is defined as the overpotential change with respect to the logarithm of the current density according to the following equation:

$$b = \frac{\partial\eta}{\partial \log(i)} = \frac{2.303\ RT}{\alpha F} \quad \text{Equation 1-21}$$

Some kinetic-based mechanisms proposed for OER are summarized in Table 1-5 [43] with the stoichiometric number and Tafel slope (indicated by *b*). In the table, the stoichiometric number is the number of times the RDS occurs for one repetition of the overall reaction [44].

For the Chemical oxide pathway, first, a water molecule is oxidized on the active site (shown by S). Then, two OH intermediates form an adsorbed O, and finally, an O_2 molecule will be formed by combining two adsorbed O. The second step, with a Tafel slope of 30 mV, characterizes this reaction mechanism, which can be one of the most efficient OER mechanisms. The last step with a Tafel slope of 15, which is only virtual, has never been reported [43].

In the electrochemical oxide path, following the primary oxidation of the water molecule, the OH groups adsorbed on the surface are oxidized to form adsorbed O on the active site. In the last step, the adsorbed O intermediates form an oxygen molecule. The second step, with a Tafel slope of 40 mV, characterizes the occurrence of this reaction mechanism. In the oxide decomposition path, acid-base dissociation of adsorbed OH groups is distinct. In this mechanism, the presence of a true oxide layer is considered.

The most unique feature of the oxide decomposition pathway, as shown in Table 1-5, is the acid-base dissociation of surface OH groups. In this mechanism, a chemical view of the evolution of oxygen at the electrode surface is introduced, indicating the presence of an oxide layer on the surface [43].

Table 1-5. Kinetic-based reaction mechanisms for OER under acidic media [43].

Reaction Steps	Stoichiometric number	*b* (mV)
Chemical oxide path (proposed by Bockris in 1956)		
$S + H_2O \rightarrow S\text{-}OH + H^+ + e^-$	4	120
$2S\text{-}OH \rightarrow S\text{-}O + H_2O$	2	30
$2S\text{-}O \rightarrow O_2 + 2S$	1	15
Electrochemical oxide path (proposed by Bockris in 1956)		
$S + H_2O \rightarrow S\text{-}OH + H^+ + e^-$	2	120
$S\text{-}OH \rightarrow S\text{-}O + H^+ + e^-$	2	40
$2S\text{-}O \rightarrow O_2 + 2S$	1	15
Oxide decomposition path (proposed by Krasil'shchikov in 1963)		
$S + H_2O \rightarrow S\text{-}OH + H^+ + e^-$	2	120
$S\text{-}OH \rightarrow S\text{-}O^- + H^+$	2	60
$S\text{-}O^- \rightarrow S\text{-}O + e^-$	2	40
$2S\text{-}O \rightarrow O_2 + 2S$	1	15

DFT-based mechanisms

A) Adsorbate evolution mechanism (AEM)

AEM has been proposed by Nørskov et al. based on DFT calculations [45-47]. This includes four proton-coupled electron transfer steps, as shown in the following equations and Figure 1-7:

$$M + H_2O \rightarrow M\text{-}OH + H^+ + e^- \quad \text{Equation 1-22}$$

$$M\text{-}OH \rightarrow M\text{-}O + H^+ + e^- \quad \text{Equation 1-23}$$

$$M\text{-}O + H_2O \rightarrow M\text{-}OOH + H^+ + e^- \quad \text{Equation 1-24}$$

$$M\text{-}OOH \rightarrow O_2 + M + H^+ + e^- \quad \text{Equation 1-25}$$

In the first step, a water molecule is adsorbed, which leads to the adsorption of the OH intermediate with the release of a proton and an electron. Then, after the release of a proton and an electron of OH, the O intermediate is formed on the active site. In the next step, another water molecule with the adsorbed O intermediate forms the adsorbed OOH. Finally, the adsorbed OOH intermediate forms an O_2 molecule, which will be desorbed. For the ideal catalyst, the Gibbs free energy (ΔG) of each step of the AEM mechanism is 1.23 eV [48].

B) Lattice oxygen mediated (LOM) mechanism

Owing to the linear relationship between the adsorption ΔG of intermediates in the AEM mechanism, the overpotential calculated through the AEM mechanism would be more than 0.37 V [49]. However, with further experimental research on various materials, electrocatalysts with lower overpotentials have been developed. So, a new mechanism was proposed to accurately study materials with overpotentials lower than 0.37 V. As shown in Figure 1-7, the first two steps of the LOM mechanism are similar to the AEM, ending at the adsorption of O intermediate. However, then, in the LOM mechanism, the adsorbed O intermediate couples with an oxygen site of the lattice and forms an oxygen molecule. As a result, an oxygen vacancy will be formed on the surface, which will be occupied by the migration of OH^- from the electrolyte [49].

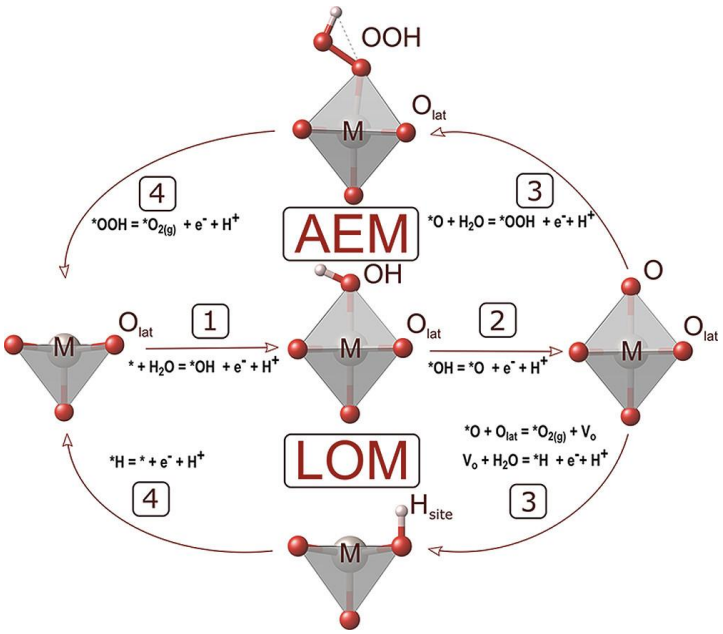

Figure 1-7. Schematic of the AEM and LOM mechanisms in OER (Reused with permission from [50]).

1.4.2. OER electrocatalyst metrics

Three metrics are considered in developing OER electrocatalysts for acidic media: activity, stability, and cost. Activity can be assessed through electrochemical tests and DFT calculations. In DFT calculations, the computational hydrogen electrode (CHE) theory developed by Nørskov et al. [51] is used to calculate the OER overpotential and Free energy diagram. In the experiments, activity is evaluated based on overpotential, turnover frequency (TOF), and specific activity. The overpotential is defined as the extra potential beyond the thermodynamic equilibrium (1.23 V) required to drive the OER. TOF shows the number of reaction products produced per active site per unit time [52]. To analyze the specific activity, the current is normalized using the geometric surface area of the working electrode or the electrochemically active surface area (ECSA) of the electrocatalyst.

In experiments, overpotential can be obtained by performing linear sweep voltammetry (LSV) or cyclic voltammetry (CV) tests in a typical three-electrode system, as shown in Figure 1-8 (a). The difference between the potential to reach a current density of 10 mA/cm^2 and equilibrium potential (1.23 V) is considered OER overpotential, as shown in Figure 1-8 (b). In the three-electrode system, the catalyst is loaded on a working electrode substrate such as glassy carbon or fluorine-doped tin oxide (FTO)-coated glass. A counter electrode, such as Pt, graphite rod, or

gold, is used to complete the circuit and enable the flow without affecting the reactions on the working electrode [53]. In addition, a reference electrode is used to record the potential against it, which can be converted to the desired standard potential, such as the reversible hydrogen electrode (RHE).

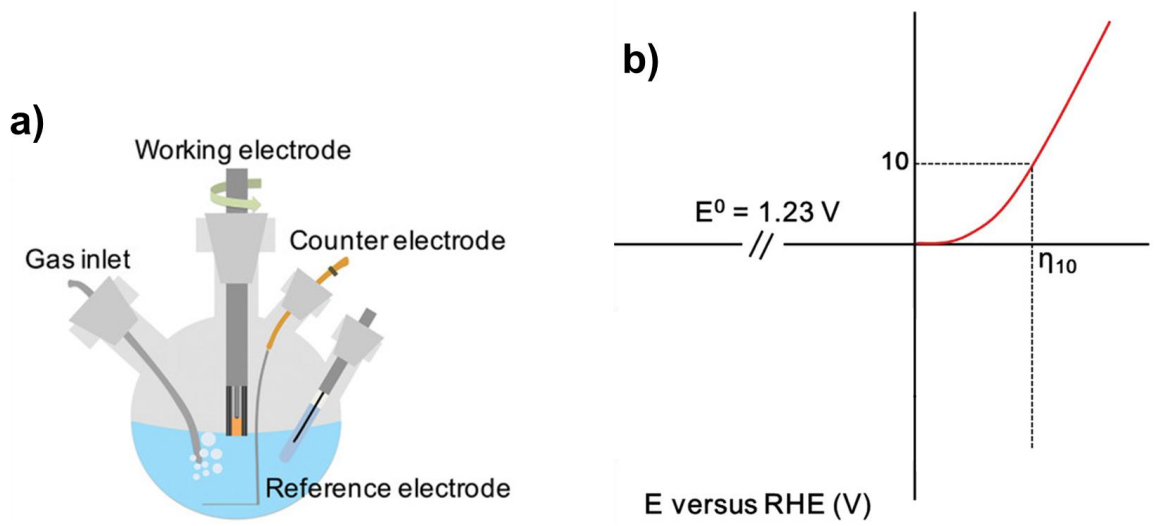

Figure 1-8. The schematic presentation of (a) the three-electrode system (Reused from [53]) and (b) the overpotential to reach a current density of 10 mA/cm^2 (Reused from [54]).

ECSA can be estimated using two sets of techniques: 1- the coulombic charge of a surface redox reaction (this method includes hydrogen underpotential deposition (HUPD), CO stripping, and underpotential deposition (UPD)) and 2- non-faradaic double layer capacitance (C_{dl}) [53].

The stability of OER electrocatalysts is assessed using tests such as CV, chronoamperometry (CA), or chronopotentiometry (CP). In CV tests, potential cycling is done between suitable limits. In this test, the upper limit should involve the current increment due to OER, as shown in Figure 1-9 (a) (the orange curves shown in the figure represents electrocatalysts that are degraded with time, and the blue color shows the stable electrocatalyst). Then, the current density variation after many cycles (up to several 10,000 cycles) is recorded, showing the stability of the electrocatalyst. In the CA test, a selected reference potential is applied to the electrode (overpotential), and then the current density variation is recorded, as shown in Figure 1-9 (b). In the CP test, a specific current density (typically 10 mA/cm^2) is held, and the potential variation to keep that current density is recorded. In addition, the stability number (S-number) was introduced recently, which is similar to TOF. S-number corresponds to the ratio of generated

oxygen molecule to dissolved metal(s); i.e., how much oxygen is generated to dissolve or deactivate one active site of the electrocatalyst [55]. As shown in Figure 1-9 (d-e), it is possible to predict the lifetime of Ir-based electrocatalysts based on the S-number.

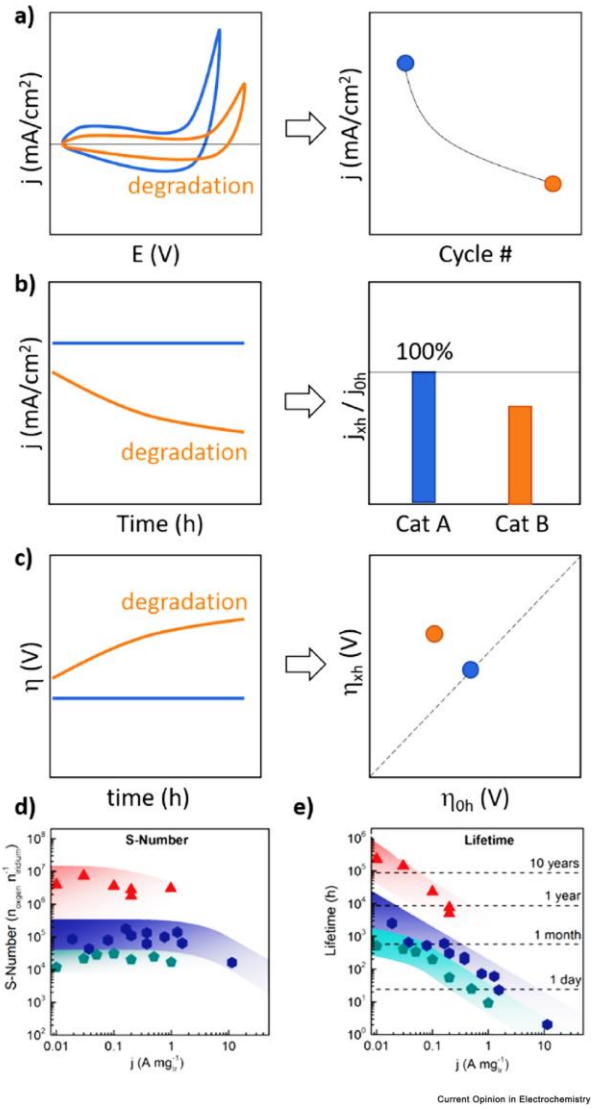

Figure 1-9. The methods to study the stability of OER electrocatalysts, including (a) cyclic voltammetry, (b) chronoamperometry, and (c) chronopotentiometry. (d) The S-number for different Ir-based electrocatalysts with (e) estimated lifetimes (Reused with permission from [55]).

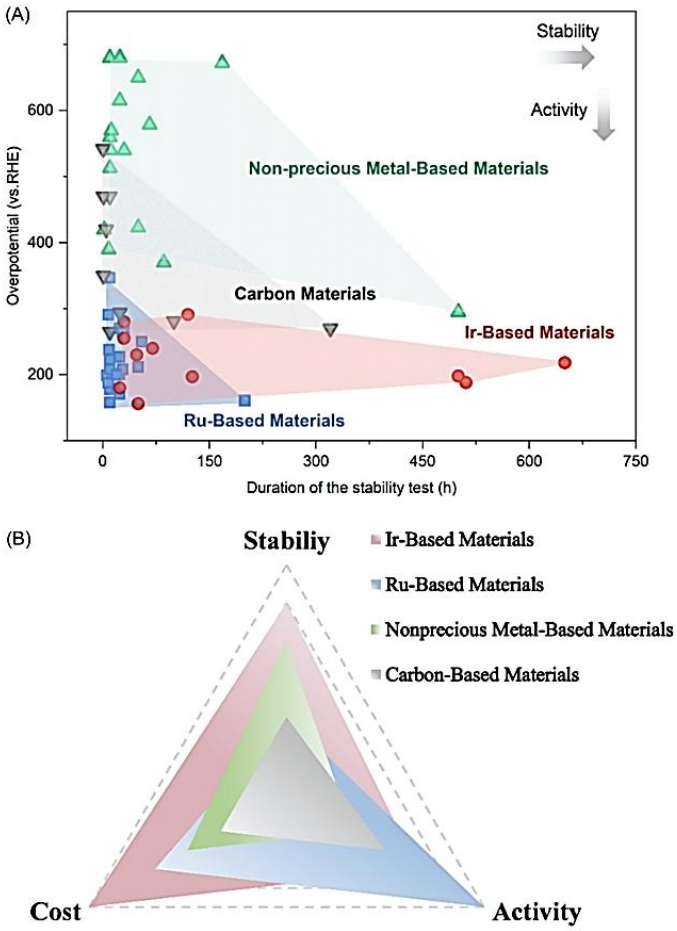

Figure 1-10. (a) Stability and OER overpotential of various electrocatalysts reported in recent years. (b) Comparing the stability, activity, and cost of non-precious metals, Ir-, Ru-, and carbon-based materials for OER under acidic media (Reused with permission from [56]).

1.5. Materials used as electrocatalysts for OER

As shown in Figure 1-10 (a-b), Ir-based electrocatalysts are the most stable, and Ru-based electrocatalysts are the most active. Carbon-based materials suffer from low stability due to oxidation at anodic potentials, and non-precious metal-based electrocatalysts are not as active as Ir- and Ru-based materials. Figure 1-10 (b) compares the cost, stability, and activity of electrocatalyst materials for OER under acidic media.

The *d* orbitals of noble metals, Ir and Ru, are unfilled and they possess unique electronic properties, leading to easy adsorption of intermediates on the surface [57]. Therefore, the adsorption energy of reaction intermediates (OH*, O*, and OOH*) on Ru and Ir-based materials

is moderate, not too strong nor too weak, which causes them to have high catalytic activity for OER and places them at the top of the Volcano plot, as shown in Figure 1-11.

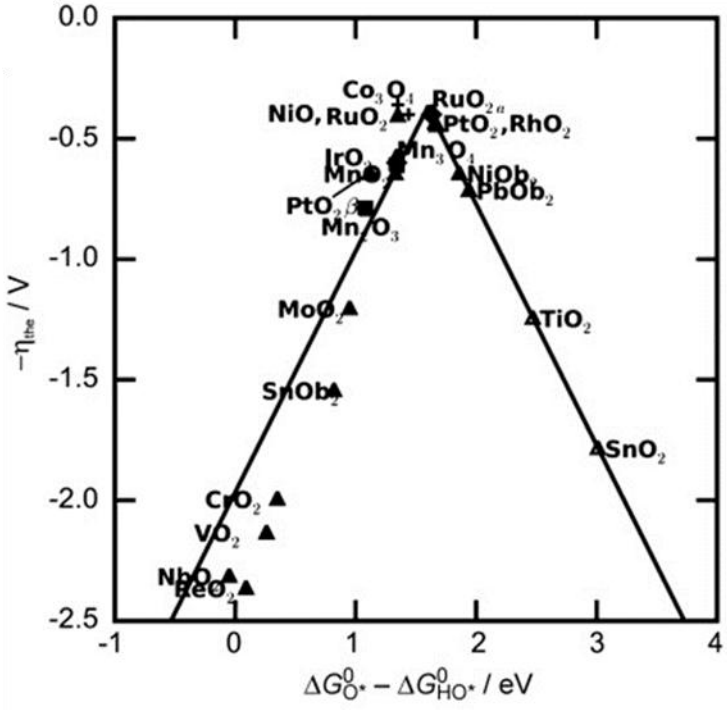

Figure 1-11. The trend of OER activity for metal oxides such as IrO_2 and RuO_2. In this figure, overpotential is plotted versus $\Delta G_{HO^*} - \Delta G_{O^*}$ (adsorption Gibbs free energy of OH* and O*). [47].

There are several mechanisms leading to the deactivation of OER electrocatalysts, including dissolution, change in the crystal phase and morphology of the catalyst, passivation, catalyst detachment from the electrode, and blockage of the catalyst surface by gas bubbles [58]. For instance, RuO_2 is oxidized in acidic media under anodic potentials to form RuO_4, which is volatile. As shown in Figure 1-12 (a), both the OER mechanism on RuO_2 and its dissolution mechanism include the formation of RuO_4 as an intermediate. The relative stability of the $RuO_2(OH)_2$ intermediate can show if the corrosion of RuO_4 occurs (into the gas phase or solution) or if it will be dissociated to O_2 and $RuO_2(OH)_2$ [58]. When higher potentials are applied to Ir-based materials, the mechanism shown with red arrows in Figure 1-12 (b) occurs, where the IrO_3 intermediate is formed. IrO_3 is highly reactive, which can be decomposed to IrO_2 and O_2 (Step S9 in Figure 1-12 (b)) or form Ir_4^{2-}. The formed Ir_4^{2-} is soluble and dissolves into the electrolyte. Moreover, IrO_2 also might be oxidized to Ir^{3+}, which is soluble [58]. Furthermore, at low potentials, IrO_2 can be reduced to $HirO_2$ intermediate, which leads to the dissolution as Ir^{3+}, as shown in green arrows in Figure 1-12 (b).

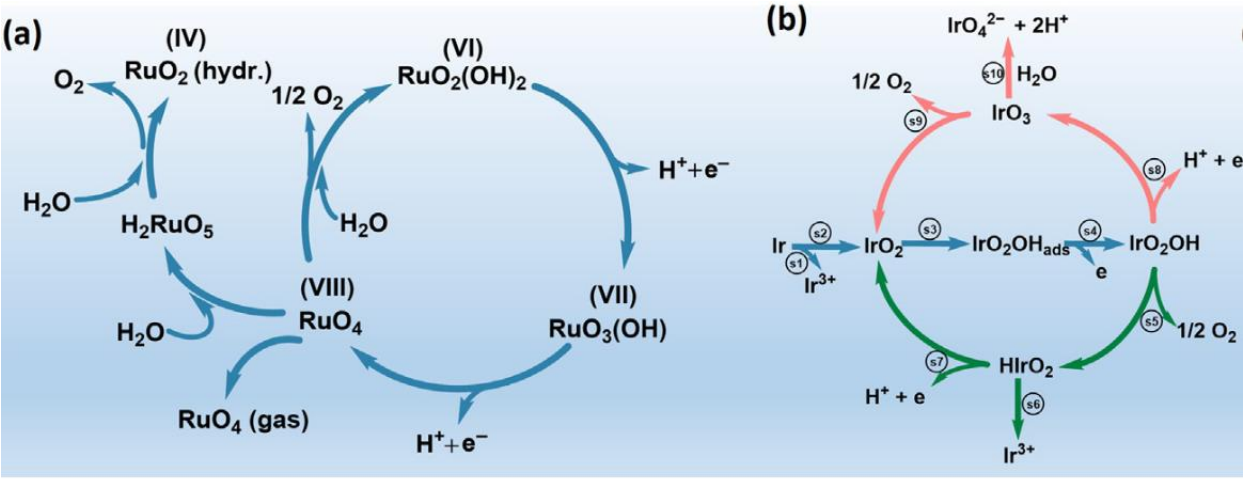

Figure 1-12. (a) The dissolution mechanism of Ru and RuO_2 electrocatalysts in acidic OER. (b) The pathways that are possible to cause the dissolution of Ir in acidic OER. Red arrows show the pathway at higher potentials, and green arrows show the mechanism at lower potentials. In addition, the intermediate steps that occur regardless of the applied potential are shown by blue arrows (Reused with permission from [58]).

Some of the state-of-the-art OER electrocatalysts based on Ir and Ru are discussed here. Ping et al. interstitially doped silicon into RuO_2 to stabilize its Ru sites and suppress the oxidation of lattice oxygen. When the molar ratio of Si to Ru was 0.1, the degradation rate of around 52 μV/h was observed in a test for 800 h, and the overpotential was 0.226 V at 10 mA/cm^2 [59]. Chang et al. periodically arranged atomic arrays of Ru on Co_3O_4, where Ru atoms also replaced lattice Co atoms. In this electrocatalyst, the Ru-Ru distance was 2.5 Å (in pure RuO_2, the distance is 3.1 Å), which led to an overpotential of 0.160 at 10 mA/cm^2 and durability of 15000 h [60]. Su et al. localized tensile-strained Ir atoms at surface cation sites of MnO_2. This electrocatalyst showed an overpotential of 0.198 V to reach a current density of 10 mA/cm^2 and mass activity of 1025 A/g of Ir [61]. Li et al. could synthesize and atomically disperse Ir^{6+} oxide, which was predicted to be more active and stable than other Ir-based oxides. To this end, they substituted the ligands of potassium hexachloroiridate(IV) oxidatively with MnO_2. This electrocatalyst showed outstanding performance of 1.7 x 10^5 A/g of Ir, which was stable at current densities of up to 2.3 A/cm^2 [62].

To decrease the economic risks of using water electrolyzers for hydrogen production in the future, it is critical to develop precious metal-free catalysts and diversify catalyst material supply; even the diversification of the precious metal-based catalysts can be helpful [63]. Based on

Figure 1-10 (a) and (b), stability is the main challenge in developing OER electrocatalysts under acidic media.

To identify cost-efficient, highly stable, and efficient electrocatalysts for OER, this thesis focussed on Nb- and Ta-based materials, which are well known to have high stability [64]. Niobium [65, 66] and Tantalum [66] are considered critical in Canada, and 8.6% of global niobium is produced in Canada. Figure 1-13(a) shows the increasing trend of publications using niobium or tantalum for catalysis, electrocatalysis, or photocatalysis, and Figure 1-13(b) shows the countries making the greatest contribution to these publications.

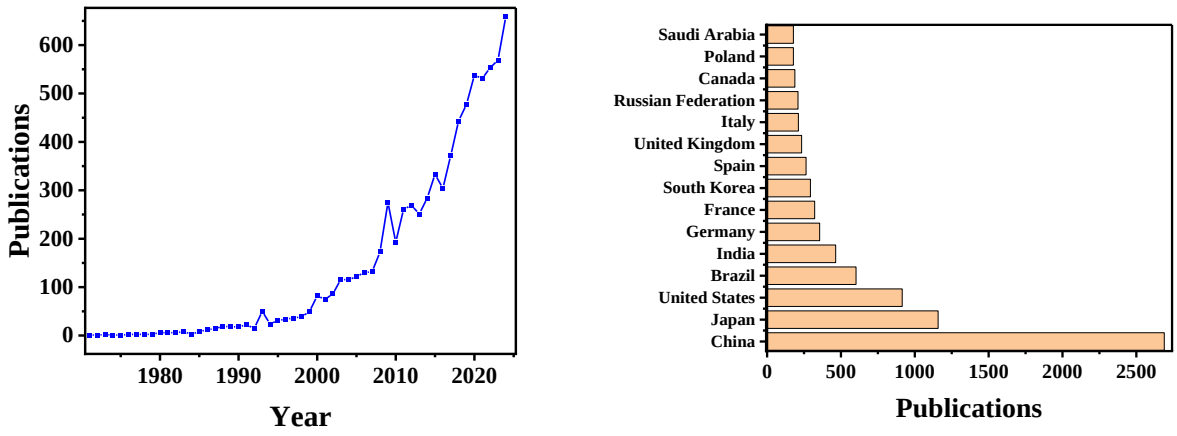

(a) (b)

Figure 1-13. (a) Publication trends for keywords including catalyst, electrocatalyst, or photocatalyst in combination with tantalum or niobium, and (b) top publishing countries.

The major advantage of metals such as Nb and Ta is their high degree of freedom [67]. In this context, the high degree of freedom implies that after various treatment methods such as doping, heat treatment, etc., these materials can have various states and electronic properties in their crystalline structures [67]. This enables the modulation of the properties of Nb- and Ta-based materials. However, the main challenge of using these materials is their low activity for OER.

Regarding the use of Nb in OER, state-of-the-art publications have focused on using Nb as a dopant [68] or designing mixed oxides with IrO_2 [69]. For instance, Ke et al. doped Nb into Van der Waals layered edge-shared 1T phase IrO_2 (1 T-IrO_2). They showed that doping 5% Nb into

1 T-IrO_2 could decrease the overpotential to 0.191 V at 10 mA/cm^2, with stable operation for over 50 days at a high current density of 1.2 A/cm^2 [68]. Moreover, Wu et al. first created oxygen vacancies in metal oxides such as Nb_2O_5, followed by immobilizing IrO_2 on them. The prepared IrO_2/Nb_2O_{5-x} showed an overpotential of 0.225 V at 10 mA/cm^2 and durability of more than 200 h [69].

In this thesis, specifically, two-dimensional (2D) transition metal carbide (MXene) materials, a new class of 2D materials, were studied due to their high conductivity and tunability of the electronic properties. So far only Ti-based MXenes have been mostly studied, with less attention paid to other materials, such as Nb-based MXenes [70]. Nb-based MXenes have been studied for OER, where the strong adsorption affinity of pristine Nb_2C with F, O, or OH termination led to poor OER performance [71]. Kan et al. [71] showed that doping Pt into Nb_2C MXene could decrease its OER overpotential. However, before starting the project, no study had focused on tuning the catalytic properties of Nb-based MXenes using terminations such as S, Cl, and F and their combinations. In addition, the other challenge of MXenes is their poor stability against oxidation and hydrolysis, which destroys the MXene structure during catalytic reactions in aqueous solutions [72]. So, it is essential to find methods to modulate the catalytic properties of Nb-based MXene without using precious metals and improve their stability to enable their use in OER electrocatalysis.

Furthermore, Ta-based materials, mostly Ta_2O_5, have been widely used in acidic OER to increase the stability of iridium oxide and decrease the Ir loading [73, 74], with an Ir/Ta ratio of 70:30 [75]. Liu et al. anchored $IrRuO_x$ on Ta_2O_5 with abundant oxygen vacancies and a high surface area. They reported that due to the synergistic role of $IrRuO_x$ and Ta_2O_5, at 0.3 mg_{Ir}/cm^2, a low overpotential of 0.235 V at 10 mA/cm^2 was observed in acidic media, and the cell potential to deliver 2 A/cm^2 was 1.91 V [76]. Huang et al. incorporated B into the IrO_2-Ta_2O_5 coating on a Ti plate through the thermal decomposition method. The sample prepared using the H_3BO_3 concentration of 0.6 M showed an overpotential of 0.210 at a current density of 10 mA/cm^2. This was attributed to the role of B species in adjusting the barrier energy of intermediates [74].

The other strategy of using Ta in OER electrocatalysis is doping it into other oxides, such as RuO_2 [77, 78]. For instance, Wang et al. doped single Ta atoms with short-range order into RuO_2, which strained the RuO_2 lattice and shifted the d-band center of Ru. As a result, an overpotential of 0.201 V at 10 mA/cm^2 and long-term stability of 280 h was observed [78]. Zhang

et al. could also stabilize RuO_2 by doping with Ta, which showed a performance decay rate of around 14 µV/h in a test for 2800 h. The overpotential of $Ta_{0.1}Ru_{0.9}O_{2-x}$ was 0.226 V at 10 mA/cm^2, which also showed the capability to be used in industrial applications. They also employed DFT calculations to reveal the role of Ta dopants in stabilizing RuO_2 and found that ΔG values for RuO_4 dissolution were increased after doping with Ta, which was due to the strong binding of RuO_2 dissolution intermediate and Ta sites [77].

In industrial applications, Ta is also used in dimensionally stable anodes (DSAs) for OER. DSAs are composed of metallic support, such as Ti or Ta, which is coated using a thin layer of metal oxides, such as IrO_2. De Nora company has commercialized RuO_2-TiO_2 and Ti/IrO_2-Ta_2O_5 (45:55 atomic%) [79]. The advantages of DSAs include high chemical stability, corrosion resistance, and long service life, which are reported to be around 8 to 9 years [79]. In this regard, Amano et al. used porous Ti felt comprising nanofibers as the substrate for IrO_2-Ta_2O_5. They investigated the role of Ti substrate and calcination temperature on the OER performance of the prepared electrocatalyst. The best performance was obtained using a calcination temperature of 350°C, where an amorphous thin layer of IrO_2-Ta_2O_5 was formed on the Ti felt. This electrocatalyst showed an overpotential of 0.27 V at 10 mA/cm^2, which had a large surface area (ECSA) [80].

However, less research has been done on using Ta-based materials as the active phase in acidic OER. There is no study on the role of the electronic properties and *d* orbitals of Ta_2O_5 in modulating its OER performance, enabling its use as an active OER electrocatalyst. In addition, sodium tantalates such as $NaTaO_3$ and $NaTa_3O_8$, which are stable under acidic media, have not been investigated for OER electrocatalysis.

1.6. Objectives of the thesis

The main contribution and the general objective of this thesis was to suggest methods to modulate Nb-based MXenes and Ta-based materials to improve their OER performance . The specific objectives include the following:

- To investigate the effect of terminating groups and defects on the catalytic and electronic properties of Nb_2C MXenes;
- To investigate the possibility of increasing the stability of MXenes by modeling MXene/graphene heterostructure

- To develop Ta oxide-based electrocatalysts for OER by creating defects, modeling a heterostructure with graphene, and finding the correlation between the properties of Ta sites and OER performance;
- To investigate sodium tantalate-based electrocatalysts, including $NaTaO_3$ and $NaTa_3O_8$, for OER under acidic media;

1.7. Structure of the thesis

Chapter 2 investigates the effect of terminating groups on the catalytic and electronic properties of Nb_2C MXene. Chapter 3 presents the DFT calculation results for the aqueous and oxidative stability of the Nb_2C/graphene heterostructure and its OER performance. In Chapter 4, the OER activity of three facets of Ta_2O_5 is investigated, and the effect of graphene on improving its OER performance is also presented. Chapter 5 presents the results of the DFT calculations for the OER performance of two sodium tantalate structures, i.e., $NaTaO_3$ and $NaTa_3O_8$. Finally, Chapter 6 concludes the results of the thesis and future perspectives. In addition, the DFT method is discussed in Appendix A.

1.8. Research Contributions

This thesis presents original research that advances the understanding and development of Nb- and Ta-based electrocatalysts for OER under acidic conditions. The scientific contributions of this work are summarized in Table 1-6.

Table 1-6. Publications from the thesis in peer-reviewed journals and manuscripts to be submitted.

Publication	Contributions
E. Ghasemy, A. Tavares, and K. Ghuman. "*Tuning the catalytic activity of Nb_2C MXenes via surface functionalization and defects*" Applied Materials Today 32 (2023): 101858	E. Ghasemy: DFT simulations, convergence tests, data analysis, writing – original draft, and manuscript editing K. Ghuman: Conceptualization, supervision, reviewing, and editing A. Tavares: Conceptualization, co-supervision, reviewing, and editing
P. Schütt, E. Ghasemy, A. C. Tavares, and K. Ghuman. "*First-Principles Study on Nb2C–X (X= S, Cl, F)/Graphene Heterostructures: Assessing Aqueous Stability and Implications for Electrocatalysis*" ACS Applied Nano Materials (2023).	P. Schütt: Data curation, methodology, visualization, writing – original draft E. Ghasemy: Data curation, methodology, visualization, writing – original draft and review A. Tavares: Conceptualization, investigation, supervision, funding acquisition, writing – review K. Ghuman: Conceptualization, methodology, supervision, project administration, funding acquisition, writing – review
E. Ghasemy, A. Tavares, and K. Ghuman,	E. Ghasemy: Data curation, methodology, visualization, writing –

"*Graphene- and facet-dependent oxygen evolution reaction activity of Ta_2O_5*" to be submitted.	original draft and review A. Tavares: Conceptualization, supervision, project administration, funding acquisition, writing – review K. Ghuman: Conceptualization, funding acquisition, investigation, methodology, supervision, writing – review
The content presented in Chapter 5 is also intended to be developed into a manuscript and submitted for peer review.	E. Ghasemy: Data curation, methodology, visualization, writing – original draft and review A. Tavares: Conceptualization, supervision, project administration, funding acquisition, writing – review K. Ghuman: Conceptualization, funding acquisition, investigation, methodology, supervision, writing – review

B) Conference Presentations

i. E. Ghasemy, A. Tavares, K. Ghuman, "Tuning the electronic properties of Ta_2O_5 for oxygen evolution reaction under acidic media: a density functional theory study", 247th ECS Meeting, May 18-22, 2025, Montréal (Oral Presentation).

ii. E. Ghasemy, P. Schütt, A. Tavares, K. Ghuman, "In silico study on the stability and oxygen evolution reaction of Nb_2C MXene and Nb_2C/graphene heterostructure", 75th Annual Meeting of the International Society of Electrochemistry, August 18-23, 2024, Montreal (Poster presentation).

iii. E. Ghasemy, A. Tavares, K. Ghuman, "Investigating catalytic activity and stability of Nb_2C MXene and Nb_2C/graphene heterostructure via surface functionalization and defects", 27th Canadian Symposium on Catalysis (CSC 2024), May 12-15, 2024, Sherbrooke (Oral presentation).

iv. E. Ghasemy, A. Tavares, K. Ghuman, "Tuning the catalytic activity of Nb_2C MXenes via surface functionalization and defects", Computational Materials North Workshop: August 3-4, 2023, Queen's University, Kingston, ON (Oral presentation).

v. E. Ghasemy, K. Ghuman, A. Tavares, "In Silico Design of Niobium Based MXenes for Acidic Electrocatalysis", 2021 MRS fall meeting & Exhibit, December 6-8, 2021, Virtual (Oral presentation).

2 Tuning the catalytic activity of Nb_2C MXenes via surface functionalization and defects

Abstract

Herein, we investigated the pathways to modulate the electronic properties and improve the activity of Nb_2C MXenes by functionalizing their surface with the terminating groups and creating surface defects. Through an in-depth density functional theory (DFT) study, the activity of Nb_2C MXenes terminated with F, Cl, S, and their combinations, denoted as Nb_2C-T, were explored, and their activities were tested for H_2O, O_2, N_2, and CO_2 adsorption and dissociation. It was found that the work function of Nb_2C-T MXenes varies from 3.79 to 5.07 eV, and Nb d-band center ranges between -2.53 to -1.53 eV. This provides the opportunities to tune their activities for specific chemical reactions since most catalytic reactions depend on the electronic properties of materials. To improve the catalytic activity of terminated Nb_2C-T further, Nb_2C-S and Nb_2C-Cl, having the highest and lowest work functions, respectively, were analyzed with defects created by removing one surface terminating group, representing partially functionalized surfaces (Nb_2C-Tx-1). The Climbing Image Nudge Elastic Band (CI-NEB) calculations for pristine and defected Nb_2C-S and Nb_2C-Cl surfaces confirmed that defected surfaces have a lower dissociation barrier for O_2, H_2O, N_2, and CO_2, and therefore, could prove as better catalysts, as compared to the pristine functionalized Nb_2C surfaces. Specifically, Nb_2C-S_{x-1} showed a dissociation barrier as low as 0 eV for O_2 and CO_2, and 0.16 and 0.17 eV for H_2O and N_2, respectively, proving it to be an attractive candidate for reactions involving the dissociation of O_2, H_2O, N_2, and CO_2. Overall, this work indicates that there is a potential to improve the catalytic performance of Nb_2C MXenes by altering its terminating groups. By choosing the right synthesis method, functionalized Nb_2C MXenes with the desired electronic properties could be prepared in the future for critical chemical reactions.

2.1. Introduction

Computational materials science provides insights into materials properties and performance, and can establish guidelines to develop materials [81, 82], specifically the ones that can not be readily synthesized in experimental labs [83, 84], for applications such as catalysis, sensors, adsorbents, etc. [85-88]. Two-dimensional (2D) materials, as a class of functional materials, offer great potential in the fields requiring active surfaces to facilitate chemical reactions [88, 89]. Parameters of 2D materials, such as thickness, functional group types, defects, dopants, or

composition, can be varied to tune their catalytic properties, which can be performed by density functional theory (DFT) calculations prior to conducting experiments [90, 91].

Among the 2D materials, the transition metal carbides/nitrides (MXenes) stand out due to their flexibility in engineering their properties [92-95]. MXenes with the general formula of $M_{n+1}X_nT$, where, M= transition metal (such as Ti, V, or Nb), X= C or N, and T= Terminating groups (such as O, OH, F, Cl, or S) are usually synthesized through selective leaching of A elements in MAX phases (A= Al, Si, Ga, etc.) [96, 97]. The flexibility in the synthesis process (i.e., MAX-phase type, etching/exfoliating agents, capability of controlling the number of atomic layers) allows one to achieve a wide range of properties in MXenes. Specifically, they can be synthesized with different terminating or functional groups by employing selective acids such as HF or molten salts to alter their properties [98]. However, despite extensive works on O, OH, and F-terminated MXenes [70], research on MXenes with terminating groups such as S, Cl, or their combinations is rare [99], and they should be investigated in detail to evaluate their properties and potential applications.

Titanium-based MXenes have been mostly studied [70], indicating the opportunity we have to improve the performance of other MXenes, such as Nb_2C. There are several reports on the decomposition and hydrolysis mechanisms of Ti-based MXenes in aqueous media, and some strategies to improve their stability have been suggested [100-102]. Wang et al. [103] intercalated $TiOF_2$ into Ti_3C_2T MXenes, which was more stable than $TiOF_2$ and $Ti_3C_2T_x$ in the long-term tests. Zeng et al. [104] synthesized S- and N-doped $Ti_3C_2T_x$ for ammonia production through electrohydrogenation of N_2, which was stable for nine consecutive cycles. Other than studies conducted to stabilize the MXenes through different methods, there have been ongoing efforts to modify their electronic and catalytic properties by engineering their surfaces via terminating groups. Ding et al. [105] experimentally demonstrated that terminating the $Ti_3C_2T_x$ MXene by the medium density of fluorine enhances their N_2 electroreduction (NRR) performance. In another experimental study, Guo et al. [106] removed the F and OH terminations and introduced Fe to the Ti-based MXene surface to prepare the MXene/$TiFeO_x$ nanocatalyst, improving their performance toward electrochemical nitrogen reduction to ammonia. Carbon and metal defects in MXenes have also been investigated to tune their catalytic properties for Oxygen Evolution Reaction (OER) and Hydrogen Evolution Reaction (HER) [107, 108].

Nb-based MXenes have been reported to have applications in electrochemical biosensing [109], supercapacitors [110], lithium-oxygen batteries [111], perovskite solar cells [112], and HER [113]. DFT calculations have focused on enhancing the HER, OER, and oxygen reduction reaction (ORR) performance of Nb-based MXenes by adding Pd [114] and Pt/Pd [71]. In a DFT study, Kan et al. [71] demonstrated that due to the intense d-states of Nb around the Fermi level, strong interactions occur between Nb_2C and O- and F- terminated Nb_2C MXenes and oxygen electrocatalysis intermediates, which hinders the ORR and OER. Chu et al. [115] decorated quantum dots of boron nitride over the Nb_2CTx MXene to improve the NRR performance. So far, only OH-, O-, and F- terminated Nb_2C MXenes have been investigated for catalytic applications [70]. S-termination has been reported to improve the stability and electrocatalytic performance of Hf-based MXenes [116], and Cl-termination is almost inevitable in the electrochemical etching synthesis of MXenes that uses HCl [117]. Despite the extensive research on the MXenes, there is no systematic study on Nb-based MXenes with various terminations aiming to investigate their electronic and catalytic properties in dissociating O_2, H_2O, N_2, and CO_2 which could prove critical for ongoing studies focusing on designing Nb_2C based catalysts. In addition, the effect of defects in terminating groups of MXenes on their catalytic properties, which occurs spontaneously due to the reaction or synthesis conditions [118], has not been studied.

The present work demonstrates the in-depth ab initio analysis of the effect of terminating groups on the electronic properties of Nb_2C MXene for adsorption and dissociation of H_2O, O_2, N_2, and CO_2. Considering essential properties such as work function, d-band center, active sites, and reaction barriers, we demonstrated the role of S, Cl, F, ClS, FS, and FCl terminating groups in tuning the electronic properties and reactivity of Nb-based MXenes. In addition, defected Nb_2C-T (denoted as Nb_2C-T_{x-1}) MXenes were also investigated in this study, exposing transition metals to the adsorbates. The results obtained in this work highlight the role of surface functionalization and defects in improving the catalytic activity of Nb_2C MXenes, thereby demonstrating the pathways to use them for reactions comprising the adsorption and dissociation of O_2, H_2O, N_2, and CO_2.

2.2. Methodology

The Nb_2C nanosheet was represented by a periodic slab model having 48 atoms (Figure 2-1 (a)), whereas the terminated Nb_2C nanosheets, denoted as Nb_2C-T, where T = F, S, Cl, FCl, FS, or ClS, comprised of 80 atoms (Figure 2-1(b)). All the models have a vacuum greater than

15 Å to eliminate spurious interactions between periodic images. To comply with the experimental conditions, we further modeled defected terminated MXenes, in which one terminating atom was removed, creating defected Nb_2C-T_{x-1} MXene (the removed termination is shown by x-1 subscript). Experimentally, Nb_2C-T surfaces can be synthesized by varying the etching acids [119]. The spin-polarized DFT calculations were performed by employing the Perdew–Burke–Ernzerhof (PBE) exchange-correlation functional in the generalized gradient approximation (GGA). All the DFT calculations were performed using the Quantum Espresso software [120]. For wavefunctions and charge density, the kinetic energy cut-off values of 50 and 500 Ry were employed, and the energy threshold for the self-consistent field convergence was set to 10^{-4} Ry. Each system was relaxed (without variable size) using Davidson iterative diagonalization until the magnitude of residual Hellman–Feynman force on each atom reached below the 10^{-2} Ry $Bohr^{-1}$. As the DFT methodology under-predicts the bandgap and delocalization of *d* and *f* electrons, the DFT+ U approach was implemented here. DFT+U adds an energy correction term Hubbards U to the DFT energy and leads to a more accurate bandgap as well as the localization of *d* and *f* electrons consistent with the experimental observations. The value of U was chosen as 6.5 eV for Nb. This value has resulted in appropriate electronic properties, which is the focus of this work, as reported in the literature [111, 121, 122]. To relax the structures, the k-point sampling of 2 ×2×1 was used, and the k-point samplings of 10×10×1 and 20×20×1 were adopted for SCF and nSCF calculations, respectively, for calculating the density of states (DOS) and partial density of states (PDOS). The charge density over each element was calculated by performing the Bader charge analysis [123]. These DFT parameters resulted in the *a*-lattice constant of 3.13 Å and the Nb-C bond length of 2.14 Å in the relaxed Nb_2C MXene, close to those reported in the literature [124, 125]. Finally, the dissociation energy, minimum energy path (MEPs), and transition states (TS) involved in the dissociation of N_2, O_2, CO_2, and H_2O over the MXenes, were determined via the Climbing Image Nudged Elastic Band (CI-NEB) method [126, 127].

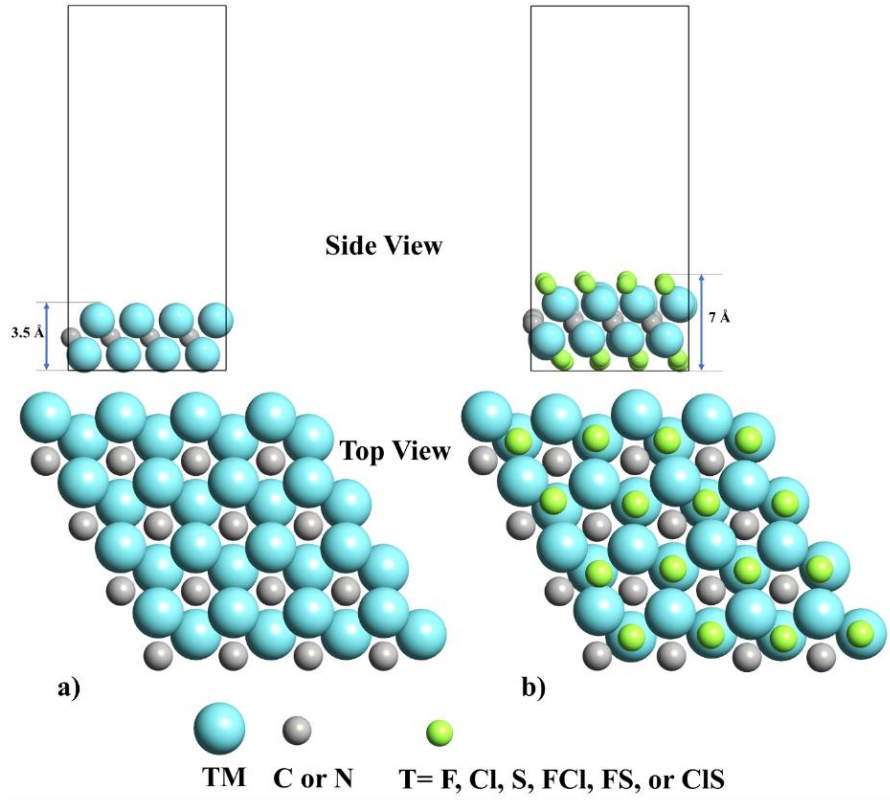

Figure 2-1. Side and top views of (a) pristine Nb_2C and (b) terminated Nb_2C (Nb_2C-T) MXenes, where T = F, Cl, S, FCl, FS, or ClS. Nb, C, and T are represented by blue, grey, and green spheres, respectively.

2.3. Results and discussion

2.3.1. Electronic Properties

To make Nb-based MXenes active for specific chemical reactions, it is necessary to tune their electronic properties accordingly. Therefore, herein, we conducted a detailed analysis of the spin-polarized DOS and PDOS for pristine and defected Nb_2C, Nb_2C-F, Nb_2C-Cl, Nb_2C-S, Nb_2C-FCl, Nb_2C-FS, and Nb_2C-ClS, represented in Figures 2-2 and 2-11.

The DOS at the Fermi level of the terminated as well as the pristine Nb_2C MXenes, indicate their metallic nature. However, the degree of metallicity is different for different terminated samples, as shown in Figure 2-2. Compared to that of pristine Nb_2C, the DOS of Nb_2C-S decreased at the Fermi level, and increased at higher energy states in the conduction band (CB). Moreover, in contrast to Cl and F terminated systems, the S(p) orbital had a higher contribution at the Fermi

level leading to strong hybridization between S(p), C(p), and Nb(d) orbitals. Contrary to Cl- and F-terminated MXenes, all Nb(d) orbitals were hybridized with other orbitals in the Nb_2C-S due to the higher electron-accepting capacity of sulfur in its outermost shell (F: $2s^2$ $2p^5$, Cl: $3s^2$ $3p^5$, and S: $3s^2$ $3p^4$). This result indicates that S termination modulates the electron-donating capability of Nb more than Cl and F terminations. Moreover, Nb(d) orbitals in Nb2C-S had the lowest contribution to the total DOS at the Fermi level compared to other structures. Similar behavior was observed for Nb_2C-FS and Nb_2C-ClS, signifying the dominant role of sulfur in altering the electronic properties, which might also affect the catalytic properties of the Nb_2C MXenes. The difference in the effect of terminating groups on the electronic properties of the Nb_2C MXenes can be ascribed to their different electronegativities, F(3.98) > Cl(3.16) > S(2.58), and the number of electrons required to fill their outermost shell (1 electron for F and Cl, and 2 electrons for S). Figure 2-2B shows that the p-orbitals of the Cl have a slightly higher contribution to the DOS at the Fermi level and higher energy states in CB compared to the p-orbitals of F in Nb_2C-F. The samples with 'F' as one of the terminating species (i.e., Nb_2C-F and Nb_2C-FCl) possessed significantly lower DOS at the Fermi level compared to that of the pristine Nb_2C. In addition, the p-orbital of F contributed significantly to the lower energy levels in the valence band (VB), compared to the Nb(d) orbitals in Nb_2C-F (Figure 2-2C), Nb_2C-FCl (Figure 2-2E), and Nb_2C-FS (Figure 2-2F) samples. This F(p) orbitals contribution gradually decreased at higher energies, with a negligible contribution at the Fermi level and CB.

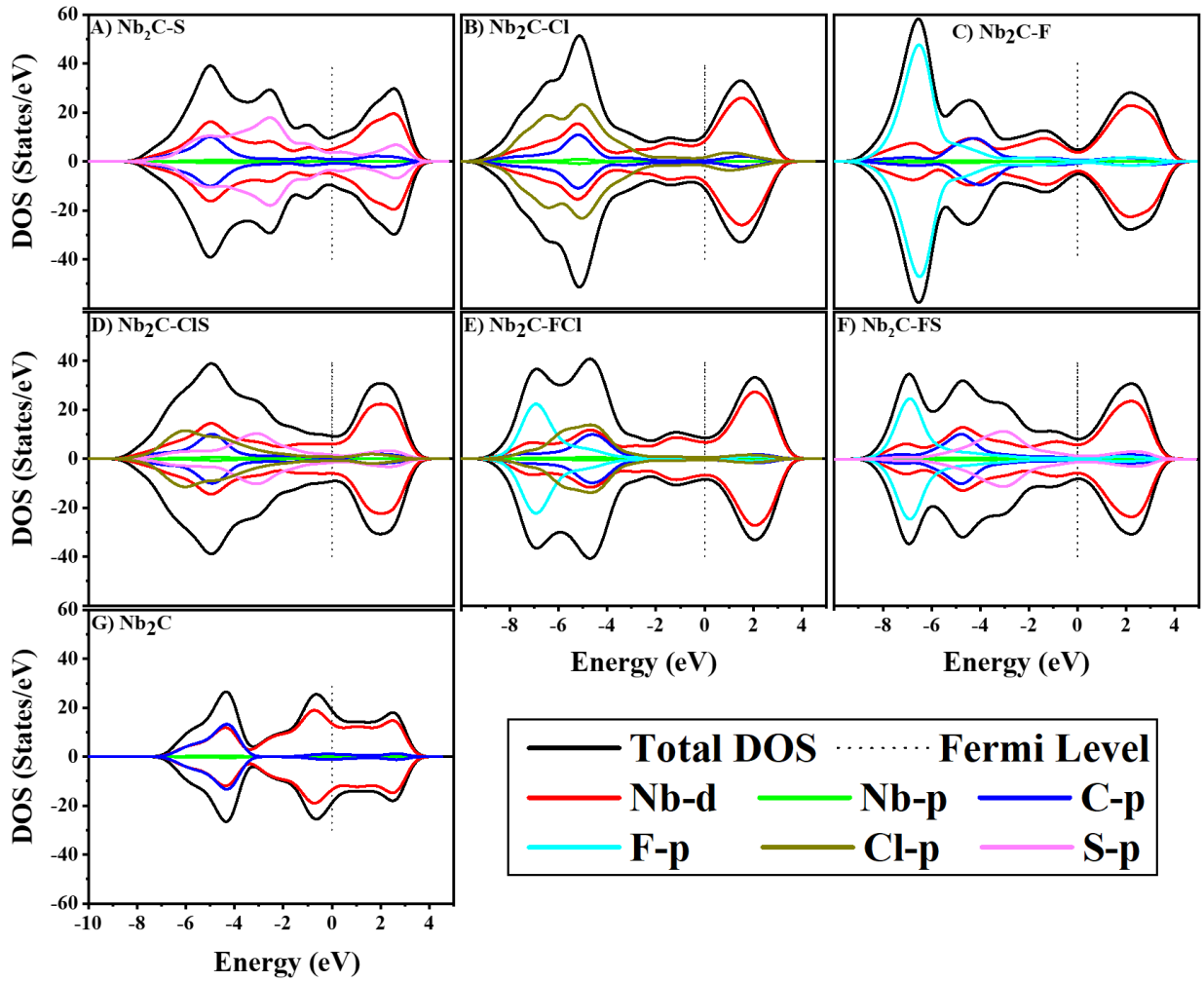

Figure 2-2. The PDOS of (a) Nb_2C-S, (b) Nb_2C-F, (c) Nb_2C-Cl, (d) Nb_2C-ClS, (e) Nb_2C-FCl, (f) Nb_2C-FS, and (g) pristine Nb_2C. The vertical dotted line represents the Fermi level.

Further, since it's probable that some terminating groups are removed during the catalytic reactions [128, 129], we also analyzed the DOS of defected Nb_2C MXenes. These are represented in Figure 2-11, and as it can be appreciated, the DOS of the defected MXenes had almost features similar to pristine ones. In the structures with mixed terminations, e.g., Nb_2C-$F_{x-1}Cl$ and Nb_2C-FCl_{x-1}, creating F- or Cl-defects did not change the Nb(d) contribution to the VB, Fermi level, or CB. However, for the Nb_2C-ClS_{x-1}, a significant increase was observed in the Cl(p) orbital contribution in the VB (at around -7 eV), compared to the pristine Nb_2C-ClS. As seen in Figure 2-11, for Nb_2C-$ClS_{x-1,}$ the Nb(d) and Cl(p) orbitals overlapped (which was not

observed in Nb_2C-$Cl_{x-1}S$) at lower VB, which indicates a stronger hybridization between the Cl(p) orbital and Nb(d) orbital in the absence of a sulfur atom.

2.3.2. d-band analysis

Interactions between the reactants and the surface of catalysts govern not only the type of products obtained but also the overall efficiency of the reaction process. As established by Sabatier, the adsorption intensity of the reactants on the catalyst surface should be neither too strong nor too weak [130]. Accordingly, the adsorption of reactants on catalysts must be modulated to facilitate the efficient adsorption or desorption of reactants, intermediates, and products. In this regard, the adsorption affinity of metal-based catalysts can be predicted by calculating the d-band center value, denoted by 'd_{bc}'. More specifically, a stronger upward shift of the d-band center with respect to the Fermi energy (i.e., the smaller absolute value of $\Delta E_{dbc}=d_{bc} - F_e$, 'F_e' being the Fermi energy), indicates the possibility of the formation of a larger number of empty anti-bonding states, leading to the stronger binding energy of the adsorbate with the metal surface [131, 132]. For a better comparison with the results obtained from the spin-polarized DFT-based methods, in this work, we have extended the conventional d-band center model by considering two band centers, one each for the spin-up and the spin-down states [133]. However, we obtained a negligible difference between spin-up and spin-down d-band centers.

The ΔE_{dbc} calculated for Nb_2C-S (-2.53 eV), Nb_2C-Cl (-2.45 eV), Nb_2C-ClS (-2.35 eV), Nb_2C-FS (-2.13 eV), Nb_2C-FCl (-1.93 eV), Nb_2C-F (-1.72 eV), and Nb_2C (-1.53 eV), shown in Figures 2-3 a, S2, and Table 2-1, demonstrates that adding terminating groups effectively reduced the adsorption affinity of Nb_2C MXene by tuning ΔE_{dbc} values. Nb_2C-S and Nb_2C-Cl had the largest ΔE_{dbc} values, suggesting that S- and Cl- termination might decrease the adsorption affinity compared to Nb_2C and Nb_2C-F, which possessed strong adsorption intensity for O_2 and O and were reported to result in poor ORR and OER performances [71].

The ΔE_{dbc} values and d-band structure of the defected structures are given in Figures 2-3 c, 2-13, and Table 2-2. Interestingly, some of the defected surfaces (Nb_2C-Cl_{x-1}, Nb_2C-S_{x-1}, Nb_2C-$F_{x-1}S$, Nb_2C-ClS_{x-1}, and Nb_2C-$Cl_{x-1}S$) showed a right shift in their ΔE_{dbc}, compared to their pristine counterparts. However, Nb_2C-F_{x-1}, Nb_2C-$F_{x-1}Cl$, and Nb_2C-FS_{x-1} resulted in a slight left shift of their ΔE_{dbc}, compared to their pristine counterparts. The most significant changes in the ΔE_{dbc} were observed on Nb_2C-Cl_{x-1}, Nb_2C-S_{x-1}, and Nb_2C-ClS_{x-1}. This shows that the ΔE_{dbc}, and in turn,

the adsorption affinity of Nb_2C MXenes, can be a function of termination concentration, which is in line with experiments [105].

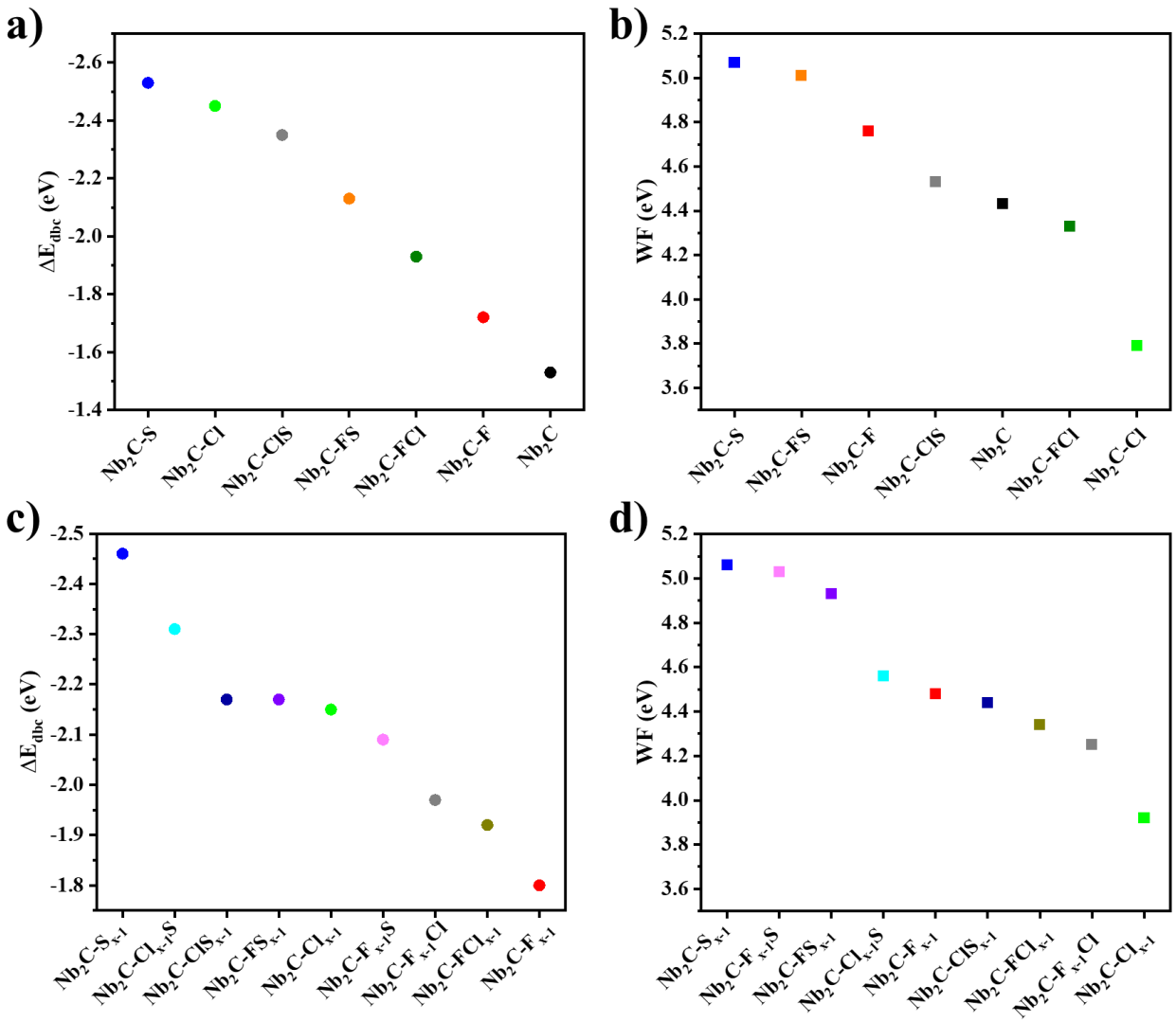

Figure 2-3. The ΔE_{dbc} and work function values of pristine and terminated Nb_2C MXenes (a-b) without and (c-d) with a defect.

2.3.3. Work Function and Bader charge

The work function, by definition, describes the energy required to remove an electron from a surface to the vacuum, thereby representing an important factor used to understand the capability of materials in donating electrons. The work function can modulate the catalytic properties by adjusting the electron transfer between active phases and reactants. Therefore, next, we studied the work function of various MXenes and their corresponding effect on the adsorption and dissociation of H_2O, O_2, N_2, and CO_2. For each catalytic reaction on a given catalyst, the optimum work function is different, and the work function is not a universal descriptor for NRR, OER, ORR, and CO_2RR; So, it cannot be a good descriptor for the adsorption and dissociation of H_2O, O_2, N_2, and CO_2. For instance, in the literature, FeTi [134], SnO_2/graphene [135], Ni@NCNTs [136], RuB_2 [137], and VS_2 [138] with work functions of 3.14, 4.83, 5.30, 5.05 and 4.83 eV, respectively, have been reported as effective NRR catalysts. For best OER performance, the benchmark catalysts such as RuO_2 and IrO_2 possess a relatively high work function, around 5.8 eV [139]. In our modeled MXene structures, as shown in Figure 2-3 b and d and Figures 2-14 and 2-15, the work function values varied from 3.79 to 5.07 eV for pristine MXenes, and from 3.92 to 5.06 eV for defected MXenes, highlighting the role of terminating groups and defects in manipulating the electron-donating properties of Nb_2C MXenes. The calculated work function for pristine Nb_2C was 4.4 eV. The highest and lowest work function values were acquired for the Nb_2C-S (5.07 eV) and Nb_2C-Cl (3.79 eV) samples, respectively. This implies that it's hard to get electrons from the former, and the latter can readily donate electrons. Moreover, the combined terminations led to values a bit higher than the average, where the Nb_2C-FS possessed the work function of 5.01 eV, closer to that of the Nb_2C-S (Figure 2-3 b and Table 2-1). Moreover, the work function values of the defected MXenes were investigated, as presented in Figure 2-3 d and Table 2-2. Creating Cl-defects had the most significant effect on the work function, with a considerable increase compared to their pristine counterparts. In contrast, MXenes with F-defects resulted in decreased work function compared to Nb_2C-F and Nb_2C-FCl and increased work function compared to Nb_2C-FS. In all cases, S-defects decreased the work function.

In order to further understand the effect of different terminations, the Bader charge analysis was conducted. The net Bader charge was calculated by subtracting the Bader charge over atoms from the number of valence electrons considered in the Pseudopotential. The positive Bader charge corresponds to electrons donated by atoms (oxidation), and negative values show the electrons gained by atoms (reduction). This analysis shows that F (-0.74 e) in Nb_2C-F, F/S (F: -

0.73 and S: -0.73 e) in Nb_2C-FS, and F (F: -0.73 e) in Nb_2C-FCl samples gained the highest electrons from Nb, indicating the highest oxidation state of Nb. Furthermore, comparing the Bader charge of Nb_2C-S, Nb_2C-ClS, and Nb_2C-FS, demonstrates that S atoms gained more electrons in the Nb_2C-ClS (S: -0.72e) and Nb_2C-FS (S: -0.73) samples as compared to Nb_2C-S (S: -0.68). Since S atoms could gain more electrons in the presence of F and Cl terminations, it seems to have an electron-accepting capability. Moreover, in the Nb_2C MXene terminated by F (Nb: 1.58 e), Cl (Nb: 1.43 e), or S (Nb: 1.49e), Nb atoms were partially oxidized, indicated by a higher Bader charge on Nb atoms in Nb_2C-T MXenes as compared to that of Nb atoms (0.84e) in the Nb_2C surface.

2.3.4. Interaction of H_2O, O_2, CO_2, and N_2 with pristine and defected Nb_2C-T surfaces

To understand the catalytic properties of pristine and defected Nb_2C-T MXenes further, we conducted the active site analysis for the adsorption of H_2O, O_2, CO_2, and N_2 and CI-NEB analysis to determine their dissociation barriers on the catalyst surfaces. For these analyses, only Nb_2C-S and Nb_2C-Cl were considered as they possess the highest and lowest work functions, respectively.

2.3.5. Adsorption of H_2O, O_2, CO_2, and N_2 on pristine and defected (S, Cl) terminated Nb_2C surfaces

At first, adsorption analysis was done on the four unique adsorption sites of Nb_2C-S and Nb_2C-Cl surfaces: Top T site, Bridge T site, HCP Nb site, and FCC C site, as represented in Figure 2-16a. For Nb_2C-Cl_{x-1} and Nb_2C-S_{x-1}, the adsorption sites that were investigated include: the HCP Nb site, Bridge Nb site, FCC C site, and Top T site, as displayed in Figure 2-16 b. The adsorbates were placed in a very close vicinity (~1 Å) to the active sites of these surfaces. After optimization, it was observed that Nb_2C-S could dissociatively adsorb H_2O (dissociating it into H and OH, Figure 2-4 b) on neighboring S sites, but it was not active toward N_2. In contrast, Nb_2C-Cl was unable to dissociate or adsorb H_2O, however, it could adsorb N_2 on its Nb site (Figure 2-4 a). For O_2 or CO_2, none of the investigated sites on the pristine surfaces were active.

It is well known that in catalysis, adsorbates form a bond with transition metal by donating electrons to the HOMO of transition metal and accepting electrons to their anti-bonding LUMO [140-142]. According to a recent study conducted on N_2 adsorption on Nb_2O_5 and Nb_2O, along with the charge transfer between Nb and N_2, the electrons on neighboring Nb atoms also participate and are back transferred to the adsorbed N_2, resulting in the elongation of N_2 bond

[143]. Since Nb in Nb_2C-Cl has a lower oxidation state (Bader charge of 1.43e) and possesses more d-electrons compared to Nb (with Bader charge of 1.49e) in Nb_2C-S, it is easier for Nb in Nb_2C-Cl to back donate d-electrons to the N_2, along with the transfer of electrons from N_2 to the empty orbitals of Nb.

Both surfaces have similar ΔE_{dbc} values, Nb_2C-Cl (-2.45 eV) and Nb_2C-S (-2.53 eV), which stands for the adsorption affinity of Nb. However, there is a significant difference in their work function values (Nb_2C-S: 5.07 eV, and Nb_2C-Cl: 3.79 eV) which can be the reason for their different behaviors in the adsorption of H_2O and N_2. Nb_2C-Cl with the lowest work function (higher electron-donating capability) adsorbed N_2 (with no interaction with H_2O), and Nb_2C-S with the highest work function (lower electron-donating capability) dissociatively adsorbed H_2O (with no interaction with N_2).

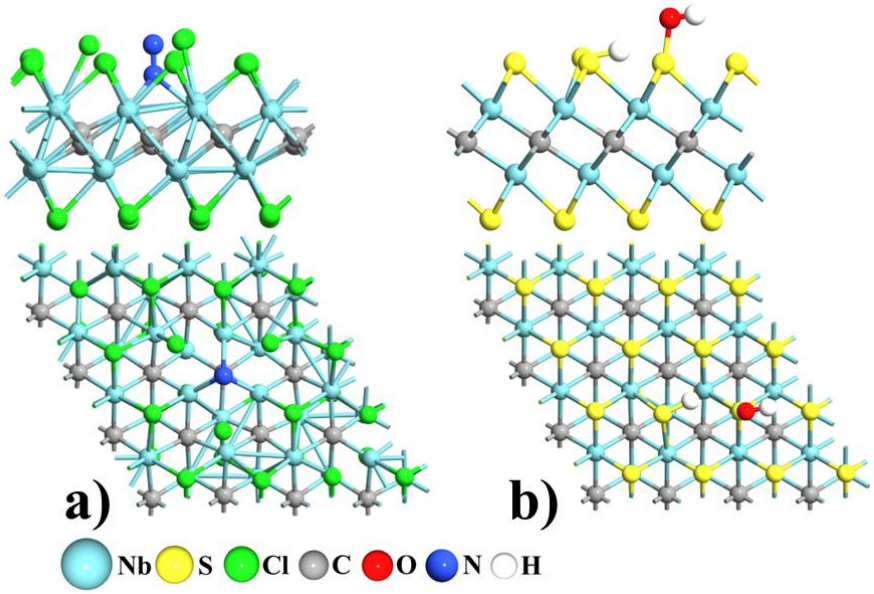

Figure 2-4. Results obtained after optimizing a) N_2 on the Nb site of Nb_2C-Cl; and b) H_2O on the top S site of Nb_2C-S.

The adsorption analysis on defected MXenes revealed their excellent activity, confirming the critical role of terminating groups and defects in modifying the adsorption affinity of Nb. For Nb_2C-S_{x-1}, N_2 was still repelled, with no interaction observed between considered sites and N_2. On the contrary, for O_2, H_2O, and CO_2 molecules, Nb_2C-S_{x-1} was active, leading to their

dissociations. OH and O remained adsorbed on the surface after H_2O and O_2 dissociation (Figure 2-5a and 2-5b), however, CO_2 was converted to an adsorbed C, and CO not bonding to the surface (Figure 2-5c).

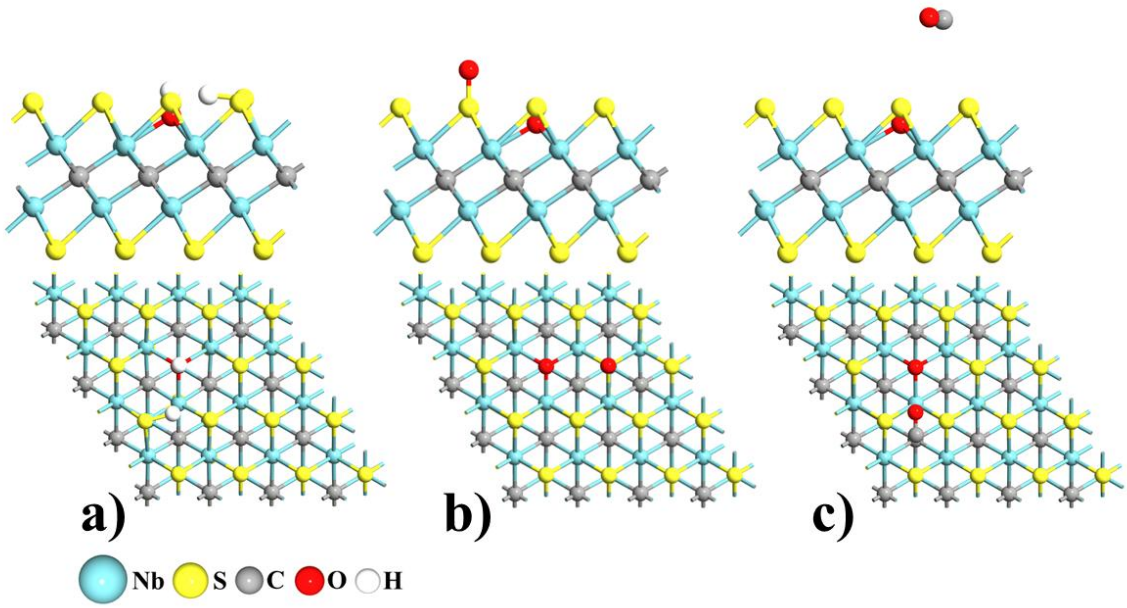

Figure 2-5. Results obtained after optimizing a) H_2O, b) O_2, and c) CO_2 on Nb_2C-S_{x-1}.

For nitrogen adsorption, Nb_2C-Cl_{x-1} (WF: 3.92 eV) was more active than Nb_2C-S_{x-1}, leading to nitrogen adsorption on the bridge Nb-Nb site (Figure 2-6d). In addition, H_2O was dissociated to H and OH (Figure 2-6a), and the O_2 molecule was dissociated to an adsorbed O, and O not bonding to the Nb_2C-Cl_{x-1} surface (Figure 2-6b). The CO_2 molecule was bent and adsorbed over the Nb-Nb site of the Nb_2C-Cl_{x-1} surface (Figure 2-6c), indicating its higher catalytic activity compared to pristine Nb_2C-Cl, which did not show any interaction with H_2O, O_2, or CO_2.

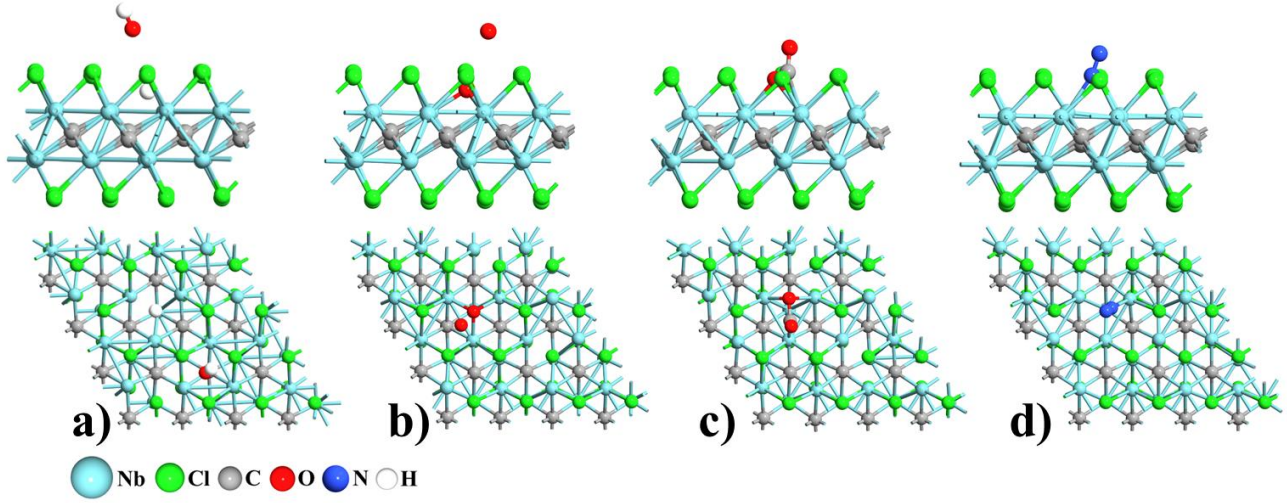

Figure 2-6. Results obtained after optimizing a) H_2O, b) O_2, c) CO_2, and d) N_2 on Nb_2C-Cl_{x-1}.

2.3.6. Dissociation of H_2O, O_2, CO_2, and N_2 on pristine and defected (S, Cl) terminated Nb_2C surfaces

To evaluate the intrinsic activity of the MXenes, minimum energy paths (MEPs) and dissociation barriers for H_2O, O_2, CO_2, and N_2 molecules on pristine (Nb_2C-S and Nb_2C-Cl), and defected (Nb_2C-S_{x-1} and Nb_2C-Cl_{x-1}) surfaces were calculated via CI-NEB.

The initial states for NEB calculations were obtained by optimizing the adsorbate molecules (H_2O, O_2, N_2, and CO_2) on the Nb_2C-S, Nb_2C-Cl, Nb_2C-$S_{x-1,}$ and Nb_2C-Cl_{x-}1 surfaces by placing them at a distance greater than 2.5 Å from sites shown in Figure 2-16 on each surface. The final states were obtained by optimizing the four surfaces with the dissociated species (i.e., (OH, H), (N, N), (O, O), and (CO, O)), for which the active sites shown in Figure 2-16 were considered. The optimized configurations for the first (IS) and final (FS) states are shown in Figures 2-7 to 2-10. The activation energy barrier (Ea) is calculated as the difference between the IS and the highest energy in the MEP curve (transition state, TS).

2.3.7. (i) NEB results of Pristine Nb_2C-S and Nb_2C-Cl

First, NEB analysis was done on Nb_2C MXenes terminated by S and Cl, without defects. Since in the NEB calculations of Nb_2C-S and Nb_2C-Cl, S and Cl sites were exposed to molecules, these results help evaluate the role of terminations in the dissociation reactions. For O_2 dissociation, Nb_2C-S showed a lower total activation energy of 1.09 eV compared to Nb_2C-Cl

(4.78 eV), as presented in Figure 2-17. Moreover, H_2O dissociation was also more feasible on Nb_2C-S, with a total activation energy of 2.19 eV, compared with Nb_2C-Cl with 5.69 eV (Figure 2-18). Similarly, the CO_2 activation on the Nb_2C-Cl was not feasible, requiring considerable energy (total activation energy of 7.53 eV, Figure 2-19). In contrast, Nb_2C-S showed a lower CO_2 dissociation barrier (4.78 eV) compared to the Nb_2C-Cl surface (Figure 2-19). These indicate the higher contribution of S termination in the dissociation reaction, leading to lower activation energies for Nb_2C-S. From this, it can be stated that sulfur termination not only modulates the electronic properties of Nb atoms but also contributes to the dissociation of O_2, H_2O, and CO_2. However, the NEB analysis conducted for N_2 dissociation on the pristine structures showed an extremely high dissociation barrier, as expected from the strong N≡N triple bond [144], confirming that S and Cl active sites of the pristine surfaces are not active for this reaction. [145, 146]

2.3.8. (ii) NEB results of Nb_2C-S_{x-1} and Nb_2C-Cl_{x-1}

In this section, the dissociation barrier on MXenes terminated by S and Cl with a defect in termination is investigated, where Nb sites were exposed to the molecules. This enables studying the activity of exposed Nb sites after being terminated by Cl and S. Almost the same results were obtained for O_2 dissociation on Nb_2C-Cl_{x-1} and Nb_2C-S_{x-1} (Figure 2-7), with total activation energies of 0.45 and 0.46 eV, respectively. After creating the defect, the total activation energy of Cl and S terminated surfaces was decreased by 4.33 and 0.63 eV, respectively, compared with their pristine counterparts for O2 dissociation. This indicates that although Cl termination can tune the activity and electronic properties of Nb_2C MXenes, its full coverage can significantly inhibit the contribution of Nb sites in the reaction. In contrast, Nb_2C-S with or without a defect has higher activity for O_2 dissociation, showing the effectiveness of S termination for reactions involving O_2 dissociation. After O_2 approached the active sites over the Nb_2C-S_{x-1} and Nb_2C-Cl_{x-1} surface, it was dissociated with a zero dissociation barrier. After dissociation, the two O atoms were adsorbed on Nb sites in Nb_2C-Cl_{x-1} with a distance of 1.9 Å (Figure 2-7 b) and on S and Nb sites of the Nb_2C-S_{x-1} surface with the distances of 1.49 and 2.06 Å, respectively (Figure 2-7 a).

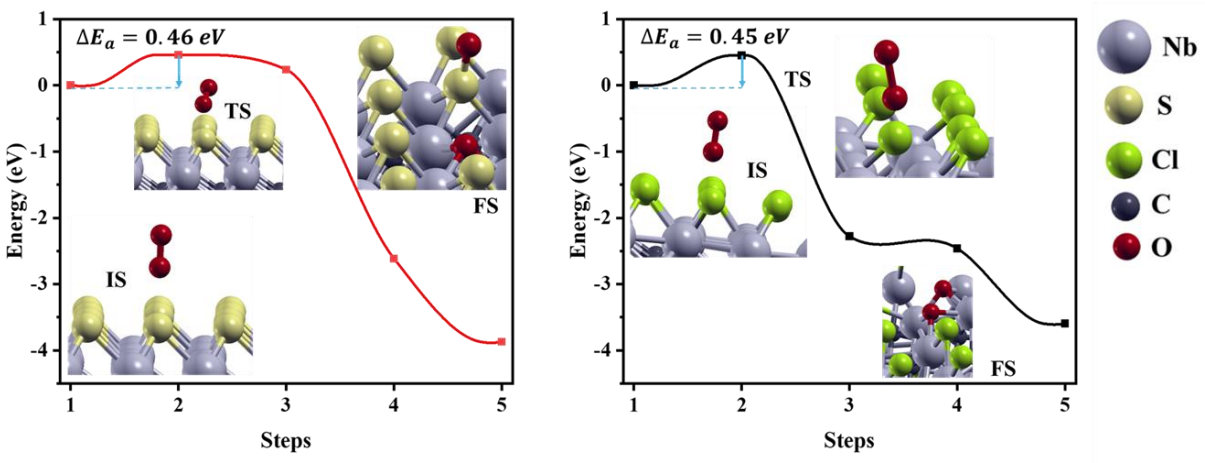

a) b)

Figure 2-7. The minimum energy path for O_2 dissociation on a) Nb_2C-S_{x-1} and b) Nb_2C-Cl_{x-1}.

The NEB analysis for H_2O dissociation on Nb_2C-S_{x-1} showed that there was an adsorption barrier of about 1.04 eV in the physisorbing of the H_2O molecule (between IS and step 2 in Figure 2-8 a, where the Nb—O distance decreased from 4.52 to 3.75 Å), after which H_2O was dissociated with a dissociation barrier of 0.16 eV (between step 2 and TS in Figure 2-8 a, one H-O distance increased to 1.25 Å and the other H-O bond length was 0.91 Å). The H and OH of dissociated H_2O were adsorbed on S and Nb sites with H-S and OH-Nb bond lengths of 1.44 and 2.22 Å, respectively. The transition state corresponded to the state where H_2O was dissociated to H and OH, without bonding to the surface atoms. Finally, the overall reaction was endothermic, with a reaction energy of 0.16 eV. On the contrary, Nb_2C-Cl_{x-1} had a larger barrier in H_2O adsorption and dissociation (Figure 2-8b). The total activation energy of H_2O on Nb_2C-Cl_{x-1} was 2.06 eV. After creating a defect, the total activation energy for H_2O dissociation on S and Cl terminated Nb_2C was decreased by 0.99 and 3.63 eV, respectively, compared to their pristine counterparts. These results indicate that choosing a proper termination (i.e., S) and creating defects can both significantly affect the activity of MXenes. Lower total activation energy and small dissociation energy (0.16 eV) of H_2O on Nb_2C-$S_{x-1}$is attributed to its higher work function. This is because Nb_2C-S_{x-1} has a higher electron-accepting capability compared to Nb_2C-Cl_{x-1}, which is reported to enhance the OER performance that involves H_2O dissociation [147, 148].

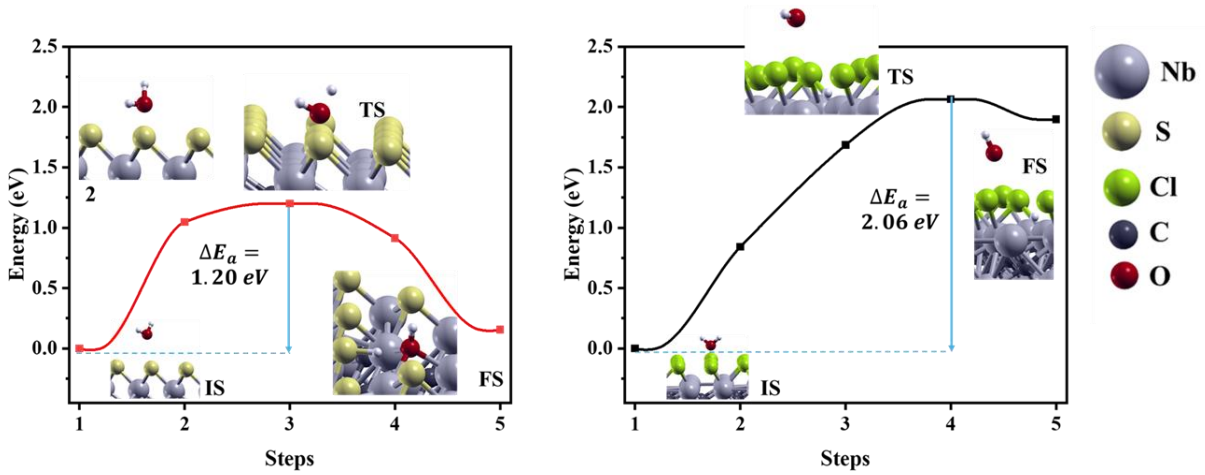

Figure 2-8. The minimum energy path for H_2O dissociation on a) Nb_2C-S_{x-1} and b) Nb_2C-Cl_{x-1}.

Nb_2C-S_{x-1} was also more active than Nb_2C-Cl_{x-1} for N_2 dissociation (Figure 2-9), with a total activation energy of 3.25 eV. When N_2 approached the active sites of the Nb_2C-S_{x-1}, it could be dissociated with a dissociation barrier of 0.17 eV (between step 4 and FS in Figure 2-9 a) to two adsorbed N atoms on S and Nb atoms with N-S and N-Nb distances of 1.71 and 1.95 Å, respectively. For Nb_2C-Cl_{x-1}, the total activation energy was 4.82 eV (Figure 2-9 b). Based on adsorption analysis, showing that Nb_2C-Cl_{x-1} was active in adsorbing N_2 (Figure 2-6 d), it can be stated that Nb_2C-Cl_{x-1} might follow the nitrogen reduction reaction through the associated pathway. In contrast, according to the NEB result of Nb_2C-S_{x-1} in dissociating N_2 with a lower barrier energy, it is inferred that it might follow the dissociative pathway, which needs to be further analyzed in future works. It's clear that dissociating the strong N_2 bond requires highly active Nb sites since the pristine S and Cl terminated MXenes showed poor performance for N_2 dissociation.

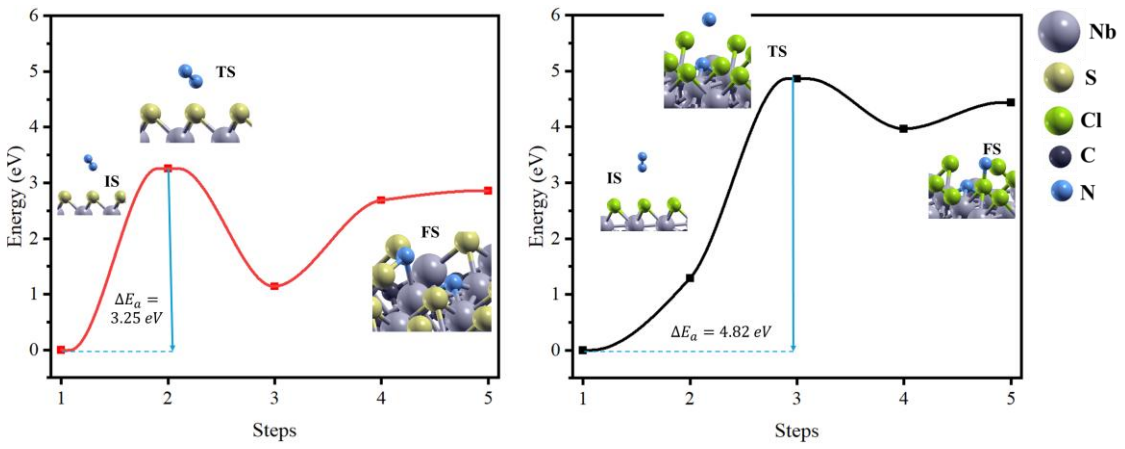

a) b)

Figure 2-9. The minimum energy path for nitrogen dissociation on a) Nb_2C-S_{x-1} and b) Nb_2C-Cl_{x-1}.

In the NEB analysis of CO_2 dissociation on the Nb_2C-S_{x-1}, first, the C-O bond length was increased from 1.17 Å at IS to 1.40 Å at TS without bonding to the surface. The barrier energy for the first step was 3.18 eV. Then, between TS and FS states, CO_2 was dissociated to CO and O, where O was adsorbed on the Nb site forming an O-Nb bond with a length of 2.01 Å, as shown in Figure 2-10 a (FS state). The second step, which led to CO_2 dissociation (IS to FS), occurred with no barrier. This demonstrates the reactivity of Nb_2C-S_{x-1} toward CO_2 dissociation in a condition that CO_2 is located over the active sites of the Nb_2C-S_{x-1}. This behavior is similar to that on the pristine Nb_2C-S, with the difference being a much lower adsorption barrier on the Nb_2C-S_{x-1}. This can be attributed to the presence of electron-rich sites over Nb atoms after removing an S atom. In addition, although pristine Nb_2C-S is active in dissociating CO_2, its lower adsorption affinity might hinder the reaction, which can be solved by creating a vacancy in terminating groups that naturally occurs during the catalyst operation [118].

On Nb_2C-Cl_{x-1}, first, CO_2 was marginally bent after approaching the surface. Then, it was dissociated to O adsorbed (with the Cl-O bond length of 1.58Å) and CO without bonding to the surface atoms (Figure 2-10 b, FS state). The total activation energy of CO_2 dissociation on Nb_2C-Cl_{x-1} was 5.84 eV. In the transition state, CO_2 was dissociated to CO (with a C-O bond length of 1.07 Å) and O (with a C-O bond length of 1.79 Å) without bonding to the surface atoms.

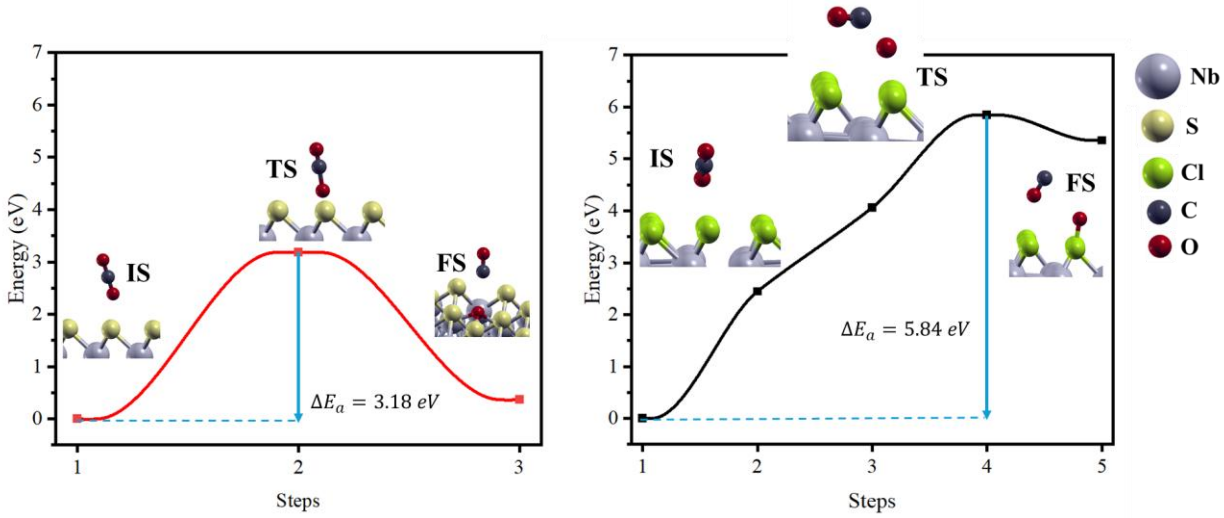

Figure 2-10. The minimum energy path for CO_2 dissociation on a) Nb_2C-S_{x-1} and b) Nb_2C-Cl_{x-1}.

2.4. Conclusions

This work highlighted the critical role of terminating groups, S, Cl, F, and their combinations, in tuning the reactivity and electronic properties of Nb_2C MXenes. We found that by varying the terminating groups, the work function values in the range of 3.79-5.07 eV can be obtained, with the lowest and highest values corresponding to Cl or S terminated Nb_2C MXenes, respectively. Moreover, the d-band center, determining the adsorption affinity of the transition metals toward electrocatalytic intermediates, can be varied from -1.53 eV (for Nb_2C without terminations) to –2.53 eV (for Nb_2C with S termination). In this regard, S- and Cl-terminations could solve the drawback of Nb-based MXenes, strong adsorption affinity, via shifting the d-band center of Nb away from Fermi energy. Furthermore, the minimum energy path related to the dissociation of O_2, N_2, H_2O, and CO_2, confirmed that the dissociation barrier is highly sensitive to the terminating groups. Specifically, the S-terminated Nb_2C surface (with and without defects) showed the best catalytic activity for O_2, CO_2, N_2, and H_2O activation among all the studied surfaces. The NEB results on pristine Nb_2C-S showed total activation energies of 1.04 and 2.19 eV for O_2 and H_2O dissociation. By creating a vacancy in termination groups, the total activation energies for dissociating the aforementioned molecules were decreased further. The total activation energy of 0.46, 1.2, 3.2, and 3.18 eV was obtained for O_2, H_2O, N_2, and CO_2 dissociation on Nb_2C-S_{x-1}, respectively. This work provides new pathways to improve the catalytic activity of Nb_2C-based MXenes. It demonstrates that by tuning the synthesis

environments of Nb_2C MXenes in experiments, one can achieve Nb_2C MXenes with functional groups possessing the desired properties required for catalyzing the chemical reactions.

2.5. Supplementary materials

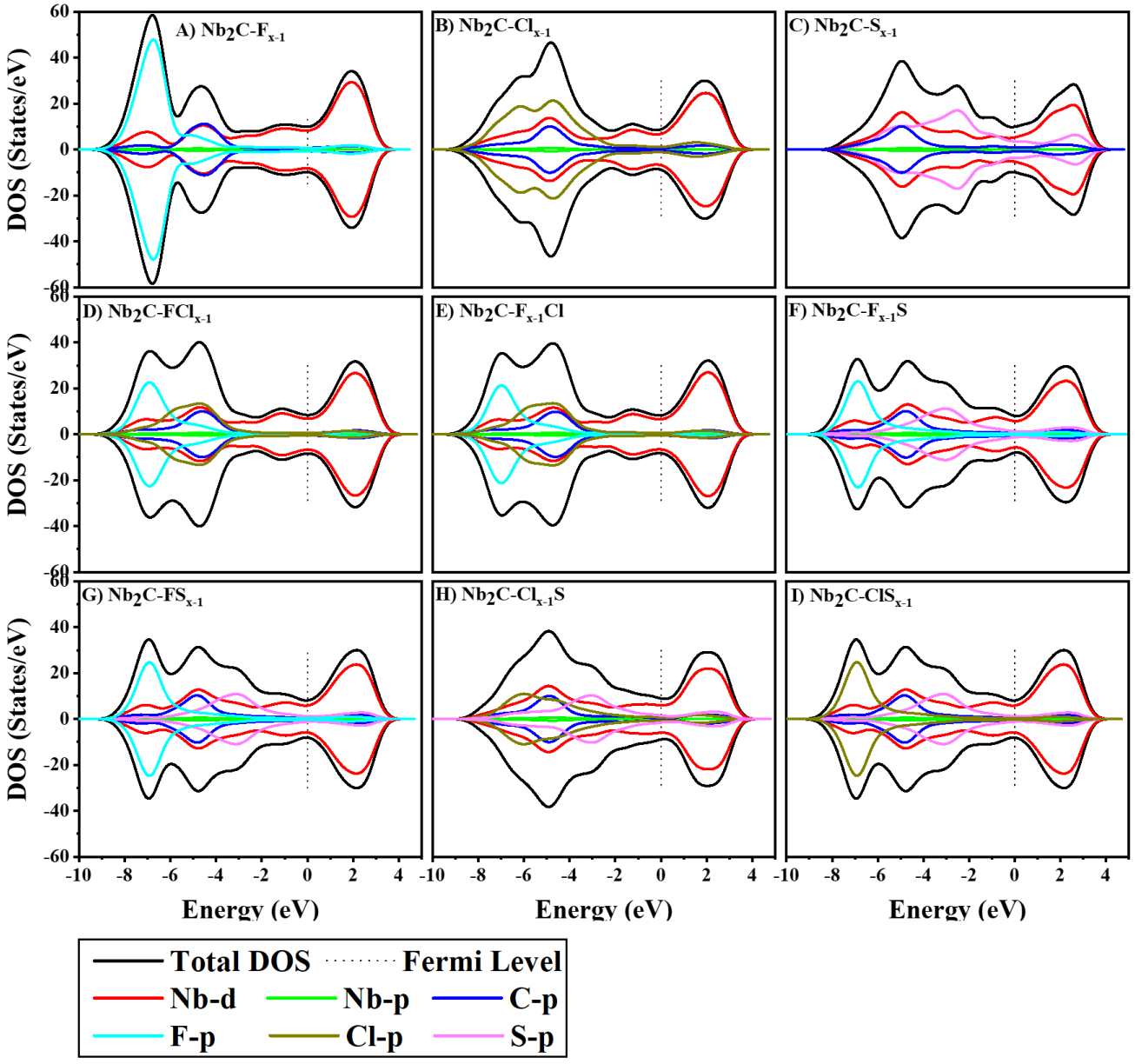

Figure 2-11. The partial density of states of (A) Nb_2C-F-defected, (B) Nb_2C-Cl-defected, (C) Nb_2C-S-defected, (D) Nb_2C-FCl-Cldefected, (E) Nb_2C-FCl-Fdefected, (F) Nb_2C-FS-Fdefected, (G) Nb_2C-FS-Sdefected, (H) Nb_2C-ClS-Cldefected, and (I) Nb_2C-ClS-Sdefected.

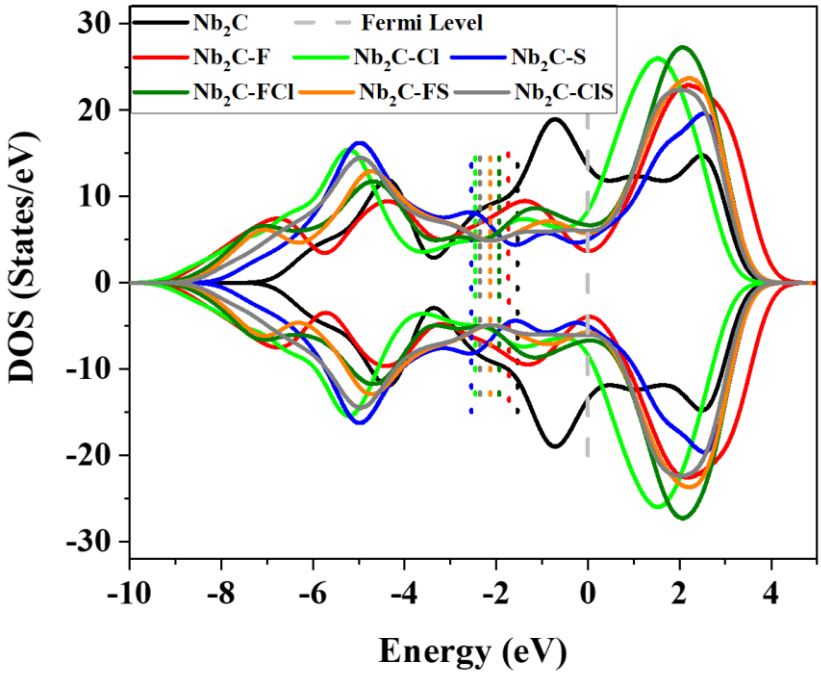

Figure 2-12. The d-band structure of Nb in the pristine Nb_2C and terminated Nb_2C MXenes. The d-band center of Nb in each MXene is represented by dashed colored lines, and the Fermi level is represented by a dashed grey line at 0 eV.

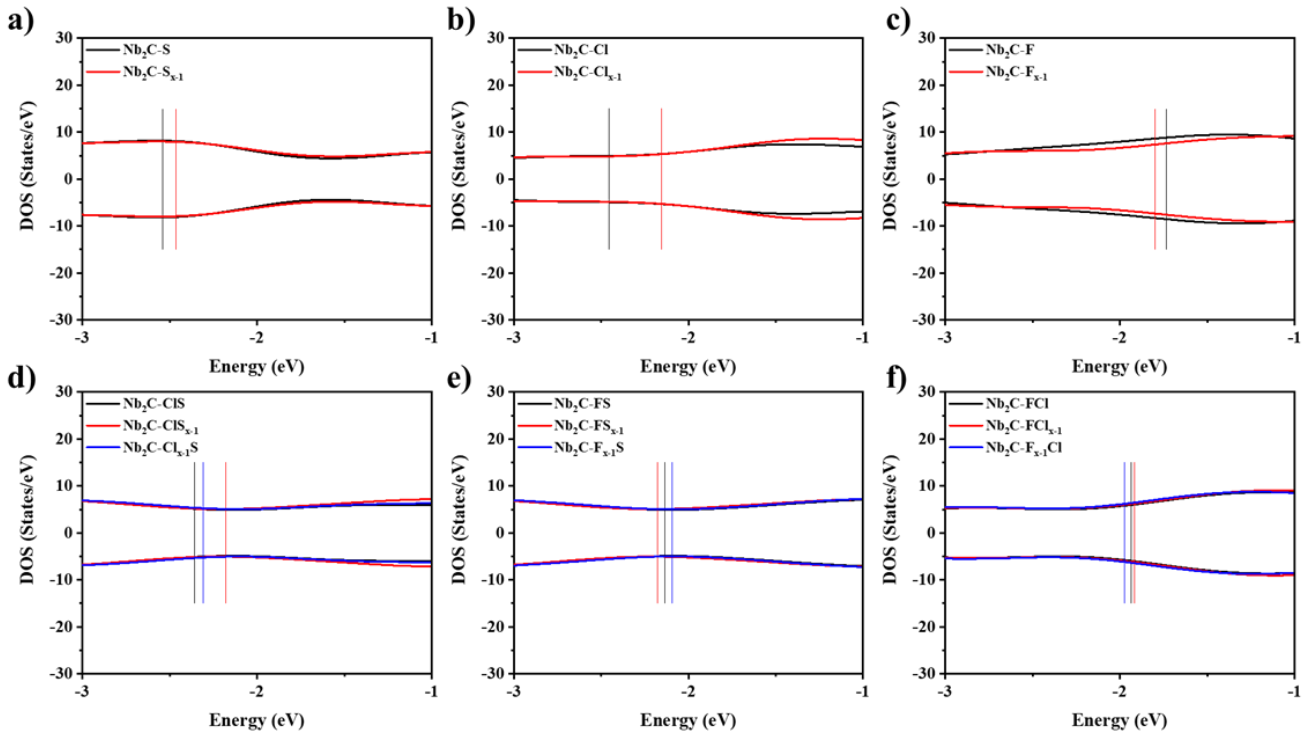

Figure 2-13. The d-band structure of Nb in the pristine and defected a) Nb_2C-F, b) Nb_2C-Cl, c) Nb_2C-S, d) Nb_2C-FCl, e) Nb_2C-FS, and f) Nb_2C-ClS. The relative vertical solid lines show the d-band center of each structure.

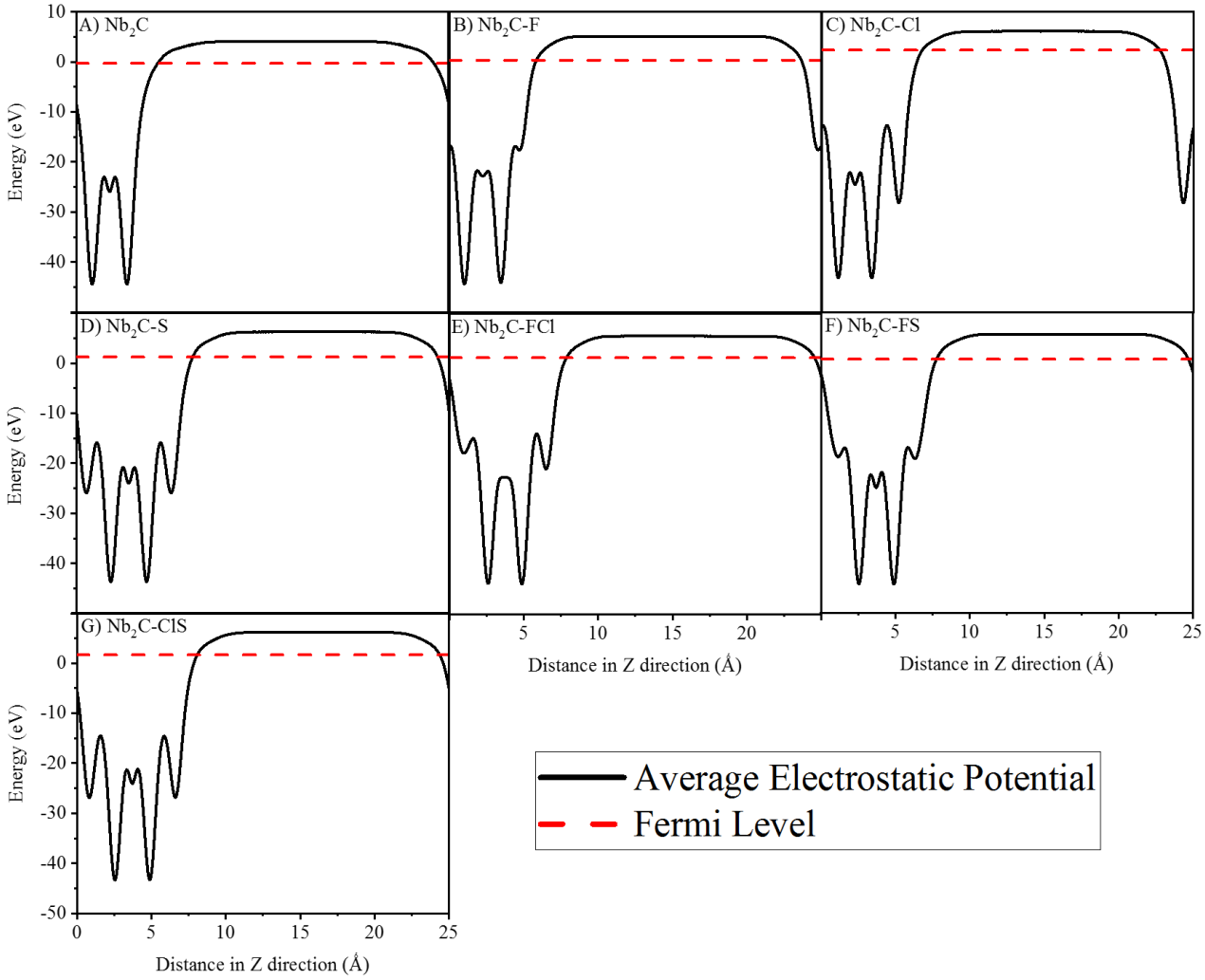

Figure 2-14. The planar average of the electrostatic potential along the z-axis for the (a) Nb_2C, (b)Nb_2C-F, (c) Nb_2C-Cl, (d) Nb_2C-S, (e) Nb_2C-FCl, (f) Nb_2C-FS, and Nb_2C-ClS. (Red line represents the Fermi level.)

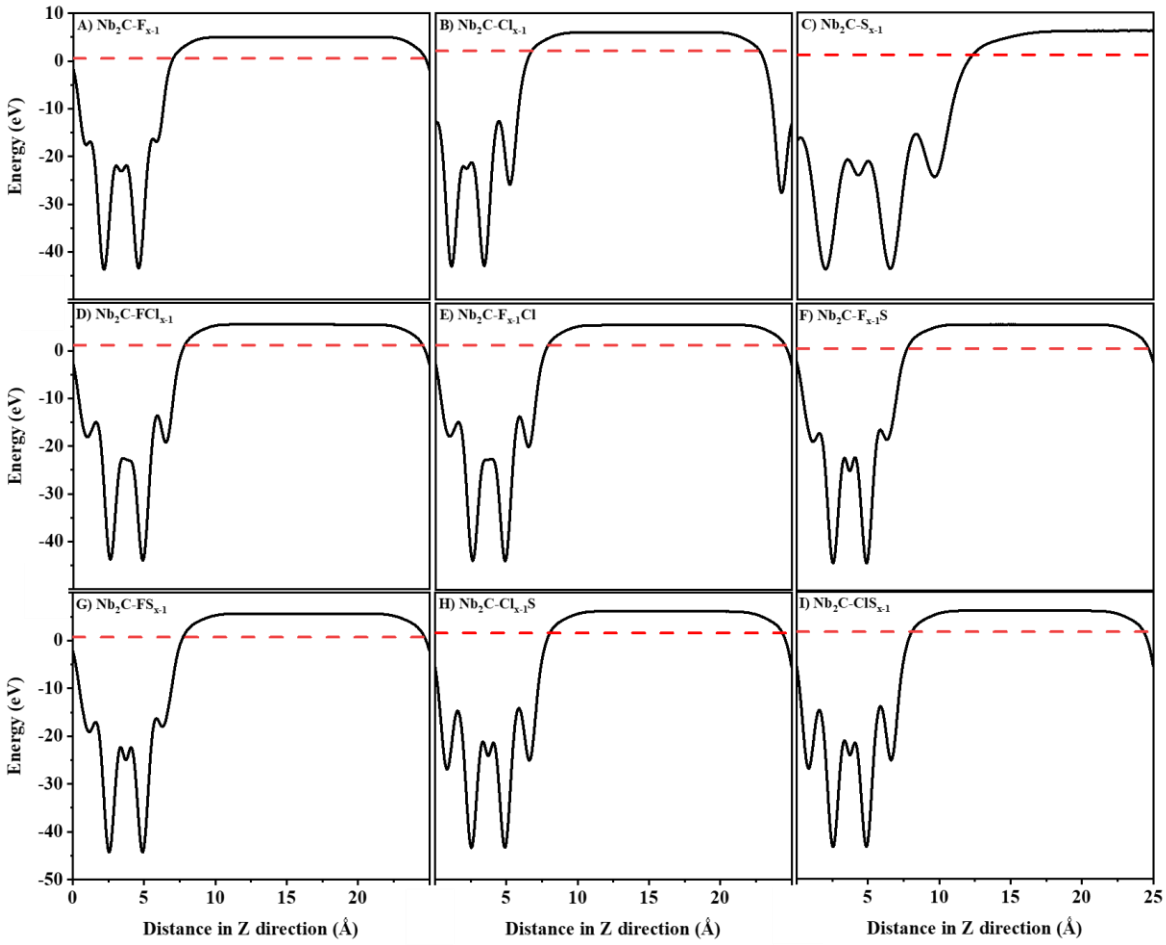

Figure 2-15. The planar average of the electrostatic potential along the z-axis for (A) $Nb_2C\text{-}F_{x\text{-}1}$ defected, (B) $Nb_2C\text{-}Cl_{x\text{-}1}$, (C) $Nb_2C\text{-}S_{x\text{-}1}$, (D) $Nb_2C\text{-}FCl_{x\text{-}1}$, (E) $Nb_2C\text{-}F_{x\text{-}1}Cl$, (F) $Nb_2C\text{-}F_{x\text{-}1}S$, (G) $Nb_2C\text{-}FS_{x\text{-}1}$, (H) $Nb_2C\text{-}Cl_{x\text{-}1}S$, and (I) $Nb_2C\text{-}ClS_{x\text{-}1}$. Subscript (x-1) represents the defect of the coresponding species (Red line represents the Fermi level.)

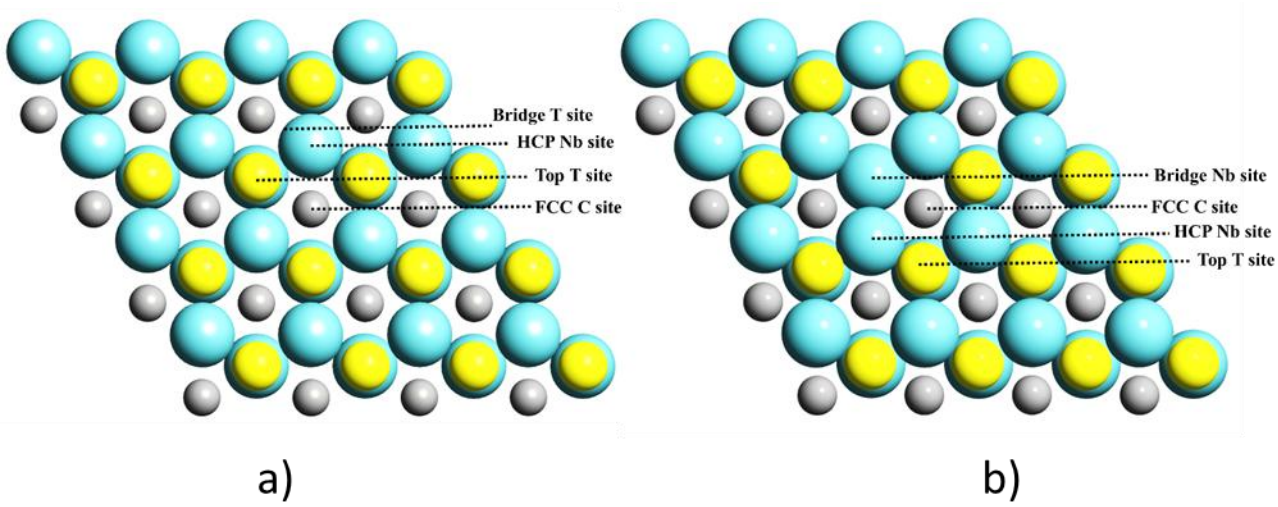

Figure 2-16. Different sites considered in the adsorption analysis of A) Nb_2C-Cl and Nb_2C-S, and B) Nb_2C-Cl_{x-1} and Nb_2C-S_{x-1}.

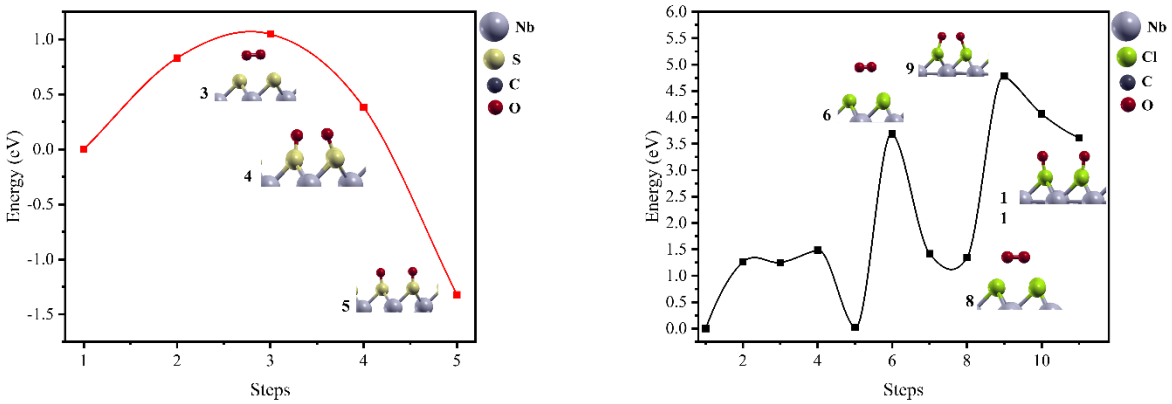

Figure 2-17. The minimum energy path for oxygen dissociation on pristine A) Nb_2C-S and B) Nb_2C-Cl.

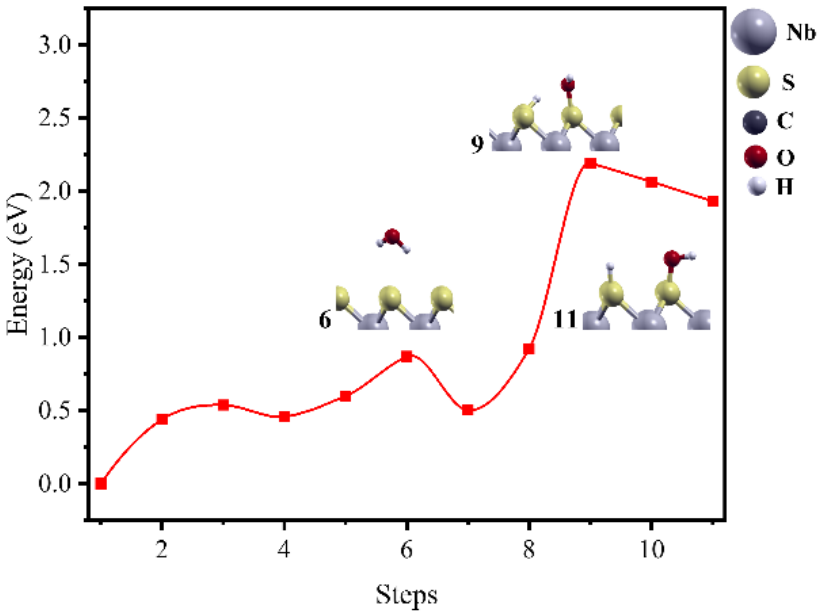

Figure 2-18. The minimum energy path for water dissociation on pristine Nb_2C-S.

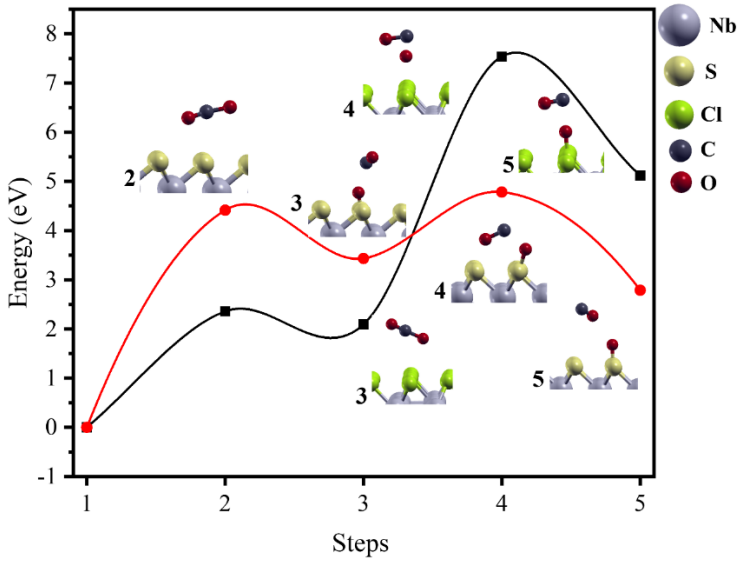

Figure 2-19. The minimum energy path for CO_2 dissociation on pristine Nb_2C-S (red line) and Nb_2C-Cl (black line).

Table 2-1. Total energy, formation energy, and position of the d-band center (with respect to Fermi energy) of the pristine Nb_2C MXene and the terminated MXenes.

Structure	Formation energy per atom (eV)	ΔE_{dbc} (eV)	Work Function (eV)
Nb_2C-S	-0.90	-2.53	5.07
Nb_2C-Cl	-0.94	-2.45	3.79
Nb_2C-ClS	-0.94	-2.35	4.53
Nb_2C-FCl	-1.32	-1.93	4.33
Nb_2C-FS	-1.31	-2.13	5.01
Nb_2C-F	-1.65	-1.72	4.76
Nb_2C	0.32	-1.53	4.43

Table 2-2. Total energy, formation energy, and position of the d-band center (with respect to Fermi energy) for the defected Nb_2C-T MXenes.

Structure	Formation energy per atom (eV)	ΔE_{dbc} (eV)	Work Function (ev)
Nb_2C-F_{x-1}	-1.61	-1.80	4.48
Nb_2C-Cl_{x-1}	-0.93	-2.15	3.92
Nb_2C-S_{x-1}	-0.89	-2.46	5.06
Nb_2C-$F_{x-1}Cl$	-1.28	-1.97	4.25
Nb_2C-FCl_{x-1}	-1.30	-1.92	4.34
Nb_2C-$F_{x-1}S$	-1.28	-2.09	5.03
Nb_2C-FS_{x-1}	-1.30	-2.17	4.93
Nb_2C-$Cl_{x-1}S$	-0.93	-2.31	4.56
Nb_2C-ClS_{x-1}	-0.93	-2.17	4.44

3 First-Principles Study on Nb_2C-X (X = S, Cl, F)/Graphene Heterostructures: Assessing Aqueous Stability and Implications for Electrocatalysis

Abstract

Nb_2C-X MXenes (X = S, Cl, F) have the potential to be promising economical (electro)catalysts, but their degradation in oxidative and aqueous environments remains a major concern. In this work, the resistance to oxidation and hydrolysis of heterostructures made of Nb_2C-X MXenes and graphene was explored using density functional theory. We found that Nb_2C-X/graphene heterostructures are less prone to oxidation compared to pristine Nb_2C-X MXene. Especially, Nb_2C-F/graphene was found to possess higher oxidative resistance compared to those of Nb_2C-S/graphene and Nb_2C-Cl/graphene. An analysis of the electronic properties of the Nb_2C-X/graphene heterostructures indicated improved conductivity compared to that of pristine Nb_2C-X structures and gave insight into the influence of graphene on the MXene's electronic structure. In addition, the resistance to hydrolysis of pristine Nb_2C-S and the Nb_2C-S/graphene heterostructures was compared. Nudged elastic band calculations indicated significantly higher activation energies for water adsorption and dissociation on the Nb_2C-S/graphene heterostructure as compared to that on pristine Nb_2C-S, which are the first steps in MXene decomposition in aqueous media. Moreover, an assessment of the oxygen evolution reaction (OER) performance showed a significantly lower overpotential for the OER on Nb_2C-S/graphene compared to that of pristine Nb_2C-S, indicating the improved electrocatalytic activity of the heterostructure. This work presents the critical role of graphene in improving the resistance to oxidation and stability in aqueous media of MXenes, which is a valuable insight for the synthesis of stable MXene-based (electro)catalysts.

3.1. Introduction

Sustainable production of fuels and chemicals is crucial for transitioning toward carbon-neutral economies [149]. To exploit the potential of electrochemical technologies for facing these challenges, high-performance electrocatalysts are needed. Precious metal-based catalysts possess desirable properties for most electrochemical reactions, including hydrogen evolution (HER) [150], oxygen evolution (OER) [151], oxygen reduction (ORR) [152], nitrogen reduction (NRR) [153], and carbon dioxide reduction (CO_2RR) [154]. However, the scarcity and high cost of precious metal-based electrocatalysts pose restrictions to their large-scale application [155].

Research efforts have therefore been focused on discovering new materials that are easily accessible and suitable for performing electrocatalysis. However, identifying active catalysts that are also stable in acidic or alkaline media is the most important challenge to be solved in order to exploit nonprecious metals in electrocatalysis [156].

In the past years, two-dimensional transition metal carbides and nitrides, referred to as MXenes, have received increasing attention due to their exceptional electronic and structural properties [157-159]. In contrast to noble metals, most transition metals are abundant on earth. As high catalytic performance for water splitting, ORR, NRR, and nitrate reduction reactions has been reported in theoretical works, MXenes are considered promising candidates for replacing precious metal-based electrocatalysts [160-164]. Additionally, it is possible to customize the properties of MXenes by varying their terminating groups (denoted as X) [70, 93], by creating carbon or metal defects [107, 108], or by designing hybrid structures [165, 166].

Generally, MXenes are described by the formula $M_{n+1}X_nT_x$ (n = 1–3), where X denotes carbon or nitrogen and M stands for a transition state (TS) metal such as Ti, Mo, V, or Nb. MXenes are usually synthesized through selective etching from a corresponding MAX phase with the chemical composition $M_{n+1}AX_n$, where A denotes an element from groups 13 to 16. The surface functional groups obtained in this process largely depend on the employed acid, though the composition of the terminating groups can be modified subsequently [159]. Alternatively, MXenes having Cl functional groups have been prepared via an element replacement approach using molten salts [167]. In the last stage, heterostructures and composites might be designed through different approaches, such as mechanical mixing, self-assembly, or hydrothermal techniques [168]. Scheme 1 shows a simple scheme illustrating the synthesis of MXenes and MXene/graphene heterostructures.

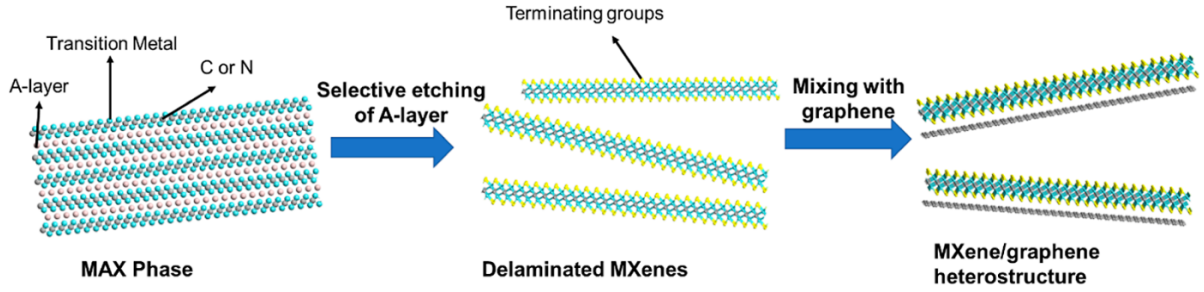

Scheme 3-1. Simple Scheme Illustrating the Synthesis of MXenes and MXene/Graphene Heterostructures.

Up to now, a majority of studies have focused on Ti-based MXenes, which have been the first to be synthesized [169]. However, the more novel Nb-based MXenes have demonstrated advantageous properties for a variety of applications, including biosensing, photocatalytic, and electrochemical applications [159]. For instance, Nb_2CT_x hybrid materials have been introduced as electrode materials in Li- and Na-ion batteries due to their high conductivity [170, 171]. Furthermore, a lower overpotential along with increased long-term stability in alkaline and acidic media was observed compared to that in other MXenes when employing $Nb_4C_3T_x$ as a catalyst for the HER [113].

However, the stability of MXenes in aqueous solutions has been a major concern as they are prone to oxidation and hydrolysis [172]. Thus, several experimental studies on the degradation process and stability of MXenes have been conducted, where Ti-based MXene was predominantly chosen as a representative of the MXene family [172-174]. Additionally, it has been established that Nb_2C-X turns into Nb oxide when exposed to an oxidative environment or high temperatures [175]. Recent works have highlighted the dominant role of water molecules rather than oxygen in the MXene's degradation and described hydrolysis as the main oxidation mechanism [172, 176]. For instance, Wu et al. recently employed ab initio molecular dynamics to explore the degradation mechanism of $Ti_3C_2O_2$ and found that water molecules adsorbed on Ti were deprotonated and formed a Ti–OH group, leading to Ti atoms being pulled out of the surface. Consequently, they proposed to charge the surface negatively by employing anionic salts so that the hydrogen atoms of water molecules orient toward the MXene's surface [72]. This strategy has been employed in experimental attempts to stabilize other MXenes as well [102, 177]. However, while combining the MXenes with salt ions improved their stability, it might result in a loss of catalytic performance. Alternative strategies include carefully controlling the MXenes' environment to prevent oxidation, but eliminating oxidative species, including water molecules, hydroxy species, carbon dioxide, or dissolved oxygen, is not possible when using the MXene for OER, ORR, and HER electrocatalyses [178].

Table 3-3 provides a short overview of MXenes and MXene-based hybrid systems that have been used for electrocatalysis and the performance of their electrodes over time, while more detailed review articles summarizing the potential of MXenes for electrocatalytic applications are available [95, 161, 179].

There is also evidence that surface terminations alter the MXene's stability [167, 180]. O- and OH-terminations are thought to encourage the oxidation process as OH-groups might be

protonated, rendering transition metal atoms more electrophilic and thus facilitating a nucleophilic attack of H_2O or O_2 [72, 175]. F-terminated MXenes were found to be more stable with F atoms bonding stronger to the surface, which means that they are harder to remove when increasing the temperature, according to a recent study focused on Ti, Nb, and Mo MXenes [175, 181]. Cl terminations increased the MXenes' stability, and S-terminations could also improve the stability of Hf-based MXene [116]. However, only a few studies have been conducted on Cl- and S-functionalized MXenes [167, 175]. As Nb-based MXenes having Cl- or S-termini have not been synthesized, and their oxidation stability has not been investigated yet. Still, based on the existing literature, one can easily speculate on their degradation mechanism. It is plausible that the surface functional groups of Nb_2C-X MXenes would be replaced by oxygen first as O-terminated Nb MXene is generally thermodynamically more stable [174, 175, 182]. Once the terminating groups are replaced by oxygen, further oxidation can easily take place. Also, the removal of surface functional groups would render Nb atoms accessible for interactions with oxidative species such as water molecules.

An alternative strategy to stabilize MXenes is to design hybrid structures. Up to now, research has been conducted on a variety of MXene heterostructures, including 0D/2D, 1D/2D, and 2D/2D materials [157, 183-186]. Overall, the catalytic activity was preserved or even improved after hybridization [186]. Sc, V, and Ti-based MXene/graphene heterostructures have been studied for metal ion battery applications recently [187, 188]. It was predicted by first-principles calculations that incorporating graphene layers in the MXene's structure would prevent restacking effects and improve the electric conductivity [188]. Overall, it is well acknowledged that MXene/graphene van der Waals heterostructures are promising candidates to stabilize MXene without degrading its catalytic activity. However, there are no studies that have investigated the stability and resistance to oxidation of functionalized Nb_2C MXene/graphene heterostructures yet.

In this work, we aim to investigate whether forming a heterostructure of Nb_2C MXene and graphene would improve the resistance to oxidation and hydrolysis of Nb_2C-X. As the computational strategies for exploring oxidation stability are limited, we compared the thermodynamic formation energies of uniformly terminated MXenes with those where oxygen replaced one of the termination groups. Furthermore, we performed density functional theory (DFT) calculations for Nb_2C/graphene and Nb_2C-X/graphene heterostructures with F, S, and Cl surface functionalization to explore the oxidation stability of terminated Nb_2C-X/graphene heterostructures relative to one of the pristine Nb_2C-X materials. F and Cl are the common

terminations formed during the conventional exfoliation by HF and electrochemical exfoliation by HCl, respectively, and our previous work showed the high catalytic activity of Nb_2C terminated by S [189]. Nudged elastic band (NEB) calculations were conducted to analyze the resistance to hydrolysis of pristine MXenes and heterostructures as the decomposition of MXenes in the presence of water starts with water adsorption and dissociation [72]. Finally, we further explored the electrocatalytic activity of Nb_2C-S and Nb_2C-S/graphene in this work by considering the free energy diagrams for the OER. This study provides insights into the potential oxidation mechanisms of Nb_2C MXenes, enabling the formulation of strategies to enhance their resistance to oxidation and hydrolysis, as discussed in the Conclusions.

3.2. Computational Methods

DFT calculations were performed using the Quantum Espresso software [190, 191]. To accurately describe the d and f electrons of Nb, DFT + *U* calculations based on the Hubbard model were applied. The *U*-value for Nb was set to 6.5 eV, which led to reasonable results in our previous study and is in agreement with other examples in the literature [71, 111, 121, 189]. Furthermore, all calculations were spin-polarized, and the Perdew–Burke–Ernzerhof (PBE) generalized gradient approximation (GGA) exchange–correlation functional was employed [120]. Since weakly interacting heterostructures were studied and the importance of applying a van der Waals correction has been highlighted in the literature for MoS_2/Ti_2C and MoS_2/Ti_2CY_2 (Y = F and OH) heterostructures, the DFT-D2 van der Waals correction of Grimme was added [192, 193]. Kinetic energy cutoff values of 50 and 500 Ry were used for wave functions and charge density, and the energy threshold for self-consistent field (SCF) calculations was set to 10^{-6} Ry. The terminated MXene/graphene structures were relaxed until interatomic forces had declined beneath 10^{-3} Ry $Bohr^{-1}$ and the change in total energy was less than 10^{-4} Ry between SCF steps. The force convergence threshold was set to 10^{-2} Ry $Bohr^{-1}$ for nonterminated Nb_2C/graphene. Structural optimization was performed at the gamma point for heterostructures, and a 2 × 2 × 1 Monkhorst–Pack *k*-point grid was employed for SCF and non-SCF calculations.

To model the heterostructures, a 4 × 4 supercell of Nb_2C and Nb_2C-X (X = S, Cl, F) was combined with a 5 × 5 supercell of graphene, leading to a minimum lattice mismatch with a strain of 1.05 and 1.26%, respectively, which is comparable to other theoretical studies [188, 194-196]. A vacuum layer greater than 26.5 Å was employed in the slab model to avoid interactions between periodically repeated images (convergence test results by changing the vacuum layer thickness are given in Table 3-4). For each structure, the interfacial binding

energy E_{Int}, per C atom in the graphene layer, was calculated according to Equation 3-1, where E_{Het}, E_{MX}, E_G, and n_c represent the total energy of the heterostructure, the MXene, and the graphene layer, and the number of C atoms in graphene, respectively. Following an approach similar to those in previous studies on MXene/graphene heterostructures, the interlayer distance was optimized with respect to the interfacial binding energy in order to identify the ground state [187, 188].

$$E_{Int} = \frac{1}{n_c}\left(E_{Het} - E_{MX} - E_G\right) \quad \text{Equation 3-1}$$

To explore the stability of the structures against oxygen, we calculated the thermodynamic reaction energy ΔE (per atom) to form Nb_2C-$X_{x-1}O$ and Nb_2C-$X_{x-1}O$/graphene from Nb_2C-X and Nb_2C-X/graphene, respectively, as shown in Equations 3-2 and 3-3. 'X' denotes the surface functional group in the following equations.

$$Nb_2CX + 1/2\,O_2 \rightarrow Nb_2CX_{x-1}O + X \quad \text{Equation 3-2}$$

$$Nb_2CX/graphene + 1/2\,O_2 \rightarrow Nb_2CX_{x-1}O/graphene + X \quad \text{Equation 3-3}$$

To derive the reaction energy from the chemical Equations 3-2 and 3-3, the energy of the reactants was subtracted from the energy of the products, leading to Equations 3-4 and 3-5. If the obtained reaction energy is negative, the formation of the structure containing oxygen is an exothermic process and thus more favorable. Equally, a positive reaction energy means that energy must be supplied externally in order for the reaction to happen since the products are less stable than the reactants. We therefore compared the reaction energy ΔE_1 for the pristine case to the reaction energy ΔE_2 for the heterostructures to assess whether hybridizing with graphene would decrease the affinity for oxygen replacement in the structure.

$$\Delta E_1 = E(Nb_2CX_{x-1}O) + E(X) - E(Nb_2CX_x) - E(O) \quad \text{Equation 3-4}$$

$$\Delta E_2 = E(Nb_2CX_{x-1}O/graphene) + E(X) - E(Nb_2CX_x/graphene) - E(O) \quad \text{Equation 3-5}$$

Similarly, formation energies per atom (E_{form}) were derived as shown in Equation 3-6 to compare the thermodynamic stability of the individual structures. E_{total} represents the total energy while n_x and E_x express the number of atoms of the element x present in the structure and the energy per atom in the respective element's ground state.

$$E_{\text{form}} = \frac{1}{\sum_x n_x}(E_{\text{total}} - \sum_x n_x \cdot E_x)$$ Equation 3-6

Moreover, the OER performance of Nb_2C-S and Nb_2C-S/graphene was investigated by calculating the theoretical OER overpotential (η) based on the computational hydrogen electrode (CHE) [51].The associative reaction mechanism, including four steps, was considered, assuming O*, OH*, and OOH* as the reaction intermediates:

$$H_2O + * \rightarrow OH^* + H^+ + e^-$$ Equation 3-7

$$OH^* \rightarrow O^* + H^+ + e^-$$ Equation 3-8

$$H_2O + O^* \rightarrow OOH^* + H^+ + e^-$$ Equation 3-9

$$OOH^* \rightarrow O_2 + * + H^+ + e^-$$ Equation 3-10

where, * indicates the surface, and O*, OH*, and OOH* are adsorbed on the surface. The following equations were used to calculate adsorption ΔE:

$$\Delta E_{O^*} = E(O^*) - E(*) - [E(H_2O_{(g)}) - E(H_{2(g)})]$$ Equation 3-11

$$\Delta E_{OH^*} = E(OH^*) - E(*) - [E(H_2O_{(g)}) - 0.5\,E(H_{2(g)})]$$ Equation 3-12

$$\Delta E_{OOH^*} = E(OOH^*) - E(*) - [2\,E(H_2O_{(g)}) - 1.5\,E(H_{2(g)})]$$ Equation 3-13

in these equations, E(*), $E(O^*)$, $E(OH^*)$, and $E(OOH^*)$ indicate the total energy of the surface without adsorbates, and with adsorbed O*, OH*, and OOH*, respectively. Then, $\Delta G_{adsorption}$ of each intermediate was calculated according to $\Delta G_{adsorption} = \Delta E_{adsorption} + \Delta G_{correction}$. For O*, OH*, and OOH*, $\Delta G_{correction}$ values of 0.044, 0.295, and 0.377 eV were considered [51]. In the reference, $\Delta G_{correction}$ values were calculated considering the contribution of zero-point energy (ZPE), thermal enthalpy, and entropy corrections. Finally, according to the following equations, ΔG of each step at U=0 V and OER overpotential were calculated:

$$\Delta G(step\ 1) = \Delta G(OH^*) - \Delta G(H_2O) = \Delta G(OH^*) - 0 = \Delta G(OH^*)$$ Equation 3-14

$$\Delta G(step\ 2) = \Delta G(O^*) - \Delta G(OH^*)$$ Equation 3-15

$$\Delta G(step\ 3) = \Delta G(OOH^*) - \Delta G(O^*)$$ Equation 3-16

$$\Delta G(step\ 4) = \Delta G_{O_2} - \Delta G(OOH^*) = 4.92 - \Delta G(OOH^*)$$ Equation 3-17

$$\eta = \max[\Delta G(step\ 1);\ \Delta G(step\ 2);\ \Delta G(step\ 3);\ \Delta G(step\ 4)]\ /e\ - 1.23\ V$$ Equation 3-18

Finally, to investigate whether making a heterostructure improves the stability of MXenes against hydrolysis, an analysis of the energy barrier for dissociating a water molecule on the prepared heterostructure was conducted using the Climbing-Image NEB method [126, 197].

3.3. Results and Discussion

3.3.1. Structural Optimization

Pristine Nb_2C/graphene and Nb_2C-X/graphene (X = S, Cl, or F) heterostructures were modeled. Initial interlayer distances varied from 1.5 to 2.5 Å for the Nb_2C/graphene structure (Table 3-5) and from 2.4 to 4 Å (Tables 3-6 to 3-8) for the terminated Nb_2C-X/graphene heterostructures. The structures were optimized using the Broyden–Fetcher–Goldfarb–Shannon (BFGS) algorithm, and the final interlayer distances and total energies were obtained. The interlayer distance refers to the minimal distance between MXene and the graphene layer. Due to the unpassivated surface of pristine Nb_2C, covalent bonds were formed between the MXene and graphene layer, which differs from a van der Waals heterostructure. These bonds affected the planar geometry of the two layers, giving rise to a noticeable curvature within the structure, as shown in Figure 3-10. The minimal distance between Nb in MXene and C in the graphene layer was approximately 1.5 Å, corresponding to the covalent bond length. Also, we found that the starting interlayer distance had little effect on the final configuration of the Nb_2C/graphene heterostructure. By contrast, interactions between terminated MXene and graphene were weak, leading to final structures with preserved planar geometries of the single layers and larger interlayer distances in the range of 2.8–3.6 Å. Similar behavior has been reported by Paul et al. for Ti carbide/graphene heterostructures [198].

We proceeded by calculating the interfacial binding energy (E_{Int}) as per Equation 3-1 from the total energy of the heterostructure, MXene, and graphene layer. The interfacial binding energy was negative for all structures, favoring the formation of the heterostructure, as shown in Table 3-9.

We further evaluated the effect of the interlayer distance on the stability of the terminated Nb_2C-X/graphene heterostructures. Figure 3-1 shows the obtained interlayer distances and

corresponding interfacial binding energies for Cl-, S-, and F-terminated Nb_2C-X/graphene heterostructures. Detailed results can be found in Tables 3-5 to 3-8 in the Supporting Information.

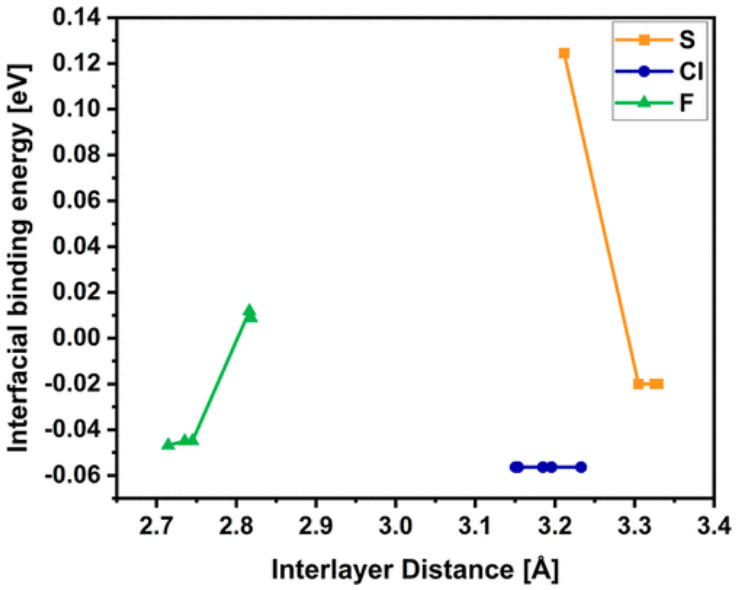

Figure 3-1. Interlayer distance and corresponding interfacial binding energies for the Nb_2C-F/graphene, Nb_2C-S/graphene, and Nb_2C-Cl/graphene heterostructures.

Starting from different interlayer distances, three final structures with close energies and interlayer distances were obtained for Nb_2C-S/graphene. Similarly, the interlayer distances ranged from 3.15 to 3.23 Å for optimized Nb_2C-Cl/graphene structures. All the obtained values for the interfacial binding energy exhibited a variation of less than 0.03 meV, suggesting the thermodynamic stability and experimental feasibility of the obtained structures. The interlayer distance for Nb_2C-Cl/graphene was, therefore, fixed to 3.19 Å. Optimized Nb_2C-F/graphene possessed a smaller interlayer distance of 2.71 Å. Three final Nb_2C-F/graphene structures with little variation in the total energies and interlayer distances were identified. Optimal interlayer distances and corresponding interfacial binding energies are given in Table 3-1. The final structures of the functionalized MXenes are shown in Figure 3-2, while the optimized structure of Nb_2C/graphene is shown in Figure 3-10.

Table 3-1. Optimized interlayer distance and interfacial binding energy for Nb_2C/graphene and Nb_2C-X/graphene (X = F, Cl, S) heterostructures.

System	Distance between graphene and Nb_2C-X (Å)	Interfacial binding energy (eV)
Nb_2C/graphene	1.45	–0.67
Nb_2C-S/graphene	3.31	–0.10
Nb_2C-Cl/graphene	3.19	–0.07
Nb_2C-F/graphene	2.71	–0.04

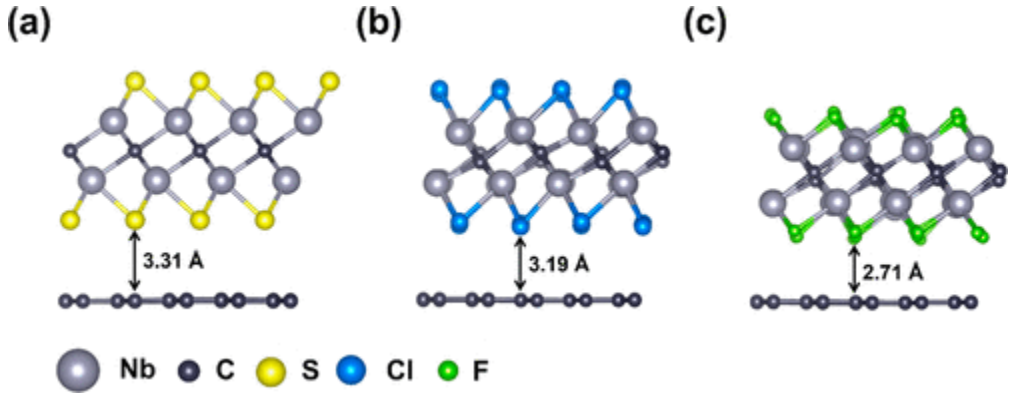

Figure 3-2. Optimized Nb_2C-S/graphene (a), Nb_2C-Cl/graphene (b), and Nb_2C-F/graphene (c).

As expected, the highest interfacial binding energy was found for Nb_2C/graphene, which is plausible due to the formation of covalent bonds between MXene and the graphene layer. Terminated Nb_2C-X/graphene heterostructures had interfacial binding energies ranging from −0.10 eV for Nb_2C-S/graphene to −0.04 eV for Nb_2C-F/graphene, predicting attractive interactions for all structures, while the strongest interactions would occur between Nb_2C-S and graphene.

The optimized interlayer distances for S-, Cl-, and F-terminated MXene/graphene heterostructures demonstrated a strong correlation with the electronegativity (EN) of the heteroatoms on the MXene's surface. Fluorine has the highest EN (EN = 3.98), leading to the smallest interlayer distance. The interlayer distance increased when less electronegative chlorine (EN = 3.16) was present on the surface, while the largest interlayer distance was obtained when sulfur (EN = 2.58) formed the surface terminating groups. This trend of the interlayer distance is also explained by considering the covalent atomic radii (r_{cov}) of the

heteroatoms, with fluorine having the smallest r_{cov} (64 pm), followed by chlorine (r_{cov} = 99 pm) and sulfur (r_{cov} = 103 pm).

3.3.2. Electronic Properties

The density of states (DOS) and partial density of states (PDOS) were calculated for Nb_2C-S/graphene, Nb_2C-Cl/graphene, and Nb_2C-F/graphene (Figure 3-3). Additionally, the projected DOS for Nb p and d orbitals, the p orbitals of the C atom in MXene, the p orbitals of the C atoms in the graphene layer, and the p orbitals of the surface functional groups (S, Cl, or F) were obtained. Figure 3-4 shows the PDOS for graphene C p orbitals in pristine graphene and the heterostructures.

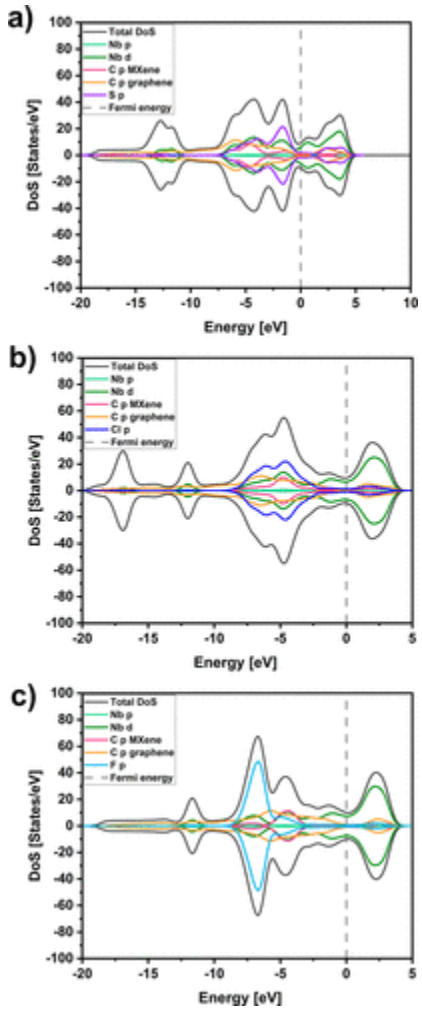

Figure 3-3. DOS and projected DOS for (a) Nb_2C-S/graphene, (b) Nb_2C-Cl/graphene, and (c) Nb_2C-F/graphene.

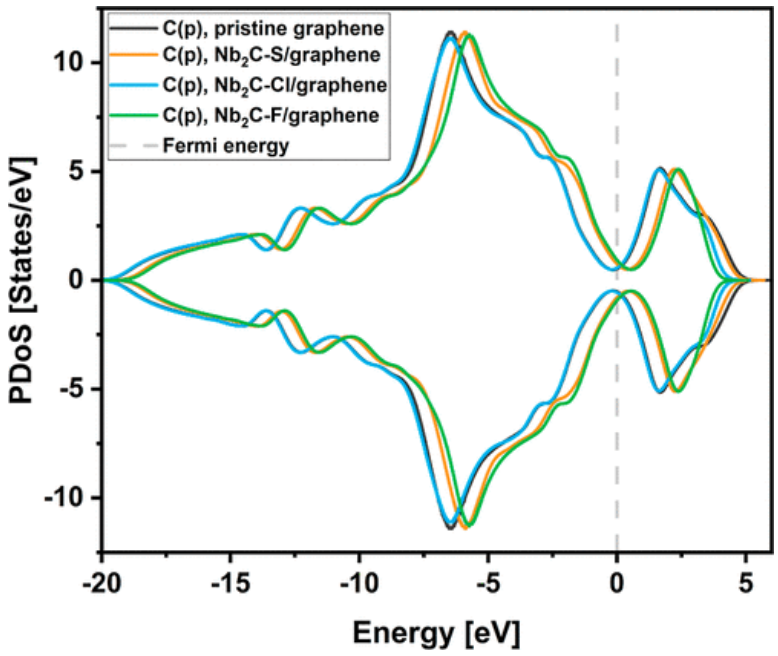

Figure 3-4. Projected DOS for graphene C p orbitals in pristine graphene and Nb_2C-S/graphene, Nb_2C-Cl/graphene, and Nb_2C-F/graphene.

Compared to that in the pristine Nb_2C-X structures (Figure 3-11), the DOS at the Fermi energy of the MXenes was not significantly changed as C p orbitals in graphene contributed only a little near the Fermi level. All three heterostructures were still metallic, while the degree of metallicity was the lowest for Nb_2C-S/graphene and the highest for Nb_2C-F/graphene. The PDOS for C p orbitals in graphene was overall the same for all three heterostructures, although it was shifted to higher energy for Nb_2C-S/graphene and Nb_2C-F/graphene. Equally, the DOS at intermediate energy was increased in each case, suggesting a higher conductivity of the heterostructures compared to that in the pristine Nb_2C-X structures. This finding agrees with the results of the study by Du et al. for Ti-based MXene/graphene heterostructures [188].

Generally, the shape of the DOS curve was only slightly altered for Nb_2C-F and Nb_2C-Cl once graphene was introduced. The contribution of Nb d orbitals did not change significantly in Nb_2C-F/graphene compared to that in pristine Nb_2C-F, and no additional maximum was observed in the conduction band of the heterostructure. For Nb_2C-Cl/graphene, the PDOS for C p graphene orbitals was slightly increased at higher energies in the conduction band compared to that in the other heterostructures.

On the contrary, forming a heterostructure with graphene considerably modified the DOS for Nb_2C-S. Interestingly, the contribution of Nb d orbitals to the conduction band was increased, and S p orbitals were hybridized with C p orbitals of graphene at higher energies in the conduction band. Nb d, C p, and S p orbitals of MXene were strongly hybridized in the valence band, whereby the overlap of Nb d and S p orbitals around −2 eV was particularly large. This implies stronger bonding between the Nb and S atoms induced by graphene.

Similarly, the position of the d-band center of Nb relative to the Fermi energy was computed for each heterostructure. The obtained d-band center values are listed in Table 3-2. Compared to that in the pristine Nb_2C-X structures studied in our previous work, the d-band center values shifted toward the Fermi energy in heterostructures, which indicates a higher affinity toward the adsorption of molecules on the Nb_2C-X/graphene surface [189].

Table 3-2. d-band center values relative to the Fermi energy for Nb_2C-X/graphene (X = S, Cl, F) heterostructures.

surface terminations	d-band center with respect toFermi energy in heterostructures (eV)
S	–1.82 (spin up) –1.81 (spin down)
Cl	–1.85
F	–1.43

Overall, this analysis shows that the electronic structures of terminated Nb_2C MXenes undergo modification upon forming a heterostructure with graphene, potentially influencing its catalytic activity.

3.3.3. Oxidation Stability of Nb_2C-X/Graphene and Pristine Nb_2C-X

MXene surfaces are prone to oxidation, and the degradation processes are usually accompanied by a loss of structural and catalytic properties. Although the oxidation mechanism of MXenes is not clarified yet, there is evidence that the surface functional groups alter the MXenes' stability [167, 180]. If the surface functional groups are replaced by oxygen, the oxidative resistance of the MXene might suffer as the surface would be more electrophilic, facilitating further degradation [72, 175]. We therefore explored whether replacing one surface functional group with oxygen would be thermodynamically favorable.

In order to conduct this analysis, we computed the total energy for both pristine Nb_2C-X and Nb_2C-X/graphene, then one surface group was replaced with oxygen, and the total energies of these structures were recalculated. As shown in Figure 3-5, oxygen is bridging between the Nb sites in the considered structures for Nb_2C-$S_{x-1}O$, Nb_2C-$Cl_{x-1}O$, and Nb_2C-$F_{x-1}O$, as well as in the corresponding Nb_2C-$X_{x-1}O$/graphene heterostructures. It should be noted that especially for the S-terminated MXene and MXene/graphene structures, the surface functional groups might potentially be oxidized instead of Nb. This would most probably favor the removal of the surface functional group and facilitate oxidation in a similar manner.

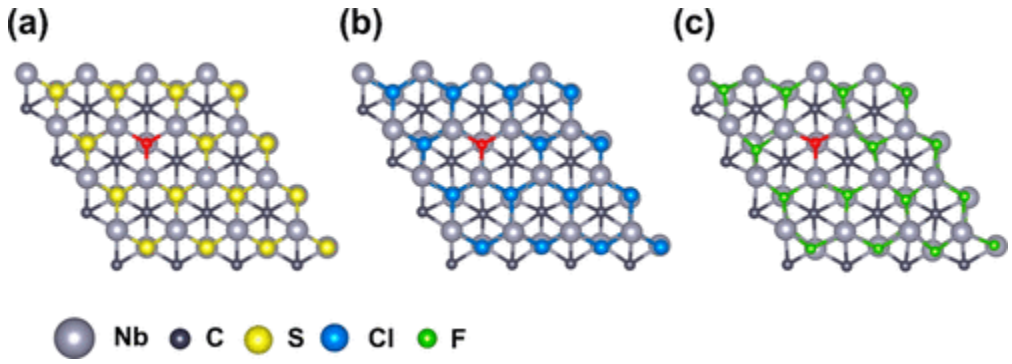

Figure 3-5. Top view of optimized Nb_2C-$S_{x-1}O$ (a), Nb_2C-$Cl_{x-1}O$ (b), and Nb_2C-$F_{x-1}O$ (c), showing the position of oxygen on the surface.

The formation energies per atom were obtained using Equation 3-6, and the structures containing oxygen were compared to those having uniform terminations. For each functionalization, the difference between the formation energy of Nb_2C-X/graphene and Nb_2C-$X_{x-1}O$/graphene and pristine Nb_2C-$X_{x-1}O$ and Nb_2C-X was obtained. The changes in the formation energies for S-, Cl-, and F-terminated structures, with and without an oxygen atom, are visualized in Figure 3-6. The formation energy values for each structure are listed in Table 3-9 in the Supporting Information. Detailed information on the computed energies can be found in Tables 3-10 to 3-12 in the Supporting Information.

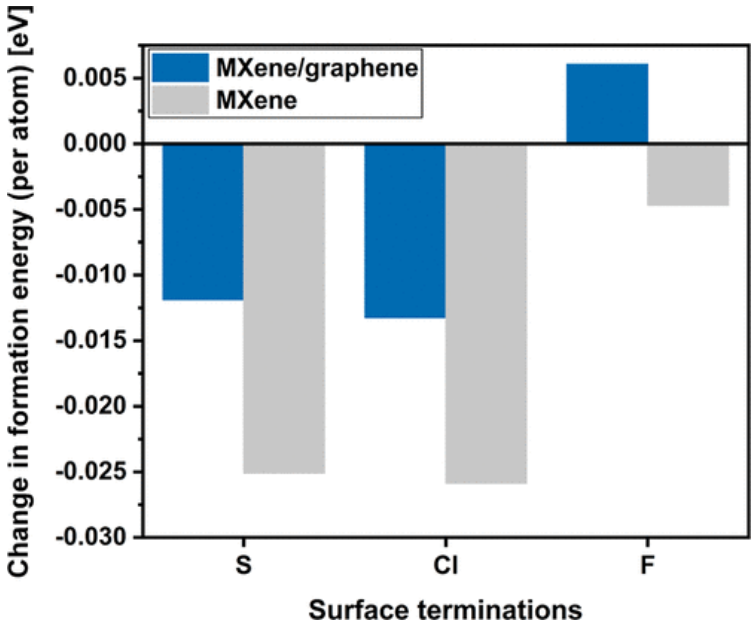

Figure 3-6. Change in the formation energies for Nb_2C-X/graphene heterostructures and pristine Nb_2C-X with S, Cl, and F terminations when one surface functional group is replaced with oxygen.

For S and Cl surface terminations, the change in formation energy between Nb_2C-$X_{x-1}O$/graphene and Nb_2C-X/graphene is approximately twice as large compared with the change in formation energy when replacing a surface functional group in pristine MXene. This indicates that the heterostructure of MXene and graphene is relatively more stable against oxygen replacement than the pristine Nb_2C-X. Interestingly, the change in formation energy when forming Nb_2C-$F_{x-1}O$/graphene from Nb_2C-F/graphene is positive and, therefore, less likely to happen. Even for the nonhybridized Nb_2C-F, the energy gain is comparatively small when an oxygen atom is introduced. Likewise, the formation energy per atom of both Nb_2C-F and Nb_2C-F/graphene is significantly lower than that for the corresponding S- and Cl- terminated structures, emphasizing the stability of the F-terminated Nb_2C-X structures with and without graphene.

A similar trend is observed when considering the reaction energy ΔE (per atom) for forming Nb_2C-$X_{x-1}O$ and Nb_2C-$X_{x-1}O$/graphene from Nb_2C-X and Nb_2C-X/graphene, respectively (refer to 4.5. for details). The reaction energy was calculated according to Equations 3-4 and 3-5. One surface functional group atom was replaced with an oxygen atom in the Nb_2C-X/graphene heterostructures, where X = S, Cl, and F. The obtained reaction energies were compared with

the corresponding values for pristine Nb_2C-X MXene, as shown in Figure 3-12. The obtained reaction energies are listed in Table 3-13 in the Supporting Information.

However, this analysis takes only the thermodynamic aspects into account, neglecting kinetics completely. As a next step, ab initio molecular dynamic simulations could provide further insight into the structure's stability and degradation mechanism.

3.3.4. NEB Calculations for Water Dissociation on the Nb_2C-S Surface

To study the reactivity of Nb_2C-based MXenes with water molecules, NEB calculations were conducted. As found by Wu et al., [72] the first steps to the decomposition of the Ti-based MXenes in the presence of water are adsorption and dissociation of water molecules over the Ti site, leading to the pulling out of the Ti atoms. Based on our previous work [189] showing the promising catalytic properties of S-terminated Nb_2C, we compared the stability of pristine Nb_2C-S and the Nb_2C-S/graphene heterostructure.

For Cl- and F-terminated Nb MXene systems, a higher barrier for the dissociation of water would be expected, partially due to the higher EN of Cl and F as compared to that of S. In fact, pristine Nb_2C-Cl was found to be less active for water dissociation in our previous work [189]. Additionally, the bond between the dissociated water molecule and the Cl- but especially F-terminating groups is expected to be weaker than that for the S-terminated surface. This is due to the decreased covalency contribution, thereby lowering the affinity for dissociative water adsorption.

For the initial state (IS), a water molecule was placed approximately 4 Å above the MXene's surface, and the geometry was relaxed. Similarly, the final state (FS) was obtained by optimizing a dissociated water molecule on the Nb_2C-S surface. In our previous work on Nb_2C-S, various adsorption sites for H_2O adsorption and dissociation were explored, including adsorption on top of C, Nb, and S atoms and in between two terminating groups. The geometry where water was dissociated into OH and H adsorbed on neighboring S atoms was found to be most favorable and was therefore chosen for the investigation of water dissociation on the Nb_2C-S/graphene heterostructure [189].

Although the dissociation of water on the pristine Nb_2C-S surface was investigated via an NEB calculation in our previous work, the study was repeated here employing the same parameters and convergence thresholds that were utilized for the NEB analysis of water dissociation on the

Nb_2C-S/graphene heterostructure surface. This alignment ensures a fair comparison of the two scenarios.

The calculated minimum energy path and geometries corresponding to the respective steps of water dissociation over the Nb_2C-S/graphene heterostructure are shown in Figure 3-7. The dissociation mechanism along the calculated path comprises the following steps: first, the water molecule was rotated until the hydrogen atoms faced the MXene's surface and tilted slightly, so that the O atom was closer to the surface. Then, the water molecule dissociated, corresponding to the highest energy configuration, and the H atom and OH molecule were adsorbed on neighboring atoms. The total activation energy, including the rotation of the water molecule, was calculated as the energy difference between the IS and TS, represented by the fourth step in the NEB calculation (Figure 3-7), and estimated to be 4.06 eV. The dissociation of the water molecule on the MXene's surface is endothermic as the energy difference between the IS and FS of 2.09 eV is positive.

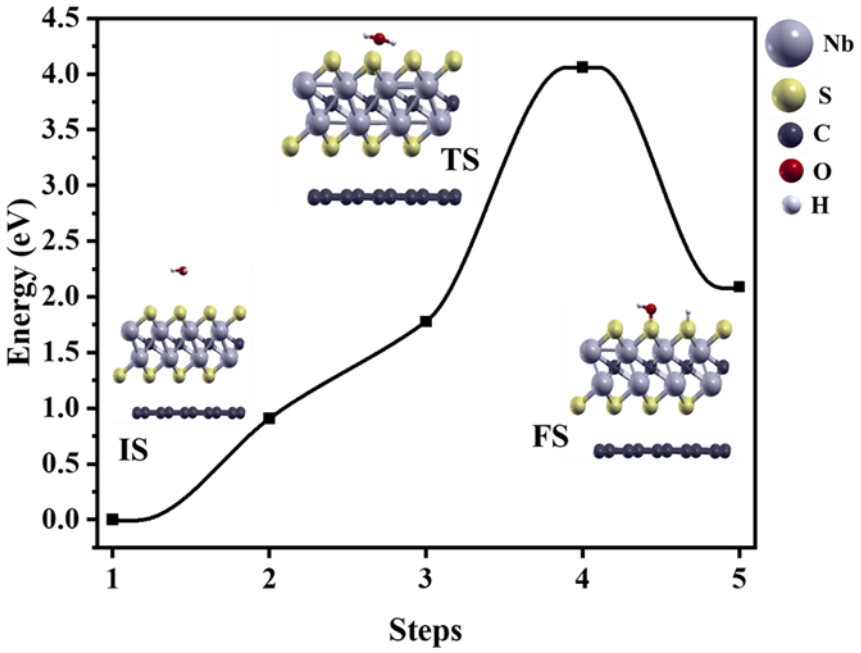

Figure 3-7. Minimum energy path for the dissociation of a water molecule on the Nb_2C-S/graphene surface and corresponding geometries of IS, TS, and FS.

It should be noted that water molecules might also intercalate between Nb_2C-X and the graphene layer, possibly influencing the interaction between the two layers and leading to a different adsorption behavior, although this has not been studied explicitly here.

The obtained minimum energy path and the corresponding geometries for each step of water dissociation on pristine Nb_2C-S are visualized in Figure 3-8. The hydrogen atoms in the water molecule were facing the surface of Nb_2C-S in the IS, corresponding to the lowest energy configuration obtained through structural optimization. In the highest energy state, the water molecule is dissociated, and the H atom is adsorbed on a S atom of the MXene, while the OH molecule is adsorbed on a neighboring atom. The dissociation of the water molecule is endothermic, with an energy difference of 2.2 eV between the IS and FS, which is similar to the reaction energy predicted for the heterostructure. The activation energy for water dissociation over pristine Nb_2C-S is around 2.5 eV.

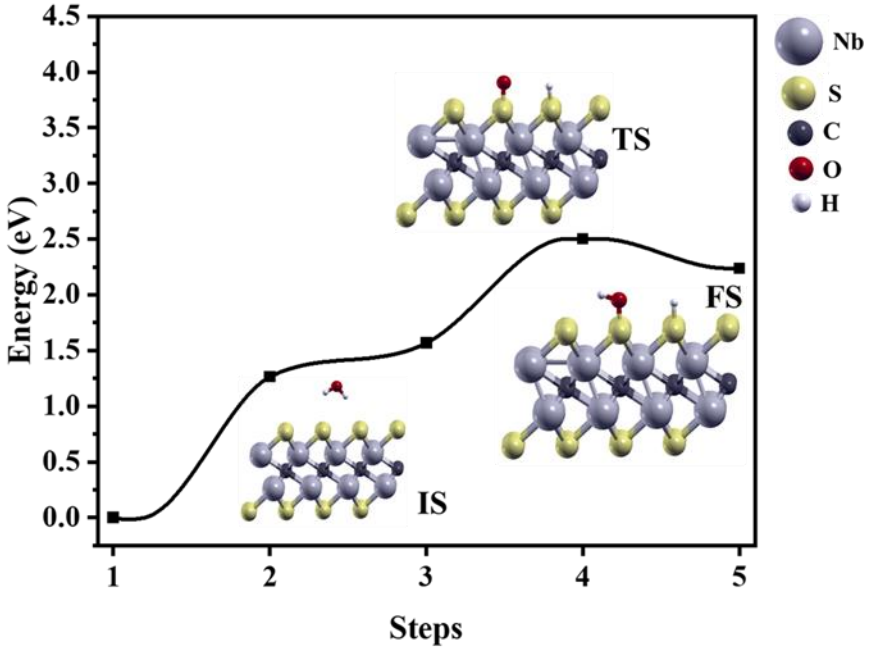

Figure 3-8. Minimum energy path for the dissociation of a water molecule on Nb_2C-S and corresponding geometries of the IS, TS, and FS.

By comparing the NEB results, it is evident that the Nb_2C/graphene heterostructure exhibits a higher energy barrier for water adsorption and dissociation, with an activation energy difference of 1.55 eV, compared to that of the Nb_2C surface. This indicates a substantial enhancement in

the aqueous stability of the Nb_2C/graphene heterostructure compared to that of the pristine Nb_2C-S, as the initial stages of MXene decomposition in the presence of water are impeded.

3.3.5. OER Performance

To investigate how the electrocatalytic activity of the studied Nb MXenes changes upon hybridization with graphene, the OER performance of Nb_2C-S and Nb_2C-S/graphene was assessed based on the free energy diagram (Figure 3-9). The figure indicates the free energy diagram at the applied potential of 0 (U = 0 V) and the potential leading to downhill energies for each step. For these calculations, two active sites on the basal plane were considered, namely, Nb–S and S–S bridge sites. On pristine Nb_2C-S, the overpotential on the Nb–S and S–S sites was 2.15 and 2.51 eV, and the rate-limiting steps were the first and the third step, respectively. By applying the potentials of 3.38 and 3.74 V, the energy diagrams on both sites of Nb_2C-S became downhill, as shown in Figure 3-9. In contrast, the OER overpotential on the Nb–S and S–S sites of Nb_2C-S/graphene was 0.93 V, and the third step was the rate-limiting step. At an applied potential of 2.16 V, all steps on the Nb–S and S–S sites of the heterostructure were downhill. This shows the influential role of hybridization with graphene, resulting in a significantly reduced overpotential. Moreover, although the OER overpotential on the Nb–S and S–S sites of pristine Nb_2C-S was different, these sites showed similar activity on Nb_2C-S/graphene. The superior OER performance on Nb_2C-S/graphene can be attributed to better electron transfer in Nb_2C-S/graphene, as evidenced in the PDOS analysis in Figure 3-3a, facilitating the first step.

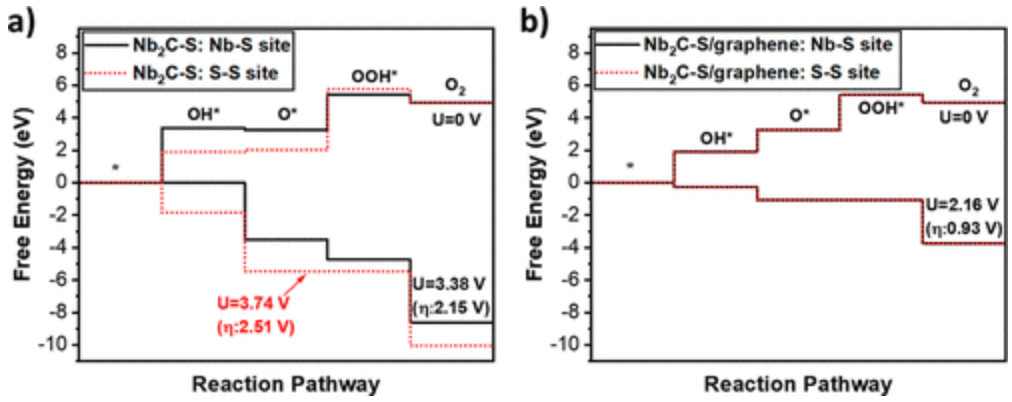

Figure 3-9. Free energy diagrams for the OER reaction pathway on Nb-S and S-S bridge sites of (a) Nb_2C-S and (b) Nb_2C-S/graphene.

3.4. Conclusions

In summary, our study revealed several key findings. The Nb_2C-X MXene/graphene heterostructures having S, Cl, and F terminating groups possess negative interfacial binding and formation energies, suggesting their structural stability. The analysis of the electronic properties demonstrated that the DOS was increased at intermediate energy levels, indicating improved conductivity upon formation of MXene/graphene heterostructures. Notably, the introduction of graphene caused alteration in PDOS for Nb d orbitals, shifting the d band center toward the Fermi energy, potentially impacting the catalytic performance of the Nb_2C-X/graphene heterostructure. This impact was most pronounced for the Nb_2S/graphene heterostructure. We conducted a thermodynamic analysis to investigate the likelihood of oxygen replacing S, Cl, and F functional groups, thus exploring the oxidation stability of the heterostructures. Compared to pristine Nb_2C-X MXenes, the oxidation stability would be improved by a factor of 2 in Nb_2C-S/graphene and Nb_2C-Cl/graphene. In addition, Nb_2C-F/graphene is no longer prone to oxidation, having much higher oxidation stability than that of Nb_2C-S/graphene, Nb_2C-Cl/graphene, and pristine Nb_2C-F. Moreover, NEB calculations showed that the activation energy of water adsorption and dissociation over the Nb_2C-S/graphene is about 1.55 eV higher than that of the pristine Nb_2C-S, demonstrating the better aqueous stability of the heterostructure. Our findings provide strong evidence that graphene can enhance the resistance to oxidation and hydrolysis of Nb_2C MXenes, which is relevant for electrochemical and biomedical applications and suggests that they might be employed as stable (electro)catalysts. Additionally, we compared the OER performance of Nb_2C-S and Nb_2C-S/graphene and found that the overpotential was significantly lower on the surface of the heterostructure, indicating improved electrocatalytic activity for the OER. Therefore, our theoretical study motivates further experimental investigations into the properties and stability of Nb_2C MXene/graphene heterostructures.

3.5. Supplementary materials

3.5.1. MXenes in Electrocatalysis

Table 3-3. Overview of MXenes and MXene-based hybrid systems used for electrocatalysis, summarizing the electrolyte employed, the reactions investigated, and the information obtained about the electrode's performance over time.

Catalyst	Electrolyte	Reaction	Electrode performance over time	Reference
Ti_2CT_x, *rich F terminations*	0.5 M H_2SO_4	HER	No significant change in HER activity for >5.5 h	Li et al. [199]
Mo_2CT_x, rich O terminations	0.5 M H_2SO_4	HER	Stable for >2 h	Seh et al. [200]
Mo_2C@2D-NPCs	1.0 M KOH	HER	Stable for >20 h	Lu et al. [201]
$Mo_2C/Ti_3C_2T_x$@NC	0.5 M H_2SO_4	HER	No significant decrease in current density after 1000 cyclovoltrammetic cycles, stable for >30 h	Wang et al. [202]
FeNi-LDH/$Ti_3C_2T_x$	1 M KOH	OER	No significant decrease in operating potential after 12 h	Yu et al. [203]
$Mn_3O_4/Ti_3C_2T_x$	0.1 M KOH	ORR	No significant decrease in potential after 100 h	Xue et al. [204]
g-$C_3N_4/Ti_3C_2T_x$	0.1 M KOH	ORR	Stable for >11 h	Yu et al. [205]
$Ti_3C_2T_x$, deposited on carbon paper	0.1 M HCl	NRR	No significant decrease in current density after 23 h	Zhao et al. [206]
$Ti_3C_2T_x$, with O and OH terminations	Under N_2	NRR	72.2% performance retention after six chronoamperometric cycles	Luo et al. [207]

3.5.2. Convergence testing

The structures were modeled with a slab model comprising a vacuum layer, in order to eliminate interactions between periodic images. Different sizes for the vacuum layer have been employed in the literature for 2D/2D MXene heterostructures. For instance, Du et. al used a vacuum layer greater than 29 Å [188], while Li et al. chose a vacuum space of 20 Å [195]. As interactions between pristine Nb carbide and graphene have been reported to be significantly stronger than for the terminated MXene/graphene heterostructure, we performed convergence tests for both systems using two different cell sizes. Nb_2C-S was chosen to represent terminated MXene structures. Results are shown in Table 3-4.

Table 3-4. Convergence tests regarding size of vacuum layer for Nb_2C-S/graphene and Nb_2C-graphene.

System	Vacuum Layer (Å)	Total Energy (eV)
Nb_2C-S/graphene	19.3	-172440.14
	28.1	-172435.28
Nb_2C/graphene	20.3	-161879.72

	29.6	-161878.40

As there was a significant deviation in the obtained energy values for Nb_2C-S/graphene, all subsequent calculations were performed using the larger cell, ensuring a vacuum layer of at least 26.5 Å for all structures. Once the simulation cell was chosen, calculations with different convergence thresholds were conducted. We found that changes in total energy were small, when the convergence thresholds were increased, but that the terminated MXene/graphene structures easily converged when default values were employed. Consequently, default values of 10^{-6} Ry for the convergence threshold for self-consistency and 10^{-3} Ry $Bohr^{-1}$ and 10^{-4} Ry for the convergence of forces and the total energy, respectively, were used for structural optimization of terminated MXene structures. The force convergence threshold was set to 10^{-2} Ry $Bohr^{-1}$ for non-terminated Nb carbide/graphene.

Structural optimization was performed at gamma point since we dealt with rather large models, consisting of 98 and 130 atoms for the pristine and terminated Nb carbide/graphene heterostructures respectively. Once optimized structures were obtained, SCF calculations employing a 2 x 2 x 1 Monkhorst-Pack k-point grid were performed for further convergence testing.

3.5.3. Optimization of the interlayer distance

For each terminated MXene heterostructure, five optimization calculations starting at different interlayer distances were performed. For Nb_2C/graphene, the number of calculations was reduced to three. Additionally, MXene and graphene were optimized separately in the simulation cell. Minimal interlayer distances in the optimized structures were obtained and total energy values were used to calculate the interfacial binding energy for each configuration according to Equation 3-1. The optained optimized structure for Nb_2C/graphene is shown in Figure 2-10. Detailed results for Nb_2C/graphene, Nb_2C-S/graphene, Nb_2C-Cl/graphene and Nb_2C-F/graphene are listed in Tables 3-5 to 3-8.

The formation energy (per atom) for the optimized Nb_2C-X and Nb_2C-X/graphene heterostructures (X = S, Cl, F), as well as for the corresponding structures containing oxygen studied in the stability analysis, are listed in Table 9-3.

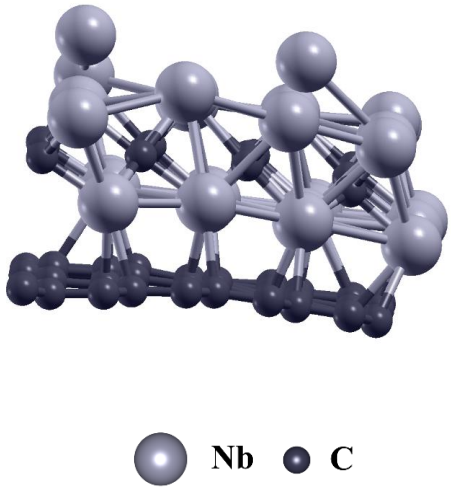

Figure 3-10. Optimized structure obtained for Nb_2C/graphene.

Table 3-5. Interlayer distance and corresponding interfacial binding energy (per atom in graphene) for Nb_2C/graphene.

Interlayer Distance (Å)	Interfacial binding energy (eV)
1.45	-0.67
1.65	-0.63
1.54	-0.62

Table 3-6. Interlayer distance and corresponding interfacial binding energy (per atom in graphene) for Nb_2C-S/graphene.

Interlayer Distance (Å)	Interfacial binding energy (eV)
3.21	0.05
3.31	-0.10
3.33	-0.10
3.33	-0.10
3.62	-0.10

Table 3-7. Interlayer distance and corresponding interfacial binding energy (per atom in graphene) for Nb_2C-Cl/graphene.

Interlayer Distance (Å)	Interfacial binding energy (eV)
3.15	-0.04
3.15	-0.04
3.18	-0.04

3.20	-0.04
3.23	-0.04

Table 3-8. Interlayer distance and corresponding interfacial binding energy (per atom in graphene) for Nb_2C-F/graphene.

Interlayer Distance (Å)	Interfacial binding energy (eV)
2.71	-0.07
2.74	-0.06
2.74	-0.06
2.82	0.01
2.82	0.01

Table 3-9. Formation energy (per atom) for pristine Nb_2C-X, Nb_2C-X/graphene heterostructures, Nb_2C-$X_{x-1}O$ and Nb_2C-$X_{x-1}O$/graphene heterostructures (X = S, Cl, F).

Structure	Formation energy per atom (eV)
Nb_2C-S_x/graphene	-0.766
Nb_2C-$S_{x-1}O$/graphene	-0.777
Nb_2C-S_x	-1.153
Nb_2C-$S_{x-1}O$	-1.179
Nb_2C-Cl_x/graphene	-0.801
Nb_2C-$Cl_{x-1}O$/graphene	-0.814
Nb_2C-Cl_x	-1.247
Nb_2C-$Cl_{x-1}O$	-1.273
Nb_2C-F_x/graphene	-1.290
Nb_2C-$F_{x-1}O$/graphene	-1.284
Nb_2C-F_x	-2.027
Nb_2C-$F_{x-1}O$	-2.032

3.5.4. Electronic properties of pristine Nb_2C-X

The Density of States (DOS) and projected density of states (PDOS) for pristine Nb_2C-X (X = S, Cl, F) are shown in Figure 2-11.

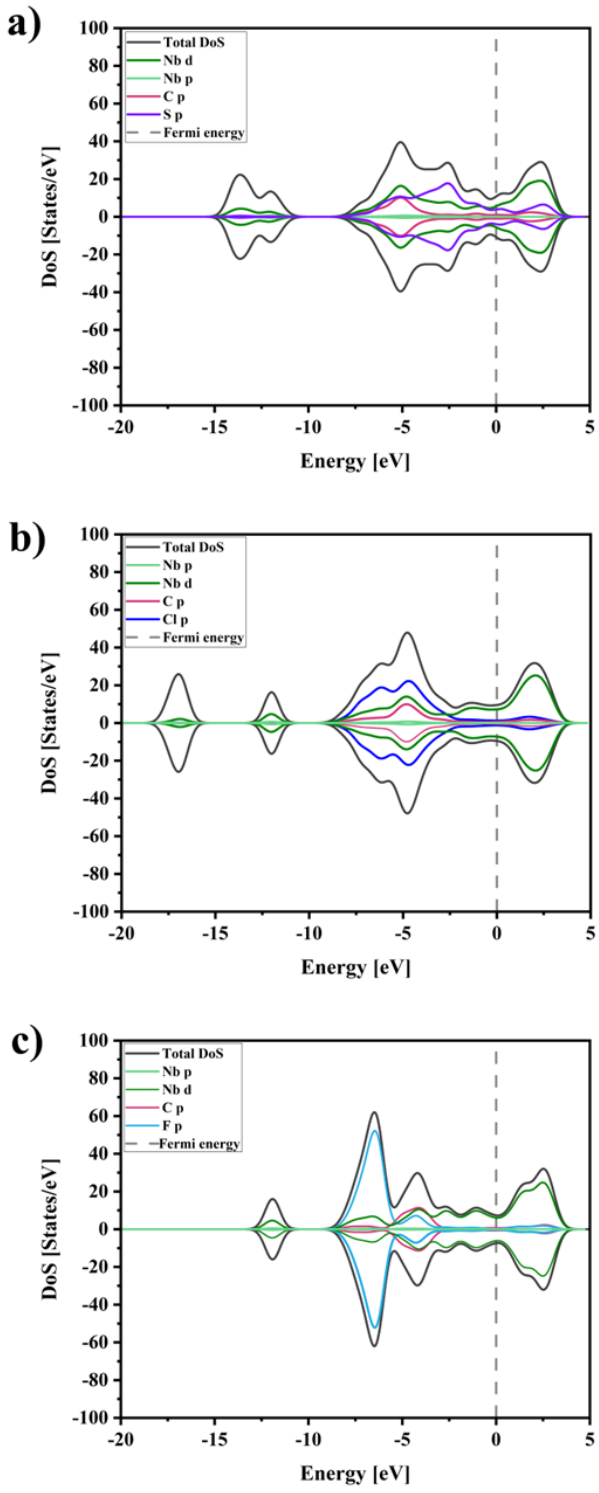

Figure 3-11**.** Density of States and Projected Density of States for (a) Nb_2C-S, (b) Nb_2C-Cl and (c) Nb_2C-F.

3.5.5. Relative stability of Nb_2C-X/graphene and pristine Nb_2C-X

As a second index of stability, the reaction energy for replacing one surface functional group with oxygen in Nb_2C-X/graphene heterostructures and pristine Nb_2C-X having S, Cl, and F terminations was considered, as visualized in Figure 2-12.

In order to calculate the reaction energy for the formation of Nb_2C-$X_{x-1}O$/graphene from Nb_2C-X/graphene and Nb_2C-$X_{x-1}O$ from Nb_2C-X (X = S, Cl, F), the total energy per atom was computed for Nb_2C-$X_{x-1}O$/graphene, Nb_2C-X/graphene, Nb_2C-$X_{x-1}O$, Nb_2C-X, O_2 and X. The obtained values for the total energy of each structure are listed in Table 3-10 to 3-12, while the calculated reaction energies are shown in Table 3-13.

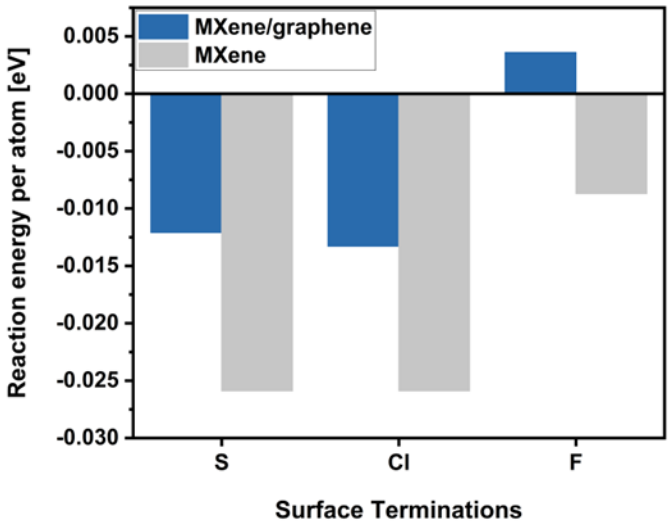

Figure 3-12. Reaction energy when replacing one surface functional group with oxygen in Nb_2C-X/graphene heterostructures and pristine Nb_2C-X with S, Cl, and F terminations.

Table 3-10. Total energy per atom for the stability analysis of S-terminated structures.

Structure	Total energy per atom (eV)
Nb_2C-S/graphene	-1326.48
Nb_2C-$S_{x-1}O$/graphene	-1328.32
Nb_2C-S	-1998.62
Nb_2C-$S_{x-1}O$	-2001.60
O_2	-564.75
S (in crystal)	-327.87

Table 3-11. Total energy per atom for the stability analysis of Cl-terminated structures.

Structure	Total energy per atom (eV)
Nb_2C-Cl/graphene	-1357.29
Nb_2C-$Cl_{x-1}O$/graphene	-1358.17
Nb_2C-Cl	-2048.72
Nb_2C-$Cl_{x-1}O$	-2050.15
O_2	-564.75
Cl_2	-452.90

Table 3-12. Total energy per atom for the stability analysis of F-terminated structures

Structure	Total energy per atom (eV)
Nb_2C-F/graphene	-1408.52
Nb_2C-$F_{x-1}O$/graphene	-1407.79
Nb_2C-F	-2131.95
Nb_2C-$F_{x-1}O$	-2130.77
O_2	-564.75
F_2	-659.32

Table 3-13. Reaction energy ΔE_1 and ΔE_2 (per atom) for replacing a surface functional group with oxygen in Nb_2C-X and Nb_2C-X/graphene (X = S, Cl, F).

Surface terminations	ΔE_1 (eV)	ΔE_2 (eV)
S	-0.025	-0.012
Cl	-0.026	-0.013
F	-0.009	0.004

4 Graphene support- and facet-dependent oxygen evolution activity of Ta_2O_5

Abstract

Ta_2O_5 is among the few metal oxides that are stable in acidic media but, due to its insulating nature, its use in electrocatalytic oxygen evolution reaction (OER) has been less explored. Herein, density functional theory calculations were performed on three different Ta_2O_5 facets, pristine and with O or Ta defects. The goal was to identify strategies to improve the OER performance of Ta_2O_5 by establishing correlations with its intrinsic properties. The study revealed that the OER activity of Ta_2O_5 is facet-dependent according to the following trend (200) > (120) > (001), which correlated with the Ta density on the topmost atomic layer. The lowest overpotential, 0.61 V, was observed at the Ta-O site of the pristine (200) facet, followed by a Ta site on the same facet with a Ta defect (0.63 V). The moderate density of states (DOS) at the Fermi level and lower Ta site density on the (200) surface contributed to its higher performance compared to other facets. The correlation analysis conducted by considering Bader charge, d-band analysis of Ta sites, and valence electrons showed strong correlations for (120) surfaces, whereas (200) surfaces had moderate correlations. As a conductive phase is often added to insulating materials in experiments, the (200) Ta_2O_5/graphene heterostructure was also studied. An overpotential as low as 0.39 V was found for the Ta-O sites of the heterostructure. According to the partial DOS (PDOS) analysis, the improved OER performance of the heterostructure can be attributed to the shift in the *d* orbitals of Ta sites toward lower energies and the increase in the DOS intensity. This study offers valuable insights for designing Ta_2O_5-based electrocatalysts for OER in acidic media.

4.1. Introduction

As a carbon-free energy vector, green hydrogen can enable clean electricity production, helping to meet the targets for reducing the emission of greenhouse gases (GHGs) [7]. It has been estimated that green hydrogen can reduce CO_2 emissions by six gigatonnes and meet 18% of energy demands [14, 208]. According to the hydrogen strategy for Canada, clean hydrogen is capable of delivering 30% of end-use energy in the country by 2050, reducing the emission of CO_2 by up to 190 Mt [5]. When powered by electricity from renewable sources, water electrolyzers can sustainably produce green hydrogen [30]. This process involves two reactions, i.e., hydrogen evolution reaction (HER) and oxygen evolution reaction (OER) on the cathode

and anode, respectively. However, the hydrogen production cost through hydrolysis (considering electricity cost of 5 cents USD/kWh) is twice the H_2 production methods based on natural gas [209].

OER is a sluggish reaction that includes four electron-proton transfer steps and requires a high overpotential [210-213]. Proton exchange membrane water electrolyzers (PEMWEs) that work in an acidic environment are superior to alkaline electrolysis technologies. This is because PEMWEs have higher efficiency, higher production rates per unit electrode area, faster electrode kinetics, and a more compact design [214]. The best OER electrocatalysts are based on Ru and Ir materials, with Ru-based materials having higher OER activity but weaker stability compared to Ir-based materials [39]. The high cost and scarcity of these catalysts increase the economic risks of water electrolyzers. These risks can be minimized by developing precious metal-free catalysts and by diversifying catalyst material supply [63]. One strategy to develop electrocatalysts for corrosive acidic environments is to select materials with good inherent acidic stability and then tune their catalytic activity by modifying their structure. Among several transition metals, Tantalum-based materials are known for their good stability under acidic media [215]. However, tantalum oxides, the most-studied Ta-based materials, are insulators in their pristine form with poor or no OER performance [216, 217].

Several efforts have been made to induce electrical conductivity and improve the OER performance of Ta_2O_5-based electrocatalysts in alkaline media. Using the pulsed laser deposition method, Xiao et al. [217] grew stable $Ta_2O_{5\pm\delta}$ nanolayers over a carbon cloth by controlling the oxygen environment. The pristine Ta_2O_5 did not have catalytic activity, but the O-rich Ta_2O_5 with a thickness of 8 nm showed an overpotential of 0.385 V at 10 mA/cm^2 in a 1 M KOH solution [217]. They reported that controlling the oxygen partial pressure and keeping the thickness of the nanolayer small could enable the efficient performance of Ta_2O_5 for OER. Liu et al. synthesized Fe-doped O-rich Ta_2O_5 nanolayers with a thickness of about 5 nm, which showed an overpotential of 0.38 V at 10 mA/cm^2 in the 1 M KOH solution with the optimal Fe concentration of 5 at.% [216]. This work reported that doping with transition metals could increase the electrical conductivity of Ta_2O_5 and activate its surface for OER.

Yue et al. synthesized tantalum dioxyfluoride (TaO_2F) over graphitized carbon [218]. When TaO_2F was loaded over the carbon material with high electrical conductivity, an improvement in the charge transfer and OER performance was observed. The authors suggested that when fluorine was introduced into the TaO_2F structure, more positive charge could be distributed by

Ta sites of TaO_2F compared to Ta_2O_5/CC (Cabot Vulcan XC 72R), Ta_2O_5, and $KTaO_3$, which benefited the adsorption and reaction of intermediates. So, TaO_2F loaded on graphitized carbon reached an overpotential of 0.360 V at 10 mA/cm^2 in the alkaline medium [218]. Ruiz-Cornejo et al. [219] supported Ta_2O_5 over highly graphitic carbon nanofibers (CNFs), in which the sample with the lowest O/Ta (non-stoichiometric composition) led to the best OER performance in the alkaline medium. Ahmed et al. [220] loaded Ta_2O_5 particles over Fe_2O_3 through the hydrothermal treatment. They reported that the Fe_2O_3/Ta_2O_5 double oxide heterostructure had a low overpotential of 0.231 V in alkaline media, which was attributed to the synergistic effect and interfacial interaction between Fe_2O_3 and Ta_2O_5 [220]. Ta_2O_5 is stable under OER polarization conditions in acidic media [221], yet there have been very few studies that have explored its performance under such an environment. Mondschein et al. [215] fabricated polycrystalline pellets of Ni_2Ta through arc melting and molding. This material could combine the corrosion resistance of Ta and the OER activity of Ni in acidic media and achieve an overpotential of 0.570 V in 0.5 M H_2SO_4.

To develop stable and active Ta_2O_5-based electrocatalysts for OER in an acid medium, it is crucial to identify strategies to enhance its performance and establish clear structure-property relationships. For instance, there have been inconsistent reports in the literature regarding the role of the O/Ta ratio in alkaline medium. Xiao et al. [217] reported better OER performance with O-rich Ta_2O_5, and Ruiz-Cornejo et al. [219] found that a lower O/Ta ratio results in better performance. Furthermore, while the use of carbon-based materials to improve the charge transfer with Ta_2O_5-based electrocatalysts has been explored, their role in altering the electronic and electrocatalytic properties of Ta_2O_5 remains unexplored.

Herein, we performed density functional theory (DFT) calculations on (200), (120), and (100) Ta_2O_5 facets to identify strategies to unlock the OER performance of the Ta_2O_5 in an acidic medium. The effect of a Ta or O defect on the electronic properties of (200) and (120) facets was studied, and thirty-five different sites on facets with or without a defect were considered for OER activity evaluation. Then, correlations were identified between the OER performance and structural and electronic properties, such as Bader charge (BC), valence electrons, and DOS of Ta_2O_5 surfaces. Finally, the effect of graphene on the electronic properties and OER performance of the most active Ta_2O_5 surface was investigated.

4.2. Computational

In this study, three Ta_2O_5 facets, (200), (120), and (001), reported to be stable in DFT calculations [217] and experiments [222], were examined, as illustrated in Figure 4-1 A-C. The orthorhombic λ-Ta_2O_5 unit cell, with lattice parameters of a= 6.24 Å, b= 2×3.69 Å, and c= 3.82 Å, was used to model the surfaces [223, 224]. The 200-Ta_2O_5/graphene heterostructure was also modeled with the mean absolute strain of 2.94% for graphene and Ta_2O_5, Figure 4-1 D. The initial distance between (200) Ta_2O_5 and graphene was changed between 2 to 5 Å to find the most stable heterostructure. As shown in Figure 4-10, the model created using the initial distance of 3 Å (final distance of 3.3 Å) had the lowest total energy and was the most stable, which was considered for OER performance evaluation. To avoid interactions between periodic images, all slab models were made with a vacuum greater than 15 Å. Spin-polarized DFT calculations were performed using the Perdew–Burke–Ernzerhof (PBE) exchange-correlation functional in the generalized gradient approximation (GGA). All the DFT calculations were conducted using the Quantum Espresso software [120]. Furthermore, we utilized the DFT-D3 correction method in Grimme's scheme [225, 226] for a more accurate description of the long-range van der Waals (vdW) interactions. The kinetic energy cut-off values of 35 and 350 Ry were used for wavefunctions and charge density, respectively. The energy threshold was set to 10^{-4} Ry for the self-consistent field (SCF) convergence. Davidson iterative diagonalization was employed to relax each system (without variable size) until the residual Hellman–Feynman force magnitude on each atom reached below the 10^{-3} Ry $Bohr^{-1}$. The DFT+ U was performed to reach more accurate electronic properties. The U value of 3.66 V was taken from the Materials Project database [227, 228], as it has been used for developing Ta-based electrocatalysts in the literature [229]. The k-point sampling of 2 ×2×1 was used to relax the structures, and the k-point samplings of 4×4×1 and 6×6×1 were adopted for the SCF and non-self-consistent field (nSCF) calculations, respectively, to calculate the DOS and partial DOS (PDOS). The BC analysis was performed to assess the electron density of each surface [123].

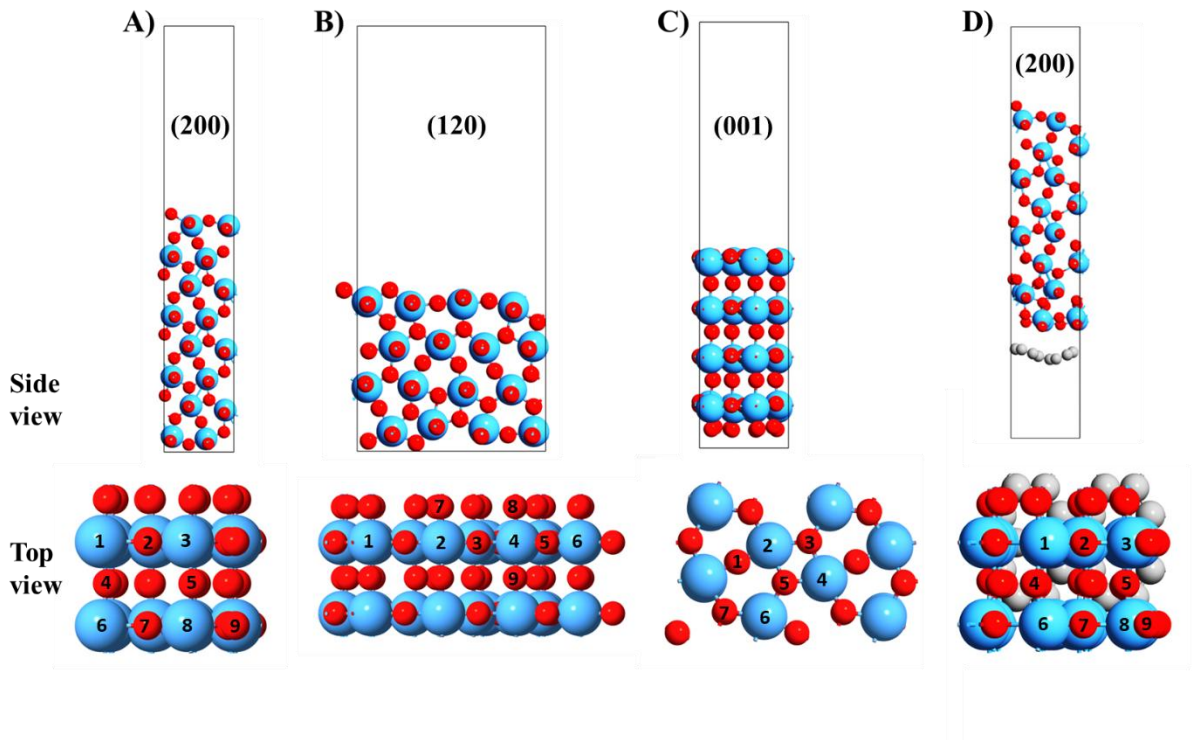

Figure 4-1. The side and top views of (A) (200), (B) (120), and (C) (001) Ta_2O_5 facets, respectively. (D) The side and top views of the 200-Ta_2O_5/graphene model. The atoms with numbers in the lower panel represent the unique Ta and O sites on the surface. The O, Ta, and C atoms are represented by red, blue, and gray spheres, respectively.

The OER performance was investigated by calculating the theoretical OER overpotential (η) according to the computational hydrogen electrode (CHE) [51]. The reaction mechanism is shown in Equations 4-1 to 4-4. The following associative reaction mechanism, including four steps, was considered:

$$H_2O + * \rightarrow OH^* + H^+ + e^- \quad \text{Equation 4-1}$$

$$OH^* \rightarrow O^* + H^+ + e^- \quad \text{Equation 4-2}$$

$$O^* + H_2O \rightarrow OOH^* + H^+ + e^- \quad \text{Equation 4-3}$$

$$OOH^* \rightarrow O_2 + * + H^+ + e^- \quad \text{Equation 4-4}$$

where, * indicates the surface, and O*, OH*, and OOH* refer to the adsorbed intermediates. To calculate the adsorption energy (ΔE) of each intermediate, Equations 4-5 to 4-7 were used:

$$\Delta E_{O^*} = E(O^*) - E(*) - [E(H_2O_{(g)}) - E(H_{2(g)})]$$ Equation 4-5

$$\Delta E_{OH^*} = E(OH^*) - E(*) - [E(H_2O_{(g)}) - 0.5\,E(H_{2(g)})]$$ Equation 4-6

$$\Delta E_{OOH^*} = E(OOH^*) - E(*) - [2\,E(H_2O_{(g)}) - 1.5\,E(H_{2(g)})]$$ Equation 4-7

in these equations, E(*), $E(O^*)$, $E(OH^*)$, and $E(OOH^*)$ are the total energy of the surface without adsorbates and with adsorbed intermediates of O*, OH*, and OOH*, respectively. After finding the adsorption ΔE of each intermediate, adsorption free energies ($\Delta G_{adsorption}$) were calculated according to Equation 4-8:

$$\Delta G_{adsorption} = \Delta E_{adsorption} + \Delta G_{correction}$$ Equation 4-8

For O*, OH*, and OOH*, $\Delta G_{correction}$ values of 0.044, 0.295, and 0.377 eV were used, respectively [51]. Finally, Gibbs free energy ($\Delta G_{Step\ 1\text{-}4}$) of each step at U=0 V and OER overpotential (η) were calculated according to Equations 4-9 to 4-13:

$$\Delta G_{Step\,1} = \Delta G_{OH*} - \Delta G(H_2O) = \Delta G_{OH*} - 0 = \Delta G_{OH*}$$ Equation 4-9

$$\Delta G_{Step\,2} = \Delta G_{O*} - \Delta G_{OH*}$$ Equation 4-10

$$\Delta G_{Step\,3} = \Delta G_{OOH*} - \Delta G_{O*}$$ Equation 4-11

$$\Delta G_{Step\,4} = \Delta G_{O_2} - \Delta G_{OOH*} = 4.92 - \Delta G_{OOH*}$$ Equation 4-12

$$\eta = \max[\Delta G_{Step\,1};\ \Delta G_{Step\,2};\ \Delta G_{Step\,3};\ \Delta G_{Step\,4}]/e - 1.23\,V$$ Equation 4-13

4.3. Results and discussion

4.3.1. OER performance of pristine and defected Ta_2O_5 surfaces

First, we investigated the OER performance of various sites on pristine and defected Ta_2O_5 facets. Specifically, (200), (120), and (001) facets were investigated as they were experimentally observed and were proved to be stabilized in DFT calculations [217]. Additionally, on (200) and (120) facets, O or Ta were removed to create defected surfaces. More precisely, O5d-200-Ta_2O_5, O7d-200-Ta_2O_5, O9d-200-Ta_2O_5, Ta1d-200-Ta_2O_5, and Ta3d-200-Ta_2O_5 surfaces were modeled by removing O5, O7, O9, Ta1, and Ta3 atoms, respectively,

from the pristine (200) surface (Figure 4-1A). In this nomenclature, "d" indicates surfaces with an O or Ta defect. Similarly, the O5d-120-Ta_2O_5, O9d-120-Ta_2O_5, Ta4d-120-Ta_2O_5, and Ta6d-120-Ta_2O_5 surfaces were modeled by removing O5, O9, Ta4, and Ta6, respectively, from the pristine (120) surface (Figure 4-1B).

The OER performance of (200) and (120) surfaces with and without defects and the pristine (001) surface is detailed in Tables 4-1 to 4-3, including the ΔG values for adsorption of reaction intermediates and Steps 1-4 (Equations 4-9 to 4-12). The defects on the (001) facet were not investigated because the pristine (001) surface showed larger overpotentials, as summarised in the SI, compared to the (200) and (120) surfaces. Figure 4-2 illustrates the OER reaction pathway for Ta or Ta-O sites with overpotentials below 0.7 V.

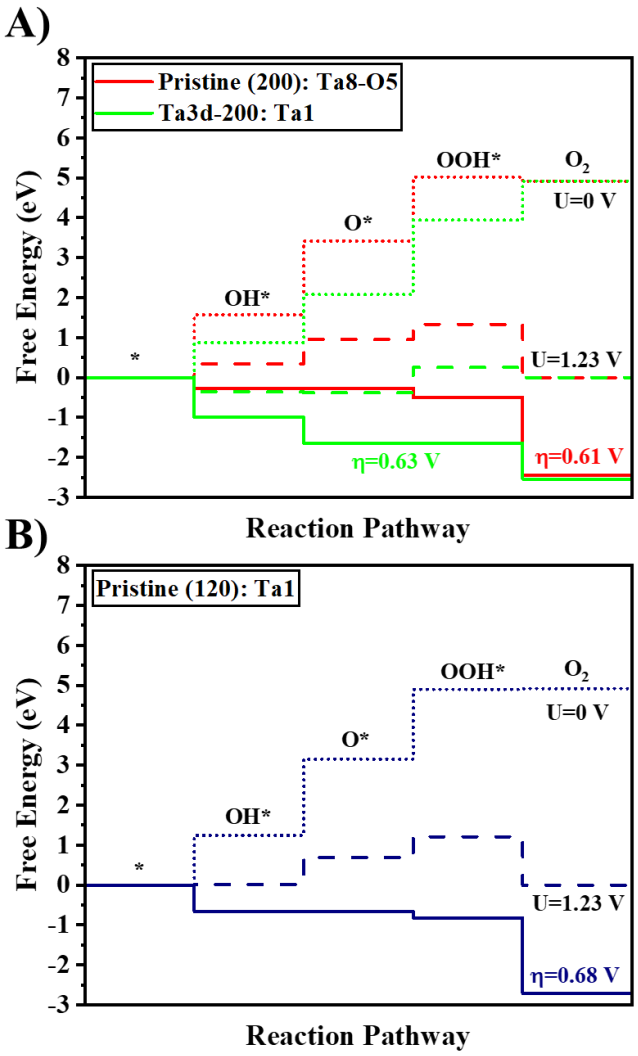

Figure 4-2. Free energy diagrams for A) the Ta8-O5 bridge on the pristine (200) surface, the Ta1 site on the Ta3d-200-Ta_2O_5 surface, and B) the Ta1 site on the pristine (120) surface. The dotted, dashed, and straight lines indicate the free energy diagrams at potentials of 0, 1.23 V, and the overpotential at which OER becomes downward, respectively.

On the pristine (200) surface, Step 2 (OH* to O*) was the rate-limiting step on the Ta8-O5 bridge site, and Step 3 (O* to OOH*) was the rate-limiting step on the two Ta sites (Table 4-1). The lowest overpotential, 0.61 V, was found on the Ta8-O5 bridge site, as illustrated in Figure 4-2 A. Creating oxygen defects increased the ΔG_{step4} on the O7d-, O5d-, and O9d-200-Ta_2O_5 surfaces, making oxygen desorption difficult. Therefore, Step 4 became rate limiting on most sites of oxygen-deficient (200) surface. In contrast, the Ta1 site on the Ta3d-200-Ta_2O_5 surface had the lowest overpotential of 0.63 V (Step 3), outperforming other single Ta sites on both pristine and O/Ta-defected surfaces.

On pristine (120), Step 2 or Step 3 was the rate-limiting step for Ta and Ta-O bridge sites, and the lowest overpotential was found on the Ta1 site (0.68 V, Figure 4-2 B). Oxygen defects in O5d- and O9d-120-Ta_2O_5 surfaces increased the ΔG_{Step4}, deteriorating the OER performance (Table 4-2). An overpotential of 0.76 V was found for the Ta2 site on the Ta6d-120-Ta_2O_5 surface, which compared favorably with respect to the similar site on the pristine (120) facet (1.03 V) and the Ta4d-120-Ta_2O_5 (1.22 V) surfaces.

The pristine (001) surface had the poorest performance (overpotentials above 1.8 V) compared to both (120) and (200) surfaces. On this surface, the conversion of O* to OOH* (step 3) limited the reaction (Table 4-3).

4.3.2. OER performance of 200-Ta_2O_5/graphene heterostructure

In practical applications, a conductive phase is added to insulating electrocatalysts to facilitate electron transport through the electrode [217-219, 230]; hence, we modeled a Ta_2O_5/graphene heterostructure and investigated its OER performance. The (200) surface was considered for this heterostructure, Figure 4-1 D, as it showed the highest OER activity. One Ta site and three Ta-O bridge sites were investigated. The OER performance parameters ($\Delta G_{Steps1-4}$, ΔG of reaction intermediates (OH*, O*, and OOH*)) and overpotential of different sites on 200-Ta_2O_5/graphene heterostructure are summarized in Table 4-4. Figure 4-3 A presents the energy diagrams for Ta6-O7 and Ta6 sites, the best-performing ones with an overpotential of 0.39 and 0.45 V, respectively. The energy diagram of the Ta6 site of 200-Ta_2O_5/graphene and of pristine (200) are further compared in Figure 4-3 B. As indicated in the figure, the overpotential of 1.07 V

on the pristine surface decreased significantly to 0.45 V on the heterostructure. This is similar to our previous study, where adding graphene decreased the OER overpotential of Nb_2C MXene [231].

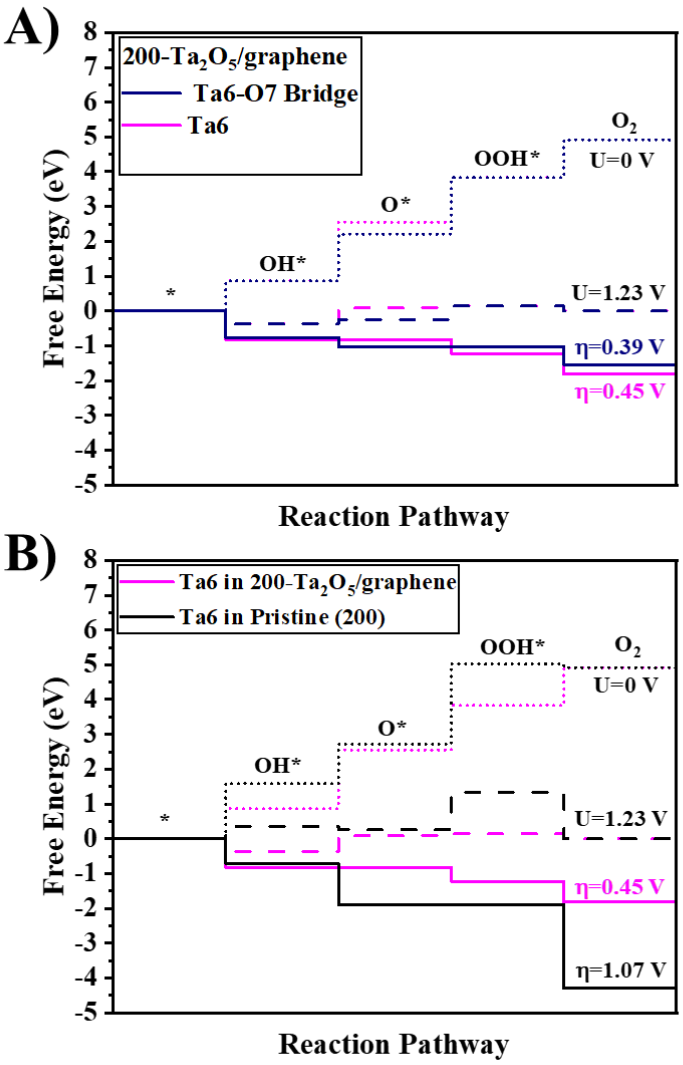

Figure 4-3. A) The reaction pathway Ta6-O7 and Ta6 sites on 200-Ta_2O_5/graphene. B) Comparing the reaction pathway of the Ta6 site on 200-Ta_2O_5/graphene and pristine (200) Ta_2O_5. The dotted, dashed, and straight lines indicate the free energy diagrams at potentials of 0, 1.23 V, and the overpotential at which OER becomes downward, respectively.

The scaling relationship for ΔG_{OOH^*} vs. ΔG_{OH^*} is plotted in Figure 4-4, showing a linear correlation for most sites. According to the figure, some sites, including Ta sites on O-defected (120) and O-defected (200) surfaces, exhibited strong adsorption of intermediates, which

increased the overpotential, as presented in Tables 4-1 and 4-2. In contrast, the intermediates were weakly adsorbed on some sites, such as Ta sites of pristine (120) and pristine (200). Since 200-Ta_2O_5/graphene heterostructure showed the lowest overpotential, it can be stated that it possessed comparatively optimum adsorption ΔG of OOH* and OH*. This figure showed $\Delta G_{OOH^*} = (0.90715\pm0.13051)\Delta G_{OH^*} + (3.29035\pm0.1922)$, which is close to the reports in the literature [51, 232]. The slope of close to 1 indicates the single-bond nature of OOH* and OH* on the surface [233, 234].

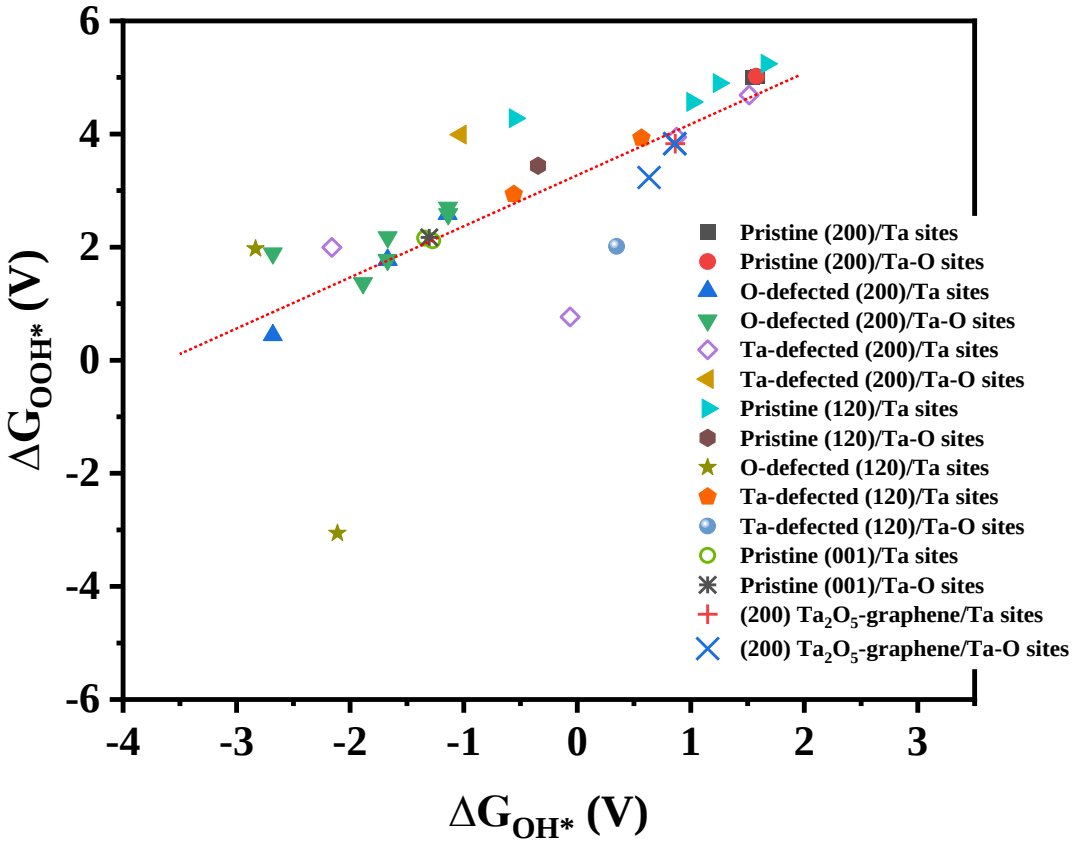

Figure 4-4. Scaling relationships of adsorption ΔG of OOH* vs. OH* for all Ta and Ta-O sites on all facets with or without a defect.

4.3.3. Analysis of Ta_2O_5 facets with or without a defect

This section deciphers the reasons behind the distinct performances of the facets. Since the geometry of different facets can affect the electrocatalytic performance [235], the compactness of each pristine facet was analyzed, as explained in SI. The surface compactness of the (001)

and (200) facets (the topmost atoms) is 0.21 atom/Å^2, and that of the (120) surface is 0.23 atom/Å^2. Moreover, the density of Ta atoms on the layers of the (001), (120), and (200) facets is 0.087, 0.072, and 0.071 Ta atoms/Å^2, respectively. Thus, the trend of OER performance for these surfaces followed the Ta density on the facets: the (001) facet with the highest Ta density shows the highest overpotentials (between 1.8 and 3.5 V, Table 4-3). Instead, on the other facets with lower Ta density, the overpotentials were below 1.1 V for the pristine (200) (Table 4-1) and between 0.68 and 2.0 V for most sites (except one with 2.6 V, Table 4-2) on the pristine (120) facet. This result is similar to RuO_2, where the (111) facet with the lowest active site density had the lowest overpotential of 0.35 V, and the (101) facet with the highest active site density had the highest overpotential of 0.60 V [236].

Figure 4-5 compares the DOS curves of the pristine facets. It shows that the (001) and (200) facets do not have a bandgap, but the former has higher DOS at the Fermi level compared to the latter. Instead, the (120) facet has a band gap, indicating an insulating behavior. The Fermi-level electrons can increase the likelihood of electron transfer to reaction intermediates [237, 238]. In the (200) facet, the DOS at the Fermi level was intermediate between the (001) and (120) facets, which may explain its better OER performance. This balance enables the optimal electronic contribution to the intermediates - neither too high (strongly adsorbing intermediates) nor too low (weakly adsorbing intermediates) - that can facilitate the efficient bonding and electron transfer between the surface and intermediates.

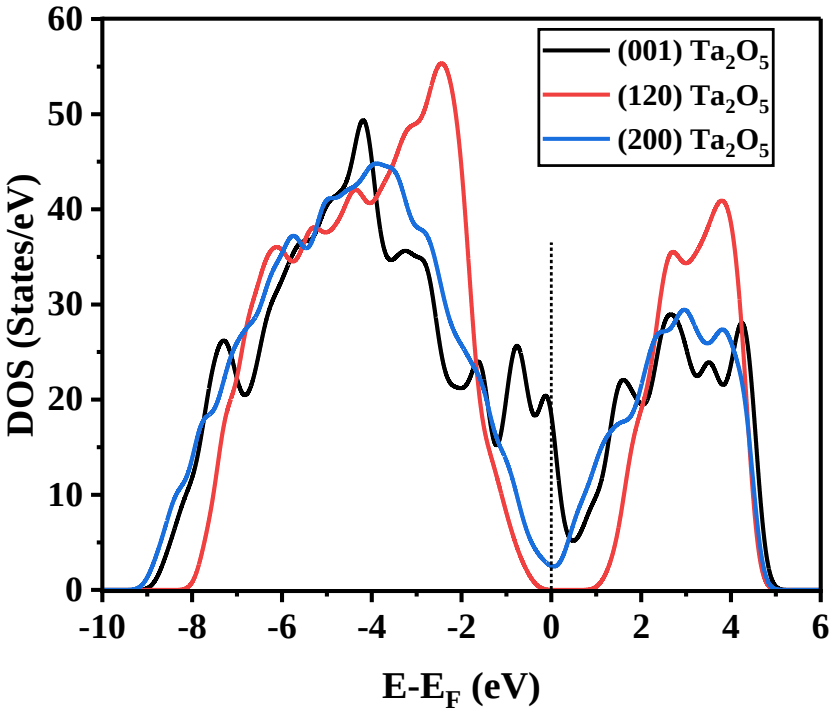

Figure 4-5. Comparing the DOS curves of pristine (001), (120), and (200) surfaces.

The total DOS analysis of (120) surfaces without and with Ta or O defects are compared in Figure 4-11 A. In the pristine (120), the Fermi level is closer to the valence band (VB) edge. In O5d- and O9d-120-Ta_2O_5 surfaces, creating O defects shifted the VB states away from the Fermi level and placed the Fermi level in the conduction band (CB). This shows the formation of the n-type semiconductor. In contrast, creating Ta defects, as in Ta6d- and Ta4d-120-Ta_2O_5, shifted the Fermi level into the VB states, indicating the formation of a p-type semiconductor [239].

The total DOS analysis of the (200) surface with and without defects is shown in Figure 4-12 A. Creating Ta defects on this surface did not introduce a bandgap, keeping its metallic nature. In the (200) surface with the Ta defect, the Fermi level was located inside the VB. However, the O defects created a bandgap and shifted the Fermi level inside the CB, exhibiting n-type semiconductor behavior. This trend was similar to the (120) facet with a Ta or O defect. This is significant because reducing the (200) surface may lead to a decrease in the electrical conductivity.

4.3.4. Analysis of the varied OER performance of different Ta sites

In addition to the electronic and geometrical analysis of the pristine and defective facets, all unique Ta sites were screened individually. To this end, the PDOS curves of (120) and (200) facets were plotted, and the *d* orbitals of each Ta site were compared since they can significantly affect the catalytic activity [240-242]. Then, the PDOS width at the Fermi level, the maximum PDOS width in the valence band (MPWV) and its position [243], maximum PDOS width in the conduction band (MPWC) and its position, valence band maxima (VBM), and conduction band minima (CBM)) of the *d* orbitals were extracted. The schematic representation of parameters derived from *d* orbitals of single Ta sites is shown in Figure 4-14. Moreover, the BC of the Ta sites and the nearest atom, and the sum of valence electrons (SVE) within 2 and 3 Å radii were calculated. Finally, heatmaps for (120) and (200) surfaces are provided in Figures 4-6 and 4-8, respectively, to highlight possible correlations between the OER performance ($\Delta G_{Steps\ 1\text{-}4}$, ΔG_{OH^*}, ΔG_{O^*}, ΔG_{OOH^*}, overpotential) and the properties of each Ta site.

Properties of Ta sites on the (120) Ta_2O_5 surface

The PDOS analysis of d orbitals of the Ta sites on the (120) surface with and without defects is shown in Figure 4-11 B. As expected, the same trends as with the total DOS analysis were found: creating O or Ta defects shifted the Fermi level to inside the CB and VB, respectively. The heatmap in Figure 4-6 shows the interdependence between properties of each Ta site (data derived from *d* orbitals, BC, and SVE within the radii of 2 and 3 Å) with OER performance metrics for this surface, which was calculated using Pearson's correlation coefficient analysis [244]. Notably, heatmaps show the relationship between different parameters, and they cannot be extended to features and data that are not included in our calculations.

Significant correlations were found between the properties of Ta *d* orbitals and OER performance metrics. MPWV showed strong correlations with $\Delta G_{Step\ 2}$, $\Delta G_{Step\ 4}$, ΔG_{O^*}, and ΔG_{OOH^*}, with its position also playing a significant role, as seen in Figures 4-6 and 4-7. The higher the MPWV, the higher the contribution of valence electrons to the reaction, and its position can control the hybridization between reaction intermediates and the active site. An increase in the MPWV could decrease $\Delta G_{Step\ 2}$ and increase $\Delta G_{Step\ 4}$, suggesting that a higher electron presence might hinder the oxygen desorption step. The MPWV position had a correlation of -0.74 with $\Delta G_{Step\ 4}$, indicating that shifting the MPWV closer to the Fermi level can decrease $\Delta G_{Step\ 4}$, thereby facilitating the oxygen desorption step. In addition, MPWV had the strongest correlation (0.88) with overpotential. The heatmap also reveals that MPWC and its

position had moderate correlations with OER performance metrics. Interestingly, $\Delta G_{Step\ 3}$ (O* to OOH*) only correlated with the PDOS width at the Fermi level, 0.73, showing that the increase in Fermi-level electrons can increase $\Delta G_{Step\ 3}$. The role of DOS width at the Fermi level in OER has been observed in the literature [245], where the increase in the DOS at the Fermi level decreased the adsorption energy gap between O* and OOH* [245].

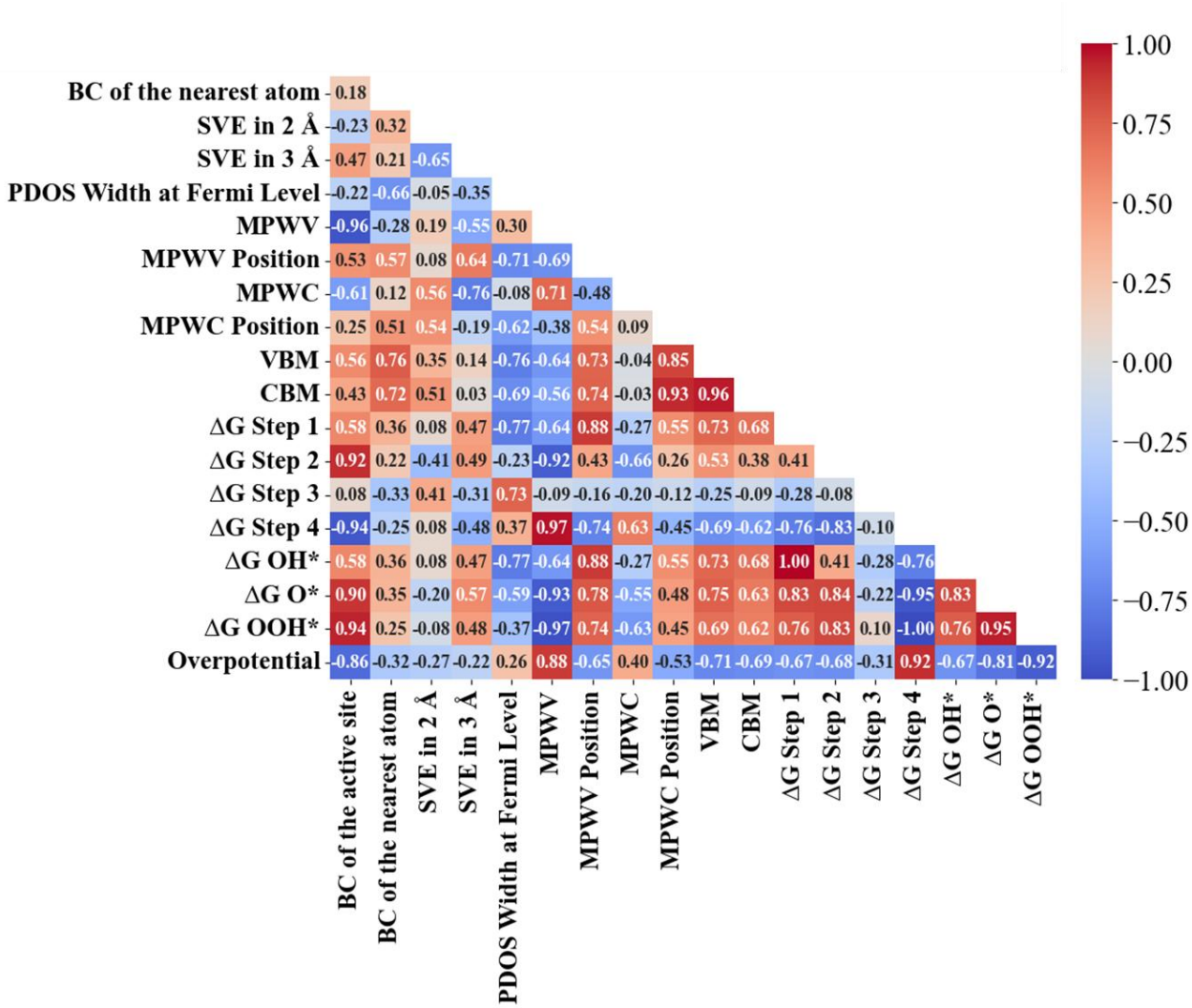

Figure 4-6. Correlations between the OER performance metrics ($\Delta G_{Step1-4}$, ΔG_{OH*}, ΔG_{O*}, ΔG_{OOH*}, and overpotential) and Bader charge (BC) of the active site and its nearest neighboring atom, the sum of valence electrons (SVE) within 2 and 3 Å radii, the PDOS width at Fermi level, the maximum PDOS width in the valence band (MPWV) and its position, maximum PDOS width in the conduction band (MPWC) and its position, the valence band maxima (VBM), and conduction band minima (CBM) for Ta sites on the (120) facet with and without defects.

The BC of Ta sites (Figures 4-6 and 4-7 B) strongly correlated with ΔG_{O^*} and ΔG_{OOH^*}, and with $\Delta G_{Step\ 2}$ and $\Delta G_{Step\ 4}$. Notably, while increasing the BC increased ΔG_{O^*} and $\Delta G_{Step\ 2}$ (OH* to O*), it simultaneously reduced $\Delta G_{Step\ 4}$ (the oxygen desorption step). Therefore, a higher BC does not necessarily enhance OER performance. However, increasing the BC of Ta sites can improve the OER performance for sites where Step 4 is rate-limiting. Moreover, a strong negative correlation of -0.86 was found between the BC of Ta atoms and the OER overpotential, which is in line with the literature showing the strong effect of BC on the OER activity of various materials [246-249]. The negative correlation suggests that a decrease in BC (i.e., lower positive charge on the Ta sites) leads to an increase in overpotential. It should be noted that BC of the nearest O atoms and SVE within 2 and 3 Å radii of Ta sites had no significant effect on the OER performance.

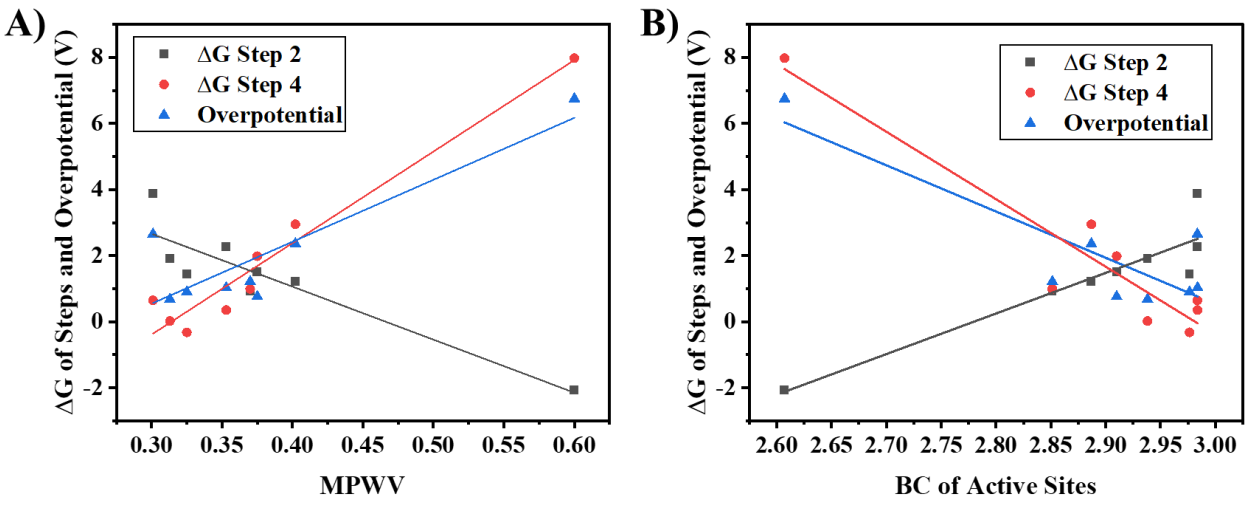

Figure 4-7. The relation between $\Delta G_{Steps2\&4}$ and overpotential and (A) MPWV and (B) BC of eight Ta sites for the (120) surfaces with and without defects.

Properties of Ta sites on the (200) Ta_2O_5 surface

The PDOS analysis of the Ta *d* orbitals of the (200) surface with and without a defect is shown in Figure 4-12 B. Similar to the (120) surfaces with O defects, the Fermi level was in the CB, and the reverse was found for structures having Ta defects. Moreover, as shown in Figure 4-12 B, the *d* orbital of Ta atoms on the pristine (200) facet did not significantly contribute to the PDOS at the Fermi level, where the *p* orbital of oxygen sites dominated.

The correlation heatmap of the (200) surface with and without defects is shown in Figure 4-8. In contrast to 120-Ta_2O_5 surfaces, (200) surfaces did not have strong correlations with the properties of Ta sites. This again indicates a significant facet-dependent behavior of Ta_2O_5 for OER, similar to other materials such as IrO_2 and Co-based electrocatalysts [236, 250, 251].

A moderate correlation was observed between the BC and $\Delta G_{Step\ 2}$ (-0.59) and between the SVE within a 3 Å radius and $\Delta G_{Step1\text{-}4}$, ΔG_{OH*}, and ΔG_{OOH}*. This suggests that the presence of valence electrons at a longer range (3 Å) is more influential in modulating the reaction than at a shorter range (2 Å). Moreover, the PDOS width at the Fermi level had correlations of -0.61 to -0.65 with ΔG_{OH*}, ΔG_{O*}, and ΔG_{OOH*}. This implies that a higher density of electrons at the Fermi level could decrease the ΔG of all intermediates and increase $\Delta G_{Step\ 4}$. Similar results have been found [252], for instance, between the adsorption energy of O_2 and DOS width at the Fermi level for N-doped graphdiyne [253].

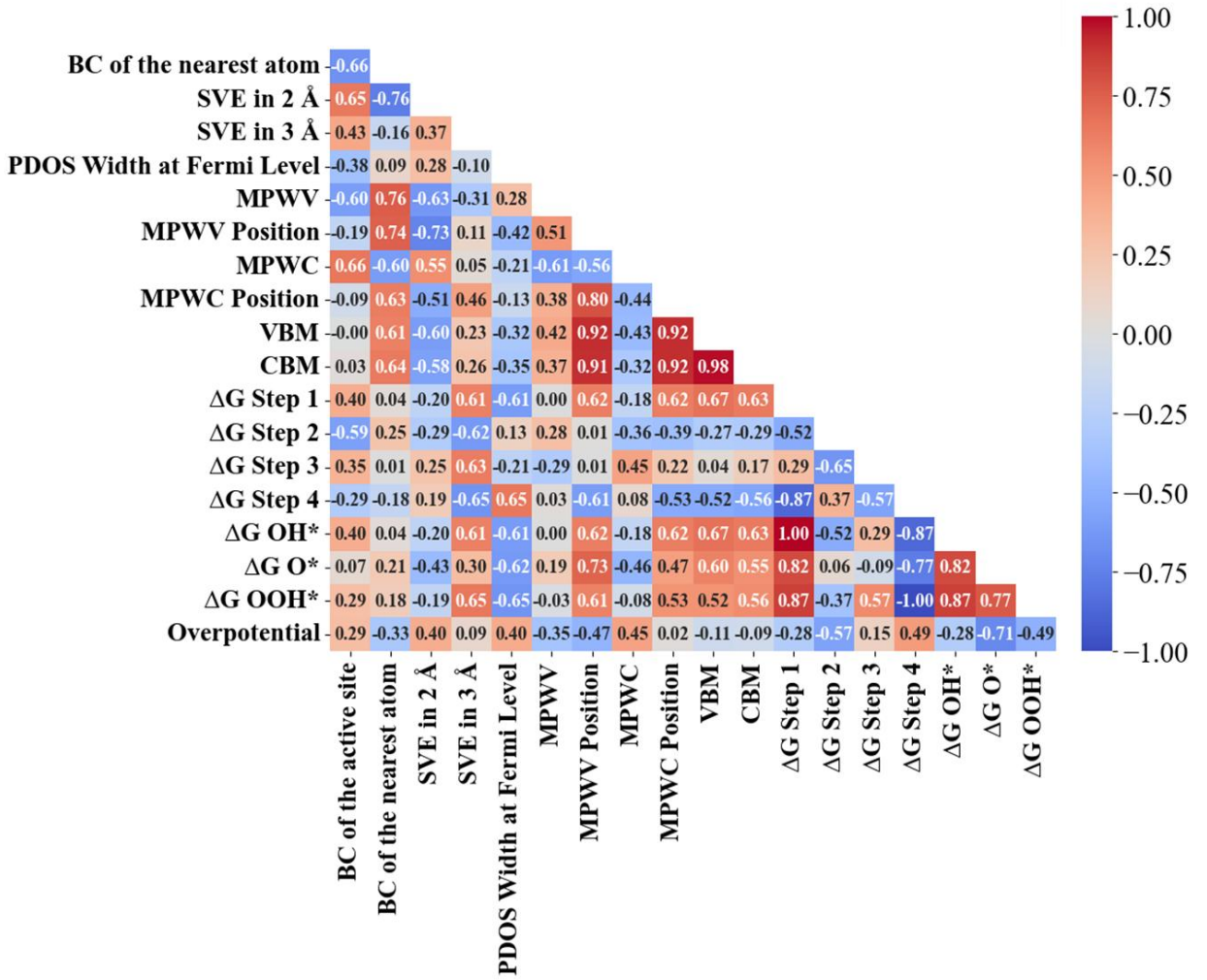

Figure 4-8. Correlations between the OER performance metrics ($\Delta G_{Step1-4}$, ΔG_{OH*}, ΔG_{O*}, ΔG_{OOH}*, and overpotential) and Bader charge (BC) of the active site and its nearest neighboring atom, the sum of valence electrons (SVE) within 2 and 3 Å radii, the PDOS width at Fermi level, the maximum PDOS width in the valence band (MPWV) and its position, maximum PDOS width in the conduction band (MPWC) and its position, the valence band maxima (VBM), and conduction band minima (CBM) for Ta sites on the (200) facet with and without defects.

4.3.5. The 200-Ta_2O_5/graphene heterostructure

Here, the effect of graphene on the electronic properties and OER performance of the (200) Ta_2O_5 facet is discussed. Figure 4-9 A compares the total DOS curves of 200-Ta_2O_5/graphene and (200) Ta_2O_5. The major difference is the higher intensity of the DOS curve in the VB and CB in the 200-Ta_2O_5/graphene structure, which can improve the orbital hybridization level between the surface and reaction intermediates. In addition, the DOS width at the Fermi level was reduced after adding graphene, which indicates the lower capability of the surface in transferring

electrons to intermediates. To analyze this further, we compared the PDOS curve of O and C *p* orbitals and Ta *d* orbitals in the heterostructure and O *p* and Ta *d* orbitals in (200) Ta_2O_5, as shown in Figure 4-9 B. Regarding the O *p* orbitals, the PDOS intensity in the VB and CB was increased after adding graphene. However, the O *p* orbitals of the (200) surface contributed more at the Fermi level compared to that of the 200-Ta_2O_5/graphene heterostructure. The PDOS intensity of Ta *d* orbitals in the VB and CB for the 200-Ta_2O_5/graphene was higher than that of the pristine (200) surface. This leads to higher valence electron contribution of Ta sites of 200-Ta_2O_5/graphene during the reaction (stronger hybridization), which might explain the better performance of Ta sites after adding graphene. In addition, the C *p* orbitals in the heterostructure overlapped with Ta d orbitals in the VB in the range of -8 to -4 eV.

Figure 4-9 C compares the PDOS curves of *d* orbitals of the Ta6 site over 200-Ta_2O_5/graphene and pristine (200). The MPWV and MPWC in the 200-Ta_2O_5/graphene were higher, and their position shifted toward lower energies. As a result, the Ta6 sites over pristine (200) and 200-Ta_2O_5/graphene surfaces had overpotentials of 0.91 and 0.46 V, respectively, where the rate-limiting step was Steps 3 and 2. This can be attributed to the higher PDOS intensity of the *d* orbital in the VB after adding graphene, which increased $\Delta G_{step\ 4}$ from -0.08 to 1.09 V and decreased $\Delta G_{step\ 3}$ from 2.14 to 1.28 V. Based on the results, it is clear that the changes in the intensity of *d* orbitals of Ta sites in heterostructure lead to significant differences in performances. Notably, an oxygen atom was close to Ta8 on the 200-Ta_2O_5/graphene surface, so we could not evaluate a single Ta8 site since the adsorbates were interacting with both Ta and O in this case.

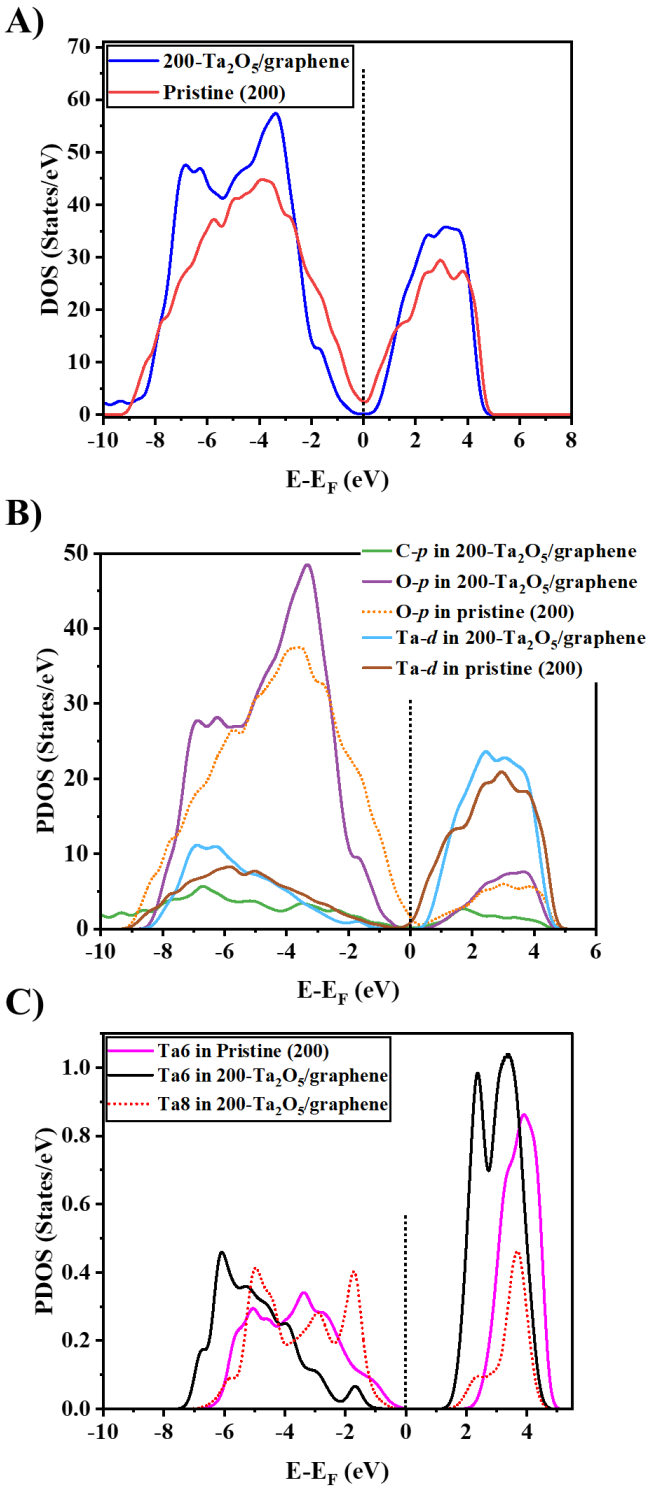

Figure 4-9. A) Comparing the DOS of 200-Ta_2O_5/graphene and pristine (200) Ta_2O_5. B) Comparing the PDOS analysis of C and O *p* orbitals and Ta *d* orbital of 200-Ta_2O_5/graphene and pristine (200) Ta_2O_5, respectively. C) PDOS analysis of the *d* orbital of the Ta6 site on 200-

Ta_2O_5/graphene and pristine (200) Ta_2O_5. D) PDOS analysis of *p* and *d* orbitals of active O and Ta sites on 200-Ta_2O_5/graphene.

4.4. Conclusion

In this work, DFT calculations were performed on the (200), (120), and (001) surfaces of Ta_2O_5 and on the 200-Ta_2O_5/graphene heterostructure to identify strategies to enhance the OER performance of Ta_2O_5. New insights into the OER activity of Ta sites on pristine facets were established. The (200) facet, with the lowest Ta site density and moderate DOS at the Fermi level, showed the lowest overpotential compared to the (120) and (001) facets. Creating Ta defects could decrease the overpotential of a Ta site on the (200) and (120) facets. However, creating O defects created a bandgap in the (200) facet and increased the overpotential on (200) and (120) facets. Correlation heatmaps were established between properties of each Ta site on the (200) and (120) facets and the OER performance metrics. On the second best-performing facet, the (120), the Bader charge and *d* orbitals of Ta sites at the VB significantly modulated the performance, correlating strongly with the Gibbs free energy (ΔG) of steps 1, 2, and 4. However, on the (200) facet, only SVE within 3 Å and PDOS width at the Fermi level exhibited moderate correlations. The 200-Ta_2O_5/graphene heterostructure showed a substantially low overpotential of 0.39 V on a Ta-O site. The PDOS analysis showed that the improved OER performance of the heterostructure was due to the shift of the *d* orbitals of Ta sites toward lower energies and the increase in the DOS intensity after adding graphene. Overall, the best strategies to unlock the potential of Ta oxide in OER is to synthesize a heterostructure formed by (200) Ta_2O_5 and graphene, prevent the formation of the (001) facet, and/or create Ta defects in Ta_2O_5 nanoparticles or thin films. If validated in experiments, these results would conduce to Ta_2O_5-based materials as promising non-precious OER electrocatalysts under acidic media.

4.5. Supplementary materials

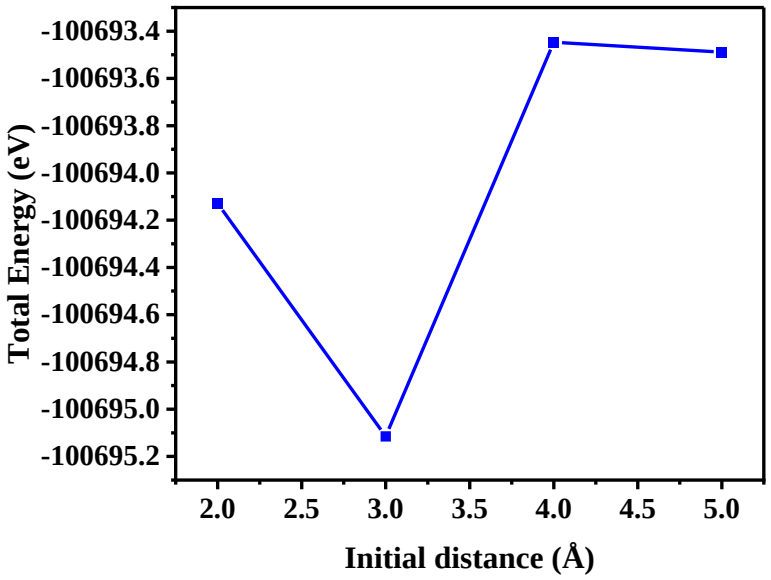

Figure 4-10. The effect of the initial distance between (200) Ta_2O_5 and graphene on the total energy of the 200-Ta_2O_5/graphene heterostructure.

Atomic density and Ta site density calculations

To calculate the topmost atomic density of the (001), (200), and (120) facets, the total number of their topmost atoms was counted (from the top-view images in Figure 4-1). Then, the lattice area normal to the Z-direction was calculated, and the atomic density was calculated according to the following equation (in atoms/Å^2):

$$\text{Atomic density} = \frac{Total\ number\ of\ atoms}{Lattice\ area} \qquad \text{Equation 4-14}$$

Moreover, to calculate the density of Ta atoms on the surface, instead of the total number of atoms, only the number of Ta atoms on the topmost layer was considered, and the same equation was used.

Table 4-1. The OER performance parameters ($\Delta G_{Steps1\text{-}4}$, adsorption ΔG of reaction intermediates (OH*, O*, and OOH*), and overpotential) of different sites on (200) Ta_2O_5 surfaces with/without Ta or O defects. The rate-limiting steps are underlined.

Surface	Site	Bader Charge	$\Delta G_{Step\ 1}$ (V)	$\Delta G_{Step\ 2}$ (V)	$\Delta G_{Step\ 3}$ (V)	$\Delta G_{Step\ 4}$ (V)	ΔG_{OH^*} (V)	ΔG_{O^*} (V)	ΔG_{OOH^*} (V)	η (V)
200-Ta_2O_5	Ta8-O5	*	1.577	<u>1.840</u>	1.605	-0.102	1.577	3.417	5.022	**0.610**
200-Ta_2O_5	Ta8	2.952	1.583	1.135	<u>2.305</u>	-0.103	1.583	2.718	5.023	1.075
200-Ta_2O_5	Ta6	2.860	1.547	1.315	<u>2.135</u>	-0.078	1.547	2.863	4.998	0.905
O5d-200-Ta_2O_5	Ta8-Ta3	*	-1.886	0.131	3.120	<u>3.555</u>	-1.886	-1.755	1.365	2.325
O5d-200-Ta_2O_5	Ta8-O7	*	-2.681	0.925	<u>3.647</u>	3.029	-2.681	-1.756	1.891	2.417
O5d-200-Ta_2O_5	Ta8	2.839	-2.680	1.051	2.070	<u>4.478</u>	-2.680	-1.628	0.442	3.248
O7d-200-Ta_2O_5	Ta6-Ta8	*	-1.671	1.518	1.928	<u>3.145</u>	-1.671	-0.152	1.775	1.915
O7d-200-Ta_2O_5	Ta8-O5	*	-1.669	1.518	2.326	<u>2.745</u>	-1.669	-0.151	2.175	1.515
O7d-200-Ta_2O_5	Ta8	2.912	-1.671	1.519	1.925	<u>3.147</u>	-1.671	-0.152	1.773	1.917
O7d-200-Ta_2O_5	Ta6	2.885	-1.669	1.510	1.930	<u>3.149</u>	-1.669	-0.158	1.771	1.919
O9d-200-Ta_2O_5	Ta6-O4	*	-1.136	1.521	2.199	<u>2.336</u>	-1.136	0.385	2.584	1.106
O9d-200-Ta_2O_5	Ta8-O9	*	-1.138	<u>4.373</u>	-0.539	2.223	-1.138	3.235	2.697	3.143
O9d-200-Ta_2O_5	Ta6	2.920	-1.141	1.535	2.191	<u>2.335</u>	-1.141	0.394	2.585	1.105
Ta1d-200-Ta_2O_5	Ta6	2.835	-2.162	2.202	1.956	<u>2.924</u>	-2.162	0.040	1.996	1.694
Ta1d-200-Ta_2O_5	Ta8	2.973	1.515	-1.437	<u>4.612</u>	0.230	1.515	0.078	4.690	3.382
Ta3d-200-Ta_2O_5	Ta8-O7	*	-1.026	<u>4.690</u>	0.325	0.931	-1.026	3.664	3.989	3.460
Ta3d-200-Ta_2O_5	Ta1	2.819	0.876	1.205	<u>1.864</u>	0.975	0.876	2.081	3.945	**0.634**
Ta3d-200-Ta_2O_5	Ta6	2.917	-0.063	0.927	-0.097	<u>4.153</u>	-0.063	0.864	0.767	2.923

Table 4-2. The OER performance parameters ($\Delta G_{Steps1-4}$, adsorption ΔG of reaction intermediates (OH*, O*, and OOH*), and overpotential) of different sites on (120) Ta_2O_5 surfaces with/without Ta or O defects. The rate-limiting steps are underlined.

Surface name	Site	Bader Charge	$\Delta G_{Step\ 1}$ (V)	$\Delta G_{Step\ 2}$ (V)	$\Delta G_{Step\ 3}$ (V)	$\Delta G_{Step\ 4}$ (V)	ΔG_{OH^*} (V)	ΔG_{O^*} (V)	ΔG_{OOH^*} (V)	η (V)
120-Ta_2O_5	Ta2-O3	*	-0.344	<u>3.287</u>	0.495	1.482	-0.344	2.943	3.438	2.057

120-Ta_2O_5	Ta2	2.984	1.013	2.261	1.293	0.353	1.013	3.274	4.567	1.031
120-Ta_2O_5	Ta4	2.983	-0.550	3.881	0.946	0.643	-0.550	3.331	4.277	2.651
120-Ta_2O_5	Ta6	2.976	1.669	1.443	2.131	-0.323	1.669	3.112	5.243	0.901
120-Ta_2O_5	Ta1	2.938	1.246	1.907	1.748	0.019	1.246	3.153	4.901	**0.677**
O5d-120-Ta_2O_5	Ta4	2.887	-2.833	1.213	3.592	2.949	-2.833	-1.621	1.971	2.362
O9d-120-Ta_2O_5	Ta4	2.607	-2.111	-2.066	1.118	7.979	-2.111	-4.177	-3.059	6.749
Ta4d-120-Ta_2O_5	Ta2	2.851	0.566	0.918	2.446	0.989	0.566	1.484	3.931	1.216
Ta6d-120-Ta_2O_5	Ta4-O5	*	0.348	-0.386	2.052	2.906	0.348	-0.038	2.014	1.676
Ta6d-120-Ta_2O_5	Ta2	2.910	-0.558	1.502	1.993	1.983	-0.558	0.944	2.937	0.763

Table 4-3. The OER performance parameters ($\Delta G_{Steps1-4}$, adsorption ΔG of reaction intermediates (OH*, O*, and OOH*), and overpotential) of different sites on (001) Ta_2O_5 surfaces. The rate-limiting steps are underlined.

Surface name	Site	Bader Charge	$\Delta G_{Step\ 1}$ (V)	$\Delta G_{Step\ 2}$ (V)	$\Delta G_{Step\ 3}$ (V)	$\Delta G_{Step\ 4}$ (V)	ΔG_{OH*} (V)	ΔG_{O*} (V)	ΔG_{OOH*} (V)	η (V)
001-Ta_2O_5	Ta6-O7	*	-1.304	-1.152	4.629	2.747	-1.304	-2.456	2.173	3.399
001-Ta_2O_5	Ta4	2.090	-1.342	0.183	3.320	2.760	-1.342	-1.159	2.160	2.090
001-Ta_2O_5	Ta6	2.647	-1.273	0.298	3.086	2.809	-1.273	-0.975	2.111	1.856

Table 4-4. The OER performance parameters ($\Delta G_{Steps1-4}$, adsorption ΔG of reaction intermediates (OH*, O*, and OOH*), and overpotential) of different sites on 200-Ta_2O_5/graphene heterostructure. The rate-limiting steps are underlined.

Surface name	Site	Bader Charge	$\Delta G_{Step\ 1}$ (V)	$\Delta G_{Step\ 2}$ (V)	$\Delta G_{Step\ 3}$ (V)	$\Delta G_{Step\ 4}$ (V)	ΔG_{OH*} (V)	ΔG_{O*} (V)	ΔG_{OOH*} (V)	η (V)
200-Ta_2O_5/graphene	Ta8-O9	*	0.633	2.135	0.465	1.687	0.633	2.768	3.233	0.905
200-Ta_2O_5/graphene	Ta6-O7	*	0.859	1.352	1.617	1.092	0.859	2.211	3.828	**0.387**
200-Ta_2O_5/graphene	Ta6-O4	*	0.860	2.915	0.054	1.092	0.860	3.775	3.828	1.685

200-Ta_2O_5/graphene	Ta6	2.904	0.863	1.685	1.283	1.089	0.863	2.548	3.831	**0.455**

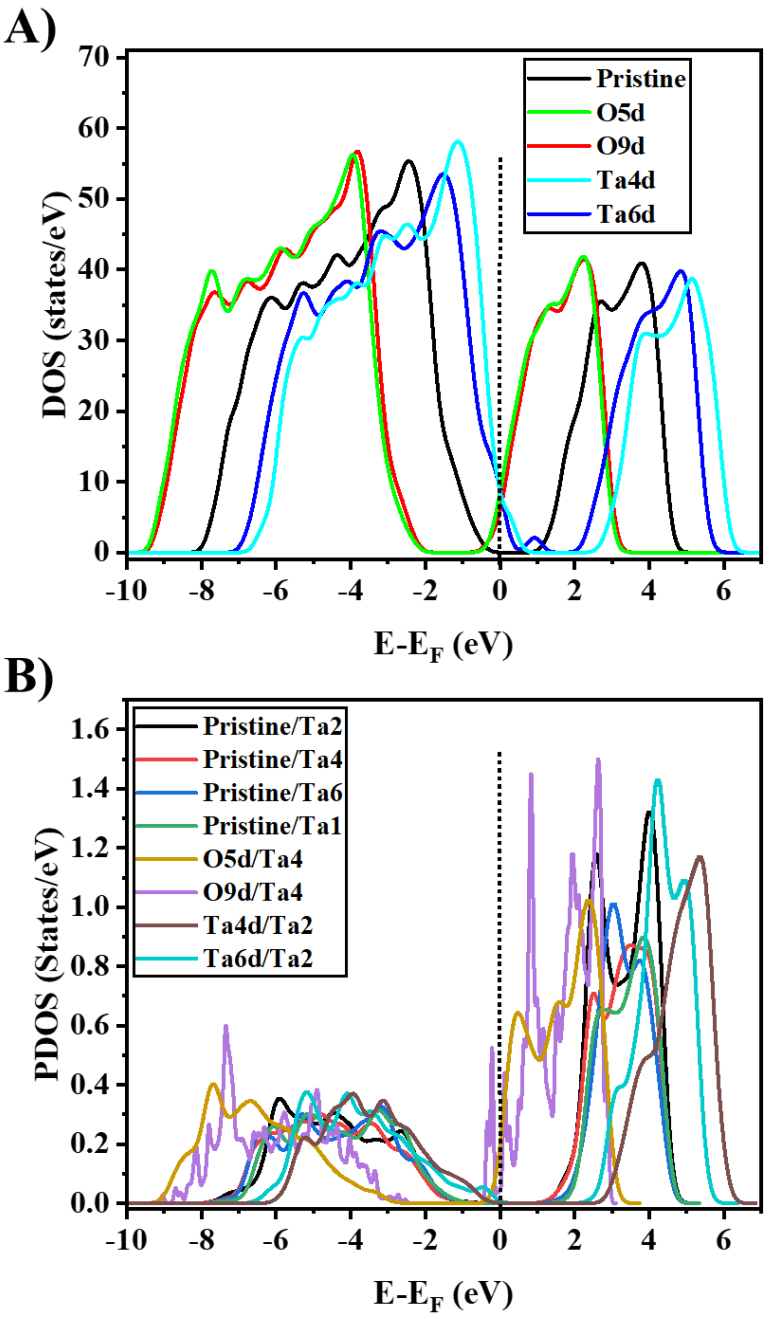

Figure 4-11. (A) The DOS curve of the (120) Ta_2O_5 surface and (B) PDOS analysis of single d orbitals of active Ta sites on the (120) Ta_2O_5 with/without Ta or O defects.

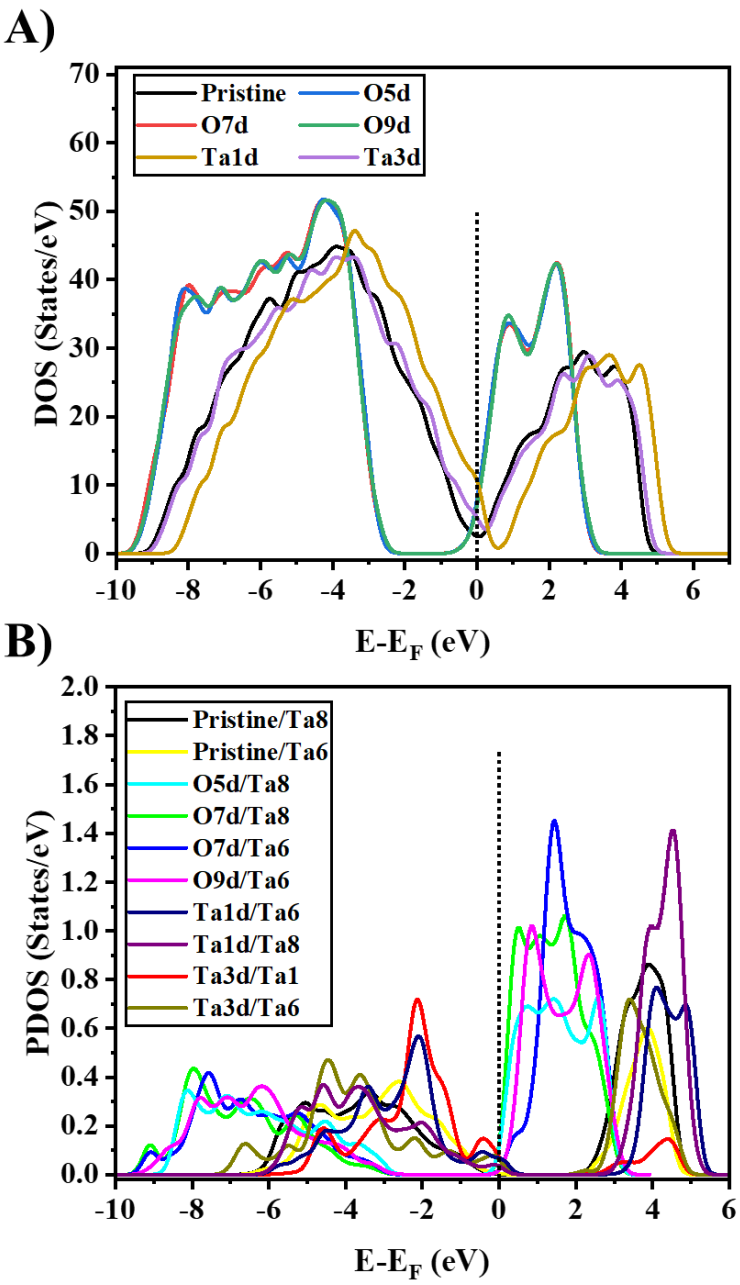

Figure 4-12. (A) The DOS curve of the (200) Ta_2O_5 surface and (B) PDOS analysis of single d orbitals of active Ta sites on the (200) Ta_2O_5 with/without Ta or O defects.

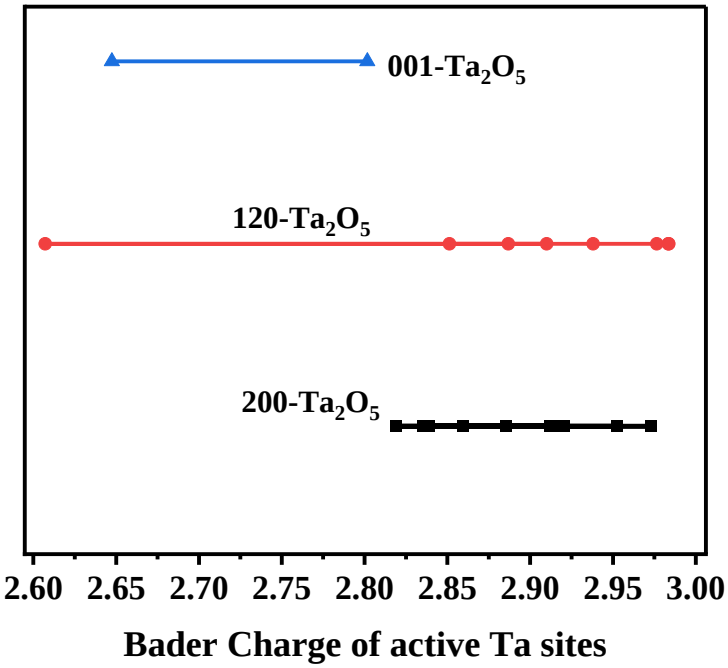

Figure 4-13. The Bader charge range of all Ta sites investigated for OER on the (200) and (120) Ta_2O_5 with and without defects and the pristine (001) Ta_2O_5 surface.

Figure 4-13 shows the range of Bader charge values for active Ta sites on (200) and (120) Ta_2O_5 with and without defects and (001) Ta_2O_5. A positive BC indicates electron loss, while a negative BC signifies electron gain, qualitatively reflecting the atom's oxidation state.

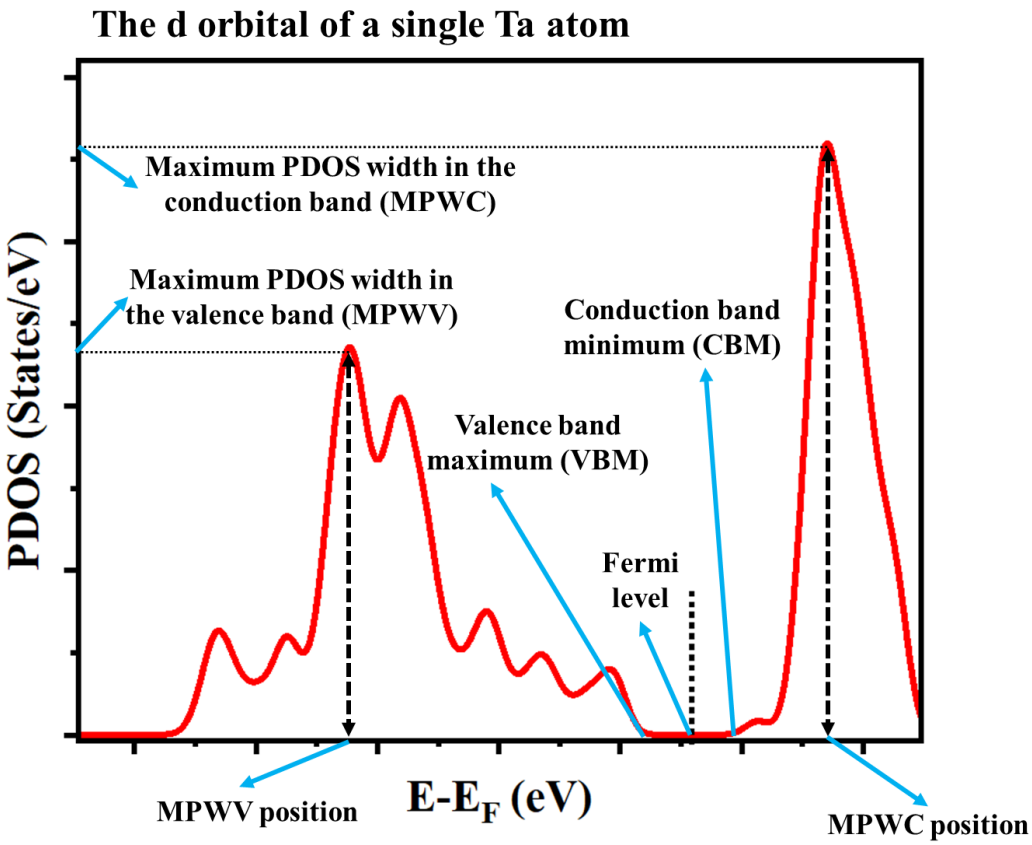

Figure 4-14. The schematic representation of PDOS. The arrows show the maximum width in the valence band (MPWV) and its position, maximum PDOS width in the conduction band (MPWC) and its position, valence band maximum (VBM), and conduction band minimum (CBM) for single d orbitals of active sites.

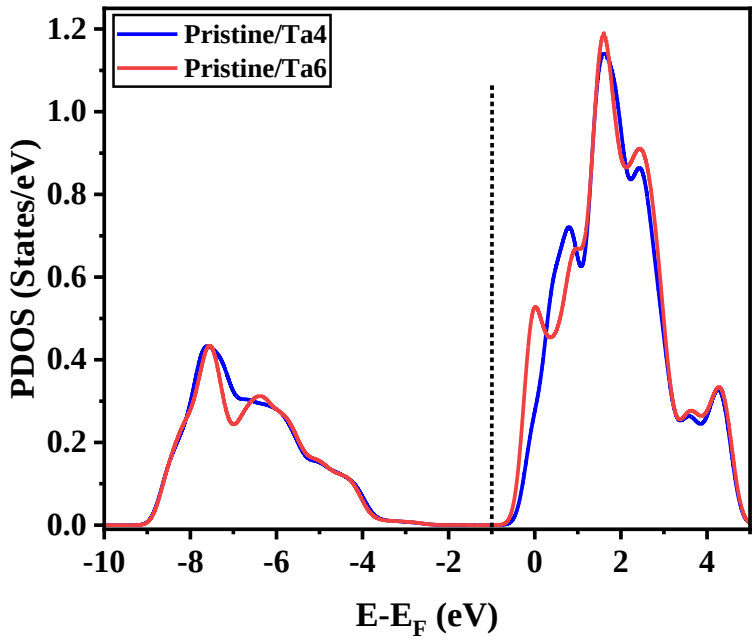

Figure 4-15. The PDOS analysis of single d orbitals of Ta4 and Ta6 atoms on the (001) Ta_2O_5 surface.

As discussed earlier, the total DOS of the (001) Ta_2O_5 surface in Figure 4-4 showed no bandgap, pointing to its conductive nature. However, the PDOS analysis of *d* orbitals of Ta4 and Ta6 atoms on this surface, illustrated in Figure 4-15, reveals that they do not contribute to the DOS around the Fermi level. The higher overpotential of Ta sites on the (100) Ta_2O_5 compared to compared to (120) Ta_2O_5 and (200) Ta_2O_5 can be attributed to the less positive Bader charges of Ta sites (lower oxidation state), Figure 4-13, and higher Ta density on the surface.

5 Density Functional Theory (DFT) insights into the oxygen evolution reaction (OER) activity of sodium tantalate

5.1. Introduction

In this chapter, sodium tantalates, which are among the Ta-based materials, were investigated for oxygen evolution reaction (OER). This is due to the successful application of sodium tantalates as oxygen reduction reaction (ORR) electrocatalysts [254, 255]. For instance, Sebastián et al. prepared $Na_2Ta_8O_{x-21}$-supported graphene through the precipitation of tantalum oxide on graphene and thermal treatment. This sodium tantalate-containing electrocatalyst with oxygen vacancies showed promising activity for ORR under acidic media and stability against methanol poisoning [254]. According to the literature, the existing sodium tantalate structures include $NaTaO_3$ [256], $Na_2Ta_4O_{11}$ [256], $Na_2Ta_8O_{21}$ [255], and $NaTa_3O_8$ [257]. Among them, the unit cells of $Na_2Ta_4O_{11}$ (102 atoms) and $NaTa_7O_{19}$ (108 atoms) are quite large, due to which we did not perform the density functional theory (DFT) calculations to analyze their performance.

$NaTaO_3$ has a large bandgap of around 4.0 eV [51] and has been widely studied for photocatalysis. The research on $NaTaO_3$ has mainly focused on bandgap engineering and improving the catalytic properties using dopants such as Bi [258], N [259], S, C, P [260], etc. For instance, using DFT calculations, Tang et al. showed that doping $NaTaO_3$ with Sr improves its OER performance. When a high concentration of Sr was doped into $NaTaO_3$, an overpotential of 0.55 V was observed [261]. Cai et al. studied the effect of adsorbing single-metal atoms (M = Fe, Co, Ni, Cu, Ru, Rh, Pd, Ag, Ir, Pt, and Au) on the electronic properties and catalytic performance of $NaTaO_3$ [262]. They showed that adsorbing Co could decrease the OER overpotential to 0.68 V [262]. In contrast to $NaTaO_3$, the $NaTa_3O_8$ structure has been rarely studied since its synthesis is challenging [257]. Thus, our study mostly focused on $NaTa_3O_8$ as a new material for surface chemistry applications. We also conducted calculations for $NaTaO_3$ for comparison.

5.2. Computational Details

In DFT calculations, a vacuum greater than 15 Å was used to prevent the interactions between periodic images. The Perdew–Burke–Ernzerhof (PBE) exchange-correlation functional in the generalized gradient approximation (GGA) was used to perform spin-polarized DFT calculations. All the DFT calculations were done using the Quantum Espresso software [120]. Furthermore, the DFT-D3 correction method in Grimme's scheme [225, 226] was employed to

better describe the long-range van der Waals (vdW) interactions between the surface and reaction intermediates. For wavefunctions and charge density, the kinetic energy cut-off values of 35 and 350 Ry were used, respectively. The energy threshold was set to 10^{-4} Ry for the self-consistent field convergence. To relax each system, davidson iterative diagonalization was utilized (without variable size) until reaching the residual Hellman–Feynman force magnitude of below the 10^{-3} Ry $Bohr^{-1}$ on each atom. To reach more accurate electronic properties, the DFT+ U was performed in accordance with the literature on $NaTaO_3$ for surface chemistry applications [264]. The U value was taken from the Materials Project database [227, 228]. The k-point sampling of 2 ×2×1 was employed to relax each system. The k-point samplings of 6×6×1 and 8×8×1 were considered for the self-consistent field (SCF) and non-self-consistent field (nSCF) calculations, respectively, to calculate the density of states (DOS) and partial DOS (PDOS). To assess the electron density of each atom, the Bader charge analysis was performed [123]. After relaxing the structure and lattice, the lattice parameters of the $NaTaO_3$ and $NaTa_3O_8$ unit cells were a= 5.501 Å, b= 5.558 Å, and c= 7.829 Å and a= 7.286 Å, b= 7.286 Å, and c= 7.286 Å, respectively. In this study, three facets of $NaTa_3O_8$ and two facets of $NaTaO_3$ were analyzed. Based on X-ray diffraction (XRD) analysis in the literature [263], (020), (101), and (001) facets of $NaTaO_3$ were chosen. However, the (001) facet could not be stabilized via DFT calculations because the calculation for relaxing the structure could not be converged. Similar DFT parameters were used to relax all facets. For the $NaTa_3O_8$ structure, no experimental data were available. So, the simulated XRD pattern of $NaTa_3O_8$ was considered and generated using the crystallographic information file (CIF) with Vesta software. In the simulated XRD pattern, the (220), (022), (121), and (202) had the highest diffraction intensity. Among them, the (121) facet could not be stabilized via DFT calculations because the calculation for relaxing the structure could not be converged, and the other three facets were considered. The facets of $NaTaO_3$ and $NaTa_3O_8$ that could be converged using the parameters mentioned above and their unique Ta sites and Na site are shown in Figures 5-1 and 5-2, respectively.

The theoretical overpotential (η) was calculated using the computational hydrogen electrode (CHE) theory [51], as explained in Section 3-2, Equations 3-7 to 3-16.

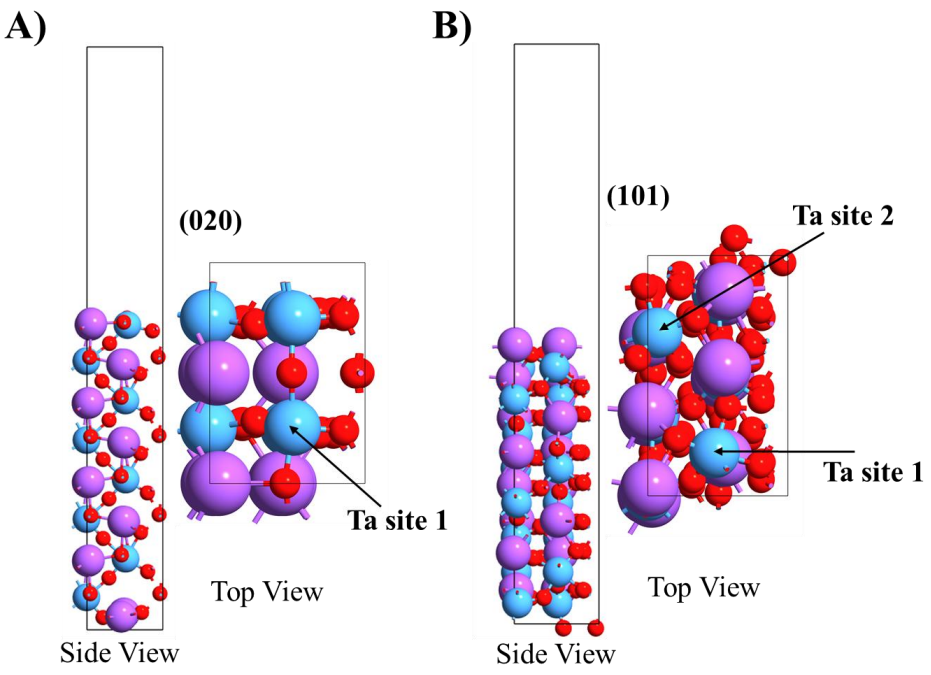

Figure 5-1. The models of A) (020) and B) (101) $NaTaO_3$ with Ta sites investigated for OER activity assessment.

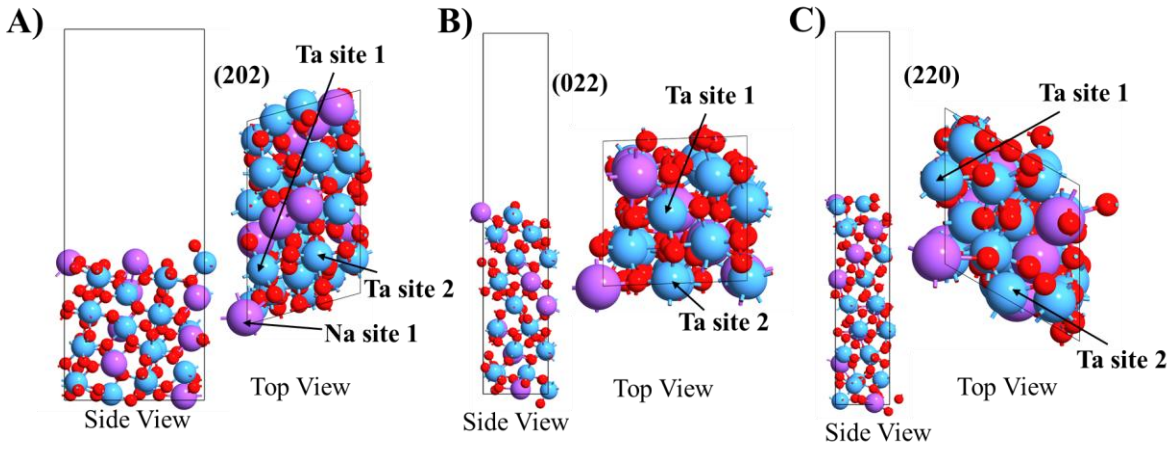

Figure -5-2. The models of A) (202), B) (022), and C) (220) $NaTa_3O_8$ with Ta sites and Na site investigated for OER activity assessment.

5.3. Electronic properties

Figure 5-3 A and B shows the total DOS curves of different facets of $NaTa_3O_8$ and $NaTaO_3$, respectively. It can be observed that the electronic properties of both structures are strongly dependent on the facet.

As shown in Figure 5-3 A, the (022) and (220) facets of $NaTa_3O_8$ had a metallic behavior with no apparent bandgap at the Fermi level, showing the presence of delocalized states for charge transfer. In contrast, the 1.72 eV bandgap of the (202) facet shows its semiconducting behavior. The higher DOS of the (022) and (220) facets at the Fermi level compared to the (202) facet suggests a strong interaction with OER intermediates. Moreover, the DOS of the (202) facet in the valence band is more than the other two facets, showing stronger localization of electronic states.

As shown in Figure 5-3 B, the (020) facet of $NaTaO_3$ did not show a band gap via the DFT+U technique. However, since there is no experimental evidence confirming whether this surface is metallic or semiconducting, we cannot determine if this result is a DFT artifact or if the (020) facet is intrinsically metallic. Moreover, in the (020) facet, delocalized states span across the Fermi level, which will be available for charge transfer. In contrast, the (101) showed a semiconducting behavior with higher DOS in the valence band. This shows the stronger presence of localized states in this (101) facet. The bandgap of the (101) is around 1.03 eV. The bandgap values obtained here are specific to the facets and are different from those reported in the experiments for the bulk material.

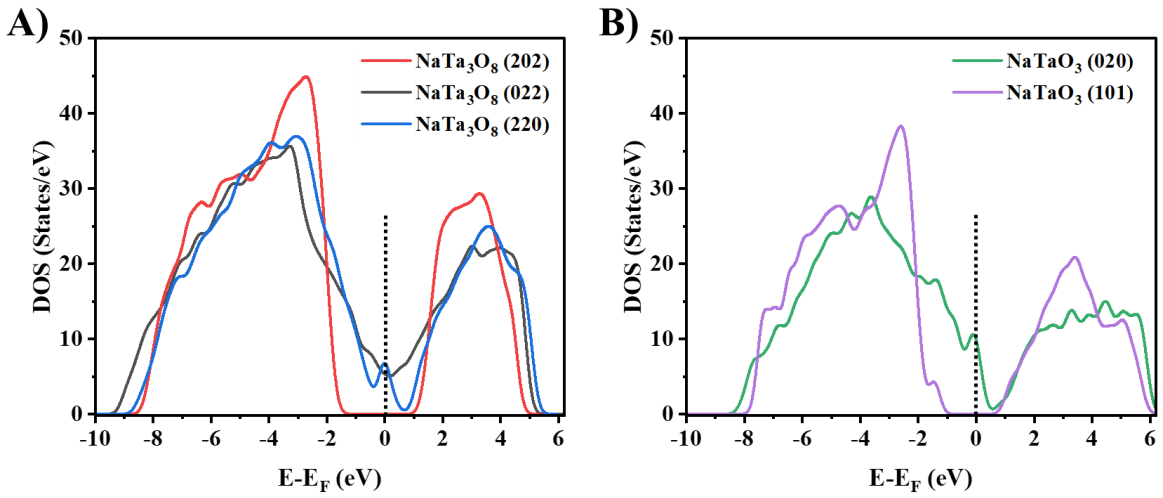

Figure 5-3. The DOS curves of different facets of A) $NaTa_3O_8$ and B) $NaTaO_3$.

The PDOS curves of $NaTaO_3$ facets in Figure 5-4 show that the Na p orbitals did not contribute to the total DOS. This suggests that Na atoms did not have significant effects on the electronic properties of $NaTaO_3$. In the (020) facet, O p orbitals had higher contributions to the valence

band with a strong hybridization with Ta d orbitals at the Fermi level. For the (101) facet, again, O p orbitals had stronger contributions in the valence band compared to Ta d orbitals.

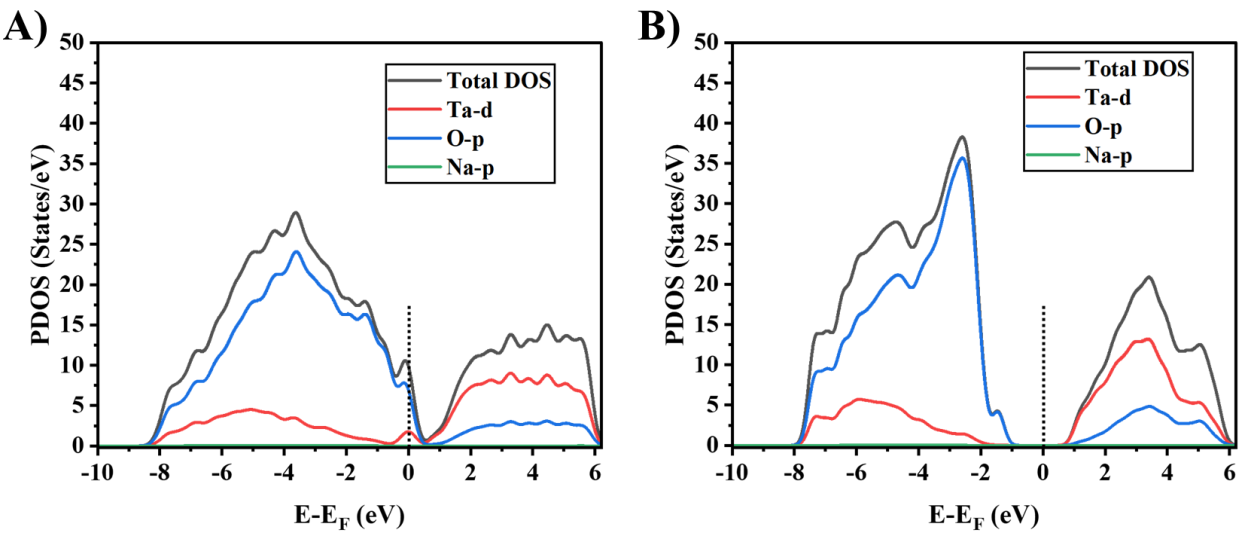

Figure 5-4. PDOS curves of A) (020) and B) (101) $NaTaO_3$.

In the PDOS curves of $NaTa_3O_8$, Na p orbitals did not contribute to the valence and conduction bands. This suggests that in both $NaTa_3O_8$ and $NaTaO_3$, sodium atoms mainly modulated the bonds between Ta and O, which in turn affected the Ta density on the topmost layer and compactness of the facets, affecting the electronic and catalytic properties of sodium tantalates. This can be an important conclusion regarding electrocatalysis, in a way that using different ions such as Na, K, Mg, etc., can affect the properties of Ta-based materials differently.

The O p orbitals in the (202) facet of $NaTa_3O_8$ (Figure 5-5 A) had higher contributions to the valence band compared to Ta d orbitals. Moreover, around the valence band edge, there was no contribution from Ta d orbitals. Ta d orbitals dominated in the conduction band, showing their possible dominance in the excited states.

Also, in the (220) and (022) facets of $NaTa_3O_8$ (Figure 5-5 B and C), O p orbitals dominated the valence band. However, in these facets, Ta d orbitals had states at the Fermi level. This suggests the stronger electronic contribution of Ta d orbitals to reaction intermediates, which might lead to strong adsorption of intermediates and harder desorption of produced O_2 in OER. Moreover, a strong overlapping between Ta d and O p orbitals was observed in the (220) facet, which might improve its structural stability due to stronger binding between Ta and O [254].

The PDOS curves of $NaTaO_3$ and $NaTa_3O_8$ also show that the Ta d orbitals, which could be the active sites for OER, strongly depend on the facet. Figure 5-6 compares the Ta d orbitals of different facets of $NaTa_3O_8$. This implies that the facet of sodium tantalate can determine the interaction of Ta d orbitals and OER intermediates, which is important to reach a balanced adsorption affinity.

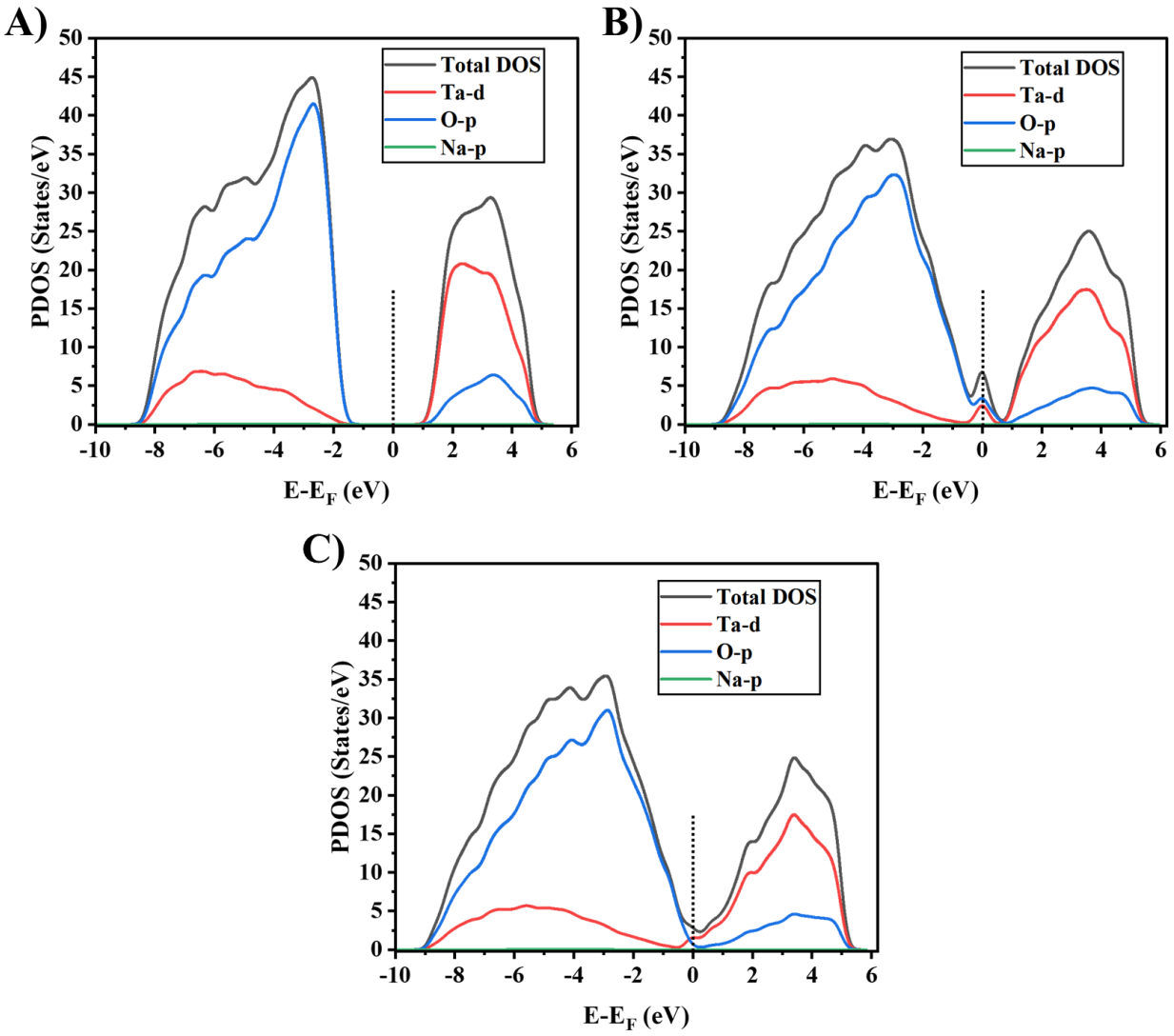

Figure 5-5. PDOS curves of A) (202), B) (220), and C) (022) $NaTa_3O_8$.

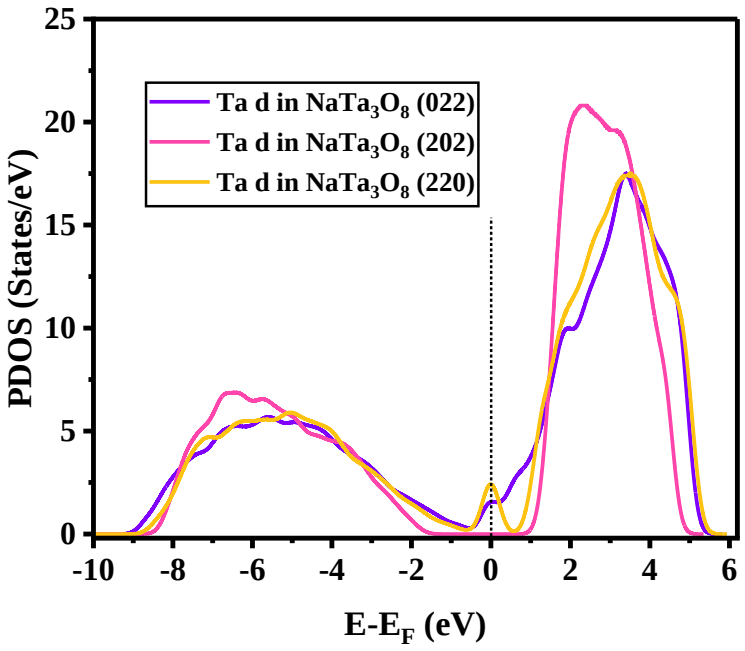

Figure 5-6. Comparing Ta d orbitals in different facets of $NaTa_3O_8$.

5.4. Surface compactness

The geometry of facets can affect their electrocatalytic properties, as reported in the literature [235] and found in the results of Chapter 4 of this thesis. In Chapter 4, we found that the facet with the lowest Ta density on the topmost layer (i.e., (200) Ta_2O_5) had the lowest overpotential. Among $NaTa_3O_8$ facets analyzed, the highest Ta density on the topmost layer was found for $NaTa_3O_8$ (202) (0.0565 Ta atoms/Å^2), followed by (220) and (022) facets, as presented in Table 5-1. In $NaTaO_3$ facets, the (020) facet had the highest Ta density of 0.0464 atoms/Å^2, and that of the (101) facet was 0.0376 atoms/Å^2. The surface compactness of the facets is also compared in Table 5-1.

Table 5-1. Surface compactness and Ta density of different facets of $NaTaO_3$ and $NaTa_3O_8$.

Structure/surface	Compactness (atoms/Å^2)	Ta density (Ta atoms/Å^2)
$NaTaO_3$ (101)	0.226	0.0376
$NaTaO_3$ (020)	0.186	0.0464
$NaTa_3O_8$ (022)	0.188	0.0377
$NaTa_3O_8$ (220)	0.218	0.0436

$NaTa_3O_8$ (202)	0.192	**0.0565**

5.5. OER activity

The Free energy diagrams for the Ta sites 1 and 2 on the $NaTa_3O_8$ (202) facet are shown in Figure 5-7 A and B. The OER performance of the (202) facet was relatively better than other facets of $NaTa_3O_8$ and $NaTaO_3$. On the (202) facet, Step 1 (* + H_2O to *OH) and Step 3 (H_2O + *O to *OOH) were the rate-determining steps for Ta site 1 and Ta site 2, respectively. As shown in Figures 5-5 and 5-6, among different $NaTa_3O_8$ facets, Ta d orbitals of (220) and (022) facets contributed to the Fermi level. However, Ta d orbitals of the (202) facet had no contributions. This can be the reason for the relatively better OER performance of Ta sites on the (202) facet compared to the (220) and (022) facets. The higher contribution of Ta d orbitals at the Fermi level led to strong adsorption of intermediates, which prevented the reaction.

In addition to the effect of Ta d orbitals on the OER performance $NaTa_3O_8$ facets, Ta density on the topmost layer was also effective. Table 5-1 shows that the (202) $NaTa_3O_8$ facet had the highest Ta density on the topmost layer (0.0565 atoms/$Å^2$), which led to the lowest overpotential on Ta sites (1.13 to 1.15 V). This is in contrast to the Ta_2O_5 facets, where we found that the (200) Ta_2O_5 facet with the lowest Ta density had the lowest OER overpotential. In addition, the other $NaTa_3O_8$ facets also followed the trend of Ta density on the topmost layer; i.e., (220) $NaTa_3O_8$ with the Ta density of 0.0436 Ta atoms/$Å^2$ had the overpotential in the range of 2.48 to 2.81 V and the (022) facet with the Ta density of 0.0377 Ta atoms/$Å^2$ showed overpotentials in the range of 3.17 to 3.21 V.

Besides Ta sites, the Na site 1 on the $NaTa_3O_8$ (202) facet had the best OER performance, with an overpotential of 0.59 V. Step 2 (*OH to *O) was rate determining on this site, as shown in Figure 5-7 C. Although the PDOS analysis showed no contribution of the Na p orbitals to the electronic properties of the $NaTa_3O_8$, the Na site performed better than the Ta sites. This can be related to the effect of surrounding atoms (O or Ta) on the catalytic activity of the Na site. The Na sites on other facets of $NaTaO_3$ and $NaTa_3O_8$ did not perform well, leading to high overpotentials.

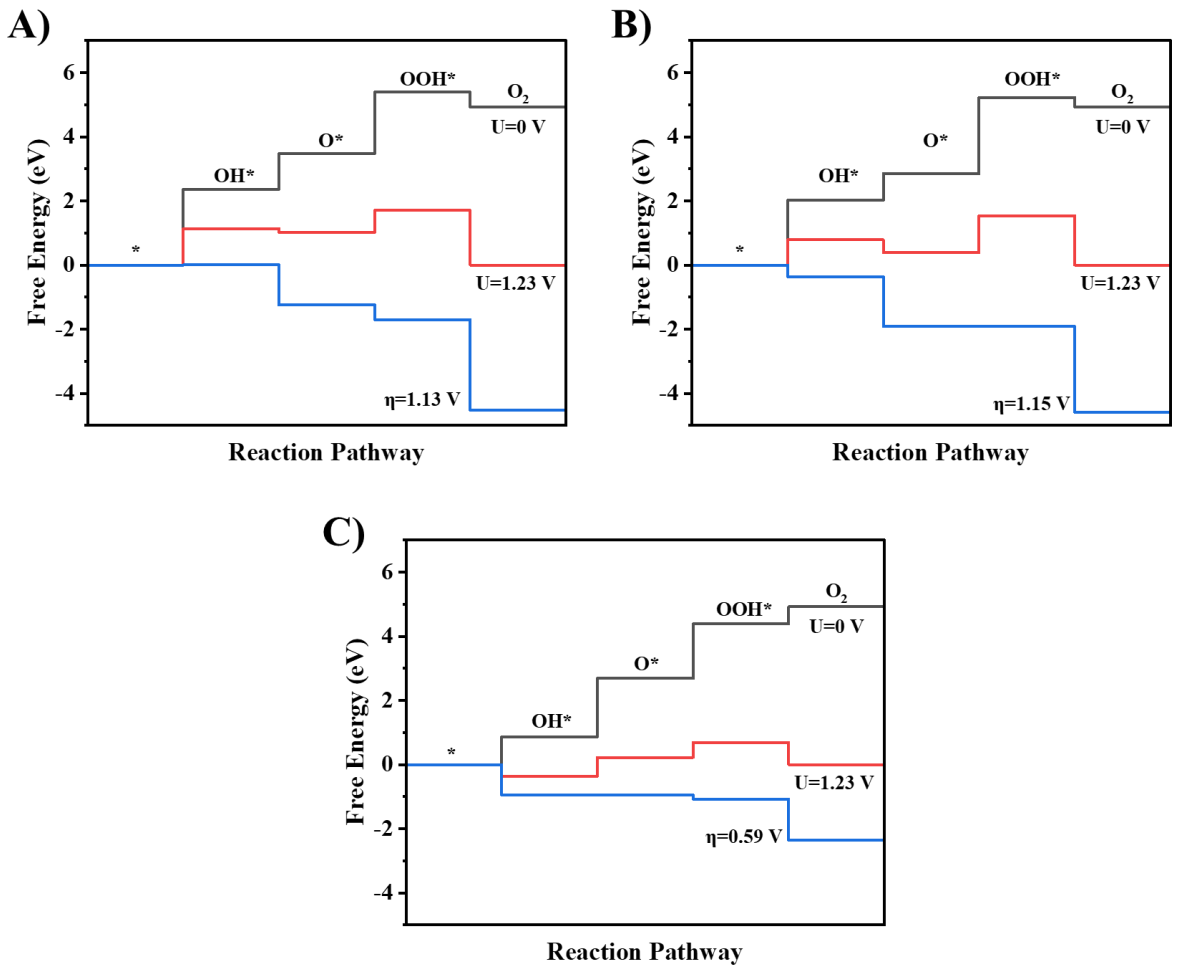

Figure 5-7. The reaction pathway and overpotential for the A) Ta-site 1, B) Ta-site 2, and C) Na site 1 on the $NaTa_3O_8$ (202) facet.

Table 5-2 compares the OER performance of various Ta sites and the Na site shown in Figures 5-1 and 5-2 for $NaTaO_3$ and $NaTa_3O_8$, respectively. Both facets of $NaTaO_3$ had poorer performance compared to $NaTa_3O_8$. The high overpotential of Ta sites on $NaTaO_3$ in the range of 4.85 to 6.08 V was due to the large $\Delta G_{Step\ 4}$ values, showing that the conversion of *OOH to O_2 (oxygen desorption) was significantly suppressed. Although the (101) and (020) facets of $NaTaO_3$ had different electronic properties, they both had very poor OER performance.

The (220) and (022) facets of the $NaTa_3O_8$ structure also had poor OER performance with overpotentials in the range of 2.48 to 3.21 V. Step 4 was the rate-determining step for Ta site 1 on the (220) facet. For the other sites on (220) and (022), Step 3 was the rate-determining step,

attributed to the conversion of *O to *OOH. Moreover, the ΔG of Step 4 on these sites was still large in the range of 3.17 to 3.71 V.

Table 5-2. The OER performance metrics (ΔG of different steps and overpotential) of different Ta sites and the Na site on $NaTaO_3$ and $NaTa_3O_8$.

Surface name	Site	$\Delta G_{Step\ 1}$ (V)	$\Delta G_{Step\ 2}$ (V)	$\Delta G_{Step\ 3}$ (V)	$\Delta G_{Step\ 4}$ (V)	η (V)
$NaTaO_3$ (101)	Ta site 1	-3.94	1.21	1.57	**6.08**	4.85
$NaTaO_3$ (101)	Ta site 2	-3.94	1.22	0.61	**7.03**	5.80
$NaTaO_3$ (020)	Ta site 1	-1.63	-0.30	-0.46	**7.31**	6.08
$NaTa_3O_8$ (220)	Ta site 1	-2.23	-0.26	3.70	**3.71**	2.48
$NaTa_3O_8$ (220)	Ta site 2	-1.80	-0.49	**4.04**	3.17	2.81
$NaTa_3O_8$ (022)	Ta site 1	-1.95	-1.10	**4.40**	3.57	3.17
$NaTa_3O_8$ (022)	Ta site 2	-1.67	-1.15	**4.44**	3.30	3.21
$NaTa_3O_8$ (202)	Ta site 1	**2.36**	1.12	1.91	-0.47	**1.13**
$NaTa_3O_8$ (202)	Ta site 2	2.01	0.83	**2.38**	-0.30	**1.15**
$NaTa_3O_8$ (202)	Na site 1	0.86	**1.82**	1.70	0.54	**0.59**

This was the first study on the OER activity of $NaTa_3O_8$, which showed a low overpotential of 0.59 V on the Na site. Although this performance is not comparable to benchmark Ir- and Ru-based electrocatalysts, it is better than most metal oxides. Typically, the pristine form of different materials can rarely achieve good electrocatalytic properties. However, the comparatively low overpotential of the $NaTa_3O_8$ (202) facet holds promise for developing an efficient OER electrocatalyst. In the follow-up projects on $NaTa_3O_8$, strategies such as using different dopants, reduction, oxidation, and creating defects can be employed to further improve their catalytic activity. Moreover, since only one facet of $NaTa_3O_8$ is active, it would be challenging to synthesize it with the preferred (202) orientation. So, it is essential to do experiments and further theoretical studies to develop active OER electrocatalysts based on $NaTa_3O_8$.

5.6. Conclusion

This chapter analyzed the electronic properties and OER performance of $NaTaO_3$ and $NaTa_3O_8$. DOS and PDOS analyses showed that the electronic properties and Ta d orbitals of both structures strongly depended on the facet. The (220) and (022) facets of $NaTa_3O_8$ and the (020) facet of $NaTaO_3$ showed a metallic behavior. However, the (202) $NaTa_3O_8$ and (101) $NaTaO_3$ facets showed a semiconducting behavior with bandgaps of 1.72 and 1.03 eV, respectively. The OER performance of $NaTa_3O_8$ facets (in the range of 1.13 to 3.21 V) was better than those of

$NaTaO_3$ (in the range of 4.85 to 6.08 V). In the $NaTa_3O_8$ structure, the (202) facet showed the lowest overpotential of 1.13 V for the Ta sites, which was significantly lower than those of the (220) and (022) facets of $NaTa_3O_8$. The overpotential on the $NaTa_3O_8$ facets followed the trend of Ta density on the topmost layer, where the (202) facet with the highest Ta density of 0.0565 Ta atoms/$Å^2$ showed the best performance. Furthermore, the lower overpotential of $NaTa_3O_8$ (202) can be because Ta d orbitals did not contribute to the Fermi level, which possibly leads to strong adsorption of OER intermediates and poor OER performance. Additionally, the Na site on the (202) $NaTa_3O_8$ facet had the lowest overpotential of 0.59 V. In future studies, strategies such as doping and defecting can be employed to further improve the OER activity of $NaTa_3O_8$.

6 Conclusion

This thesis demonstrates that Nb- and Ta-based materials are promising non-precious alternatives for oxygen evolution reaction (OER) under acidic media. Density functional theory (DFT) calculations were employed to study the OER performance of these materials. The results of each study are summarized below.

The first study on Nb_2C MXenes showed that terminating groups could modulate the electronic and catalytic properties of Nb_2C well. Among the terminations investigated, S-terminated Nb_2C exhibited the highest work function of 5.07 eV with a *d* band center positioned at -2.53 eV. Particularly, the *d* band center shifted far from the Fermi level compared to pristine Nb_2C (-1.53 eV). This showed that the shortcoming of pristine Nb_2C, strong adsorption of reaction intermediates, could be mitigated using S termination. In addition, Nb_2C-S with defects showed significant activity in dissociating H_2O, O_2, N_2, and CO_2. The dissociation barrier of Nb_2C-S_{x-1} was approximately 0 eV for O_2 and CO_2, and 0.16 and 0.17 eV for H_2O and N_2, respectively. These findings demonstrated that just by changing the terminating groups of Nb_2C, a wide range of electronic properties (such as work function) and catalytic properties can be obtained.

Building on this, the second study focused on the stability of Nb_2C-X (X=S, F, or Cl) and Nb_2C-X/graphene heterostructure toward oxidation and hydrolysis, which are essential factors for practical applications. The results revealed that in the Nb_2C-X/graphene heterostructure, the stability toward partial oxidation was improved compared to pristine Nb_2C-X. In particular, Nb_2C-S/graphene and Nb_2C-Cl/graphene showed better stability against partial oxidation compared to Nb_2C-S and Nb_2C-Cl, respectively, and Nb_2C-F/graphene was no more prone to oxidation. Furthermore, the aqueous stability of Nb_2C-S/graphene and Nb_2C-S was assessed by analyzing the dissociation barrier for water. This is because hydrolysis is the first step of MXene decomposition in aqueous media. The results showed greater barrier energy for adsorption and dissociation of water on Nb_2C-S/graphene compared to Nb_2C-S, showing its better stability against hydrolysis. Finally, Nb_2C-S/graphene showed a comparatively lower OER overpotential of 0.93 V compared to Nb_2C-S (2.15 V), highlighting the dual benefits of enhanced stability and improved catalytic performance.

Overall, the results on Nb_2C-X MXenes showed that a potential OER electrocatalyst can be prepared by creating defects, terminating with sulfur, and designing a heterostructure with graphene.

Extending beyond Nb-based materials, the thesis also explored the OER performance of Ta-based materials. Although Ta_2O_5 is among the few oxides that are stable under acidic OER, its potential has not been unlocked. Therefore, herein, Ta_2O_5 was thoroughly studied, and the findings of analyzing (200), (120), and (001) Ta_2O_5 facets provided new insights into the strong facet-dependent OER performance of Ta_2O_5. Our study clarified that the (200) Ta_2O_5/graphene heterostructure could achieve an overpotential of as low as 0.39 V, which makes it a promising candidate for acidic OER. Moreover, correlations were established between the electronic properties of Ta sites (*d* orbitals, Bader charge, and the sum of valence electrons) and OER performance metrics. The sum of valence electrons and PDOS width at the Fermi level showed moderate correlations with the OER activity of the (200) surfaces. Furthermore, Bader charge variations and *d* orbitals of Ta sites significantly affected the OER activity of the (120) facet, providing valuable insights for optimizing the Ta_2O_5-based catalysts.

Finally, sodium tantalates, including $NaTaO_3$ and $NaTa_3O_8$, were investigated as alternative Ta-based materials for OER electrocatalysis. DFT calculations indicated that the (202) $NaTa_3O_8$ facet exhibited a comparatively lower overpotential of 1.13 V on Ta sites. In addition, Na sites on the same system provided the overpotential of 0.59 V. Analyzing PDOS revealed that the presence of Ta *d* orbitals at the Fermi level could play a key role in determining the OER activity.

In summary, this thesis established that Nb- and Ta-based materials are strong candidates for the development of cost-effective OER electrocatalysts under acidic media. These findings provide helpful insights into the design strategies of Nb- and Ta-based materials, which needs to be validated experimentally for potential applications.

6.1. Future perspectives

In terms of computational materials discovery, future research on Nb_2C MXenes should study the effect of dopants on Nb_2C-X and high-entropy MXenes. High-entropy MXenes, such as $Ti_{1.1}V_{1.2}Cr_{0.8}Nb_{1.0}Mo_{0.9}C_4T_x$ [265] and $(Ti_{1/5}V_{1/5}Nb_{1/5}Ta_{1/5}Mo_{1/5})_2CT_x$ [266], have shown improved stability in supercapacitors and Li-ion batteries. However, they have been less investigated for OER. In addition, doping with elements such as N [267] and S [268] can affect the properties of Nb_2C-X MXene, which might improve its OER performance. Studying Nb_2N MXene can be another suggestion for future studies, as it is among the emerging MXenes for surface chemistry-related applications [269]. Studying the aqueous stability of Nb_2C-S and Nb_2C-S/graphene using ab initio molecular dynamics (AIMD) simulations can also provide useful

insight into their possible decomposition in aqueous media. Similar studies have been done on Ti-based MXenes [72]. Finally, the potential of Nb_2C-X MXene for other reactions, such as CO_2 reduction, ammonia production, etc., can also be studied. This can suggest specific terminations for each reaction, which unlocks the tunability of MXenes just by varying the terminating groups.

In addition to computational techniques, experiments should be done on Nb_2C-X materials for practical applications. The experiments can include the synthesis of Nb_2C nanosheets by exfoliating the Nb_2AlC MAX phase. Then, terminating groups, which depend on the synthesis method, can be removed by heat treatment and H_2 exposure [118]. Then, specific terminating groups can be applied to the Nb_2C MXene surface. Synthesis of Nb_2C/graphene [270] can also be done to study its OER performance. In general, there are many opportunities for studying Nb_2C MXenes for electrocatalysis since they are highly tunable.

Future computational studies for Ta_2O_5 include the investigation of the effect of metal oxides and other two-dimensional (2D) materials on the OER performance of Ta_2O_5/X heterostructure. Also, since the thickness of Ta_2O_5 affects its OER activity [217], the design of sandwiched Ta_2O_5 materials (thin layers of Ta2O5 within two conductive materials) can also improve its performance. The mixed oxide of Ir and Ta has been studied, and it has shown good OER performance [73]. Thus, the effect of other metal oxides on Ta_2O_5 can also be a promising approach to tuning their properties. In addition, doping Ta_2O_5 with elements such as Co, Ir, and Mg could also improve their performance for OER. The same suggestions can be followed in experiments to enable the potential of Ta_2O_5-based materials for acidic OER.

Finally, since $NaTa_3O_8$ has not been studied elsewhere, its OER activity needs to be well studied using DFT calculations by creating defects, doping, and making a heterostructure. The pristine form of $NaTa_3O_8$ surface has a low overpotential of 0.59 V, which holds promise to have good OER performance with further modifications. In terms of experiments, it is challenging to synthesize $NaTa_3O_8$, which has not been reported in the literature. So, although computational studies might find strategies to improve its OER activity, preparing the single-phase or pure $NaTa_3O_8$ with the preferred (202) orientation will be very challenging.

References

1. Horowitz, C.A., *Paris agreement.* International Legal Materials, 2016. **55**(4): p. 740-755.
2. Cho, H.H., V. Strezov, and T.J. Evans, *A review on global warming potential, challenges and opportunities of renewable hydrogen production technologies.* Sustainable Materials and Technologies, 2023. **35**: p. e00567.
3. Hren, R., et al., *Hydrogen production, storage and transport for renewable energy and chemicals: An environmental footprint assessment.* Renewable and Sustainable Energy Reviews, 2023. **173**: p. 113113.
4. Environment and C.C. Canada, *Canadian Environmental Sustainability Indicators: Greenhouse Gas Emissions.* Consulted on April, 2022, 2022.
5. *HYDROGEN STRATEGY FOR CANADA: Seizing the Opportunities for Hydrogen*. 2020; Available from: https://publications.gc.ca/site/eng/9.894114/publication.html.
6. Guan, D., et al., *Hydrogen society: from present to future.* Energy & Environmental Science, 2023. **16**(11): p. 4926-4943.
7. Reigstad, G.A., et al., *Moving toward the low-carbon hydrogen economy: Experiences and key learnings from national case studies.* Advances in Applied Energy, 2022: p. 100108.
8. Gailani, A., et al., *Assessing the potential of decarbonization options for industrial sectors.* Joule, 2024. **8**(3): p. 576-603.
9. Raabe, D., C.C. Tasan, and E.A. Olivetti, *Strategies for improving the sustainability of structural metals.* Nature, 2019. **575**(7781): p. 64-74.
10. Özgün, Ö., et al., *How much hydrogen is in green steel?* npj Materials Degradation, 2023. **7**(1): p. 78.
11. Wang, C., et al., *Green steel: Synergies between the Australian iron ore industry and the production of green hydrogen.* International Journal of Hydrogen Energy, 2023. **48**(83): p. 32277-32293.
12. Sun, B., et al., *Review on natural hydrogen wells safety.* Nature Communications, 2025. **16**(1): p. 369.
13. Mayyas, A.T., et al., *Manufacturing cost analysis for proton exchange membrane water electrolyzers*. 2019, National Renewable Energy Laboratory (NREL), Golden, CO (United States).
14. Ahmed, S.F., et al., *Sustainable hydrogen production: technological advancements and economic analysis.* International Journal of Hydrogen Energy, 2021.
15. Osman, A.I., et al., *Hydrogen production, storage, utilisation and environmental impacts: a review.* Environmental Chemistry Letters, 2021. **20**(1): p. 153-188.
16. Zainal, B.S., et al., *Recent advancement and assessment of green hydrogen production technologies.* Renewable and Sustainable Energy Reviews, 2024. **189**: p. 113941.
17. Ayub, H.M.U., et al., *A cost comparison study for hydrogen production between conventional and renewable methods.* Process Safety and Environmental Protection, 2024. **186**: p. 921-932.
18. Qureshi, F., et al., *A State-of-The-Art Review on the Latest trends in Hydrogen production, storage, and transportation techniques.* Fuel, 2023. **340**: p. 127574.
19. Mohideen, M.M., et al., *Techno-economic analysis of different shades of renewable and non-renewable energy-based hydrogen for fuel cell electric vehicles.* Renewable and Sustainable Energy Reviews, 2023. **174**: p. 113153.
20. Oni, A., et al., *Comparative assessment of blue hydrogen from steam methane reforming, autothermal reforming, and natural gas decomposition technologies for natural gas-producing regions.* Energy Conversion and Management, 2022. **254**: p. 115245.

21. Cho, H.H., V. Strezov, and T.J. Evans, *Environmental impact assessment of hydrogen production via steam methane reforming based on emissions data.* Energy Reports, 2022. **8**: p. 13585-13595.
22. Katebah, M. and P. Linke, *Analysis of hydrogen production costs in Steam-Methane Reforming considering integration with electrolysis and CO2 capture.* Cleaner Engineering and Technology, 2022. **10**: p. 100552.
23. Boscherini, M., et al., *New perspectives on catalytic hydrogen production by the reforming, partial oxidation and decomposition of methane and biogas.* Energies, 2023. **16**(17): p. 6375.
24. Ahmad, S., et al., *Hydrogen production, storage, transportation and utilization for energy sector: A current status review.* Journal of Energy Storage, 2024. **101**: p. 113733.
25. Sengodan, S., et al., *Advances in reforming and partial oxidation of hydrocarbons for hydrogen production and fuel cell applications.* Renewable and Sustainable Energy Reviews, 2018. **82**: p. 761-780.
26. Hammi, Z., et al., *Green hydrogen: a holistic review covering life cycle assessment, environmental impacts, and color analysis.* International Journal of Hydrogen Energy, 2024. **80**: p. 1030-1045.
27. Nikolaidis, P. and A. Poullikkas, *A comparative overview of hydrogen production processes.* Renewable and sustainable energy reviews, 2017. **67**: p. 597-611.
28. Muhammed, N.S., et al., *Hydrogen production, transportation, utilization, and storage: Recent advances towards sustainable energy.* Journal of Energy Storage, 2023. **73**.
29. Guerrini, E. and S. Trasatti, *Electrocatalysis in water electrolysis.* Catalysis for sustainable energy production, 2009: p. 235-269.
30. Kumar, S.S. and H. Lim, *An overview of water electrolysis technologies for green hydrogen production.* Energy reports, 2022. **8**: p. 13793-13813.
31. Kumar, S.S. and H. Lim, *Recent advances in hydrogen production through proton exchange membrane water electrolysis–a review.* Sustainable Energy & Fuels, 2023. **7**(15): p. 3560-3583.
32. Emam, A.S., et al., *A review on recent trends, challenges, and innovations in alkaline water electrolysis.* International Journal of Hydrogen Energy, 2024. **64**: p. 599-625.
33. Dash, S., et al., *Advances in green hydrogen production through alkaline water electrolysis: A comprehensive review.* International Journal of Hydrogen Energy, 2024. **83**: p. 614-629.
34. Wan, L., et al., *Key components and design strategy of the membrane electrode assembly for alkaline water electrolysis.* Energy & Environmental Science, 2023. **16**(4): p. 1384-1430.
35. Sebbahi, S., et al., *A comprehensive review of recent advances in alkaline water electrolysis for hydrogen production.* International Journal of Hydrogen Energy, 2024. **82**: p. 583-599.
36. Li, Q., et al., *Anion exchange membrane water electrolysis: the future of green hydrogen.* The Journal of Physical Chemistry C, 2023. **127**(17): p. 7901-7912.
37. Lei, H., et al., *Multiscale understanding of anion exchange membrane fuel cells: Mechanisms, electrocatalysts, polymers, and cell management.* Advanced Materials, 2025: p. 2410106.
38. Trinke, P., *Experimental and model-based investigations on gas crossover in polymer electrolyte membrane water electrolyzers.* 2021.
39. Wu, H., et al., *Recent developments of Iridium-based catalysts for oxygen evolution reaction in acidic water electrolysis.* Journal of Materials Chemistry A, 2022.
40. Suen, N.-T., et al., *Electrocatalysis for the oxygen evolution reaction: recent development and future perspectives.* Chemical Society Reviews, 2017. **46**(2): p. 337-365.

41. Reier, T., et al., *Electrocatalytic oxygen evolution reaction in acidic environments–reaction mechanisms and catalysts.* Advanced Energy Materials, 2017. **7**(1): p. 1601275.
42. Cavaliere, P., *Fundamentals of Water Electrolysis*, in *Water Electrolysis for Hydrogen Production*. 2023, Springer. p. 1-60.
43. Trasatti, S., *Oxygen evolution*, in *Encyclopedia of electrochemical power sources*. 2009, Elsevier. p. 49-55.
44. Doyle, R.L. and M.E. Lyons, *The oxygen evolution reaction: mechanistic concepts and catalyst design.* Photoelectrochemical Solar Fuel Production: From Basic Principles to Advanced Devices, 2016: p. 41-104.
45. Rossmeisl, J., et al., *Electrolysis of water on oxide surfaces.* Journal of Electroanalytical Chemistry, 2007. **607**(1-2): p. 83-89.
46. Rossmeisl, J., A. Logadottir, and J.K. Nørskov, *Electrolysis of water on (oxidized) metal surfaces.* Chemical physics, 2005. **319**(1-3): p. 178-184.
47. Man, I.C., et al., *Universality in oxygen evolution electrocatalysis on oxide surfaces.* ChemCatChem, 2011. **3**(7): p. 1159-1165.
48. Lin, Y., et al., *Electrocatalysts for the Oxygen Evolution Reaction in Acidic Media.* Adv Mater, 2023. **35**(22): p. e2210565.
49. Liu, Z., et al., *Acid oxygen evolution reaction: Mechanisms, design principles, and prospects for application in membrane electrodes.* Chemical Engineering Journal, 2024. **499**.
50. Zagalskaya, A. and V. Alexandrov, *Role of defects in the interplay between adsorbate evolving and lattice oxygen mechanisms of the oxygen evolution reaction in RuO2 and IrO2.* ACS Catalysis, 2020. **10**(6): p. 3650-3657.
51. Gunasooriya, G.K.K. and J.K. Nørskov, *Analysis of acid-stable and active oxides for the oxygen evolution reaction.* ACS Energy Letters, 2020. **5**(12): p. 3778-3787.
52. Hong, W.T., et al., *Toward the rational design of non-precious transition metal oxides for oxygen electrocatalysis.* Energy & Environmental Science, 2015. **8**(5): p. 1404-1427.
53. Wei, C., et al., *Recommended practices and benchmark activity for hydrogen and oxygen electrocatalysis in water splitting and fuel cells.* Advanced Materials, 2019. **31**(31): p. 1806296.
54. Yu, Z.Y., et al., *Clean and affordable hydrogen fuel from alkaline water splitting: past, recent progress, and future prospects.* Advanced Materials, 2021. **33**(31): p. 2007100.
55. Risch, M., *Upgrading the detection of electrocatalyst degradation during the oxygen evolution reaction.* Current Opinion in Electrochemistry, 2023. **38**: p. 101247.
56. Ma, Q. and S. Mu, *Acidic oxygen evolution reaction: Mechanism, catalyst classification, and enhancement strategies.* Interdisciplinary Materials, 2023. **2**(1): p. 53-90.
57. Qin, R., et al., *Ru/Ir-based electrocatalysts for oxygen evolution reaction in acidic conditions: From mechanisms, optimizations to challenges.* Advanced Science, 2024: p. 2309364.
58. Zeng, F., et al., *Stability and deactivation of OER electrocatalysts: A review.* Journal of Energy Chemistry, 2022. **69**: p. 301-329.
59. Ping, X., et al., *Locking the lattice oxygen in RuO2 to stabilize highly active Ru sites in acidic water oxidation.* Nature Communications, 2024. **15**(1): p. 2501.
60. Chang, J., et al., *Oxygen Radical Coupling on Short-Range Ordered Ru Atom Arrays Enables Exceptional Activity and Stability for Acidic Water Oxidation.* Journal of the American Chemical Society, 2024. **146**(19): p. 12958-12968.
61. Su, H., et al., *Tensile straining of iridium sites in manganese oxides for proton-exchange membrane water electrolysers.* Nature Communications, 2024. **15**(1): p. 95.
62. Li, A., et al., *Atomically dispersed hexavalent iridium oxide from MnO2 reduction for oxygen evolution catalysis.* Science, 2024. **384**(6696): p. 666-670.

63. Hubert, M.A., L.A. King, and T.F. Jaramillo, *Evaluating the case for reduced precious metal catalysts in proton exchange membrane electrolyzers.* ACS Energy Letters, 2021. **7**(1): p. 17-23.
64. Ma, J., et al., *Niobium/tantalum-based materials: Synthesis and applications in electrochemical energy storage.* Chemical Engineering Journal, 2020. **380**: p. 122428.
65. Gómez, M., J. Li, and X. Zeng, *Niobium: The unseen element-A comprehensive examination of its evolution, global dynamics, and outlook.* Resources, Conservation and Recycling, 2024. **209**: p. 107744.
66. 16/12/2024]; Available from: https://www.canada.ca/en/campaign/critical-minerals-in-canada/canadian-critical-minerals-strategy.html.
67. Ishihara, A., et al., *Challenge of advanced low temperature fuel cells based on high degree of freedom of group 4 and 5 metal oxides.* Current Opinion in Electrochemistry, 2020. **21**: p. 234-241.
68. Ke, J., et al., *Optimizing Acidic Oxygen Evolution Reaction via Modulation Doping in Van der Waals Layered Iridium Oxide.* Angewandte Chemie, 2025: p. e202422740.
69. Wu, Y., et al., *Modulating Carrier Oxygen Vacancies to Enhance Strong Oxide-Support Interaction in IrO2/Nb2O5-x Catalysts for Promoting Acidic Oxygen Evolution Reaction.* Advanced Functional Materials, 2024. **34**(51): p. 2410193.
70. VahidMohammadi, A., J. Rosen, and Y. Gogotsi, *The world of two-dimensional carbides and nitrides (MXenes).* Science, 2021. **372**(6547): p. eabf1581.
71. Kan, D., et al., *Rational design of bifunctional ORR/OER catalysts based on Pt/Pd-doped Nb 2 CT 2 MXene by first-principles calculations.* Journal of Materials Chemistry A, 2020. **8**(6): p. 3097-3108.
72. Wu, T., et al., *How water attacks MXene.* Chemistry of Materials, 2022. **34**(11): p. 4975-4982.
73. Li, H., et al., *Highly active and stable IrO2 and IrO2–Ta2O5 catalysts for oxygen evolution reaction.* International Journal of Hydrogen Energy, 2023. **48**(67): p. 26021-26031.
74. Huang, Q., et al., *Boron-incorporated IrO2-Ta2O5 coating as an efficient electrocatalyst for acidic oxygen evolution reaction.* Chemical Engineering Journal, 2024. **491**: p. 152040.
75. Amano, F., et al., *Structure–stability relationship of amorphous IrO2–Ta2O5 electrocatalysts on Ti felt for oxygen evolution in sulfuric acid.* The Journal of Physical Chemistry C, 2022. **126**(4): p. 1817-1827.
76. Liu, Y., et al., *An IrRuO x catalyst supported by oxygen-vacant Ta oxide for the oxygen evolution reaction and proton exchange membrane water electrolysis.* Nanoscale, 2024. **16**(19): p. 9382-9391.
77. Zhang, J., et al., *Tantalum-stabilized ruthenium oxide electrocatalysts for industrial water electrolysis.* Science, 2025. **387**(6729): p. 48-55.
78. Wang, X., et al., *RuO2 with Short-Range Ordered Tantalum Single Atoms for Enhanced Acidic Oxygen Evolution Reaction.* Advanced Energy Materials, 2024: p. 2403388.
79. Maria de Lourdes, S.V., et al., *Electrocatalytic properties of Ti/RuO2-TiO2 dimensionally stable anode type electrodes modified with SnO2 and Ta2O5 for the oxygen evolution reaction.* Applied Catalysis O: Open, 2025. **198**: p. 207025.
80. Amano, F., Y. Furusho, and Y.-M. Hwang, *Amorphous iridium and tantalum oxide layers coated on titanium felt for electrocatalytic oxygen evolution reaction.* ACS Applied Energy Materials, 2020. **3**(5): p. 4531-4538.
81. Hafner, J., C. Wolverton, and G. Ceder, *Toward computational materials design: the impact of density functional theory on materials research.* MRS bulletin, 2006. **31**(9): p. 659-668.

82. Luber, S., *Recent progress in computational exploration and design of functional materials.* Computational Materials Science, 2019. **161**: p. 127-134.
83. Kovacic, Z., B. Likozar, and M. Hus, *Photocatalytic CO2 reduction: A review of ab initio mechanism, kinetics, and multiscale modeling simulations.* ACS catalysis, 2020. **10**(24): p. 14984-15007.
84. Zhu, H., et al., *DFT practice in MXene-based materials for electrocatalysis and energy storage: From basics to applications.* Ceramics International, 2022.
85. Podrojková, N., et al., *Recent developments in the modelling of heterogeneous catalysts for CO2 conversion to chemicals.* ChemCatChem, 2020. **12**(7): p. 1802-1825.
86. Liao, X., et al., *Density functional theory for electrocatalysis.* Energy & Environmental Materials, 2022. **5**(1): p. 157-185.
87. Basharnavaz, H., A. Habibi-Yangjeh, and M. Mousavi, *Ni, Pd, and Pt-embedded graphitic carbon nitrides as excellent adsorbents for HCN removal: a DFT study.* Applied Surface Science, 2018. **456**: p. 882-889.
88. Zhuang, Y., et al., *Design of high-performance electrochemistry sensors: Elucidation of detection mechanism by DFT studies.* Journal of Electroanalytical Chemistry, 2020. **860**: p. 113905.
89. Rojaee, R. and R. Shahbazian-Yassar, *Two-dimensional materials to address the lithium battery challenges.* ACS nano, 2020. **14**(3): p. 2628-2658.
90. Zhu, X. and Y. Li, *Review of two-dimensional materials for electrochemical CO2 reduction from a theoretical perspective.* Wiley Interdisciplinary Reviews: Computational Molecular Science, 2019. **9**(6): p. e1416.
91. Handoko, A.D., S.N. Steinmann, and Z.W. Seh, *Theory-guided materials design: two-dimensional MXenes in electro-and photocatalysis.* Nanoscale Horizons, 2019. **4**(4): p. 809-827.
92. VahidMohammadi, A., J. Rosen, and Y. Gogotsi, *The world of two-dimensional carbides and nitrides (MXenes).* Science, 2021. **372**(6547).
93. Nan, J., et al., *Nanoengineering of 2D MXene-based materials for energy storage applications.* Small, 2021. **17**(9): p. 1902085.
94. You, Z., et al., *State of the art recent progress in MXene-based photocatalysts: a comprehensive review.* Nanoscale, 2021.
95. Wang, H. and J.-M. Lee, *Recent advances in structural engineering of MXene electrocatalysts.* Journal of Materials Chemistry A, 2020. **8**(21): p. 10604-10624.
96. Verger, L., et al., *MXenes: an introduction of their synthesis, select properties, and applications.* Trends in chemistry, 2019. **1**(7): p. 656-669.
97. Fu, B., et al., *MXenes: Synthesis, Optical Properties, and Applications in Ultrafast Photonics.* Small, 2021. **17**(11): p. 2006054.
98. Kamysbayev, V., et al., *Covalent surface modifications and superconductivity of two-dimensional metal carbide MXenes.* Science, 2020. **369**(6506): p. 979-983.
99. Hart, J.L., et al., *Control of MXenes' electronic properties through termination and intercalation.* Nature communications, 2019. **10**(1): p. 1-10.
100. Wu, T., et al., *How Water Attacks MXene.* Chemistry of Materials, 2022.
101. Nayak, P., et al., *Single-entity Ti3C2Tx MXene electro-oxidation.* Applied Materials Today, 2022. **26**: p. 101335.
102. Matthews, K., et al., *Guidelines for synthesis and processing of chemically stable two-dimensional V2CT x MXene.* Chemistry of Materials, 2021. **34**(2): p. 499-509.
103. Wang, Z., et al., *Stabilizing Ti3C2Tx-MXenes with TiOF2 nanospheres intercalation to improve hydrogen evolution reaction and humidity-sensing performance.* Applied Surface Science, 2019. **496**: p. 143729.

104. Zeng, Y., et al., *Synergistic performance of nitrogen and sulfur co-doped Ti3C2TX for electrohydrogenation of N2 to NH3.* Journal of Alloys and Compounds, 2021. **869**: p. 159335.
105. Ding, Y., et al., *Promoting N2 electroreduction to ammonia by fluorine-terminating Ti3C2Tx MXene.* Nano Converg, 2021. **8**(1): p. 14.
106. Guo, Y., et al., *Highly Efficient Electrochemical Reduction of Nitrogen to Ammonia on Surface Termination Modified Ti3C2Tx MXene Nanosheets.* ACS Nano, 2020. **14**(7): p. 9089-9097.
107. Tang, Y., et al., *MXene nanoarchitectonics: defect-engineered 2D MXenes towards enhanced electrochemical water splitting.* Advanced Energy Materials, 2022. **12**(12): p. 2103867.
108. Gan, J., F. Li, and Q. Tang, *Vacancies-Engineered M2CO2 MXene as an efficient hydrogen evolution reaction electrocatalyst.* The Journal of Physical Chemistry Letters, 2021. **12**(20): p. 4805-4813.
109. Song, M., et al., *Fluoride-Free 2D Niobium Carbide MXenes as Stable and Biocompatible Nanoplatforms for Electrochemical Biosensors with Ultrahigh Sensitivity.* Advanced Science, 2020. **7**(24): p. 2001546.
110. Xiao, J., et al., *A safe etching route to synthesize highly crystalline Nb2CTx MXene for high performance asymmetric supercapacitor applications.* Electrochimica Acta, 2020. **337**: p. 135803.
111. Li, G., et al., *Highly Efficient Nb2C MXene Cathode Catalyst with Uniform O-Terminated Surface for Lithium–Oxygen Batteries.* Advanced Energy Materials, 2021. **11**(1): p. 2002721.
112. Zhang, J., C. Huang, and H. Yu, *Modulate the work function of Nb2CTx MXene as the hole transport layer for perovskite solar cells.* Applied Physics Letters, 2021. **119**(3): p. 033506.
113. Tan, Y., et al., *Nb4C3Tx (MXene) as a new stable catalyst for the hydrogen evolution reaction.* International Journal of Hydrogen Energy, 2021. **46**(2): p. 1955-1966.
114. Zhang, X., et al., *Regulation of CO oxidation with Pd additives on Nb2CO2 MXene.* International Journal of Hydrogen Energy, 2021. **46**(12): p. 8477-8485.
115. Chu, K., et al., *Synergistic Enhancement of Electrocatalytic Nitrogen Reduction Over Boron Nitride Quantum Dots Decorated Nb2CTx-MXene.* Small, 2021. **17**(40): p. 2102363.
116. Ougherb, C., et al., *Effect of the sulfur termination on the properties of Hf 2 CO 2 MXene.* Physical Chemistry Chemical Physics, 2022. **24**(12): p. 7243-7252.
117. Sun, W., et al., *Electrochemical etching of Ti 2 AlC to Ti 2 CT x (MXene) in low-concentration hydrochloric acid solution.* Journal of Materials Chemistry A, 2017. **5**(41): p. 21663-21668.
118. Bjork, J. and J. Rosen, *Functionalizing MXenes by tailoring surface terminations in different chemical environments.* Chemistry of Materials, 2021. **33**(23): p. 9108-9118.
119. Naguib, M., M.W. Barsoum, and Y. Gogotsi, *Ten years of progress in the synthesis and development of MXenes.* Advanced Materials, 2021. **33**(39): p. 2103393.
120. Perdew, J.P., K. Burke, and M. Ernzerhof, *Generalized gradient approximation made simple.* Physical review letters, 1996. **77**(18): p. 3865.
121. Wang, Y., et al., *Niobium carbide MXenes with broad-band nonlinear optical response and ultrafast carrier dynamics.* ACS nano, 2020. **14**(8): p. 10492-10502.
122. Kan, D., et al., *Rational design of bifunctional ORR/OER catalysts based on Pt/Pd-doped Nb2CT2 MXene by first-principles calculations.* Journal of Materials Chemistry A, 2020. **8**(6): p. 3097-3108.

123. Henkelman, G., A. Arnaldsson, and H. Jónsson, *A fast and robust algorithm for Bader decomposition of charge density.* Computational Materials Science, 2006. **36**(3): p. 354-360.
124. Hu, J., et al., *Investigations on Nb 2 C monolayer as promising anode material for Li or non-Li ion batteries from first-principles calculations.* RSC advances, 2016. **6**(33): p. 27467-27474.
125. Zaheer, A., et al., *Nickel-adsorbed two-dimensional Nb 2 C MXene for enhanced energy storage applications.* RSC advances, 2022. **12**(8): p. 4624-4634.
126. Mills, G., H. Jónsson, and G.K. Schenter, *Reversible work transition state theory: application to dissociative adsorption of hydrogen.* Surface Science, 1995. **324**(2-3): p. 305-337.
127. Jónsson, H., G. Mills, and K.W. Jacobsen, *Classical and quantum dynamics in condensed phase simulations*. 1998, World Scientific Singapore.
128. Tang, H., et al., *Post-processing strategies for improving the electrical and mechanical properties of MXenes.* Chemical Engineering Journal, 2021. **425**: p. 131472.
129. Qian, X., et al., *Theoretical investigation of defective MXenes as potential electrocatalysts for CO reduction toward C 2 products.* Physical Chemistry Chemical Physics, 2021. **23**(21): p. 12431-12438.
130. Kuo, D.Y., et al., *Measurements of Oxygen Electroadsorption Energies and Oxygen Evolution Reaction on RuO2(110): A Discussion of the Sabatier Principle and Its Role in Electrocatalysis.* J Am Chem Soc, 2018. **140**(50): p. 17597-17605.
131. Acerbi, N., et al., *Rationalization of interactions in precious metal/ceria catalysts using the d-band center model.* Angew Chem Int Ed Engl, 2013. **52**(30): p. 7737-41.
132. Lima, F., et al., *Catalytic activity− d-band center correlation for the O2 reduction reaction on platinum in alkaline solutions.* The Journal of Physical Chemistry C, 2007. **111**(1): p. 404-410.
133. Bhattacharjee, S., U.V. Waghmare, and S.-C. Lee, *An improved d-band model of the catalytic activity of magnetic transition metal surfaces.* Scientific reports, 2016. **6**(1): p. 1-10.
134. Yang, W., et al., *Theoretical study on double-atom catalysts supported with graphene for electroreduction of nitrogen into ammonia.* Electrochimica Acta, 2020. **335**: p. 135667.
135. Chu, K., et al., *Electronically coupled SnO2 quantum dots and graphene for efficient nitrogen reduction reaction.* ACS applied materials & interfaces, 2019. **11**(35): p. 31806-31815.
136. Yuan, M., et al., *Work function regulation of nitrogen-doped carbon nanotubes triggered by metal nanoparticles for efficient electrocatalytic nitrogen fixation.* Journal of Materials Chemistry A, 2020. **8**(48): p. 26066-26074.
137. Yang, X., et al., *MBenes: emerging 2D materials as efficient electrocatalysts for the nitrogen reduction reaction.* Nanoscale horizons, 2020. **5**(7): p. 1106-1115.
138. Zhao, R., et al., *In operando identification of the V 4+-site-dependent nitrogen reduction reaction of VS x.* Journal of Materials Chemistry A, 2022. **10**(18): p. 10219-10226.
139. Matsumoto, Y. and E. Sato, *Electrocatalytic properties of transition metal oxides for oxygen evolution reaction.* Materials chemistry and physics, 1986. **14**(5): p. 397-426.
140. Légaré, M.-A., et al., *Nitrogen fixation and reduction at boron.* Science, 2018. **359**(6378): p. 896-900.
141. Kitano, M., et al., *Ammonia synthesis using a stable electride as an electron donor and reversible hydrogen store.* Nature chemistry, 2012. **4**(11): p. 934-940.
142. Ling, C., et al., *Metal-free single atom catalyst for N2 fixation driven by visible light.* Journal of the American Chemical Society, 2018. **140**(43): p. 14161-14168.
143. Huang, L., et al., *NbO2 electrocatalyst toward 32% faradaic efficiency for N2 fixation.* Small Methods, 2019. **3**(6): p. 1800386.

144. Kitano, M., et al., *Electride support boosts nitrogen dissociation over ruthenium catalyst and shifts the bottleneck in ammonia synthesis.* Nature communications, 2015. **6**(1): p. 1-9.
145. Tian, D., et al., *Density functional theory studies of transition metal carbides and nitrides as electrocatalysts.* Chemical Society Reviews, 2021.
146. Wang, X., et al., *CO 2 activation and dissociation on In 2 O 3 (110) supported Pd n Pt (4− n)(n= 0–4) catalysts: a density functional theory study.* Physical Chemistry Chemical Physics, 2021. **23**(19): p. 11557-11567.
147. Han, J., et al., *Zn doped FeCo layered double hydroxide nanoneedle arrays with partial amorphous phase for efficient oxygen evolution reaction.* ACS Sustainable Chemistry & Engineering, 2019. **7**(15): p. 13105-13114.
148. Zhu, Y.P., et al., *Surface and interface engineering of noble-metal-free electrocatalysts for efficient energy conversion processes.* Accounts of chemical research, 2017. **50**(4): p. 915-923.
149. Seh, Z.W., et al., *Combining theory and experiment in electrocatalysis: Insights into materials design.* Science, 2017. **355**(6321): p. eaad4998.
150. Yin, H., et al., *Ultrathin platinum nanowires grown on single-layered nickel hydroxide with high hydrogen evolution activity.* Nature communications, 2015. **6**(1): p. 6430.
151. Mills, A. and T. Russell, *Comparative study of new and established heterogeneous oxygen catalysts.* Journal of the Chemical Society, Faraday Transactions, 1991. **87**(8): p. 1245-1250.
152. Niu, H., et al., *Rational design and synthesis of one-dimensional platinum-based nanostructures for oxygen-reduction electrocatalysis.* Chinese Journal of Catalysis, 2022. **43**(6): p. 1459-1472.
153. Zhang, H., et al., *High performance Pd x Cu y bimetal catalysts with adjustable Faraday current efficiency for nitrogen fixation.* Inorganic Chemistry Frontiers, 2021. **8**(13): p. 3336-3341.
154. Li, J., M. Zhu, and Y.F. Han, *Recent advances in electrochemical CO2 reduction on indium‐based catalysts.* ChemCatChem, 2021. **13**(2): p. 514-531.
155. Bullock, R.M., et al., *Using nature's blueprint to expand catalysis with Earth-abundant metals.* Science, 2020. **369**(6505): p. eabc3183.
156. Masa, J., C. Andronescu, and W. Schuhmann, *Electrocatalysis as the nexus for sustainable renewable energy: the gordian knot of activity, stability, and selectivity.* Angewandte Chemie International Edition, 2020. **59**(36): p. 15298-15312.
157. Pang, J., et al., *Potential of MXene-based heterostructures for energy conversion and storage.* ACS Energy Letters, 2021. **7**(1): p. 78-96.
158. Wang, Y., et al., *Challenges and opportunities in utilizing MXenes of carbides and nitrides as electrocatalysts.* Advanced Energy Materials, 2021. **11**(3): p. 2002967.
159. Rasheed, P.A., et al., *Recent advances in niobium MXenes: Synthesis, properties, and emerging applications.* Matter, 2022. **5**(2): p. 546-572.
160. Yu, Y., J. Zhou, and Z. Sun, *Novel 2D transition‐metal carbides: ultrahigh performance electrocatalysts for overall water splitting and oxygen reduction.* Advanced Functional Materials, 2020. **30**(47): p. 2000570.
161. Peng, J., et al., *Surface and heterointerface engineering of 2D MXenes and their nanocomposites: insights into electro-and photocatalysis.* Chem, 2019. **5**(1): p. 18-50.
162. Sinopoli, A., et al., *Electrocatalytic/photocatalytic properties and aqueous media applications of 2D transition metal carbides (MXenes).* Current Opinion in Solid State and Materials Science, 2019. **23**(5): p. 100760.
163. Hu, T., et al., *Functionalized MXenes for efficient electrocatalytic nitrate reduction to ammonia.* Journal of Materials Chemistry A, 2022. **10**(16): p. 8923-8931.

164. Amrillah, T., et al., *MXenes and their derivatives as nitrogen reduction reaction catalysts: recent progress and perspectives.* Materials Today Energy, 2021. **22**: p. 100864.
165. Gong, S., et al., *Construction of S-scheme 0D/2D heterostructures for enhanced visible-light-driven CO2 reduction.* Applied Catalysis B: Environmental, 2021. **298**: p. 120521.
166. Gao, X., et al., *Synergizing aliovalent doping and interface in heterostructured NiV nitride@ oxyhydroxide core-shell nanosheet arrays enables efficient oxygen evolution.* Nano Energy, 2021. **85**: p. 105961.
167. Li, M., et al., *Element replacement approach by reaction with Lewis acidic molten salts to synthesize nanolaminated MAX phases and MXenes.* Journal of the American Chemical Society, 2019. **141**(11): p. 4730-4737.
168. Mostafavi, E. and S. Iravani, *MXene-graphene composites: a perspective on biomedical potentials.* Nano-Micro Letters, 2022. **14**(1): p. 130.
169. Naguib, M., et al., *Two-dimensional nanocrystals produced by exfoliation of Ti3AlC2*, in *MXenes*. 2023, Jenny Stanford Publishing. p. 15-29.
170. Yuan, Z., et al., *Carbon-reinforced Nb2CTx MXene/MoS2 nanosheets as a superior rate and high-capacity anode for sodium-ion batteries.* ACS nano, 2021. **15**(4): p. 7439-7450.
171. Butt, R., et al., *Niobium carbide/reduced graphene oxide hybrid porous aerogel as high capacity and long-life anode material for Li-ion batteries.* International Journal of Energy Research, 2019. **43**(9): p. 4995-5003.
172. Huang, S. and V.N. Mochalin, *Hydrolysis of 2D transition-metal carbides (MXenes) in colloidal solutions.* Inorganic chemistry, 2019. **58**(3): p. 1958-1966.
173. Olshtrem, A., et al., *Plasmon-assisted MXene grafting: tuning of surface termination and stability enhancement.* 2D Materials, 2021. **8**(4): p. 045037.
174. Zhang, C.J., et al., *Oxidation stability of colloidal two-dimensional titanium carbides (MXenes).* Chemistry of Materials, 2017. **29**(11): p. 4848-4856.
175. Cao, F., et al., *Recent advances in oxidation stable chemistry of 2D MXenes.* Advanced Materials, 2022. **34**(13): p. 2107554.
176. Habib, T., et al., *Oxidation stability of Ti3C2Tx MXene nanosheets in solvents and composite films.* npj 2D Materials and Applications, 2019. **3**(1): p. 8.
177. Wang, X., Z. Wang, and J. Qiu, *Stabilizing MXene by hydration chemistry in aqueous solution.* Angewandte Chemie, 2021. **133**(51): p. 26791-26795.
178. Xia, F., et al., *Ambient oxidation of Ti 3 C 2 MXene initialized by atomic defects.* Nanoscale, 2019. **11**(48): p. 23330-23337.
179. Li, Z. and Y. Wu, *2D early transition metal carbides (MXenes) for catalysis.* Small, 2019. **15**(29): p. 1804736.
180. Li, G., et al., *Ti3C2 sheets with an adjustable surface and feature sizes to regulate the chemical stability.* Inorganic chemistry, 2019. **58**(14): p. 9397-9403.
181. Seredych, M., et al., *High-temperature behavior and surface chemistry of carbide MXenes studied by thermal analysis.* Chemistry of Materials, 2019. **31**(9): p. 3324-3332.
182. Fu, Z., et al., *Stabilization and strengthening effects of functional groups in two-dimensional titanium carbide.* Physical Review B, 2016. **94**(10): p. 104103.
183. Gao, L., et al., *Hetero-MXenes: theory, synthesis, and emerging applications.* Advanced Materials, 2021. **33**(10): p. 2004129.
184. Abbasi, N.M., et al., *Heterostructures of titanium-based MXenes in energy conversion and storage devices.* Journal of Materials Chemistry C, 2021. **9**(27): p. 8395-8465.
185. Lim, K.R.G., et al., *2h-Mos2 on Mo2ct X Mxene nanohybrid for efficient and durable electrocatalytic hydrogen evolution.* ACS nano, 2020. **14**(11): p. 16140-16155.
186. Jiang, L., et al., *Iron-cluster-directed synthesis of 2D/2D Fe–N–C/MXene superlattice-like heterostructure with enhanced oxygen reduction electrocatalysis.* ACS nano, 2020. **14**(2): p. 2436-2444.

187. Aierken, Y., et al., *MXenes/graphene heterostructures for Li battery applications: a first principles study.* Journal of Materials Chemistry A, 2018. **6**(5): p. 2337-2345.
188. Du, Y.-T., et al., *MXene/graphene heterostructures as high-performance electrodes for Li-ion batteries.* ACS applied materials & interfaces, 2018. **10**(38): p. 32867-32873.
189. Ghasemy, E., A.C. Tavares, and K.K. Ghuman, *Tuning the catalytic activity of Nb2C MXenes via surface functionalization and defects.* Applied Materials Today, 2023. **32**: p. 101858.
190. Giannozzi, P., et al., *QUANTUM ESPRESSO: a modular and open-source software project for quantum simulations of materials.* Journal of physics: Condensed matter, 2009. **21**(39): p. 395502.
191. Giannozzi, P., et al., *Advanced capabilities for materials modelling with Quantum ESPRESSO.* Journal of physics: Condensed matter, 2017. **29**(46): p. 465901.
192. Gan, L.-Y., et al., *First-principles analysis of MoS 2/Ti 2 C and MoS 2/Ti 2 CY 2 (Y= F and OH) all-2D semiconductor/metal contacts.* Physical Review B—Condensed Matter and Materials Physics, 2013. **87**(24): p. 245307.
193. Grimme, S., *Semiempirical GGA-type density functional constructed with a long-range dispersion correction.* Journal of computational chemistry, 2006. **27**(15): p. 1787-1799.
194. Stradi, D., et al., *Method for determining optimal supercell representation of interfaces.* Journal of Physics: Condensed Matter, 2017. **29**(18): p. 185901.
195. Li, R., et al., *First-principles study of heterostructures of MXene and nitrogen-doped graphene as anode materials for Li-ion batteries.* Surfaces and Interfaces, 2020. **21**: p. 100788.
196. Zhou, S., et al., *Heterostructures of MXenes and N-doped graphene as highly active bifunctional electrocatalysts.* Nanoscale, 2018. **10**(23): p. 10876-10883.
197. Berne, B.J., G. Ciccotti, and D.F. Coker, *Classical and quantum dynamics in condensed phase simulations: Proceedings of the International School of Physics*. 1998: World Scientific.
198. Paul, P., et al., *Properties at the interface of graphene and Ti 2 C MXene.* Physical Review B, 2017. **96**(3): p. 035435.
199. Li, S., et al., *Ultrathin MXene nanosheets with rich fluorine termination groups realizing efficient electrocatalytic hydrogen evolution.* Nano energy, 2018. **47**: p. 512-518.
200. Seh, Z.W., et al., *Two-dimensional molybdenum carbide (MXene) as an efficient electrocatalyst for hydrogen evolution.* ACS Energy Letters, 2016. **1**(3): p. 589-594.
201. Lu, C., et al., *Molybdenum carbide-embedded nitrogen-doped porous carbon nanosheets as electrocatalysts for water splitting in alkaline media.* ACS nano, 2017. **11**(4): p. 3933-3942.
202. Wang, H., et al., *Confined growth of pyridinic N–Mo 2 C sites on MXenes for hydrogen evolution.* Journal of materials chemistry A, 2020. **8**(15): p. 7109-7116.
203. Yu, M., et al., *Boosting electrocatalytic oxygen evolution by synergistically coupling layered double hydroxide with MXene.* Nano Energy, 2018. **44**: p. 181-190.
204. Xue, Q., et al., *Mn 3 O 4 nanoparticles on layer-structured Ti 3 C 2 MXene towards the oxygen reduction reaction and zinc–air batteries.* Journal of Materials Chemistry A, 2017. **5**(39): p. 20818-20823.
205. Yu, X., et al., *Decorating g-C3N4 nanosheets with Ti3C2 MXene nanoparticles for efficient oxygen reduction reaction.* Langmuir, 2019. **35**(8): p. 2909-2916.
206. Zhao, J., et al., *Ti 3 C 2 T x (T= F, OH) MXene nanosheets: conductive 2D catalysts for ambient electrohydrogenation of N 2 to NH 3.* Journal of Materials Chemistry A, 2018. **6**(47): p. 24031-24035.
207. Luo, Y., et al., *Efficient electrocatalytic N2 fixation with MXene under ambient conditions.* Joule, 2019. **3**(1): p. 279-289.

208. Aba, M.M., I.L. Sauer, and N.B. Amado, *Comparative review of hydrogen and electricity as energy carriers for the energy transition.* International Journal of Hydrogen Energy, 2024. **57**: p. 660-678.
209. Ishaq, H., I. Dincer, and C. Crawford, *A review on hydrogen production and utilization: Challenges and opportunities.* International Journal of Hydrogen Energy, 2022. **47**(62): p. 26238-26264.
210. Chen, Z., et al., *Electrocatalysts for acidic oxygen evolution reaction: Achievements and perspectives.* Nano Energy, 2020. **78**: p. 105392.
211. Wu, Z.P., et al., *Non-noble-metal-based electrocatalysts toward the oxygen evolution reaction.* Advanced Functional Materials, 2020. **30**(15): p. 1910274.
212. Wang, K., et al., *Designing 3d dual transition metal electrocatalysts for oxygen evolution reaction in alkaline electrolyte: Beyond oxides.* Nano Energy, 2020. **77**: p. 105162.
213. Kaushik, S., X. Xiao, and Q. Xu, *Design strategies of electrocatalysts for acidic oxygen evolution reaction.* EnergyChem, 2023. **5**(5): p. 100104.
214. Goñi-Urtiaga, A., D. Presvytes, and K. Scott, *Solid acids as electrolyte materials for proton exchange membrane (PEM) electrolysis.* International journal of hydrogen energy, 2012. **37**(4): p. 3358-3372.
215. Mondschein, J.S., et al., *Intermetallic Ni2Ta electrocatalyst for the oxygen evolution reaction in highly acidic electrolytes.* Inorganic chemistry, 2018. **57**(10): p. 6010-6015.
216. Liu, A., et al., *Economical Fe-doped Ta2O5 electrocatalyst toward efficient oxygen evolution: a combined experimental and first-principles study.* MRS Communications, 2017. **7**(3): p. 563-569.
217. Xiao, W., et al., *High catalytic activity of oxygen-induced (200) surface of Ta2O5 nanolayer towards durable oxygen evolution reaction.* Nano Energy, 2016. **25**: p. 60-67.
218. Yue, X., Y. Jin, and P.K. Shen, *Highly stable and efficient non-precious metal electrocatalysts of tantalum dioxyfluoride used for the oxygen evolution reaction.* Journal of Materials Chemistry A, 2017. **5**(18): p. 8287-8291.
219. Ruiz-Cornejo, J.C., et al., *Carbon nanofiber-supported tantalum oxides as durable catalyst for the oxygen evolution reaction in alkaline media.* Renewable Energy, 2021. **178**: p. 307-317.
220. Ahmed, I., et al., *Bifunctional electrochemical OER and HER activity of Ta 2 O 5 nanoparticles over Fe 2 O 3 nanoparticles.* New Journal of Chemistry, 2023. **47**(37): p. 17284-17292.
221. Wang, Z., et al., *Predicting aqueous stability of solid with computed Pourbaix diagram using SCAN functional.* npj Computational Materials, 2020. **6**(1): p. 160.
222. Boughaba, S., et al., *Synthesis of tantalum pentoxide films by pulsed laser deposition: material characterization and scale-up.* Thin Solid Films, 2000. **358**(1-2): p. 104-113.
223. Hur, J.-H., *First principles study of the strain effect on band gap of λ phase Ta2O5.* Computational Materials Science, 2019. **164**: p. 17-21.
224. Lee, S.-H., et al., *Hidden structural order in orthorhombic Ta 2 O 5.* Physical review letters, 2013. **110**(23): p. 235502.
225. Grimme, S., et al., *A consistent and accurate ab initio parametrization of density functional dispersion correction (DFT-D) for the 94 elements H-Pu.* The Journal of chemical physics, 2010. **132**(15).
226. Grimme, S., S. Ehrlich, and L. Goerigk, *Effect of the damping function in dispersion corrected density functional theory.* Journal of computational chemistry, 2011. **32**(7): p. 1456-1465.
227. Wang, L., T. Maxisch, and G. Ceder, *Oxidation energies of transition metal oxides within the GGA+ U framework.* Physical Review B, 2006. **73**(19): p. 195107.
228. Jain, A., et al., *Formation enthalpies by mixing GGA and GGA+ U calculations.* Physical Review B, 2011. **84**(4): p. 045115.

229. Back, S., A.H. Bagherzadeh Mostaghimi, and S. Siahrostami, *Enhancing Oxygen Reduction Reaction Activity Using Single Atom Catalyst Supported on Tantalum Pentoxide.* ChemCatChem, 2022. **14**(11): p. e202101763.
230. Miao, X., et al., *Insulating High-Entropy Ruthenium Oxide as a Highly Efficient Oxygen-Evolving Electrocatalyst in Acid.* ACS Catalysis, 2023. **13**(6): p. 3983-3989.
231. Schütt, P., et al., *First-Principles Study on Nb2C–X (X= S, Cl, F)/Graphene Heterostructures: Assessing Aqueous Stability and Implications for Electrocatalysis.* ACS Applied Nano Materials, 2023. **6**(23): p. 21829-21838.
232. Back, S., K. Tran, and Z.W. Ulissi, *Toward a design of active oxygen evolution catalysts: insights from automated density functional theory calculations and machine learning.* Acs Catalysis, 2019. **9**(9): p. 7651-7659.
233. Zhang, J., et al., *Advances in thermodynamic-kinetic model for analyzing the oxygen evolution reaction.* Acs Catalysis, 2020. **10**(15): p. 8597-8610.
234. Feng, J., et al., *Accelerating the Discovery of Metastable IrO2 for the Oxygen Evolution Reaction by the Self-Learning-Input Graph Neural Network.* JACS Au, 2023. **3**(4): p. 1131-1140.
235. Solla-Gullon, J., F. Vidal-Iglesias, and J. Feliu, *Shape dependent electrocatalysis.* Annual Reports Section" C"(Physical Chemistry), 2011. **107**: p. 263-297.
236. Saha, S., P. Gayen, and V.K. Ramani, *Facet-dependent chlorine and oxygen evolution selectivity on RuO2: An ab initio atomistic thermodynamic study.* ChemCatChem, 2020. **12**(19): p. 4922-4929.
237. Soin, N., et al., *Microstructural and electrochemical properties of vertically aligned few layered graphene (FLG) nanoflakes and their application in methanol oxidation.* Materials Chemistry and Physics, 2011. **129**(3): p. 1051-1057.
238. Ji, L., et al., *Modification of electron structure on the semiconducting single-walled carbon nanotubes for effectively electrosensing guanine and adenine.* Analytica Chimica Acta, 2019. **1079**: p. 86-93.
239. Rastogi, P., et al., *Doping strategies for monolayer MoS2 via surface adsorption: a systematic study.* The Journal of Physical Chemistry C, 2014. **118**(51): p. 30309-30314.
240. Ma, N., et al., *Curvature effects regulate the catalytic activity of Co@ N4-doped carbon nanotubes as bifunctional ORR/OER catalysts.* Journal of Colloid and Interface Science, 2024. **654**: p. 1458-1468.
241. Xin, H., et al., *Effects of d-band shape on the surface reactivity of transition-metal alloys.* Physical Review B, 2014. **89**(11): p. 115114.
242. Xin, H. and S. Linic, *Communications: Exceptions to the d-band model of chemisorption on metal surfaces: The dominant role of repulsion between adsorbate states and metal d-states.* The Journal of chemical physics, 2010. **132**(22).
243. Jiao, Y., et al., *Activity origin and catalyst design principles for electrocatalytic hydrogen evolution on heteroatom-doped graphene.* Nature Energy, 2016. **1**(10): p. 1-9.
244. Cohen, I., et al., *Pearson correlation coefficient.* Noise reduction in speech processing, 2009: p. 1-4.
245. Wang, L., et al., *Surface reconstruction engineering of cobalt phosphides by Ru inducement to form hollow Ru-RuPx-CoxP pre-electrocatalysts with accelerated oxygen evolution reaction.* Nano Energy, 2018. **53**: p. 270-276.
246. Fu, Z., et al., *Rational design of MXene-based vacancy-confined single-atom catalyst for efficient oxygen evolution reaction.* Journal of Energy Chemistry, 2024. **98**: p. 663-669.
247. Yang, C., et al., *Electronic properties of double-atom catalysts for electrocatalytic oxygen evolution reaction in alkaline solution: a DFT study.* Nanoscale, 2022. **14**(1): p. 187-195.
248. Zhou, Y., et al., *Theoretical Investigation of Single-, Double-, and Triple-p-block Metals Anchored on g-CN Monolayer for Oxygen Electrocatalysis.* The Journal of Physical Chemistry Letters, 2024. **15**(46): p. 11454-11461.

249. Zhang, Z., et al., *First-principles study of oxygen evolution on Co3O4 with short-range ordered Ir doping.* Molecular Catalysis, 2023. **535**: p. 112852.
250. Kwon, S., et al., *Facet-Dependent Oxygen Evolution Reaction Activity of IrO2 from Quantum Mechanics and Experiments.* Journal of the American Chemical Society, 2024.
251. Davis, E.M., et al., *Facet Dependence of the Oxygen Evolution Reaction on Co3O4, CoFe2O4, and Fe3O4 Epitaxial Film Electrocatalysts.* Journal of the American Chemical Society, 2024.
252. Pan, D., et al., *Impacts of ruthenium valence state on the electrocatalytic activity of ruthenium ion-complexed graphitic carbon nitride/reduced graphene oxide nanosheets towards hydrogen evolution reaction.* Journal of Colloid and Interface Science, 2023. **629**: p. 591-597.
253. Wang, Y., et al., *DFT investigation of the oxygen reduction reaction over nitrogen (N) doped graphdiyne as an electrocatalyst: the importance of pre-adsorbed OH* and the solvation effect.* Materials Advances, 2023. **4**(24): p. 6542-6552.
254. Sebastián, D., et al., *Graphene-Supported Substoichiometric Sodium Tantalate as a Methanol-Tolerant, Non-Noble-Metal Catalyst for the Electroreduction of Oxygen.* ChemCatChem, 2015. **7**(6): p. 911-915.
255. Zhang, G., et al., *Engineering of a Low-Cost, Highly Active, and Durable Tantalate–Graphene Hybrid Electrocatalyst for Oxygen Reduction.* Advanced Energy Materials, 2020. **10**(24): p. 2000075.
256. Şahin, E.O., et al., *Sodium tantalates: monitoring crystallization via in situ total X-ray scattering.* CrystEngComm, 2023. **25**(15): p. 2256-2263.
257. Heyns, A., K.-J. Range, and M. Wildenauer, *The vibrational spectra of NbBO4, TaBO4, NaNb3O8 and NaTa3O8.* Spectrochimica Acta Part A: Molecular Spectroscopy, 1990. **46**(11): p. 1621-1628.
258. Alves, G.A., et al., *Band gap narrowing of Bi-doped NaTaO3 for photocatalytic hydrogen evolution under simulated sunlight: a pseudocubic phase induced by doping.* ACS Applied Energy Materials, 2020. **4**(1): p. 671-679.
259. Modak, B., K. Srinivasu, and S.K. Ghosh, *Band gap engineering of natao 3 using density functional theory: a charge compensated codoping strategy.* Physical Chemistry Chemical Physics, 2014. **16**(32): p. 17116-17124.
260. Wang, B., et al., *Anion-doped NaTaO3 for visible light photocatalysis.* The Journal of Physical Chemistry C, 2013. **117**(44): p. 22518-22524.
261. Tang, Z.-K., et al., *Understanding the influence of cation doping on the surface chemistry of NaTaO3 from first principles.* ACS Catalysis, 2019. **9**(11): p. 10528-10535.
262. Cai, J., et al., *First-Principles Investigation on Electronic Properties and Surface Reactions of NaTaO3 Adsorbed with Single-Metal Atoms.* The Journal of Physical Chemistry C, 2023. **127**(14): p. 6702-6713.
263. Hu, C.-C. and H. Teng, *Influence of structural features on the photocatalytic activity of NaTaO3 powders from different synthesis methods.* Applied Catalysis A: General, 2007. **331**: p. 44-50.
264. Liu, Y., et al., *DFT Electronic Structure and Vibrational Signatures of Intermediates in Water Oxidation on Perovskite NaTaO3.* The Journal of Physical Chemistry C, 2023. **127**(44): p. 21514-21525.
265. Ma, W., et al., *A novel high-entropy MXene Ti1. 1V1. 2Cr0. 8Nb1. 0Mo0. 9C4Tx for high-performance supercapacitor.* Scripta Materialia, 2023. **235**: p. 115596.
266. Chen, L., et al., *Two-Dimensional MXenes Derived from Medium/High-Entropy MAX Phases M2GaC (M= Ti/V/Nb/Ta/Mo) and their Electrochemical Performance.* Small Methods, 2023. **7**(8): p. 2300054.

267. Dai, Y., et al., *Designing Highly Efficient Electrocatalyst for ORR and OER Based on Nb2CO2 MXene: The Role of Transition Metals and N-Doping Content.* Langmuir, 2024. **40**(33): p. 17815-17825.
268. Zhang, W., et al., *Sulfur and nitrogen codoped Nb2C MXene for dendrite-free lithium metal battery.* Electrochimica Acta, 2021. **390**: p. 138812.
269. Wang, Y., et al., *Nb 2 N monolayer as a promising anode material for Li/Na/K/Ca-ion batteries: a DFT calculation.* Physical Chemistry Chemical Physics, 2021. **23**(21): p. 12288-12295.
270. Mao, T., et al., *Self-standing reduced graphene oxide/Nb2C MXene paper electrode with three-dimensional open structure for high-rate potassium ion storage.* Journal of Physics and Chemistry of Solids, 2022. **169**: p. 110838.
271. Berezin, F.A. and M. Shubin, *The Schrödinger Equation*. Vol. 66. 2012: Springer Science & Business Media.
272. Burke, K., *Perspective on density functional theory.* The Journal of chemical physics, 2012. **136**(15).
273. Hohenberg, P. and W. Kohn, *Inhomogeneous electron gas.* Physical review, 1964. **136**(3B): p. B864.
274. Kohn, W. and L.J. Sham, *Self-consistent equations including exchange and correlation effects.* Physical review, 1965. **140**(4A): p. A1133.
275. Sholl, D.S. and J.A. Steckel, *Density functional theory: a practical introduction*. 2022: John Wiley & Sons.
276. Tsuneda, T., *Exchange-Correlation Functionals*, in *Density Functional Theory in Quantum Chemistry*. 2014, Springer Japan: Tokyo. p. 101-124.

Appendix A. Density functional theory (DFT) method

Density Functional Theory (DFT) is a strong tool based on quantum mechanics, which can explore the electronic and catalytic properties of materials. DFT has become an important means in various fields, such as physics, chemistry, and materials science, which analyzes the behavior of electrons within atoms, molecules, and solids. In contrast to traditional methods relying on complex wave functions, the DFT method simplifies the many-body problem by focusing on electron density as the core quantity. So, it can efficiently study the systems with many particles with high accuracy.

This chapter introduces key concepts in quantum mechanics, the challenges associated with these principles, and how DFT offers a practical solution for analyzing complex systems efficiently.

A.1 Schrödinger equation

Schrödinger equation describes the behavior of quantum mechanical systems [271]. The time-independent form of the Schrödinger equation is as follows:

$$\hat{H}\Psi(\vec{\boldsymbol{r}}) = E\Psi(\vec{\boldsymbol{r}}) \qquad \text{Equation 0-1}$$

in this equation, $\hat{H}$ is the Hamiltonian (total energy) operator, *E* is the energy level of the system, and $\Psi(\vec{\boldsymbol{r}})$ is the wavefunction of the system. The Hamiltonian (total energy) operator is given in the following equation:

$$\hat{H} = \frac{\hbar}{2m}\nabla^2 + V(\vec{\boldsymbol{r}}) \qquad \text{Equation 0-2}$$

where, $\hbar$ refers to the reduced Planck's constant, *m* is the mass of the particle, and ∇^2 is the Laplacian operator. The left term in Equation A-2 is kinetic energy, and the second term ($V(\vec{\boldsymbol{r}})$) is the total potential energy. Solving the Schrödinger equation for large systems is computationally infeasible, and its solution is only available for a small number of physical systems. This is due to the dimensionality of the wavefunction. For instance, the wavefunction would have 3N dimensions for a system containing N electrons. DFT has been developed to address this issue and solve the Schrödinger equation for large systems [272]. Generally, DFT simplifies the problem by decreasing the dimensionality of the calculations.

A.2 The Kohn-Sham equations

The theoretical foundations of DFT were established by Pierre Hohenberg and Walter Kohn in the 1960s. They introduced the concept that the ground-state energy of a system can be determined based on the density of electrons, which simplified the many-body quantum problem. Then, Kohn-Sham reformulated the many-electron Schrödinger equation to a set of single-electron equations. In other words, the many-bodied equation for all N electrons is not solved at once, and the problem is divided. So, the equation is solved for a single electron that is physically affected by other electrons through the charge density of all N electrons [273-275]. The Kohn-Sham equation is as follows:

$$\left[-\frac{\hbar}{2m}\nabla^2 + V(\vec{\boldsymbol{r}}) + V_H(\vec{\boldsymbol{r}}) + V_{XC}(\vec{\boldsymbol{r}})\right]\varphi_i(\vec{\boldsymbol{r}}) = \varepsilon_i\varphi_i(\vec{\boldsymbol{r}}) \qquad \text{Equation 0-3}$$

in this equation, $\varphi_i(\vec{\boldsymbol{r}})$ denotes the one-electron wavefunction and ε_i is the Kohn-Sham electron energy level. Similar to the Schrödinger equation, the first term ($-\frac{\hbar}{2m}\nabla^2$) of the Kohn-Sham equation is related to the electron kinetic energy. $V(\vec{\boldsymbol{r}})$ is related to the electrostatic interaction between the electron and nuclei. In the equation, $V_H(\vec{\boldsymbol{r}})$ refers to the Hartree potential, which is the Coulomb repulsion of the given electron and the charge density of all electrons in the system (electron-electron repulsion). Moreover, the $V_{XC}(\vec{\boldsymbol{r}})$ is called exchange-correlation potential, which is discussed in Section 2.4. While $V(\vec{\boldsymbol{r}})$ and $V_H(\vec{\boldsymbol{r}})$ can be directly calculated, the exchange-correlation potential ($V_{XC}(\vec{\boldsymbol{r}})$) is approximated in DFT methods, which is critical to the accuracy of the DFT calculations.

A.3 Plane-Wave Basis Sets and Periodic Boundary Conditions

For solid-sate systems, DFT calculations use periodic boundary conditions to model the complicated structures. So, to show the one-electron wavefunctions, a linear set of plane waves is used. The electronic wavefunctions are expanded using plane-wave basis sets, which are given in reciprocal space as follows:

$$\varphi_{\vec{\boldsymbol{k}}}(\vec{\boldsymbol{r}}) = \sum_{\vec{\boldsymbol{G}}} C_{\vec{\boldsymbol{G}}+\vec{\boldsymbol{k}}}\exp(\mathrm{i}(\vec{\boldsymbol{G}}+\vec{\boldsymbol{k}}).\vec{\boldsymbol{r}}) \qquad \text{Equation A-4}$$

in this equation, $\vec{\boldsymbol{k}}$ is the wavefactor in the reciprocal space, $\vec{\boldsymbol{G}}$ is the reciprocal lattice vector, $C_{\vec{\boldsymbol{G}}+\vec{\boldsymbol{k}}}$ are Fourier coefficients, and $\exp(\mathrm{i}(\vec{\boldsymbol{G}}+\vec{\boldsymbol{k}}).\vec{\boldsymbol{r}}$ is a planewave. To simplify the DFT

calculations, limiting the number of $\vec{G}$ vectors determines the energy cut-off for the plane waves in the calculations.

A.4 Exchange-Correlation functionals

Finding the exact form of the exchange-correlation functional is complicated for most systems. So, approximations are used, and their quality can strongly affect the accuracy of DFT calculations. The main approximations include local-density approximation (LDA), generalized gradient approximation (GGA), and Heyd-Scuseria-Ernzerhof (HSE) hybrid functional [275].

A.4.1 LDA

The LDA method considers the homogeneous electron gas model. In LDA, it is assumed that the exchange-correlation energy at each point only depends on the local electron density.

$$E_{xc}^{\mathrm{LDA}} = \int \rho(\mathbf{r})\varepsilon_{xc}(\rho)d\mathbf{r} \qquad \text{Equation 0-5}$$

in this equation, ε_{xc} refers to the exchange-correlation energy per electron of the homogeneous electron gas at point **r**. This approximation works well for systems with high or uniform charge density, such as metallic systems. However, it has poor accuracy for systems with varying charge density and localized charge density. Moreover, LDA is not suitable for finding the binding energies and band gap for the semiconductors.

A.4.2 GGA

In the GGA method, the gradient of electron density or distribution inhomogeneity is considered to improve LDA. The GGA equation is shown in the following:

$$E_{xc}^{\mathrm{GGA}} = \int \rho(\mathbf{r})\varepsilon_{xc}(\rho,\nabla\rho)d\mathbf{r} \qquad \text{Equation 0-6}$$

in this equation, E_{xc}^{GGA} is the exchange-correlation energy in GGA, $\rho(\mathbf{r})$ shows electron density at position **r**, and $\varepsilon_{xc}(\rho,\nabla\rho)$ denotes exchange-correlation energy density per electron. The GGA method has better accuracy for systems with inhomogeneous charge densities. Moreover, it can predict bond length and reaction energies better than the LDA method. The Perdew-Burke-Ernzerhof (PBE) functional is the most used GGA functional, which has been used in our DFT calculations.

A.4.3 DFT + U

The DFT + U approach has been developed to address the errors in DFT calculations by GGA and LDA for systems with strongly localized electrons. Transition metal oxides are the main materials that the GGA and LDA approaches fail to analyze their electronic properties. In fact, the strong on-site Coloumb interactions between localized d or f electrons cannot be accurately described using GGA and LDA. In the DFT + U method, on-site potential (Hubbard-U) is added to localized electrons (d or f electrons), and the non-local electrons (s electrons) are treated using standard LDA or GGA approaches.

In the Hubbard-U model used in our calculations, the Coloumb interaction is considered on a mean-field level. So, the total energy in DFT + U is given by:

$$E_{\mathrm{DFT}+U} = E_{\mathrm{DFT}} + E_U - E_{DC} \qquad \text{Equation 0-7}$$

in this equation, E_{DFT} is the total energy calculated using standard GGA or LDA approaches. The E_U term is the total energy calculated by adding the extra potential to localized d and f electrons. Then, E_{DC} is used to subtract the double-counting part since the total energy of d or f electrons is already included in the E_{DFT} term.

A.4.4 HSE Hybrid Functional

In the HSE hybrid functional, the PBE exchange-correlation functional is modified by incorporating a fraction of the Hartree-Fock exchange integral for the short-range part [276]. A major drawback of GGA exchange functionals, such as PBE, is that they cannot accurately describe exchange interactions at long range. As a result, GGA exchange functionals result in inaccurate bandgap energies for semiconductors compared to experimental values. In HSE hybrid functionals, part of the short-range GGA exchange is replaced with Hartree-Fock exchange, which makes bandgap energies closer to experimental values. In this method,

$$E_{xc}^{\mathrm{HSE}} = aE_x^{\mathrm{SR-HF}} + (1-a)E_x^{\mathrm{PBE}} + E_c^{\mathrm{PBE}} \qquad \text{Equation A-8}$$

in this equation, $E_x^{\mathrm{SR-HF}}$ refers to the short-range part of the Hartree-Fock exchange integral. Moreover, E_x^{PBE} and E_C^{PBE} denote the PBE exchange functional used for the remaining interactions and PBE correlation effects, respectively. In this functional, a is the mixing parameter; for instance, when $a = 1/4$ is used, 25% of the short-range Hartree-Fock exchange is included, and the remaining 75% will be based on the PBE exchange functional. The main advantage of the HSE hybrid functional is the high accuracy in investigating the electronic

properties of semiconductors. However, this method is computationally more expensive than DFT + U, which causes it to be less practical in simulating large systems.

A.5 DFT parameters

Different parameters determine the accuracy of DFT calculations [275]. This includes the pseudopotentials, cut-off energy, k-point sampling, and convergence criteria. Pseudopotentials determine how the core electrons of each atom are treated and define which electrons are considered in the calculations as valence electrons. Typically, all electrons are not included in DFT calculations, and the pseudopotentials consider the simplified version of calculations and analyze the interactions between valence electrons and the core.

The maximum kinetic energy of plane waves in the basis set expansion is determined using the cut-off energy, which is a critical parameter to achieve accurate results. When the cut-off energy is higher, more plane waves are included, which improves the accuracy of the calculations.

Sampling the Brillouin zone is crucial to calculate the electronic properties of periodic systems. The Brillouin zone is defined as the smallest repeating unit in the reciprocal space. Sampling the Brillouin zone accurately leads to a better representation of the electronic structure. In k-point sampling, discrete points in the Brillouin zone are selected to represent the electronic wavefunctions of a periodic system. The Brillouin zone is the fundamental region in the reciprocal space, containing all the unique wavefactors required to describe the periodicity of the system. The Monkhorst-pack grid is the most common approach for k-point sampling. In this approach, a uniform grid of k-points is generated in the Brillouin zone, controlling the density of points along each reciprocal lattice vector. The grid can ensure that the sample is efficient while the symmetry of the crystal is preserved.

The convergence criteria in DFT calculations include energy convergence, force convergence, and charge density convergence. The energy convergence is the total energy difference between two iterations. The force convergence is attributed to the atomic forces on each atom during the optimization of the structure. Charge density convergence is essential for self-consistency in the Kohn-Sham equations.